Combined Exposure to Cobalt and Nickel: Exploring their Impact on Cellular Metabolism, Oxidative Stress, and Genomic Integrity

Dissertation

Zur Erlangung des Doktorgrades
der Naturwissenschaft (Dr. rer. nat.) in der Fachgruppe Chemie und Biologie
der Mathematisch Naturwissenschaftlichen Fakultät
der Bergischen Universität Wuppertal

vorgelegt von
Alicia Thiel
aus Hagen

– 2024 –

Dekan:in:	Prof. Dr. Francesco Knechtli
Erste:r Gutachter:in:	Prof. Dr. Julia Bornhorst
Zweite:r Gutachter:in:	Prof. Dr. Martin Simon
Tag der mündlichen Prüfung:	06.09.2024

Introductory remarks on the structure of the dissertation

The following dissertation is written in a semi-cumulative style, including five first-authorship publications presented in chapters 3 – 7. Each of these chapters comprises papers that have been either published in or submitted to peer-reviewed journals. The initial chapters 1 and 2 provide the general theoretical background to the project, while each paper introduction gives more detailed information. The thesis concludes with a final discussion and outlook in chapter 8. Supplementary materials for each chapter are gathered in the appendix.

Each published paper within this dissertation retains all comments and feedback from co-authors, reviewers, and editors during manuscript preparation and peer-reviewing process and is integrated in this thesis unchanged. To facilitate better comprehension, references, figures, and tables are numbered sequentially throughout the entire dissertation. Given that these papers are published in different journals, variations in structure, abbreviations, and spelling (British and American English) are present. To maintain a consistent design in this thesis, some figures and tables have been modified, but the scientific content remains unchanged.

Table of Content

Figures

Tables

List of Abbreviations

4-HNE	4-hydroxynonenal
8-oxodG	8-oxoguanine
Ac-DEVD-AFC	*N*-acetyl-asp-glu-val-asp-7-amino-4-trifluoromethylcoumarin
ACN	acetonitrile
ADP	adenosine diphosphate
AFC	7-amino-4-trifluoromethylcoumarin
AMP	adenosine monophosphate
AMPK	AMP-activated protein kinase
AP-1	activator protein 1
ARE	antioxidant response element
ATF4	activating transcription factor 4
ATP	adenosine triphosphate
AU	alkaline unwinding
BCA	bicinchoninic acid
BER	base excision repair
BLVR	biliverdin reductase
BSO	*L*-buthionine-(S,R)-sulfoximine
bw	bodyweight
C. elegans	*Caenorhabditis elegans*
Ca	calcium
CAD	collision gas
Carboxy-DCFH-DA	carboxy-2',7'-dichlorodihydrofluorescein-diacetate
CAT	catalase
CE	collision energy
Cer	ceramide
CGC	caenorhabditis genetics center

Co	cobalt
Cul3	cullin3
CUR	curtain gas
CXP	collision cell exit potential
DAD	diode array detector
DAG	diacylglycerol
DAPI	4′,6-diamidino-2-phenylindole
DDR	DNA damage response
DEG	differentially expressed genes
dhCer	dihydroceramide
dhSM	dihydrosphingomyelin
dhSph	dihydrosphingosine
DMSO	dimethyl sulfoxide
DMT-1	divalent metal transporter 1
DNA	deoxyribonucleic acid
DP	declustering potential
DSB	double-strand breaks
dsDNA	double-stranded DNA
DTNB	5‘,5‘-dithiobis(2-nitrobenzoic acid)
DTT	dithiothreitol
E. coli	*Escherichia coli*
ECD	electrochemical detection
EDTA	ethylenediaminetetraacetic acid
EFSA	European Food Safety Authority
ELISA	enzyme-linked immunosorbent assay
EP	entrance potential
EPO	erythropoietin
ESI	electrospray ion source
ETC	electron transport chain

FA	formic acid
FBS	fetal bovine serum
FD	fluorescence detection
Fe	iron
FPG	formamidopyrimidine DNA glycosylase
FTH	ferritin heavy chain
FTL	ferritin light chain
GCL	γ-glutamate-cysteine ligase
GO	gene ontology
GPC3	glypican-3
GPx	glutathione peroxidase
GR	glutathione reductase
GSH	glutathione
GSR	glutathione reductase
GSS	glutathione synthetase
GSSG	glutathione disulfide
GST	glutathione S-transferase
H_2O_2	hydrogen peroxide
HIF-1	hypoxia-inducible factor 1
HMOX-1	heme oxygenase-1
HPLC	high performance liquid chromatography
HR	homologous recombination
HSA	human serum albumin
IARC	International Agency for Research on Cancer
ICP-OES	inductively coupled plasma-optical emission spectrometry
IS	ion spray voltage
KEAP1	Kelch like-ECH-associated protein 1
LacCer	lactosylceramide

LC-MS/MS	liquid chromatography-tandem mass spectrometry
LDH	lactate dehydrogenase
LIB	lithium-ion battery
LOD	limit of detection
LOQ	limit of quantification
m/z	mass to charge ratio
MDA	malondialdehyde
MEM	Eagle's Minimum Essential Medium
MMR	mismatch repair
Mn	manganese
MoM	metal-on-metal
MRM	multiple reaction monitoring
mRNA	messenger ribonucleic acid
mtDNA	mitochondrial DNA
NaCl	sodium chloride
NADH	nicotinamide adenine dinucleotide
NADPH	nicotinamide adenine dinucleotide phosphate
NEA	non-essential amino acids
NEM	N-ethylmaleimide
NER	nucleotide excision repair
NF-κB	nuclear factor kappa-light-chain-enhancer of activated B cells
NGM	nematode growth medium
NHEJ	non-homologous end joining
Ni	nickel
NO	nitric oxide
NOX	NADPH oxidase
NQO1	NAD(P)H quinone oxidoreductase 1

Nrf2	nuclear factor erythroid 2-related factor 2
$O_2^{\bullet-}$	superoxide anion
OD	optical density
OGG1	8-oxoguanine DNA glycosylase-1
$^{\bullet}OH$	hydroxyl radical
OPA	*o*-phthalaldehyde
p53	tumor protein p53
PARG	PAR glycohydrolase
PARP	poly(ADP-ribose) polymerase
PARylation	poly-ADP-ribosylation
PBS	phosphate buffer saline
PCA	principal component analysis
PKC	protein kinase C
PRDX	peroxiredoxin
RNA	ribonucleic acid
ROS	reactive oxygen species
RONS	reactive oxygen and nitrogen species
RT-qPCR	reverse transcription-quantitative polymerase chain reaction
SD	standard deviation
SEM	standard error of the mean
SM	sphingomyelin
sMaf	small Maf proteins
SOD	superoxide dismutase
Sph	sphingosine
SQSTM1	sequestosome 1
SRXN	sulfiredoxin
SSA	sulfosalicylic acid
ssDNA	single-stranded DNA

TBA	thiobarbituric acid
*t*BOOH	*tert*-butylhydroperoxide
TCA	tricarboxylic acid
TEM	temperature
TMRM	tetramethylrhodamine methyl ester
Tf	transferrin
TfR	transferrin receptor
TRPM7	transient receptor potential melastatin type 7
TXN	thioredoxin
TXNRD	thioredoxin reductase
Ub	ubiquitin
UV	ultraviolet detection
WGP	wheat grass powder
WT	wild type
Y	yttrium
ZIP	Zrt- and Irt-like protein family
Zn	zinc
γ-GCS	γ-glutamylcysteine synthetase

Summary

Metal toxicity poses significant environmental and human health risks, with cobalt (Co) and nickel (Ni) being particularly concerning due to their extensive use in industrial applications. These metals are crucial in the production of lithium-ion batteries, alloys, catalysts, and pigments, leading to heightened environmental contamination and, consequently, human exposure through food and drinking water. Notably, Co is integral in metal-on-metal (MoM) hip implants, raising concerns about its toxicity when released into the body. Overexposure to Co and Ni can cause serious health issues, including neurological, cardiovascular, and thyroid dysfunctions. Furthermore, both metals are recognized carcinogens upon inhalation, classified by the International Agency for Research on Cancer (IARC) as group 2A and group 1 carcinogens, respectively. Despite substantial evidence of their individual toxicities, limited data exists on the combined effects of Co and Ni, which is a more realistic exposure scenario given their frequent co-occurrence in the environment. This research aimed to fill this gap by investigating the combined impact of Co and Ni on liver carcinoma cells (HepG2) and astrocytoma cells (CCF-STTG1), given that the liver and brain are potentially important targets in Co and Ni intoxication. Additionally, the model organism *Paramecium tetraurelia* was used to elucidate potential ecological implications of metal contamination.

Glutathione (GSH) plays a pivotal role in cellular health, crucial for maintaining redox balance and facilitating detoxification processes, with its reduced form predominating under normal conditions. Oxidative stress can shift GSH levels, increasing the oxidized form GSSG, which highlights the importance of accurately measuring both GSH and GSSG to assess oxidative status and cellular injury. Commonly used methods often lacked the sensitivity and specificity to detect low levels of GSSG, particularly when dealing with small sample sizes or complex biological matrices. To address these limitations, the first part of this thesis focused on the development of a novel LC-MS/MS method,

allowing for the simultaneous quantification of GSH and GSSG across various biological matrices. This new method focused on improving existing techniques by simplifying sample preparation, enhancing specificity, and accelerating the overall analysis process, thereby providing a reliable and stable tool for investigating oxidative stress and cellular health.

HepG2 cells demonstrated higher sensitivity to Co and Ni, consistent with a higher cellular amount, compared to CCF-STTG1 cells. Notably, Co exposure led to the highest toxicity and cellular accumulation compared to Ni. This differential sensitivity highlights the importance of target cell type in assessing metal toxicity. Simultaneous exposure to both metals revealed an interaction in their transport mechanisms, with prioritized Co uptake and decreased Ni levels compared to individual treatment. DMT-1 was identified as a key transporter for both metals, with its presence in cell nuclei and mitochondrial membranes indicating these organelles as important targets for Co and Ni toxicity. Investigation of alterations in cellular metabolism in HepG2 cells revealed the activation and nuclear translocation of Nrf2 by both metals. This activation led to increased expression of genes related to Nrf2-response pathways, discovered by transcriptomic analysis. To verify these analysis, transcriptomic analysis was combined with quantitative and analytical methods, providing detailed insights into altered metabolic pathways. Combined Co and Ni exposure notably affected iron metabolism, by upregulating the gene and protein expression of heme degrading HMOX-1 and iron storage protein FTL. Additionally, genes associated with glutathione synthesis were increasingly expressed, with corresponding changes in the levels of the amino acids glutamate, glutamine, and cysteine. Exposure to Co and Ni also significantly altered sphingolipid and diacylglycerol metabolism. LC-MS/MS revealed enhanced levels of dihydroceramides, dihydrosphingomyelins, and diacylglycerols, but decreased cellular amount of ceramides, sphingosine and lactosylceramides. High Co concentrations resulted in significant increased ROS production, which corresponded with elevated GSSG levels and oxidative DNA damage, assessed by fluorescent dye,

LC-MS/MS, and FPG modified comet assay, respectively. The oxidative stress induced by Co primarily caused single-strand breaks, whereas Ni exposure led to the formation of double-strand breaks. Both metals activated the DNA damage response pathway PARylation. The genotoxic effects of Co and Ni were further evidenced by induction of micronuclei, indicating chromosomal damage. Additionally, exposure to Co and Ni disrupted normal cell division, resulting in multinucleated HepG2 cells. This aberrant cell division was associated with the activation of caspase-3 and the release of lactate dehydrogenase (LDH), markers of apoptotic and necrotic cell death.

Investigating the toxicological risks of Co and Ni on aquatic organisms using the ciliate *Paramecium tetraurelia* and its feeding bacteria *Klebsiella planticola* revealed higher sensitivity in paramecia to Ni compared to Co, despite similar cellular metal levels. Interestingly, combined exposure, especially under starvation, increased toxicity in paramecia and led to higher Ni levels than with single metal exposure. Transcriptomic analysis indicated that Co exposure upregulated pathways involved in amino acid metabolism while Ni disrupts inositol and phospholipid biosynthesis, with both metals causing redox stress and impairing DNA repair mechanisms. Feeding paramecia with metal-incubated *Klebsiella* resulted in increased metal accumulation and heightened toxicity, suggesting that bacteria play a role in metal uptake within the food chain.

In conclusion, this thesis provided novel insights into the cellular alterations and molecular mechanisms caused by Co and Ni, for further understanding of metal stress. Exposing HepG2 cells with both metals revealed their involvement in the activation of Nrf2 signaling pathway, affecting lipid metabolism and impairing genomic integrity. Simultaneous treatment of both metals exacerbated these effects, revealing a potential synergistic toxicity that underscores the importance of studying combined metal exposures. Additionally, the study underlined the ecological implications of Co and Ni contamination, demonstrating increased metal uptake and toxicity in paramecia and a significant role of bacteria in metal bioaccumulation within the food chain.

Chapter 1

Motivation and Scope of the Thesis

Chapter 1 – Motivation and Scope of the Thesis

1.1. Motivation of the thesis

The two trace elements Cobalt (Co) and Nickel (Ni) are significant in industrial use, with advancements in a variety of applications, especially for lithium-ion batteries, alloys, catalysts, cosmetics, pigments, and metal-on-metal (MoM) hip implants [1,2]. Besides this, their extensive use raises significant environmental and human health concerns caused by an overexposure. These metals contribute to environmental contamination and human ingestion via food, water, and occupational exposure, with notable levels found in vegetables, grains, seafood, and nuts [1,3]. Co is an essential trace element necessary as a co-factor in vitamin B12 and amino acid and protein formation, while Ni lacks a recognized biological function in humans [4]. Both metals pose serious health threats, including neurological, cardiovascular, and thyroid dysfunctions, as well as a carcinogenic potential [5,6].

Previous studies focused mainly on individual toxicity of Co and Ni, but simultaneous exposure is the more realistic scenario given their co-occurrence in the environment. Literature suggests hypotheses about Co and Ni toxicity mechanisms, revealing the role of Co generating reactive oxygen and nitrogen species (RONS), leading to oxidative stress, cellular death, and DNA damage [7]. Similarly, Ni exposure is linked to DNA crosslinks, impaired DNA repair, and mitochondrial dysfunction [8]. This thesis aimed to gain deeper understanding of Co and Ni toxicity mechanisms and explore potential synergistic effects of both metals. By combining untargeted transcriptomic analysis with analytical and quantitative methods, the impact of Co and Ni on human liver carcinoma cells (HepG2) and human astrocytoma cells (CCF-STTG1) was assessed, targeting different organs affected by Co and Ni. Additionally, potential ecotoxicological effects were investigated using the *in vivo* model organism *Paramecium tetraurelia*, providing insights into environmental implications of Co and Ni.

1.2. Scope of the thesis

This thesis focused on the following key points:

- Development of a LC-MS/MS method for simultaneous quantification of reduced and oxidized glutathione in different biological matrices

- Comparison of two different human cancer cell lines regarding bioavailability, oxidative stress, and cell death mechanisms caused by individual and simultaneous treatment with Co and Ni

- Further investigation of toxicity mechanisms in liver carcinoma cells exposed to Co and Ni, combining untargeted transcriptomic analysis with targeted analytical methods

- Assessment of the genotoxic potential of single and combined Co and Ni exposure in liver carcinoma cells

- Investigation of the ecotoxicological potential of Co and Ni by assessing the toxicity, bioavailability, and transcriptomic alterations in *Paramecium tetraurelia*

Chapter 2

General background information

Chapter 2 – General background information

2.1. Cobalt and Nickel

2.1.1. Sources and exposure

The two trace elements Cobalt (Co) and Nickel (Ni) are widely distributed in the environment, often found in the earth's crust in conjunction with other elements like copper. Major mining ores of Co and Ni are located in tropical regions, North America, northern Siberia, and central Africa [9]. Due to their versatile chemical properties, both metals are essential for a variety of industrial applications. They are crucial components in lithium-ion batteries, which are increasingly important due to the rise of electric vehicles, laptops, and smartphones [10]. Additionally, Co and Ni are used in alloys, catalysts, and pigments [11,12]. Ni, in particular, is widely used in the stainless-steel industry, producing kitchenware or medical instruments [13]. The ubiquitous use of Co and Ni leads to multiple exposure pathways. The most affected individuals are workers in mining and manufacturing industries or residents near industrial areas with contaminated air, water, or soil [2]. In the medical sector, Co is commonly used in hip implants, particularly in cobalt-chromium (CoCr) alloys, due to their durability and strength [14]. Despite these benefits, there are concerns regarding the release of metal ions into the human body due to implant corrosion, which can lead to adverse reactions. Consequently, patients require regular monitoring, and the use of metal-on-metal (MoM) hip implants decreased due to the associated risks [15]. Additionally, Co has been misused in the context of doping in sports, since it can stimulate the production of erythropoietin (EPO), which promotes the formation of red blood cells and subsequent improves oxygen delivery to muscles. Due to these effects and the potential serious health risks, Co is listed as a prohibited substance by the World Anti-Doping Agency [16]. Since Ni is resistant to oxidation and corrosion, it is commonly used in jewelry and other items with daily contact. In the European population, approximately 8 – 19 % of adults and 8 – 10 % of

children suffer from Ni-related contact allergies and dermatitis, with a higher prevalence among women. To limit Ni release from consumer products, the European Union's Nickel Directive regulates the amount of Ni released from these items [17].

Dietary intake of these metals also contributes to exposure. Highest Co concentrations are found in seafood (0.01 mg/kg), grains (0.01 mg/kg), nuts (0.09 mg/kg) and green leafy vegetables (0.009 mg/kg), leading to a daily exposure of about 0.1 – 0.5 µg/kg bw Co per day [3]. Next to this, people may take supplements containing Co, often in form of vitamin B12, to address deficiencies common among vegetarians, due to its primary presence in animal products [18]. Vitamin B12 is exclusively synthesized by microorganisms, thus it is not necessary to consume Co supplements directly, instead, active forms of B12 are essential [19]. The recommended daily intake of vitamin B12 is approximately 2.4 µg, containing about 0.1 µg of Co [18]. A deficiency state for Ni in humans has not been defined [20]. Foods with high Ni content are mostly plant-based, such as legumes, soy, and nuts (2.2 mg/kg) or cocoa (1.4 mg/kg), and spices (1.2 mg/kg), resulting in a daily intake of about 1.57 µg/kg bw Ni for elderly [6]. For Ni, the European Food Safety Authority (EFSA) has set a tolerable upper intake level (UL) at 13 µg/kg bw [6]. To safeguard industrial workers from inhalation risks associated with Co and Ni, there are established occupational safety guidelines for both metals [21].

2.1.2. Homeostasis

Co is an essential trace element in the human body since it is a key component of vitamin B12. This in turn is crucial for maintaining neurological and immune functions, producing red blood cells, and synthesizing DNA [22]. Additionally, Co acts as a cofactor in various enzymatic reactions within the cell metabolism [23]. Ni, on the other hand, does not have an established biological function in humans. However, it is essential in archaea, bacteria, or plants and its potential

role in human metabolism is often discussed [24]. The primary route of Co and Ni uptake for the general population is oral intake, resulting in absorption in the small intestine (5 – 20 % Co; 1 – 5 % Ni). Once absorbed, Co and Ni are transported in the bloodstream [4], where both metals are mainly bound to human serum albumin (HSA) [12,25]. Next to this, inhalation of small particles or dermal retention through skin contact are possible pathways for metal intake [26]. Both metals are distributed to various organs as kidney, heart, and brain, but the liver is the main target for storage [27,28].

Co and Ni exist in several oxidation states in biological systems, ranging from -1 to +4 for Ni and +1 to +5 for Co. However, the divalent Co(II) and Ni(II) is the most stable form [26,29]. Both Co and Ni belong to the same chemical group as Fe and have a similar ionic radius (Fe: 0.77 Å; Co: 0.72 Å; Ni: 0.69 Å), which endows them with comparable chemical properties crucial for cellular homeostasis [12]. However, specific mechanisms for the cellular transport of Co and Ni are not fully understood. Discussed transporters for both metals into cells are summarized in figure 1. One known transporter involved in Co and Ni homeostasis is the divalent metal transporter 1 (DMT-1), a proton-coupled transporter located on the plasma membrane and intracellularly in the nucleus and in the outer mitochondrial membrane, suggesting these organelles contain the highest amount of both metals [30,31]. DMT-1 can transport a variety of divalent metals, leading to possible interferences among other metals by competing for transport priority. It has been reported that DMT-1 has a higher affinity for Co compared to Ni [32]. In addition, Co(III) and Ni(II) may bind to the iron transport protein transferrin, suggesting transferrin receptor 1 (TfR1) as an option for their cellular transport [33,34]. The Zrt- and Irt-like protein family (ZIP, SLC39A) are the main transporters of Zn [35], but especially ZIP8 and 14 are also known to be symporters of various divalent cations, including Co and Ni [36,37]. Additionally, the cation channel transient receptor potential melastatin type 7 (TRPM7) is involved in homeostasis of both metals [38]. Since both metals

are transported by the same proteins and channels within cells, which exhibit different affinities for Co, Ni, and other metals, interactions affecting their cellular uptake are plausible. This interplay has been investigated in more detail in chapter 4. Knowledge about cellular storage proteins and exporters of Co and Ni remains still elusive and has to be addressed in future studies.

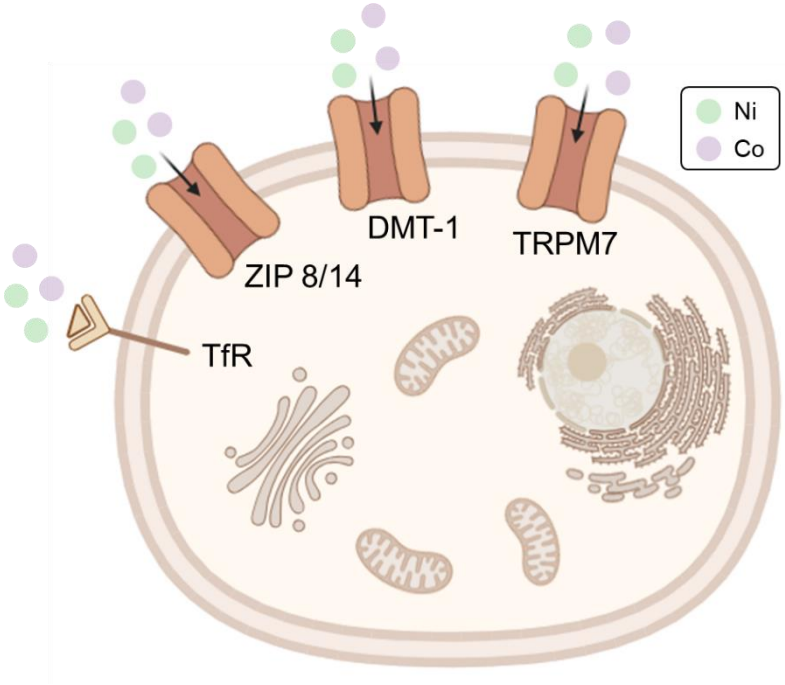

Figure 1: Schematic visualization of the transport mechanisms presumed for Co and Ni in human cells. Both metals are imported via the same transporters followed by further distribution into the cell compartments. This figure is partly designed using BioRender software.

2.1.3. Health effects and toxicity mechanisms

2.1.3.1. Cobalt

Long-term exposure to Co, whether through occupational settings, from failure of MoM hip implants, or by oral intake is associated with a variety of adverse health effects. These include cardiovascular diseases [39], thyroid dysfunction, or neurological impacts such as cognitive impairment, or hearing and visual disturbances [40]. Chronic dermal contact or inhalation may result in skin sensitization [41] and respiratory issues [42]. The International Agency for Research on Cancer (IARC) classified Co upon inhalation as possibly carcinogenic (group 2A) [43,44]. Co exerts its health effects through several

cellular processes. It occurs predominantly in two different oxidation states, +2 and +3, with Co(II) being more stable under typical redox and pH conditions. However, the possible conversion to the redox-active Co(III) makes it important in the generation of reactive oxygen species (ROS) from hydrogen peroxide (H_2O_2) via Fenton-like reactions. This in excess is leading to oxidative stress resulting in damage to for example DNA, proteins and lipids [45]. The formation of oxidative stress and its consequences are explained more detailed in chapter 2.2. The mitochondria are particularly vulnerable to Co toxicity, identified by a decreased mitochondrial membrane potential, which is causing mitochondrial dysfunction. An impaired function is associated with an altered calcium (Ca^{2+}) signaling, disrupted energy production and the formation of pro-apoptotic factors [46]. Furthermore, Co acts as a hypoxia-mimicking agent by activating hypoxia-inducible factor 1 alpha (HIF-1α) [47]. This activation triggers the transcription of HIF-target genes involved in the promotion of tumor development and growth [48]. Co can also substitute for other metal ions in enzymes, resulting in their inhibition and may disrupt the cellular homeostasis of other essential metals, thus affecting critical biological functions. For instance, it is reported that Co may inhibit thyroid iodine uptake by binding to necessary enzymes, such as tyrosine iodinase, necessary for the iodination of tyrosine [12]. Genotoxic effects of Co arise primarily through two mechanisms, including the ROS generation via Fenton-like reactions and the inhibition of DNA repair mechanisms. *In vitro* studies have shown that Co overexposure may lead to the formation of strand breaks, micronuclei formation, and DNA-protein crosslinks, as well as inhibition of DNA repair enzymes [8]. In addition, Zn ions in zinc finger motifs of DNA repair proteins can be substituted by other metal cations such as Co, primarily leading to their alteration and the inhibition of the nucleotide excision repair (NER) pathway [49]. However, to date, there is no evidence to suggest that cobalt causes cancer development through oral exposure.

2.1.3.2. Nickel

Acute toxicity of Ni primarily arises from inhalation of dust or fumes in occupational settings, leading to respiratory irritation and dermatitis upon skin contact [50]. Ni compounds are classified by the IARC as group 1 carcinogens, indicating a significant risk of lung cancer with chronic exposure [51]. Additionally, elevated levels of Ni are associated with neurotoxicity [52], cardiovascular diseases [53], and kidney damage [20]. Major mechanisms of Ni toxicity upon oral exposure involve the disruption of cellular redox balance through ROS generation, perturbing mitochondrial function or inhibiting the antioxidative defense systems [54,55]. In addition, Ni has an impact on cellular energy metabolism by inhibiting HIF prolyl hydroxylases, and thereby stabilizing HIF-1α. This accumulation leads to a decreased oxygen consumption and increased glycolysis, enhancing cell survival under anaerobic conditions [56]. Studies have shown that Ni causes mitochondrial dysfunction by altering the membrane potential and decreasing ATP and mitochondrial DNA concentrations [57]. Ni toxicity also involves mechanisms that damage the DNA and disrupt cellular repair processes. One major mechanism is the modification of nucleoside bases, such as the formation of 8-oxodG, a process linked to elevated ROS levels [58]. Additionally, Ni exposure is also associated with DNA strand breaks, cross-links, and the formation of DNA adducts, contributing to genetic damage. Furthermore, Ni inhibits crucial DNA repair processes, such as NER and base excision repair (BER). This inhibition is proposed as the main factor for the carcinogenic potential of Ni. It was observed that the expression of BER DNA glycosylase human OGG1 (hOGG1) was decreased in the serum of nickel smelting workers, a reduction linked to impacts such as aging, neurodegenerative diseases, and cancer [59]. Ni disrupts the NER pathway primarily through affecting the incision step by binding to repair enzymes and preventing them from proper functioning. This impairment of DNA damage repair mechanisms results in the accumulation of mutations and genomic instability [60].

2.2. Oxidative stress and cellular metabolism

The main discussed pathway of toxicity for Co and Ni is linked to oxidative stress and its associated consequences [7,61]. This cellular state arises due to an imbalance between the formation of ROS and their detoxification through antioxidant defenses. Hydrogen peroxide (H_2O_2), superoxide anions ($O_2^{\bullet-}$), and hydroxyl radicals ($^{\bullet}OH$) are the main molecules categorized as ROS, which can originate from both endogenous and exogenous sources [62]. Endogenously, ROS are natural byproducts of cellular metabolism, particularly generated during ATP production in the mitochondrial electron transport chain (ETC) [63]. Next to this, ROS may arise mediated by NADPH oxidases (NOX) or during drug metabolism in the liver, maintained by cytochrome P450 enzymes [64]. Exogenous sources of ROS include stressors such as ultraviolet radiation, dietary factors (nutrients, alcohol, drugs), and environmental pollutants as cigarette smoke or heavy metals [64]. Metals can act as co-factors in a process called Fenton reaction, wherein Fe(II), for example, reacts with H_2O_2 to produce $^{\bullet}OH$. Although this reaction is primarily associated with Fe(II), other divalent metals such as Co(II) and Ni(II) can also participate in Fenton-like reactions, further contributing to ROS production [65]. In moderate quantities, ROS are vital for cellular signaling and immune response. However, excessive concentrations can severely impair cellular components. Among these is DNA damage, which may result in mutations, lipid peroxidation impairing membrane integrity, and protein oxidation affecting the function of proteins. Such impairments may contribute to mitochondrial dysfunction triggering cellular death mechanisms like apoptosis [63]. Cells possess an intricate antioxidant defense system to counteract these harmful effects and neutralize ROS. This includes enzymatic antioxidants like superoxide dismutase (SOD), catalase, and glutathione peroxidase (GPx), as well as non-enzymatic antioxidants such as vitamin C and E and glutathione (GSH) [62]. However, inhibition of these antioxidative systems leads to ROS accumulation and significantly increases the risk of

oxidative stress with its associated consequences. Persistent oxidative stress is linked to a wide range of diseases, such as COPD, cardiovascular diseases, neurodegenerative disorders as Alzheimer's and Parkinson's, and cancer development. Balancing ROS production and antioxidant defenses is therefore crucial to maintain cellular health and prevent oxidative stress-induced diseases [66].

2.2.1. Nrf2 signaling

In response to oxidative stress, several transcription factors are activated to regulate gene expression across various signaling pathways. Key transcription factors include nuclear factor erythroid 2-related factor 2 (Nrf2), activator protein 1 (AP-1), tumor protein p53 (p53) and nuclear factor kappa-light-chain-enhancer of activated B cells (NF-κB) [67]. Although each of them has a specific role in cellular processes, they are linked to each other in maintaining cellular homeostasis. One of the best-known orchestrators of the cellular stress response is Nrf2, whose activity is tightly regulated transcriptional, post-transcriptional and post-translational [68]. Under unstressed conditions, Nrf2 is bound in the cytosol by Kelch like-ECH-associated protein 1 (KEAP1). This binding facilitates the ubiquitination and subsequent degradation by Cullin 3, resulting in low basal levels of Nrf2 [68]. Stressors like ROS or electrophiles can modify the cysteine residues on KEAP1, followed by the release of Nrf2 and its translocation into the nucleus. Once in the nucleus, Nrf2 forms a heterodimer with small Maf proteins for binding to antioxidant response element (ARE), a specific DNA sequence in the promotor regions of its target genes (figure 2) [69]. This binding initiates the transcription of numerous genes, which are crucial for antioxidative defense, detoxification of xenobiotics, NADPH regeneration, and heme metabolism, thus turning Nrf2 essential for cellular homeostasis (figure 3) [68].

One of the most abundant antioxidants is GSH, whose synthesis and regeneration is directly controlled by Nrf2, a topic that will be explored in more

detail in the following section. Further antioxidant enzymes regulated by Nrf2 are NAD(P)H quinone oxidoreductase 1 (NQO1), SODs, catalase, and components of the thioredoxin-based system [70]. Nrf2 supports the regeneration of NADPH, which is an essential cofactor for a variety of antioxidant enzymes, by positively regulating NADPH-producing enzymes which belong to cellular pathways as glycolysis and tricarboxylic acid (TCA) cycle [71]. Lastly, Nrf2 is involved in Fe metabolism and storage, to prevent radical production via the Fenton reaction and promoting the degradation of heme by heme oxygenase-1 (HMOX-1) [70]. Along with the regulation of the antioxidant response, Nrf2 is attributed further regulatory functions in cell metabolism, as the expression of enzymes involved in glycolysis, pentose phosphate pathway, biosynthesis of purines, and glutamine and lipid metabolism [72]. Next to this, Nrf2 can affect the cell metabolism indirectly through crosstalk with other transcription factors, such as activating transcription factor 4 (ATF4) and hypoxia-inducible factor 1-alpha (HIF-1α) [73,74]. In diseases with oxidative stress as a key pathological factor, Nrf2 exhibits significant therapeutical potential by enhancing its activation. Apart from that, a chronic overactivation potentially has adverse effects. High levels of Nrf2 can promote cancer cell proliferation by inhibiting apoptosis or enhancing glycolysis and antioxidant systems. It is also related to the establishment of a resistance to chemotherapeutics. Therefore, cells must tightly regulate the balance of Nrf2 activation and degradation for normal cellular function and health [75,76].

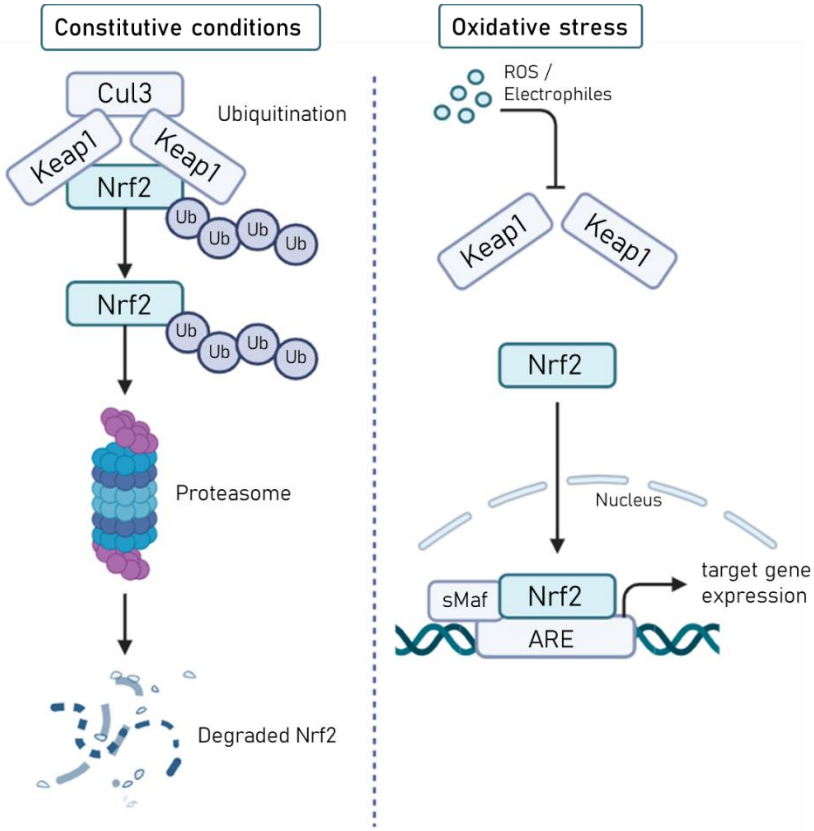

Figure 2: Regulation of the Nrf2 pathway under constitutive and stressed conditions in human cells. Nrf2 is under basal levels bound to Keap1 and degraded through proteasome activity. Activation by ROS or electrophiles leads to a release by Keap1 and translocation of Nrf2 into the nucleus, binding to ARE gene sequences and initiating the transcription of antioxidative genes. The illustration is partly designed using BioRender software and adapted from [77].

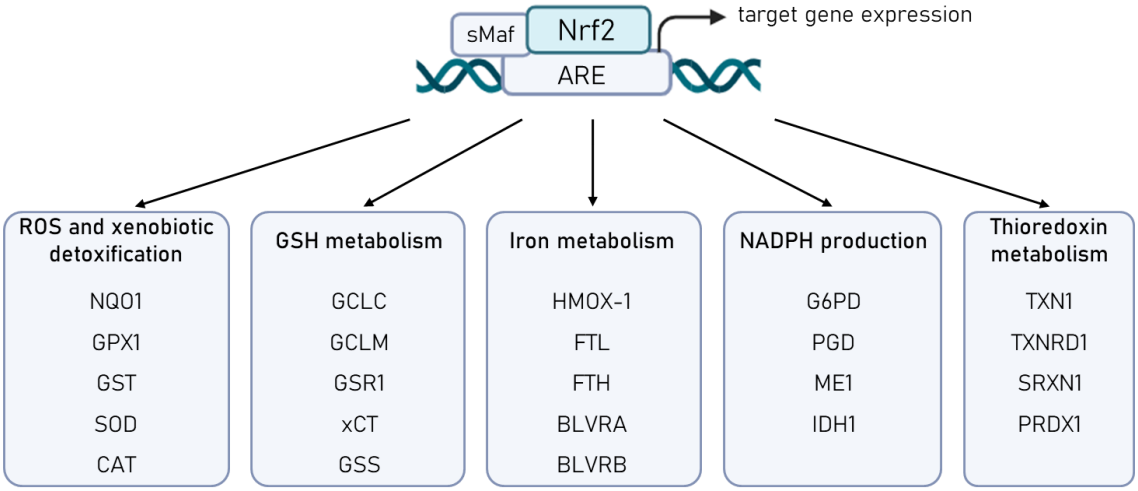

Figure 3: Selection of Nrf2-regulated genes of different pathways in cellular metabolism. The illustration is partly designed using BioRender software and adapted and modified from [68,78].

2.2.2. Glutathione metabolism

GSH, composed of the three amino acids glutamate, cysteine, and glycine, is abundant in high concentrations across all cell types. It is predominantly found in the liver, maintaining detoxification processes, and protecting cells from oxidative damage [79]. GSH can directly scavenge ROS by donating electrons and converting into its oxidized form glutathione disulfide (GSSG), through a reaction catalyzed by GPx (figure 4). Additionally, GSH facilitates the excretion of xenobiotics in phase II drug metabolism mediated by glutathione S-transferases (GSTs) [80]. Maintaining adequate cellular GSH levels is therefore essential, and the GSH/GSSG ratio is commonly used as a marker for oxidative stress and diminished antioxidative capacity [81]. The first step of GSH synthesis is catalyzed by glutamate-cysteine ligase (GCL) forming γ-glutamylcysteine, followed by the addition of glycine with glutathione synthetase (GSS) as the supporting enzyme. The cellular amount of glutamine and cysteine is maintained by the antiporter xCT (SLC7A11), transporting cystine into the cell with simultaneous carriage of glutamate out of the cell. Imported cystine is converted to cysteine, which subsequently contributes to GSH synthesis. Additionally, GSSG can be regenerated back to GSH by glutathione reductase 1 (GSR), which requires NADPH as a cofactor [80]. The expression of xCT, GSTs, GCL, GSS and GSR1 is regulated by Nrf2, highlighting the role of this transcription factor in antioxidant defense and the detoxification and excretion of xenobiotics [76].

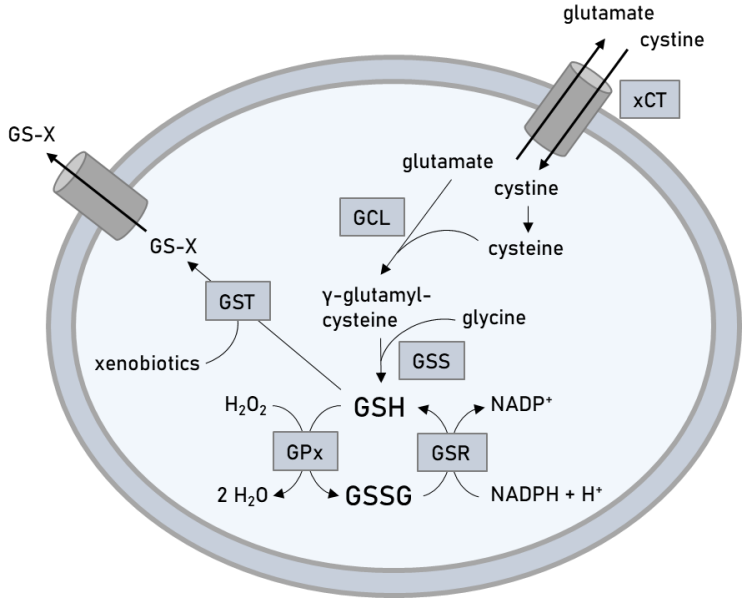

Figure 4: GSH synthesis, regulation, and antioxidative mechanisms in human cells for the detoxification of ROS and xenobiotics. Adapted and modified from [80].

2.2.3. Biomarkers of oxidative stress

Oxidative stress markers are crucial in the assessment of the biological redox status and disease development and progression in a toxicological context (table 1). For direct measurement of intracellular ROS formation, a variety of fluorescent sensors are available, including the widely used probe 2',7'-dichlorodihydroflurescein diacetate (DCFH-DA), the mitochondria targeted dye MitoSOX or the H_2O_2 detecting substance Amplex Red. Additionally, there are chemiluminescent probes or derivatization agents for analytical measurement [82,83]. Since ROS are highly reactive metabolites, these methods have limitations in terms of selectivity, quantification capabilities, and susceptibility to artifacts [84]. The presence of ROS can also be determined indirectly by measuring specific compounds that result from oxidative damage to lipids, proteins, or DNA. Various methods are available for assessing each biomarker, all with its own advantages and limitations. The most investigated end products of lipid peroxidation include malondialdehyde (MDA), which can be quantified spectrophotometrically using thiobarbituric acid (TBA) or more specifically via high-performance liquid chromatography (HPLC) combined with

ultraviolet (UV) or fluorescence detection (FD) [85,86]. Other markers include 4-hydroxynonenal (4-HNE) and isoprostanes [87,88]. Amino acid residues in proteins can undergo oxidative modifications, which are partly irreversible, such as carbonylation and nitrosylation. Carbonylated proteins are often quantified using reagents like 2,4-dinitrophenylhydrazine (DNPH) and fluorescein-5-thiosemicarbazide (FTC), or with an commercially available enzyme-linked immunosorbent assay (ELISA) [89]. The most common oxidative DNA damage focuses on the nucleic base guanin, forming 8-oxo-7,8-dihydro-2'-deoxyguanosine (8-oxodG). The best methodology for quantification is HPLC-MS/MS, followed by using ELISA assays [90].

Oxidative stress can also arise from an overburdened or impaired antioxidative defense system. Alterations in key enzymes or the transcription factor Nrf2 serve as indicators of ROS generation. The activation and translocation of Nrf2 can be assessed through immunoblotting or immunofluorescence staining using anti-Nrf2 antibodies [91]. Nrf2 activity can also be indirectly determined by measuring the expression of its target genes by reverse transcription-quantitative polymerase chain reaction (RT-qPCR) and the corresponding protein levels via Western blot or immunofluorescence staining. To gain a comprehensive understanding of oxidative damage and discover novel biomarkers, gene expression profiling through microarray, RNA-sequencing, and CHIP-seq techniques can be employed [92]. The amount of GSH, GSSG, and their ratio are valuable markers for assessing the redox status of an organism. In recent years, numerous methods have been developed for quantifying these analytes. A common approach is the enzymatic recycling assay, which is based on the reaction of GSH with DTNB to form a chromophore that can be measured spectrophotometrically [93]. However, this assay is limited in sensitivity and specificity, thus chromatography-based methods have been established. These include HPLC coupled with UV, FD or electrochemical (ECD) detection, or the more sensitive mass spectrometric (MS) detection [81]. A detailed comparison of

GSH and GSSG quantification methods is provided in chapter 3. In addition to GSH, antioxidant enzymes such as SOD and GPx are crucial biomarkers for cellular redox status. They can be investigated using immunological techniques such as RT-qPCR for gene expression, and Western blot or immunofluorescence staining for protein expression [94]. However, an increase in gene or protein amount does not necessarily correlate with higher enzyme activity, thus it is important to evaluate their function, which is primarily carried out by spectrophotometric assays [95]. A summarized overview of biomarkers for oxidative stress and possible methods for their assessment is provided in table 1. Each method comes with its own advantages and limitations, thus it is essential to combine approaches for a comprehensive overview of oxidative stress. This includes direct ROS measurement, evaluation of damage to biomolecules, and the analysis of cellular antioxidative defenses.

Table 1: Summary of commonly used biomarkers for oxidative stress and possible methods for evaluation.

Type of Biomarker	Specific Biomarker	Methods	
Intracellular ROS	ROS formation	Fluorescent probes: DCFH-DA; Amplex Red; MitoSOX Chemiluminescent probes: Lucigenin; Luminol LC-MS/MS: derivatization with 2,3-DHBA or 2,5-DHBA	[82] [82] [83]
Lipid-peroxidation	MDA	Spectrophotometrically: TBARS HPLC-UV, -FD	[86] [85]
	4-HNE	GC-MS/MS, LC-MS/MS Immunoassay	[88] [96]
	Isoprostanes	GC-MS/MS, LC-MS/MS Immunoassay	[87]
Protein oxidation	Protein carbonylation	Spectrophotometrically: DNPH Fluorometrically: FTC Immunoassay	[97] [98] [89]
Oxidative DNA damage	8-oxodG	Immunoassay LC-MS/MS	[90] [99]
Antioxidant enzymes (SOD, CAT, GPx, GR)	Gene expression	RT-qPCR	[94]
	Protein expression	Western blot	[94]
	Enzyme activity	Chemiluminescent/spectrophotometric	[95]
GSH metabolism	GSH/GSSG ratio	Spectrophotometric enzymatic redox-cycling assay HPLC-UV, -FD, -ECD LC-MS/MS	[93] [100–102] [81]
Nrf2 signaling	Nrf2 translocation	Western blot Immunofluorescence	[91]
	Nrf2 target genes	RT-qPCR Western Blot Immunofluorescence	[92]

2.3. Genotoxicity and DNA damage response

Genotoxicity refers to the ability of hazardous substances to damage the genetic information within cells, leading to genomic instability and mutations. These genetic alterations are associated with several diseases, most notably cancer [103]. Thus, understanding the genotoxic potential of such compounds is crucial to estimate and mitigate risks to human and environmental health.

Organisms are continuously exposed to both endogenous and exogenous factors that lead to more than 10,000 DNA lesions per cell each day [104]. DNA damage refers to any alteration in the DNA structure that can cause cellular injury and reduce cell viability [105]. Endogenous DNA damage occurs as a byproduct of intracellular processes, including hydrolysis, alkylation, and oxidation of DNA components. Oxidative damage to DNA bases often results in the formation of 8-oxodG, a common lesion. Additionally, DNA bases may undergo methylation, alkylation or deamination, producing various modified bases. These modifications are possibly leading to mismatch of DNA bases during replication [106]. Exogenous sources of DNA damage include chemical agents, ionizing and ultraviolet radiation, as well as environmental pollutants such as heavy metals. These agents primarily induce the production of ROS, leading to single- and double-strand breaks, base loss, or the formation of adducts that impair base pairing or block DNA replication [107]. For each type of DNA damage, cells have evolved specific mechanisms to sense and repair these damages and to preserve genomic stability. If these damages remain unrepaired, they may lead to persistent mutations, which contribute to the development of cancer and other diseases [106]. The complex network of DNA damage response (DDR) is responsible for sensing the DNA damage, coordinating repair mechanisms and, if necessary, inducing programmed cell death (apoptosis) to eliminate severely damaged cells. The activity and localization of DNA damage proteins are tightly controlled by post-translational modifications, which modulate the chromatin structure to provide docking sites for DNA repair proteins. These modifications

include phosphorylation, ubiquitylation, sumoylation, and poly-ADP-ribosylation (PARylation) [108]. Poly(ADP-ribose) polymerases (PARPs), particularly PARP1, are key enzymes in the process of PARylation, activated by single- and double-strand DNA breaks [109]. These enzymes are responsible for the synthesis and attachment of ADP-ribose units to glutamate, aspartate, and lysine residues on histone and non-histone proteins or PARP1 itself, using NAD^+ as the substrate. Through the formed PAR chains of approximately 200 ADP-ribose units, proteins involved in DNA damage repair can interact non-covalently and get recruited to damage sites [110]. After finishing this process, PAR chains are rapidly degraded by PAR glycohydrolase (PARG) or ADP-ribosylhydrolase 3 (ARH3) [109]. This entire cycle of PARP activation and degradation occurs within minutes, ensuring an efficient DNA repair [111]. The choice for a DNA repair mechanism mainly depends on the specific type of DNA damage encountered. For example, single-strand breaks or damage to individual bases are primarily addressed by base excision repair (BER). Mismatch repair (MMR) is typically activated to correct base mismatches that arise during DNA replication, while bulky adducts or crosslinks are repaired by nucleotide excision repair (NER) [112]. DNA double-strand breaks are occurring less frequently than other lesions and are particularly challenging to repair. The two main mechanisms for repairing double-strand breaks are homologous recombination (HR) and non-homologous end joining (NHEJ) [107]. Figure 5 provides an overview of common types of DNA damage, the respective repair pathways, and the damage consequences.

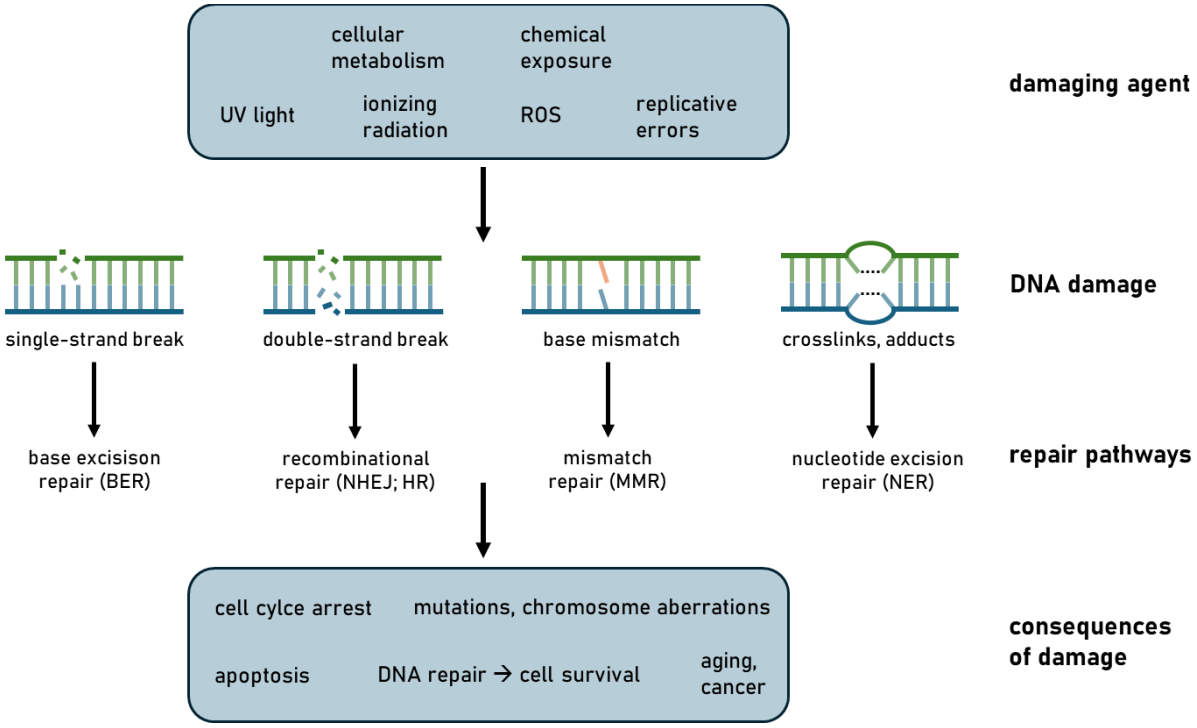

Figure 5: Simplified overview of common DNA damage, repair pathways and consequences. Adapted and modified from [113].

2.3.1. Genotoxicity testing

Assessing genotoxicity is essential for the evaluation of the potential hazards of several substances on human health and the environment. Thereby it is crucial to have validated and reliable methods for the detection of DNA damage, chromosomal stability and repair mechanisms. A commonly used technique is for example the comet assay, also known as single-cell gel electrophoresis, which detects DNA damage such as strand breaks and other lesions, as well as incomplete BER. It is based on a gel electrophoresis, where the negatively charged, damaged DNA migrates towards the anode, forming a comet-like appearance. This can be visualized and quantified by fluorescence microscopy after DNA staining. The extent of DNA migration correlates with the level of damage [114]. By using the BER enzyme formamidopyrimidine DNA glycosylase (Fpg), the comet assay can be modified for specifically detecting oxidized purines, mainly 8-oxodG [115]. Next to this, the most used methods for detecting the oxidative damage marker 8-oxodG are immunoassays such as ELISA or

analytical-based methods like HPLC-ECD or HPLC-MS/MS [116]. Alkaline unwinding (AU) is a well-established genotoxicity test for the investigation of single-strand breaks. In principle, the amount of double-stranded DNA (dsDNA) is determined after unwinding the DNA under alkaline conditions. By comparing the amount of dsDNA and single-stranded DNA (ssDNA), which is formed at sites of single-strand breaks, this DNA damage can be detected [117]. In response to double-strand breaks, the histone 2AX becomes phosphorylated and forms γ-H2AX, a marker crucial for DNA damage repair by recruiting repair proteins. The formed γ-H2AX foci can be visualized and quantified using immunofluorescence with specific antibodies, immunoblotting, or flow cytometry. Therefore, γ-H2AX represents an established marker for cellular double-strand breaks [118]. The micronucleus assay is another key method for genotoxicity testing on the chromosomal level. Micronuclei are formed from chromosomal fragments or chromosomes, which are not incorporated during cell division, indicating chromosomal instability and DNA damage. It is based on scoring the micronuclei frequency in cells and can be automated using microscope-aided systems or flow cytometry [119]. The above mentioned posttranslational modification PARylation, which is activated by strand breaks and essential in DDR, can be assessed analytically using LC-MS/MS and via immunofluorescence techniques, providing insights into DNA damage related processes [120,121]. An overview of commonly used biomarkers for genotoxicity and possible testing methods is provided in table 2.

Table 2: Summary of commonly used biomarkers for genotoxicity and DNA damage and possible methods for evaluation.

Type of Biomarker	Specific Biomarker	Methods	
General genotoxic potential		Comet assay	[114]
		Micronucleus test	[119]
Oxidative base modification	8-oxodG	Immunoassay	[90]
		HPLC-MS/MS	[99]
Single-strand breaks		Alkaline unwinding (AU)	[117]
Double-strand breaks	γ-H2AX	Immunofluorescence, Immunoblotting	[118]
		Flow cytometry	[122]
DNA damage response	PARylation	Immunofluorescence	[120]
		LC-MS/MS	

2.4. Testing systems

To investigate the effects of Co(II) and Ni(II) exposure in terms of cellular uptake, gene regulation, changes in metabolism, and genotoxic effects, different testing systems were employed. Two different cancer cell lines served as *in vitro* models, while *Paramecium tetraurelia*, an *in vivo* model organism, was also utilized. All of them possess the capability for Co and Ni homeostasis and are therefore suitable models for this study.

2.4.1. Human liver carcinoma cells (HepG2)

The liver is the main organ for the distribution, storage, and excretion of substances, making it vulnerable to the toxic effects of metals. Both Co and Ni tend to accumulate in the liver at higher concentrations compared to other organs, potentially impairing its function [27,28]. To investigate the possible liver toxicity of Co and Ni, an *in vitro* cell culture model, the human hepatoma cell line HepG2, was utilized. This cell line was derived from a liver biopsy of a 15-year-old Caucasian male and is one of the most widely used cell models in pharmacological and toxicological research. Other commonly used cell lines for hepatotoxicity studies include Hep3B, Huh7, and HepaRG, each originated from

different tumors [123]. While cancerous cell lines have limitations compared to primary hepatocytes, they also offer notable advantages. These include an easy handling, a long life span, high proliferation rates, and a stable phenotype. HepG2 cells, in particular, have been extensively characterized over the years, with detailed information available regarding their genome, transcriptome, and proteome [124]. They exhibit several liver-specific functions similar to human hepatocytes, such as synthesis of plasma proteins, cholesterol and triglyceride metabolism, glycogen synthesis, and insulin signaling [125]. Despite this, HepG2 cells are limited in their utility in regulatory studies, primarily due to their lower activity of cytochrome P450 and phase II metabolic enzymes [126]. Additionally, at the transcriptome level, HepG2 cells show an upregulation of approximately 50 genes associated with cancer, distinguishing them from primary hepatocytes [127]. Nevertheless, HepG2 cells are a valuable model for investigating the mechanisms of Co and Ni toxicity, even if their limitations must be considered when interpreting results.

2.4.2. Human astrocytoma cells (CCF-STTG1)

Co and Ni are present in the brain to a lesser extent compared to the liver. However, there are several reports indicating that these metals can impair brain function. Especially patients with MoM hip implants often exhibit elevated serum Co levels, which have been linked to symptoms such as cognitive impairment, hearing impairment, vision loss, and neuropathy [128]. An overexposure to Ni is associated with neurological disorders, manifesting as headaches, giddiness, tiredness, lethargy, and ataxia. Additionally, studies on rats reported the induction of apoptosis in neurons as well as disrupted neurotransmitters following Ni treatment [57]. To examine the neurotoxic effects of both Co and Ni, an astrocytoma cell model was used. This CCF-STTG1 cell line was established from a Grade IV astrocytoma from a 68-year-old Caucasian female [129]. Astrocytes, a type of glial cells, play crucial roles for maintaining brain health. They are protecting neurons against oxidative stress, support neuronal

outgrowth, maintain the blood-brain barrier, and provide precursors for neurotransmitters. Similar to the hepatocytes, the cancerous CCF-STTG1 cells possess several limitations, since they may not represent normal astrocyte functions. Despite this, their easier handling, high proliferation rates und reproducibility offer advantages compared to primary human astrocytes [130,131].

2.4.3. *Paramecium tetraurelia*

The increasing presence of Co and Ni in the environment, originating from different industrial or natural sources, raises concerns about their potential impact on microorganisms within their ecosystems. Understanding their ecotoxicological effects is crucial to understand the implications of metal contamination [132]. Among these microorganisms, the unicellular eukaryotic organism *Paramecium tetraurelia* is attributed to the group of ciliates and offers a highly complex cellular structure [133]. By consuming bacteria, paramecia are playing a foundational role in the aquatic food chain. Thus, they also have the capacity to transfer contaminants such as heavy metals to higher trophic levels [134]. In recent years, paramecia became increasingly popular as model organisms for ecotoxicological studies. The main approaches were related to the determination of lethal doses, substance accumulation, and behavioral or morphological changes [135]. They offer several advantages for toxicity testing. Due to their absence of a cell wall, these organisms are highly sensitive to a wide range of pollutants and respond more rapidly, thereby serving as an effective indicator of environmental contamination [133]. Additionally, as they are single-celled organisms, they are similar to the cell culture models part of the 3R concept (replacement, reduction, refinement), which aims to minimize ethical concerns in animal testing. The complete sequencing of the whole genome of *P. tetraurelia* enables their use in molecular studies, including genomic, transcriptomic, and proteomic analyses. Despite these advantages, there are some limitations, primarily due to the lack of standard protocols for toxicity tests and laboratory procedures [134].

Abstract:

Alterations in reduced and oxidized glutathione (GSH/GSSG) levels represent an important marker for oxidative stress and potential disease progression in toxicological research. Since GSH can be oxidized rapidly, using a stable and reliable method for sample preparation and GSH/GSSG quantification is essential to obtain reproducible data. Here we describe an optimised sample processing combined with a liquid chromatography-tandem mass spectrometry (LC-MS/MS) method, validated for different biological matrices (lysates from HepG2 cells, *C. elegans*, and mouse liver tissue). To avoid autoxidation of GSH, samples were treated with the thiol-masking agent N-ethylmaleimide (NEM) and sulfosalicylic acid (SSA) in a single step. With an analysis time of 5 min, the developed LC-MS/MS method offers simultaneous determination of GSH and GSSG at high sample throughput with high sensitivity. This is especially interesting with respect of screening for oxidative and protective properties of substances in *in vitro* and *in vivo* models, e.g. *C. elegans*. In addition to method validation parameters (linearity, limit of detection (LOD), limit of quantification (LOQ), recovery, interday, intraday), we verified the method by using menadione and L-buthionine-(S,R)-sulfoximine (BSO) as well established modulators of cellular GSH and GSSG concentrations. Thereby menadione proved to be a reliable positive control also in *C. elegans*.

Chapter 3

Simultaneous quantitation of oxidized and reduced glutathione via LC-MS/ MS to study the redox state and drug-mediated modulation in cells, worms and animal tissue

Based on:

Alicia Thiel, Ann-Kathrin Weishaupt, Merle M. Nicolai, Kristina Lossow, Anna P. Kipp, Tanja Schwerdtle and Julia Bornhorst

Journal of Chromatography B, **2023**, 123742.

DOI: 10.1016/j.chromb.2023.123742

Highlights:

- Simultaneous quantification of GSH and GSSG based on LC-MS/MS
- Fast and reliable method for sample preparation, using NEM as thiol masking agent
- Sensitive and specific measurement with short analysis time
- Validation in several biological matrices using established modulators of GSH and GSSG

Keywords:

LC-MS/MS; glutathione; glutathione disulfide; biological matrices

Chapter 3 – Simultaneous quantitation of oxidized and reduced glutathione via LC-MS/ MS to study the redox state and drug-mediated modulation in cells, worms and animal tissue

3.1. Introduction

The tripeptide glutathione (γ-glutamyl-L-cysteinylglycine, GSH) is present in all organs with physiological intracellular concentrations in the millimolar range. Among others, the chemical properties and relative abundance of GSH make it well suited for acting as a conjugating agent in phase II metabolism as well as serving as an antioxidant in redox homeostasis. Under normal conditions, GSH occurs mainly in its reduced form, whereas oxidative conditions lead to oxidation of two GSH molecules, forming glutathione disulfide (GSSG) (fig. 6) [94,136]. GSH can reduce a variety of toxins such as peroxides or free radicals by acting as an electron donor [137]. The NADPH-dependent enzyme GSH reductase (GR) is converting GSSG back to GSH, leading to a typical GSH/GSSG ratio of about 100:1 under physiological conditions [138]. Furthermore, electrophilic xenobiotics can be eliminated via GSH conjugation, catalysed by GSH *S*-transferases [139]. A GSH deficiency is related to oxidative stress and consequently plays a central role in the pathogenesis of several diseases such as Diabetes mellitus, Alzheimer's or Parkinson's disease [79,140]. Alterations in GSH and GSSG levels or a low GSH/GSSG ratio are commonly used as a biomarker of oxidative stress and injury in toxicological studies. Consequently, a reliable and specific method for the quantification is needed, and due to the low abundance, the method has to be sensitive for the quantification of GSSG in different biological samples. A very popular and convenient technique is the enzymatic recycling method, based on the conversion to a chromophore after conjugation to GSH [93,141]. However, this assay lacks sensitivity and

specificity and allows only an indirect determination of GSSG by masking of thiol groups in the sample using 2-vinylpyridine. To overcome this limitation, chromatography based methods have been established, including high performance liquid chromatography (HPLC) with ultraviolet (UV) [100,142,143], fluorescence (FD) [101,144,145] or electrochemical detection (ECD) [102,146,147]. UV and FD mostly need time-consuming derivatization because GSH lacks a chromophore or fluorophore. But most derivatizing agents like 5‘,5‘-dithiobis(2-nitrobenzoic acid) (DTNB) or *o*-phthalaldehyde (OPA) require an alkaline pH, which promotes auto-oxidation to GSSG [148]. UV and FD methods are also less sensitive, compared to mass spectrometric detection (MS), and they are not applicable for simultaneous determination of both analytes [136]. ECD provides concurrent measurement and avoids the derivatization step, but a high potential is needed for small analyte amounts found in GSSG, resulting in a short lifetime of the electrode and loss of signal after a few measurements [146,149]. Among these methods, liquid chromatography-tandem mass spectrometry (LC-MS/MS) offers the most reliable, fast, specific, and sensitive method, especially for small amounts of analytes and small sample sizes [150–152].

Since GSH can be oxidized rapidly another limitation for its detection is the fast and controlled collection, preparation, and analysis of samples. To avoid an overestimation of GSSG, N-ethylmaleimide (NEM) provides, among others, a potent alkylating agent for GSH conjugation. NEM prevents oxidation and ensures the accurate quantification of GSH in form of GSH-NEM. Next to this, NEM also inhibits the activity of GR, contributing to precise measurement of the GSH/GSSG ratio [153]. The schematic reaction is displayed in figure 7. Performing sample processing in acidic pH by using sulfosalicylic acid (SSA) inhibits γ-glutamyl transferase and therefore avoids the loss of GSH [154]. In order to quantify reliable and valid GSH and GSSG concentrations, a standardised protocol is needed for sample preparation combined with a highly specific and sensitive measurement. Therefore, we developed a method for the

simultaneous quantification of specifically GSH-NEM and GSSG, applicable in different biological matrices (lysates from mammalian cells, *Caenorhabditis elegans* (*C. elegans*), and mouse liver tissue) using LC-MS/MS, which allows the study of their redox state and susceptibility to oxidative stress. This method offers a rapid sample processing and analytical procedure (5 min), avoiding artefactual GSSG formation and providing a high sample throughput. Additionally, we validated the method by using two different positive controls, L-buthionine-(S,R)-sulfoximine (BSO) and menadione. BSO acts as an inhibitor of γ-glutamylcysteine synthetase (γ-GCS), which is the key enzyme in GSH synthesis, leading to depleted GSH levels [102,155]. Menadione (2-methyl-1,4-naphtoquinone, vitamin-K3) has a quinone structure and produces intracellular semiquinone radicals upon overdosage, leading to oxidative damage [156,157].

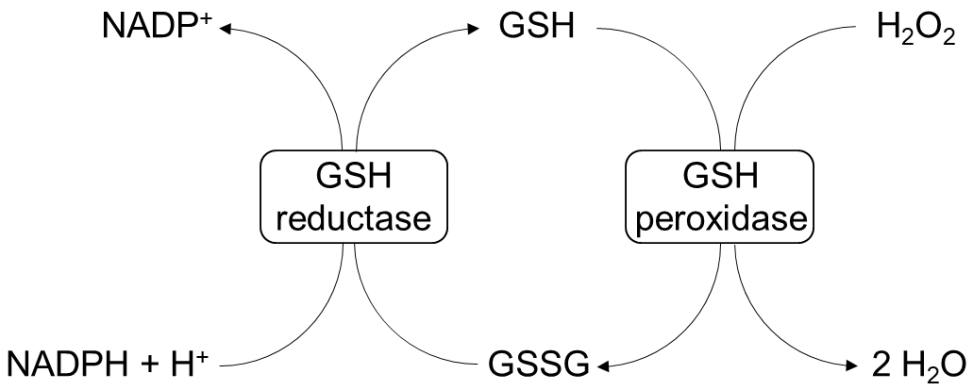

Figure 6: Schematic glutathione metabolism pathway (GSH: reduced glutathione, GSSG: oxidised glutathione, NADPH: nicotinamide adenine dinucleotide phosphate, H_2O_2: hydrogen peroxide).

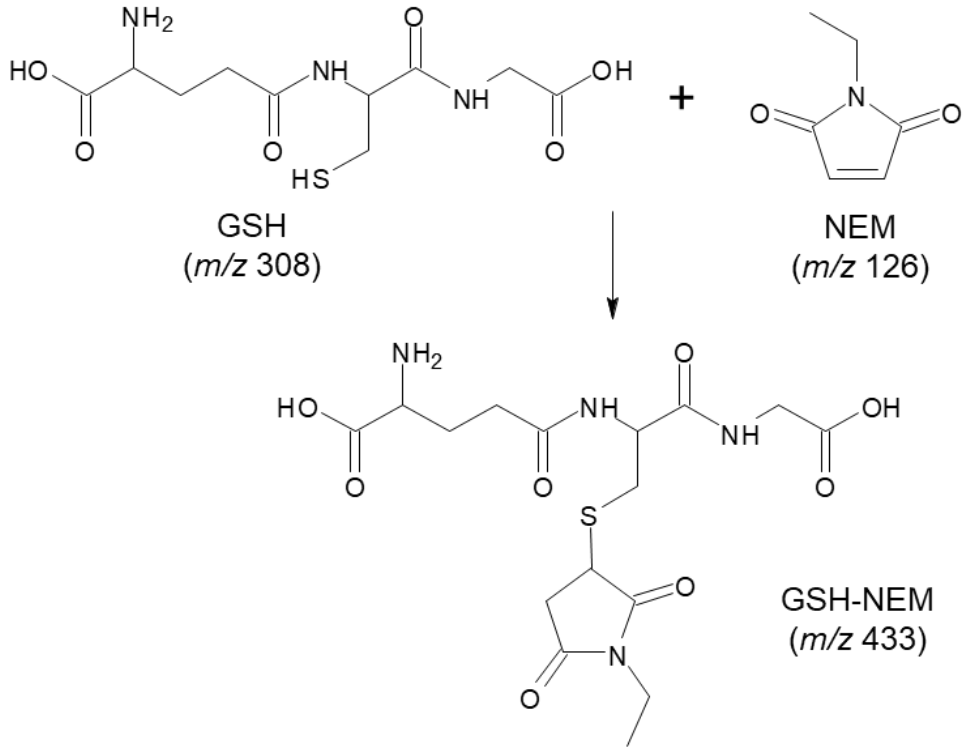

Figure 7: Schematic representation of the reaction of GSH with NEM (GSH: reduced glutathione, NEM: N-ethylmaleimide).

3.2. Materials and Methods

3.2.1. Standard solutions

N-ethylmaleimide (NEM) and GSSG (both Sigma-Aldrich) were dissolved in bidistilled water for a 10 mM stock solution and 5 mM stock solution, respectively. GSH-NEM standard was prepared in 10 mM NEM solution to a final concentration of 5 mM GSH (Sigma-Aldrich). Aliquots of GSH-NEM and GSSG were stored at -80 °C and repeated freezing and thawing of the standard solutions should be avoided.

3.2.2. Cell culture and treatment

HepG2 cells were cultured in Eagle's Minimum Essential Medium (MEM; Sigma Aldrich) supplemented with 10 % fetal bovine serum (FBS; Sigma Aldrich), 2 % (*v/v*) penicillin/ streptomycin (Sigma Aldrich) and 1 % (*v/v*) non-essential amino acids (NEA; Sigma Aldrich) at 37 °C, 100 % humidity and 5 % CO_2 [158].

Subculturing was performed every second day by using 0.25 % trypsin-EDTA (Sigma Aldrich). 5.5 x 10^5 cells were seeded in cell culture dishes with 6 cm diameter and treated with 1 µM, 5 µM and 10 µM L-buthionine-(S,R)-sulfoximine (BSO, Cayman chemical) (24 h after seeding) for 24 h or with 50 µM and 100 µM menadione (Sigma Aldrich) (48 h after seeding) for 1 h. 100 mM stock solutions were prepared freshly in bidistilled water (BSO) or DMSO (menadione). After the respective incubation time, cells were detached using 0.25 % trypsin-EDTA and washed with ice-cold PBS containing 5 % FBS before the suspension was centrifuged at 150 x g and 4 °C for 5 min. The cell pellet was re-suspended in ice-cold PBS and centrifuged again at 2370 x g and 4 °C for 4 min. After removing the supernatant, the pellets were stored at -80 °C.

3.2.3. *C. elegans* handling and treatment

C. elegans wildtype strain Bristol N2 (WT) (obtained from Caenorhabditis Genetic Center (CGC; University of Minnesota)) was cultivated on 8P agar plates coated with *Escherichia coli* strain NA22 at 20 °C as previously described [159]. After synchronization, L1 larvae were placed on nematode growth medium (NGM) containing plates coated with *E. coli* strain OP50-I until reaching larvae stage L4. 3000 synchronous L4 stage worms per concentration were then exposed to 200 µM or 500 µM menadione for 1 h in M9 buffer with a total volume of 1 mL. Worms were then washed three times with 85 mM NaCl + 0.01 % Tween and pelletized by centrifugation at 380 g. Worm pellets in 100 µL M9 were directly frozen in liquid nitrogen and stored at -80 °C.

3.2.4. Murine tissue

Murine liver tissue was obtained from C57BL6Jrj mice (Janvier). For this purpose, the blood was taken in the course of sacrifice by means of cardiac puncture and the liver tissue was immediately snap-frozen. Animal experiment was approved by the Ministry of Environment, Health and Consumer Protection of the federal state of Brandenburg, Germany (2347-44-2017).

3.2.5. Sample preparation

For preparation of the LC-MS/MS measurement, cell pellets were re-suspended in 300 µL freshly prepared, ice-cold extraction buffer (16 mM KH_2PO_4, 84 mM K_2HPO_4, 8.8 mM EDTA, 2 mM NEM, 1 % Triton X-100, 0.6 % SSA) and homogenized by using a Bead Ruptor after adding zirconia beads (biolab products) for 20 s, four times. Worm pellets were re-suspended in 200 µL cold extraction buffer and for mouse liver tissue ~50 mg was dissolved in 300 µL cold buffer. For both samples, tissue disruption was started by three freeze-thaw cycles (1 min liquid nitrogen, 1 min 37 °C water bath) followed by homogenising four times for 20 s using the Bead Ruptor. All extracts were filtrated using Spin-X® centrifuge tube filters (0.22 µM; Corning), centrifuged at 18620 x g, 4 °C for 5 min and diluted if necessary (worms undiluted, HepG2 cells 1:10, liver tissue 1:400) before LC-MS/MS analysis. An aliquot was frozen at -20 °C for protein quantification using a standard BCA assay (Sigma-Aldrich).

3.2.6. LC-MS/MS parameters

Quantification of GSH-NEM and GSSG was performed on an Agilent 1290 Infinity II LC System coupled to a Sciex QTrap 6500+ triple-quadrupole mass spectrometer with an electrospray ion source in positive mode (ESI+). Compounds were separated using a Waters Atlantis T3 column (5 µm, 2.1 x 150 mm) with a pre-column of the same material, tempered at 20 °C. Eluent A consisted of water with 0.1 % formic acid (LC-MS grade, fisher chemicals), and Eluent B contained acetonitrile (LC-MS grade, VWR) with 0.1 % formic acid. After injection of 3 µL sample volume, the run with a gradient of 0 % - 35 % Eluent B over 2 min was started, followed by 35 % - 40 % Eluent B over 1.5 min, 40 % - 100 % Eluent B over 0.5 min and a final step to 100 % Eluent A over 1 min. The total run time was 5 min at a flow rate of 0.3 mL/ min. Samples were always freshly prepared and stored in a cooled autosampler until measurement. The following ion source parameters were determined for MS: entrance potential (EP)

10.0 V; curtain gas (CUR) 40.0 psi; collision gas (CAD) medium; ion spray voltage (IS) 4000.0 V; temperature (TEM) 550 °C; ion source gas 1 and 2 (GS1 and 2) 40.0 psi. The dwell time for both analytes was set at 35 ms. Four mass transitions were used for multiple reaction monitoring (MRM) analysis of GSH-NEM, whereas three mass transitions were applied for the analysis of GSSG. The mass transitions and the respective optimised collision energy (CE), collision cell exit potential (CXP) and declustering potential (DP) are shown in table 3.

Table 3: Parameters for detection of GSH-NEM and GSSG. Shown are the used quantifier (*) and different qualifiers for analyte identification.

Analyte	Fragmentation [*m/z*]	Collision energy [V]	Collision cell exit potential [V]	Declustering potential [V]
GSH	308 > 179	18	9	37
GSH-NEM	433 > 304*	20	9	22
	433 > 201	30	10	35
	433 > 287	29	17	21
	433 > 358	24	11	36
GSSG	613 > 484*	24	9	37
	613 > 355	32	19	37
	613 > 595	26	16	35

3.2.7. Method validation

For method validation the following parameters were verified: linearity, limit of detection (LOD), limit of quantification (LOQ), recovery, intraday and interday variation. Linearity, LODs and LOQs, were determined in matrices of HepG2 cells, *C. elegans* and mouse liver tissue. The recovery, intraday and interday were assessed with HepG2 lysate. The linearity was evaluated for GSH-NEM in a concentration range of 0 – 10 µM and for GSSG between 0 – 200 nM. GSH-NEM and GSSG concentrations were calculated by external calibration in the linear range indicated above. For LOD and LOQ determination, signal-to-noise ratios were plotted against the GSH-NEM or GSSG concentration and calculated

as LOD = 3/slope or LOQ = 10/slope. S/N ratios were calculated using the Multiquant Software (Sciex, Version 3.0.3). Recovery was assessed by comparison of five samples with known GSH-NEM and GSSG concentrations and five matrix containing samples, spiked with GSH-NEM and GSSG in defined concentrations. To calculate the intraday variation, GSH-NEM and GSSG concentrations in six different HepG2 samples which were pelletized, prepared, and analysed on the same day were quantified using external calibration and normalization to protein content. Interday variation was determined in ten different HepG2 samples that were pelletized, prepared, and measured on different days and calculated the same way as intraday variation. GSH-NEM and GSSG concentrations were normalized to protein content when intra- and interday variations were determined.

3.2.8. Statistics

Statistical analysis was performed using GraphPad Prism software 6.01 (GraphPad, La Jolla, CA, USA). Data is presented as mean + SD (cells) or SEM (*C. elegans* and mouse samples) with significance depicted as *p<0.05, **p<0.01 and ***p<0.001 compared to untreated control.

3.3. Results

3.3.1. Method development for quantification of GSH-NEM and GSSG via LC-MS/MS

The chromatographic as well as the detection conditions were optimised using GSH-NEM and GSSG standard solutions with respect to optimal separation and maximum sensitivity of MS detection in MRM mode. GSH-NEM standard aliquots were prepared using newly bought and opened GSH, diluted in a NEM solution and frozen in small aliquots at -80 °C, to avoid the observed autoxidation inside the barrel. Every aliquot was only used once to prevent oxidation process due to repeated freezing and thawing. Good baseline separation of the two compounds was achieved using the reversed-phase C_{18} Waters Atlantis T3 column with the

mobile phases and gradient mentioned in the materials and methods section and a flow rate of 0.3 mL/min. The column was tempered at 20 °C, since 30 °C and 40 °C did not lead to any chromatographic improvement. The obtained retention times were 2.81 min for GSSG and 3.26 min for GSH-NEM, with a total run time of 5 min. For MS optimization, the ion source parameters mentioned in materials and methods and table 3 were generated by using the *Compound Optimization software wizard* (Sciex). For determination of *m/z* ratios of the parent ions Q1 scans were performed followed by product ion scans to identify the fragmentation pattern. For GSH-NEM, the most abundant fragment ion (*m/z* 433 > 304) was used for quantification, whereas the other three mass transitions were used as qualifiers. Because of matrix effects, the second most intense fragment ion was used as the quantifier for GSSG (*m/z* 613 > 484), and the other two mass transitions were used as qualifiers. Representative chromatograms are displayed in figure 8. To verify the conjugation of GSH and NEM, the mass transition of unbound GSH (*m/z* 308 > 179) was measured additionally. Since GSSG is also present double charged ([M + $2H^+$ = 308]), the *m/z* 308 > 179 mentioned above was also measured for this analyte. Because this fragmentation pathway is less abundant, only the single charged GSSG was considered for quantification. The chemical structures of GSH-NEM and GSSG and the respective underlying fragmentation patterns are schematically shown in figure 9.

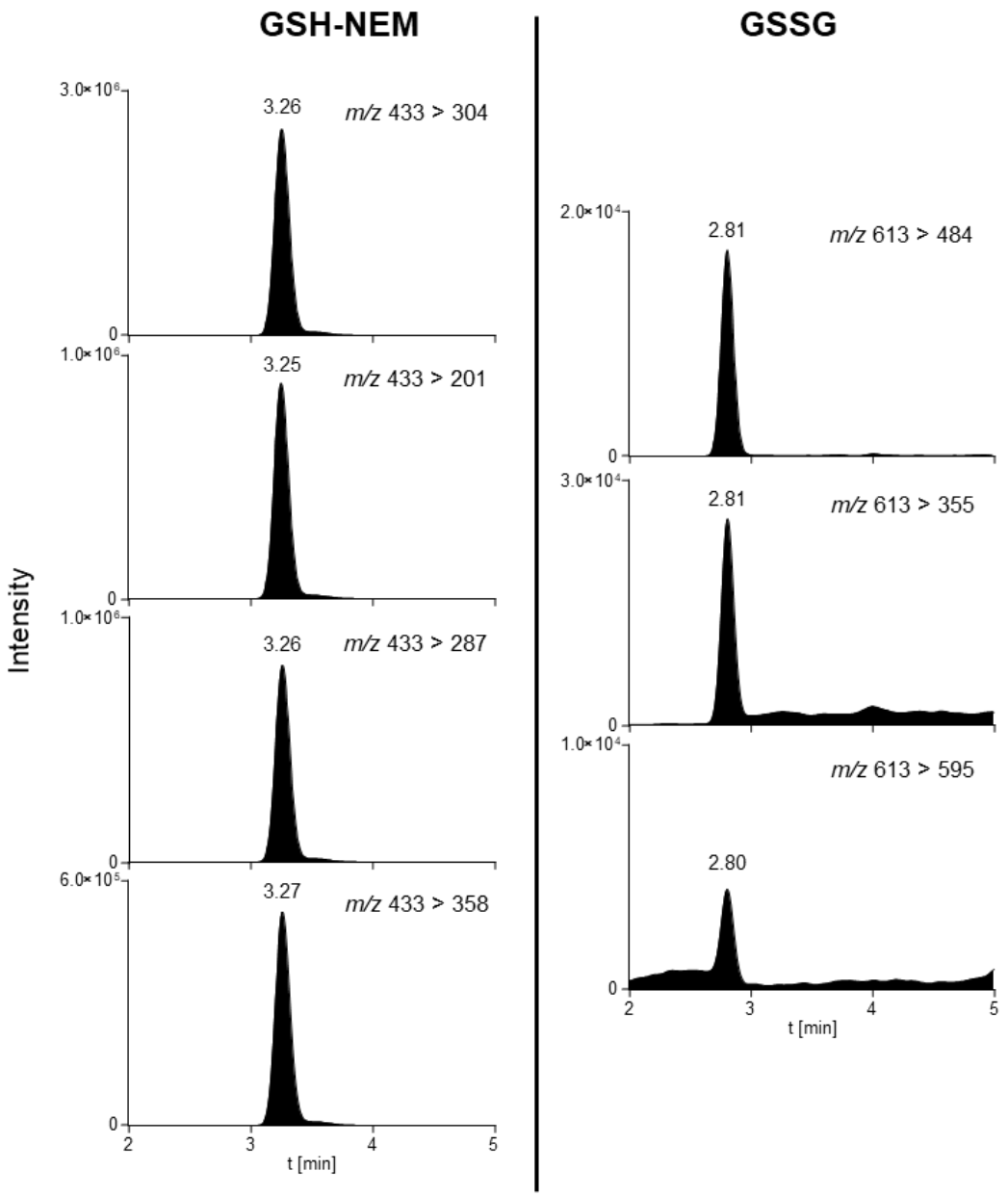

Figure 8: Representative MRM chromatograms of GSH-NEM and GSSG in extraction buffer. Four mass transitions were recorded for GSH-NEM (left panel) whereas three mass transitions were examined for GSSG detection (right panel). Optimal collision energies for each depicted MRM transition are given in table 3.

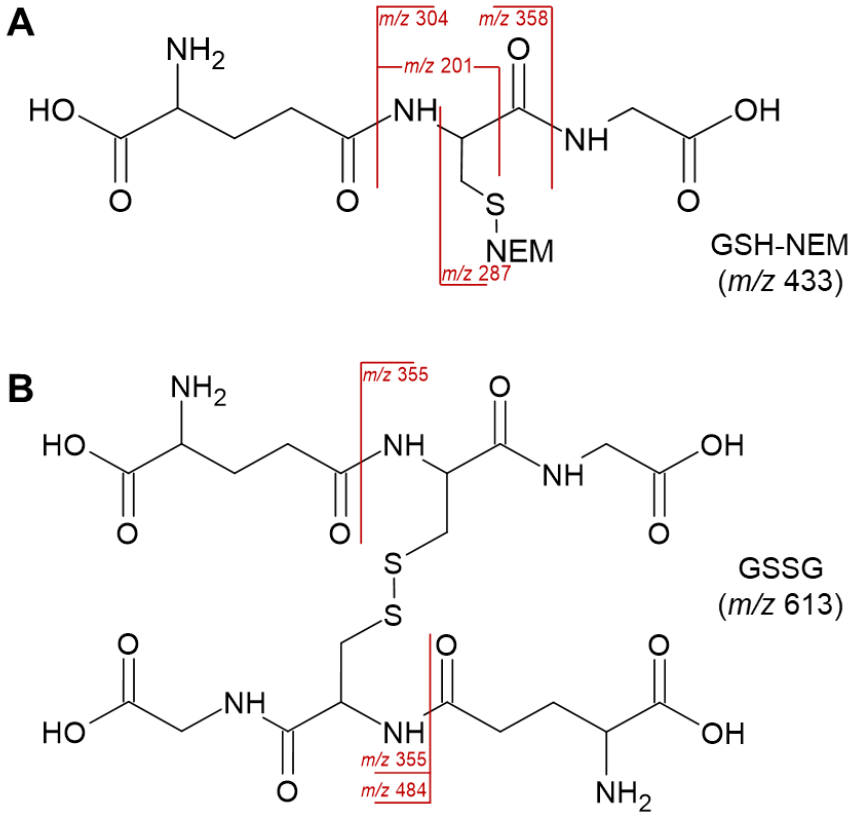

Figure 9: Chemical structures of GSH-NEM [M + H+ = 433] (A) and GSSG [M + H+ = 613] (B) with their underlying fragmentation reactions yielding the most abundant product ions.

3.3.2. Method validation

The GSH-NEM and GSSG calibration, consisting of standard solutions spiked with lysates of HepG2, *C. elegans* or mouse liver tissue each, showed linearity in the indicated ranges of GSH-NEM: 0 – 10 µM and GSSG: 0 – 200 nM with correlation coefficients displayed in table 4. For the quantifiers, no matrix-based interfering peaks could be observed (fig. 10). The LOD which is defined as LOD = 3/slope of S/N ratio plotted against the respective analyte concentration, was found at GSH-NEM concentrations of 0.61 nM in HepG2 cells, 0.20 nM in *C. elegans* and 0.17 nM in mouse liver tissue, whereas the GSSG concentrations are 0.02 nM in HepG2 cells and *C. elegans* and 0.01 nM in mouse liver tissue. LOQ is defined as LOQ = 10/slope, with GSH-NEM concentrations at 2.04 nM (HepG2), 0.67 nM (*C. elegans*) and 0.56 nM (mouse liver) and GSSG concentrations at 0.06 nM (HepG2) and 0.05 nM (*C. elegans* and mouse liver).

The mean recovery, expressing the remaining signal intensity after analyte loss and/or degradation during sample preparation as well as ion suppression in ESI+ source by co-extracted matrix components, was in lysate (HepG2 cells; 5 samples) in the range of 75.7 ± 2.7 % for GSH-NEM and 90.3 ± 2.0 % for GSSG indicating satisfactory recovery of the method. Intraday accuracy in six HepG2 samples, measured on the same day, was at 10.2 % for GSH-NEM and 9.7 % for GSSG, whereas the interday variation of eleven HepG2 samples, measured on different days was found at 11.4 % for GSH-NEM and 13.8 % for GSSG. In summary, the data indicate a credible and reproducible method under the experimental conditions mentioned above.

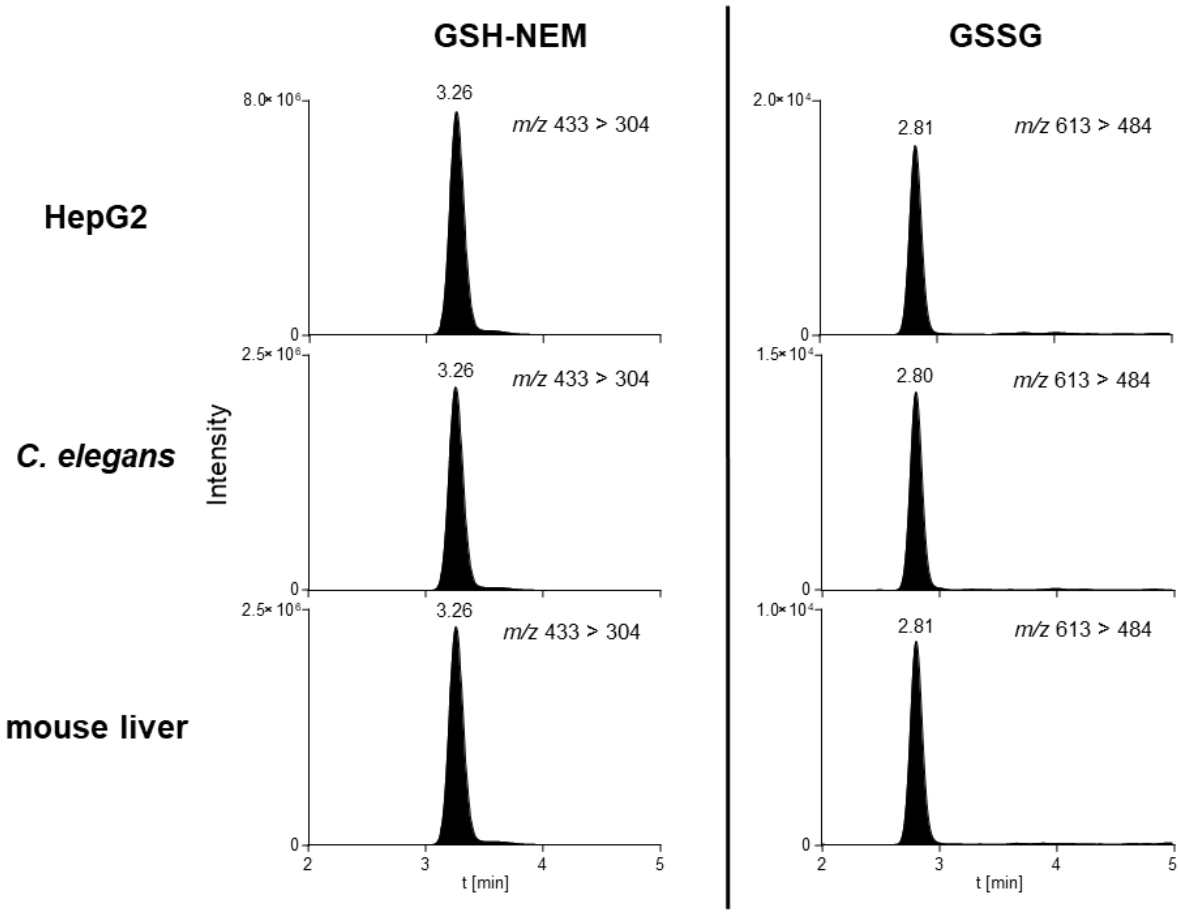

Figure 10: Representative MRM chromatograms of GSH-NEM and GSSG in HepG2 cells (upper row), C. elegans (middle row) or mouse liver tissue (lower row). Only the quantifier mass transitions are shown.

Table 4: Method validation parameters (LOD, LOQ, linearity) for quantification of GSH-NEM and GSSG in different matrices.

parameter	GSH-NEM			GSSG		
	HepG2	*C. elegans*	mouse liver	HepG2	*C. elegans*	mouse liver
limit of detection [nM][1]	0.61	0.20	0.17	0.02	0.02	0.01
limit of quantification [nM][2]	2.04	0.67	0.56	0.06	0.05	0.05
linearity [R^2][3]	0.98534	0.99927	0.99379	0.99682	0.99690	0.99844

[1]: defined as LOD = 3/slope of the S/N ratio plotted against the respective concentration of the calibration.

[2]: defined as LOQ = 10/slope of the S/N ratio plotted against the respective concentration of the calibration.

[3]: area of the analyte was plotted against the spiked concentration of the analyte in ranges of 0 – 10 µM for GSH-NEM and 0 – 200 nM for GSSG.

3.3.3. Drug-mediated modulation of GSH-NEM and GSSG in cell and worm lysates

The developed LC-MS/MS-based method was applied to quantify GSH-NEM and GSSG in different matrices (HepG2 cells and *C. elegans*) after treatment with varying concentrations of BSO and menadione. BSO is an inhibitor of γ-GCS, which is an important enzyme in GSH synthesis in cells. Consequently, use of BSO leads to lower GSH concentrations, which has already been shown in different cell types, including HepG2 cells [102,155]. Menadione has a quinone structure and can be reduced in a one-electron transfer reaction, which leads to radical formation and subsequently among others to an oxidation of GSH to GSSG [157]. The incubation with 1, 5 or 10 µM BSO for 24 h in HepG2 cells resulted in a concentration-dependent reduction of both GSH-NEM and GSSG, significantly already at 5 µM BSO. After 10 µM BSO, the GSH-NEM and GSSG concentration decreases to 26.5 % (fig. 11A) and 11.9 % (fig. 11B), respectively, compared to untreated cells. GSH-NEM content of HepG2 cells after 1 h incubation with 100 µM menadione was significantly lower than that of untreated

control (54.6 %; fig. 12A). GSSG level concurrently increased to 196.8 % (fig. 12B) compared to control. This consequently leads to a decrease in the GSH-NEM/GSSG ratio (fig. 12C). In *C. elegans*, 1 h menadione treatment did not lead to alterations in GSH-NEM concentration (fig. 13A). GSSG level significantly increases to 249.6 % (fig. 13B) after 500 µM menadione compared to untreated worms, resulting in a significantly lower GSH-NEM/GSSG ratio of 0.47 ± 0.11 (fig. 13C) compared to control.

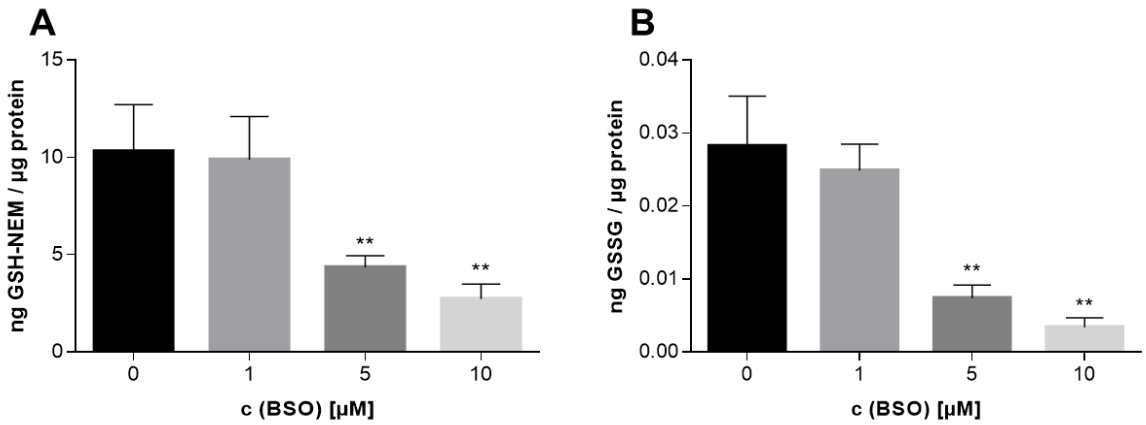

Figure 11: GSH-NEM concentration (A) and GSSG concentration (B) after 24 h BSO (L-buthionine-(S,R)-sulfoximine) treatment in HepG2 cells, measured via LC-MS/MS and normalized to protein amount. Data is presented as mean + SD of n ≥ 3 independent experiments. Statistical significance was tested by an unpaired t-test depicted as **p ≤ 0.01: compared to untreated control.

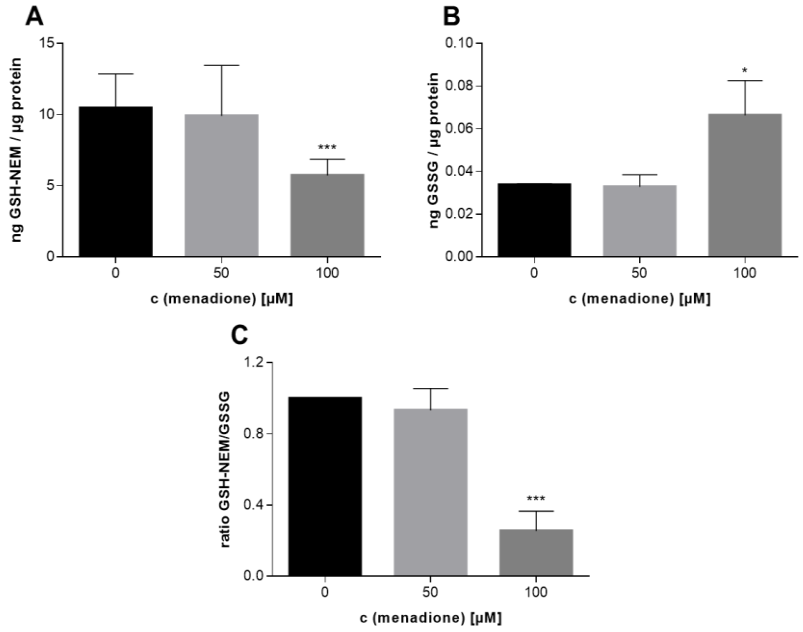

Figure 12: GSH-NEM concentration (A), GSSG concentration (B) and GSH-NEM/GSSG ratio (C) after 1 h menadione treatment in HepG2 cells, measured via LC-MS/MS and normalized to protein amount. Data is presented as mean + SD of n ≥ 5 independent experiments. Statistical significance was tested by an unpaired t-test with Welch's correction depicted as *p ≤ 0.05, ***p ≤ 0.001: compared to untreated control.

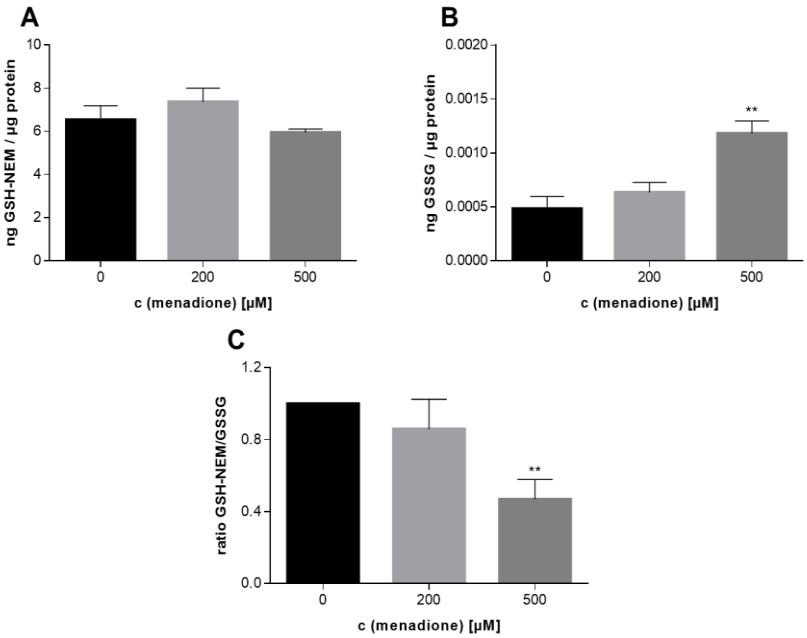

Figure 13: GSH-NEM concentration (A), GSSG concentration (B) and GSH-NEM/GSSG ratio (C) after 1 h menadione treatment in C. elegans, measured via LC-MS/MS and normalized to protein amount. Data is presented as mean + SEM of n ≥ 5 independent experiments. Statistical significance was tested by an unpaired t-test with Welch's correction depicted as **p ≤ 0.01: compared to untreated control.

3.4. Discussion

Alterations in cellular levels of GSH and GSSG are often used as a marker for oxidative stress [160]. The aim of this study was to establish a sensitive and reproducible LC-MS/MS method for the simultaneous quantification of GSH and GSSG, especially applicable in different biological matrices. The fast and optimised sample preparation, with NEM used as a thiol masking agent, prevents the oxidation of GSH and resulting artefactual GSSG concentrations. With a total run time of 5 min, the short HPLC method enables a high sample throughput. The recent developments regarding sample preparation have dramatically improved the reliability of GSH and GSSG measurements, particularly as an indicator of oxidative stress in various types of biological samples and address a wide range of issues that have historically contributed to erroneous estimates of GSH and GSSG such as auto-oxidation of GSH or specificity in case of enzymatic assays. In general, the enzymatic GSH recycling assay, originally described by Tietze in 1969 [141] and modified by Griffith in 1980 and Rahman *et al.* in 2007 [93,161], is very popular. It is based on the conjugation of thiol groups with DTNB to form a TNB-adduct and the chromophore 5-thio-2-nitrobenzoic acid (TNB), following back-reduction of the adduct by GR and NADPH and a spectrophotometrically measurement of the released TNB at 412 nm, quantifying indirectly the total thiol amount. The determination of disulfides can be provided by adding a thiol masking agent (e.g. NEM or 2-vinylpyridine (2-VP)) [162]. Analytical methods are more sensitive compared to the enzymatic assay, which is important for low GSSG amounts or small sample sizes. Especially MS detection provides a higher specificity, since DTNB interacts with all thiol groups and a simultaneous determination of reduced and oxidized thiols is not possible [163]. A variety of analytical techniques have been developed for GSH and GSSG measurement, with HPLC methods being most commonly used. Unlike methods quantifying via HPLC-UV or HPLC-FD, analysis via LC-MS/MS does not need additional time-consuming derivatization

steps [100,101,142]. Even though HPLC-UV, HPLC-FD and HPLC-ECD may be applicable to measure GSH and GSSG in many types of samples, they are often inadequate for the simultaneous measurement due to lack of sensitivity to quantify GSSG as for example in *C. elegans* samples. Advantages and limitations of the most commonly used GSH and GSSG determination methods are displayed in table 5.

Since thiol moieties are highly unstable and undergo biochemical changes such as oxidation, we enacted critical steps to obtain reliable data. We selected NEM as a protective thiol-masking agent to prevent artefactual GSH oxidation and inhibit GR activity. Thereby, it is important to use freshly thawed aliquots for GSH-NEM calibration, to avoid freeze-thaw cycles and to add NEM to the extraction buffer. Via the specific mass transition for GSH, the successful NEM conjugation can be monitored. NEM has been used before to cell culture and blood samples [150,152,154]. Quantification via specific mass transitions, this MS-based method also allows the determination of a variety other GSH complexes. Due to the instability of GSH at room temperature, the sample preparation was completely processed on ice or at 4 °C until injection to LC-MS/MS system. A further critical step is the pH of the extraction buffer. SSA is needed for acidification and deproteination, to prevent an overestimation of GSSG and a loss of GSH, as the acidic pH inhibits γ-glutamyl transferase [154]. Moreover, the presented method is characterised by its detection sensitivity and minimal sample loading exceeding that of other MS-based methods [150,151]. Carroll *et al.* analysed GSH and GSSG in hematopoietic stem cells, but in absence of a thiol masking agent like NEM [164]. Herzog *et al.* provided a LC-ESI-MS/MS method for the analysis of GSH-NEM and GSSG in cultured human fibroblasts and yeast cells, obtaining comparable LODs and LOQs for both analytes [152]. Most of the other published LC-MS/MS-based methods are validated for biological fluids, like blood, urine, or saliva [150,165,166]. As the assessment of redox balance after toxicological treatment in model organisms

such as mammalian cells or *C. elegans* becomes increasingly important, it is essential to establish a reliable method for this investigation. Recently published studies quantifying GSH in *C. elegans* mainly perform the non-analytical recycling assay [167–170], with few exceptions doing HPLC-FD with OPA as derivatizing agent [171,172]. Similar situation can be observed for GSH and GSSG quantification in HepG2 cells, where enzymatic determination is also the most popular method [173–176], leading to varying GSH levels due to the lack of specificity. As we observed during method validation in Q1 scan, GSH is already instable in the vessel and oxidizes rapidly under unmasked conditions to GSSG, resulting in artefactual higher GSH amounts when calculated via external calibration in the recycling assay.

The applicability of our LC-MS/MS method was verified by exposing HepG2 cells with BSO and menadione and *C. elegans* with menadione, where the quantified GSH-NEM and GSSG levels demonstrated a good reproducibility. While exposing HepG2 cells 24 h to BSO resulted in decreased GSH-NEM and GSSG amounts starting at 5 µM (fig. 11), menadione led to decreasing GSH-NEM levels and concurrently increasing GSSG content, starting at 100 µM (fig. 12). Comparable to our data, Bayram *et al.* observed a decreased GSH concentration of about 50 % when incubating HepG2 cells with 5 µM BSO for 24 h, measured with HPLC-ECD. Since electrochemical detectors require a high potential for small analyte amounts, GSSG measurement was not performed [102]. Steinmeier *et al.* exposed astrocytes with various menadione concentrations, resulting in similar effects as in HepG2 cells, as menadione-induced radicals deplete GSH and lead to an accumulation of GSSG [157]. A decreased GSH/GSSG ratio associated with menadione has also been observed by Herzog *et al.* in human fibroblasts [152]. In *C. elegans*, a menadione-induced GSSG formation could be observed, whereas the GSH-NEM amount showed no alterations (fig. 13). Contrary to HepG2 cells, *C. elegans* contains significantly less GSSG, while GSH content is comparable, resulting in different ratios.

This indicates that a menadione-induced oxidation could cause less alteration in GSH level than in cells, and therefore no significant reduction was observed. In the literature GSH has not been determined after menadione treatment in *C. elegans* to our knowledge; however, our results demonstrate that menadione, a valid positive control in mammalian cells, is also potent in *C. elegans*. With this short method it is now possible to determine the impact of pro- and antioxidative substances on human cell and *C. elegans* in a high sample throughout. In addition to mammalian cells and *C. elegans*, our developed and validated LC-MS/MS-based method is applicable on other matrices, like mouse liver tissue.

Table 5: Advantages and limitations of commonly used GSH and GSSG quantification methods.

Method	Advantages	Limitations
enzymatic assay [93,141,161]	less expensive requires little lab equipment	unspecific no simultaneous determination indirect measurement of GSSG
HPLC-UV/FD [100,101,142,145]	more sensitive compared to enzymatic assay less expensive than LC-MS/MS	time-consuming derivatization no simultaneous determination
HPLC-ECD [102,146,147]	no derivatization simultaneous determination of GSH and GSSG	high potential needed rapid loss of signal
HPLC-MS/MS [150–152,164]	high sensitivity and specificity simultaneous determination of GSH and GSSG no derivatization	high costs experienced user needed

3.5. Conclusion

We have developed a rapid and sensitive LC-MS/MS method for a simultaneous and reproducible quantification of GSH and GSSG in several biological matrices, focusing on optimised sample preparation in order to avoid artefactual GSSG levels. Due to the short measurement time of 5 min, the method is suitable for high sample throughput with only small sample amounts required. The combination of NEM and SSA, added directly for sample preparation, prevented

GSSG back-reduction and resulted in precise data for both GSH and GSSG. In addition, we validated the method using menadione and BSO in HepG2 cells, whereas menadione proved to be a reliable positive control also in *C. elegans*. This method is applicable to other matrices such as mouse liver tissue and is also suitable for quantification of other thiols or GSH complexes.

3.6. Acknowledgement

This work was supported by the DFG Research Unit TraceAge (FOR 2558, BO4103/4-2, HA4318/4-2. We thank the Caenorhabditis elegans Center (CGC; University of Minnesota), which is funded by the NIH Office of Research Infrastructure Programs (P40 OD010440), for providing the N2 Bristol *C. elegans* strain used in this study.

3.7. Author contribution statement

Alicia Thiel: Conzeptualization, Data curation, Formal analysis, Methodology, Visualization, Writing – original draft, Writing – review & editing. **Ann-Kathrin Weishaupt:** Data curation, Methodology, Writing – review & editing. **Merle M. Nicolai:** Data curation, Methodology, Writing – review & editing. **Kristina Lossow:** Writing – review & editing. **Anna P. Kipp:** Writing – review & editing. **Tanja Schwerdtle:** Writing – review & editing. **Julia Bornhorst:** Conzeptualization, Funding acquisition, Project administration, Supervision, Writing – review & editing.

Abstract:

The two trace elements cobalt (Co) and nickel (Ni) are widely distributed in the environment due to the increasing industrial application, for example in lithium-ion batteries. Both metals are known to cause detrimental health impacts to humans when overexposed and both are supposed to be a risk factor for various diseases. The individual toxicity of Co and Ni has been partially investigated, however the underlying mechanisms, as well as the interactions of both remain unknown.

In this study, we focused on the treatment of liver carcinoma (HepG2) and astrocytoma (CCF-STTG1) cells as a model for the target sites of these two metals. We investigated their effects in single and combined exposure on cell survival, cell death mechanisms, bioavailability, and the induction of oxidative stress. The combination of $CoCl_2$ and $NiCl_2$ resulted in higher Co levels with subsequent decreased amount of Ni compared to the individual treatment. Only $CoCl_2$ and the combination of both metals led to RONS induction and increased GSSG formation, while apoptosis and necrosis seem to be involved in the cell death mechanisms of both $CoCl_2$ and $NiCl_2$. Collectively, this study demonstrates cell-type specific toxicity, with HepG2 representing the more sensitive cell line. Importantly, combined exposure to $CoCl_2$ and $NiCl_2$ is more toxic than single exposure, which may originate partly from the respective cellular Co and Ni content. Our data imply that the major mechanism of joint toxicity is associated with oxidative stress. More studies are needed to assess toxicity after combined exposure to elements such as Co and Ni to advance an improved hazard prediction for less artificial and more real-life exposure scenarios.

Chapter 4

Single is not combined: the role of Co and Ni bioavailability on toxicity mechanisms in liver and brain cells

Based on:

Alicia Thiel, Vivien Michaelis, Marco Restle, Sabrina Figge, Martin Simon, Tanja Schwerdtle, Julia Bornhorst

Chemosphere, **2024**, 142091.

DOI: 10.1016/j.chemosphere.2024.142091

Highlights:

- liver carcinoma cells are more sensitive to Co and Ni toxicity than astrocytoma cells
- combined exposure resulted in higher cellular Co amount and decreased cellular Ni level compared to single metal treatment
- involvement of DMT-1 in Co and Ni transport in HepG2 cells was demonstrated
- oxidative stress is a sensitive mechanism for Co and combined toxicity of Co and Ni

Keywords:

Cobalt; Nickel; cellular metal content; oxidative stress; metal interactions

Chapter 4 – Single is not combined: the role of Co and Ni bioavailability on toxicity mechanisms in liver and brain cells

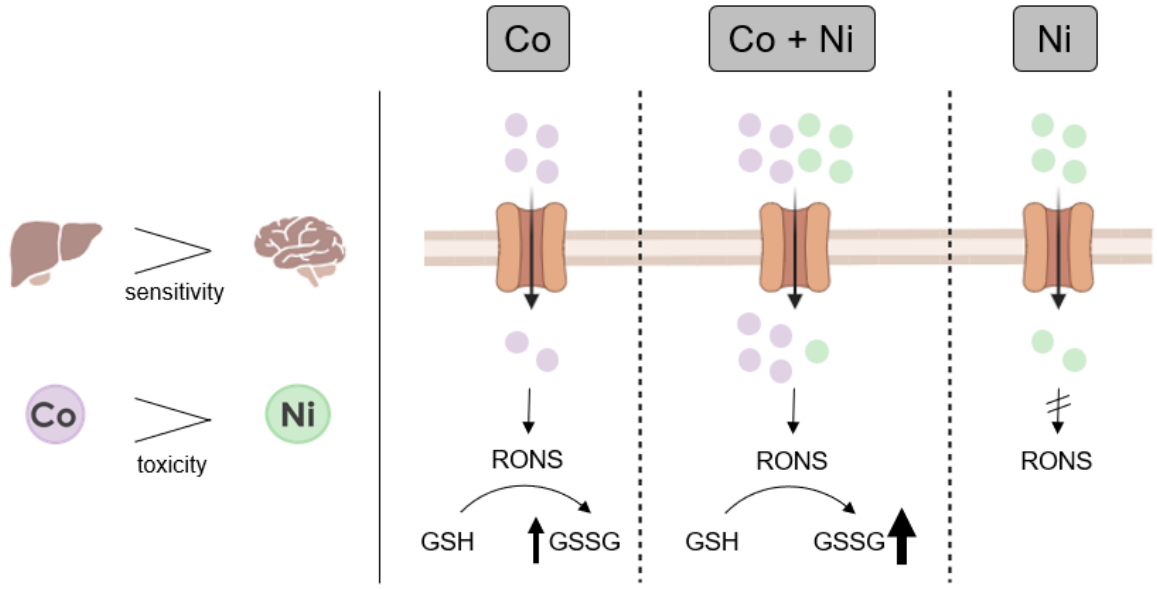

Figure 14: Graphical abstract of 'Single is not combined: the role of Co and Ni bioavailability on toxicity mechanisms in liver and brain cells'.

4.1. Introduction

The industrial application of Cobalt (Co) and Nickel (Ni) is gaining importance, especially due to the constantly increasing use of lithium-ion batteries. Moreover, both metals are involved in the production of alloys, catalysts, cosmetics and pigments, as well as in the medical sector in metal-on-metal (MoM) hip implants [1,7]. In some items such as toys and their components, Co may be present as an impurity of the Ni-containing alloys [177]. The high spread of products containing these metals unavoidably leads to higher environmental pollution, resulting in increased ingestion by humans via food or drinking water besides occupational exposure. High Co and Ni levels were found in vegetables, grains, seafood, nuts, and cocoa as well as in acidic beverages [1,178], resulting in chronic dietary exposure of about 0.1 – 0.5 µg/ kg bw per day for Co [3] and a range of 1.57 µg/ kg bw Ni per day for elderly up to 14.6 µg/ kg bw per day for

toddlers [6]. Regarding the biological role, Co is an essential trace element occurring in organic and inorganic forms and is mainly necessary as a cofactor in vitamin B_{12}. Moreover, Co is important for the formation of amino acids and proteins, for example in nerve cells. In contrast, a biological function of Ni in higher organisms as humans is not yet established [4,26]. Due to the possibly elevated concentrations of exposure, potential adverse human health impacts by Co and Ni are of increasing concern.

Inhalation exposure in occupational and non-occupational contexts is a main route for Ni and Co toxicity in the respiratory tract, in the lung, and immune system. Both metals are confirmed to be carcinogenic upon inhalation by the International Agency for Research on Cancer (IARC) (Co: group 2A; Ni: group 1) [43,44,51]. However, the general exposure of humans mainly concerns oral ingestion, which is supposed to entail a number of adverse effects, such as neurological (e.g. lethargy, ataxia, hearing and visual impairment), cardiovascular and thyroid dysfunction [2,5,179]. Epidemiological data from well-conducted studies on oral exposure are very limited. However, concerns are rising since case reports show evidence that Ni or Co exposure causes neurological abnormalities [52,180,181]. Despite human studies are rare, several rodent studies indicate that Ni as well as Co can disturb the neurobehavioral functions (for Co summarized in [182]; for Ni summarized in [52]). Additionally, in rodent studies upon oral Ni or Co administration, a decreased body weight, changes in liver weight, and histopathological changes in the liver were observed as well as altered liver enzymes and inflammation [183–185].

Although some studies provide evidence about underlying mechanisms of Co and/or Ni toxicity, it is not yet fully understood at the cellular level. Exposure to Co ions have been found to generate reactive oxygen and nitrogen species (RONS) via Fenton-like reaction, leading to oxidative stress which is proposed to be one of the main modes of action regarding Co-induced toxicity [7]. This in turn can lead among others to DNA damage, like single-strand breaks or

micronuclei [8]. Additionally, Co is able to mimic hypoxia by stabilizing hypoxia-inducible factor (HIF), resulting in an increased erythropoietin (EPO) synthesis [186]. Therefore, it is used by athletes as a performance enhancing supplement and has been included into the World Anti-Doping Agency's prohibited list since 2015 [187]. Ni toxicity is associated with DNA crosslinks and inhibition of DNA repair, also suggested to be induced mainly by oxidative stress [61]. Moreover, Ni may lead to loss of mitochondrial membrane potential and downregulation of Bcl-2, leading to enhanced apoptosis [188]. It is also discussed to impair the transport of essential ions like calcium [11] and may lead to enhanced EPO mRNA expression like Co [189]. Though toxicological studies of Co and Ni exist individually, only a few studies considered the effects of combined exposure, which is the more realistic setting.

First evidence about potential synergistic effects of dual exposure to Co and Ni base on lung cells, but all those studies lack bioavailability data which is mandatory for understanding the dose-response relationships of toxic effects [190,191]. Molecular data implicate further an interaction since Co and Ni are discussed to have some shared import transporters [4] which makes data collection on combined toxicity even more necessary. In the human body, Co and Ni are predominantly present in liver, kidney or heart and also in smaller quantities in brain and pancreas [26,192]. Since the liver is the main target for distribution and storage of metals and adverse effects on the liver have been reported upon oral Co and Ni administration [183,185], liver carcinoma cells (HepG2) are used as one *in vitro* model. A further target upon oral intake is the brain, where Astrocytes occur to protect neurons against oxidative stress as well as to support neurons by fostering among others their survival and neurite outgrowth. Due to studies reporting the adverse effect of Co and Ni on brain function, astrocytoma cells (CCF-STTG1) represent the second *in vitro* model [193]. By using two different cell types which are relevant upon oral intake, mechanisms of Co- and Ni-induced toxicity will be compared regarding organ-

specific bioavailability and toxicity mechanisms, focusing on oxidative stress markers and cell death mechanisms. The results of single treatment will be compared to those of dual exposure of Co and Ni, which are applied in an industrial relevant mixture of 6:1 (Ni:Co) [194].

4.2. Materials and Methods

4.2.1. Cell culture maintenance and treatment scenario

Human hepatocarcinoma cells (HepG2) were cultured using Eagle's Minimum Essential Medium (MEM; Sigma Aldrich) supplemented with 10 % fetal bovine serum (FBS; Sigma Aldrich), 2 % (*v/v*) penicillin/ streptomycin (Sigma Aldrich) and 1 % (*v/v*) non-essential amino acids (NEA; Sigma Aldrich) as described previously [158]. The human astrocytoma cell line (CCF-STTG1) was cultivated in RPMI 1640 medium (Sigma Aldrich), supplemented with 10 % fetal bovine serum (FBS; Sigma Aldrich), 2 % (*v/v*) penicillin/ streptomycin (Sigma Aldrich) and 1 % L-glutamine (Sigma Aldrich) [195]. Culture conditions were kept for both cell lines at 37 °C, 100 % humidity and 5 % CO_2. Sub-culturing was carried out every second day for HepG2 cells and once a week for CCF-STTG1 cells by using a 0.25 % trypsin-EDTA solution (Sigma Aldrich).

For treatment of Co and Ni, $CoCl_2$ (Thermo Fischer Scientific; 99.9 %) and $NiCl_2$ (Sigma Aldrich; 99.9 %) were dissolved in bidistilled water before the experiment. For single metal treatment, logarithmically growing cells were incubated for 2, 6, 24 or 48 h, depending upon the experiment. Combined treatment for cytotoxicity was performed using fixed concentrations of either Co (25 µM) or Ni (150 µM) and varying amounts of the respective other metal. For the remaining assays, two different combinations (HepG2: 12.5 µM Co + 75 µM Ni and 25 µM Co + 150 µM Ni; CCF-STTG1: 25 µM Co + 150 µM Ni and 100 µM Co + 600 µM Ni) were used. All combinations were incubated simultaneously for 2, 6 or 24 h.

4.2.2. Cytotoxicity of Co and Ni

In both cell lines, cytotoxic effects of Co and/or Ni were investigated by determination of cell number (via Hoechst assay) and cellular metabolic activity (via Resazurin assay).

Cell number (Hoechst assay)

For indirect determination of the cell number, the DNA intercalating dye Hoechst 33258 (Sigma Aldrich) was used as previously described [196]. After 10 min fixation with 3.8 % formaldehyde in phosphate buffered saline (PBS), cells were permeabilized with 0.22 % Triton™ X-100 in PBS for another 10 min and stained with 6 µM Hoechst dye in PBS for 30 min. After washing with PBS, fluorescence was directly measured using a Tecan microplate reader (Tecan Infinite Pro M200; Ex.: 355 nm, Em.: 460 nm).

Cellular metabolic activity (Resazurin assay)

Investigation of metabolic activity is based on the reduction of nonfluorescent resazurin to fluorescent resorufin by dehydrogenases of living cells as described before [197]. Cells were incubated with 5 µg/mL Resazurin (Sigma Aldrich) in culture media for 3 h at 37 °C after 24 h or 48 h treatment with Co and/or Ni. Fluorescence was detected by a Tecan microplate reader (Tecan Infinite Pro M200; Ex.: 540 nm, Em.: 590 nm).

4.2.3. Cellular bioavailability of Co and Ni

To assess cellular bioavailability of Co and Ni, cells were seeded in 6 cm cell culture dishes (growth area: 22.1 cm^2) or 10 cm cell culture dishes (growth area: 60 cm^2). After the respective incubation time, cells were pelletized using 0.25 % trypsin-EDTA for detaching. Cell suspension was washed with ice-cold PBS containing 5 % FBS, centrifuged at 150 x g and 4 °C for 5 min and the remaining cell pellet was re-suspended in ice-cold PBS, followed by a second centrifugation at 2370 x g and 4 °C for 4 min. The supernatant was removed, and cell pellets

were stored at -80 °C until further digestion and analyses. For ICP-OES sample preparation, pellets were resuspended in bidistilled water, homogenized using an ultrasonic probe (20 s, cycle: 1, amplitude: 100 %; Hielscher UP100H) and dried at 95 °C overnight. 100 µg/L Yttrium (Y) (ICP-Standard-Solution ROTI®Star, Carl Roth) was added as internal standard and further digested in 1:1 65 % nitric acid (Suprapur®, VWR) and 30 % hydrogen peroxide (Sigma Aldrich) at 95 °C overnight. Ashed samples were dissolved in 2 % nitric acid and total metal content was measured using inductively coupled plasma-optical emission spectrometry (ICP-OES; Avio 220 Max, PerkinElmer). Verification of each measurement was provided with Standard Reference Material® 1643f (National Institute of Standards and Technology) and Certified Reference Material BCR®-274 (single cell protein, Institute for Reference Materials and Measurements), which was digested according to samples. Measurement parameters are displayed in table 6. Obtained metal concentrations were normalized to sample protein amount, quantified via standard BCA assay (Sigma-Aldrich).

Table 6: ICP-OES (Avio 220 Max, PerkinElmer) measurement parameters.

parameter	conditions
plasma power [W]	1500
cooling gas flow [L/min]	10.0
auxiliary gas flow [L/min]	0.2
nebulizer flow [L/min]	0.7
nebulizer	MicroMist™
torch alignment	axial
element wavelengths [nm]	Co: 238.892; Ni: 231.604; Y: 371.029
software analysis	Syngistix™
LOQ Co [µg/L]	0.6
LOQ Ni [µg/L]	3.1

4.2.4. Inhibition of divalent metal transporter 1 (DMT-1)

To investigate the impact of DMT-1 on Co and Ni bioavailability in HepG2 cells, the DMT-1 blocker 2 (MedChemExpress) was used [198]. For that, the inhibitor stock solution was prepared in dimethyl sulfoxide (DMSO) and 3 µM (with a final DMSO concentration ≤ 1 %) of the blocker were incubated for 30 min before the following 24 h treatment of Co and Ni. The cells were pelletized and further prepared as mentioned above, with subsequent ICP-OES measurement to determine the total metal content.

4.2.5. Cellular RONS level

Effects of Co and Ni on the formation of reactive oxygen and nitrogen species (RONS) were investigated using the oxidation-sensitive fluorescent probe 6-carboxy-2',7'-dichlorodihydrofluorescein-diacetate (carboxy-DCFH-DA) as described in [195]. After 24 h incubation with Co and/or Ni, cells were loaded with 15 µM carboxy-DCFH-DA in cell culture medium for 20 min at 37 °C. Cells were washed twice with warm medium and again incubated with Co and/or Ni or 100 µM *tert*-butylhydroperoxide (*t*BOOH) as a positive control. RONS generation was monitored every hour up to 6 h using a Tecan microplate reader (Tecan Infinite Pro M200; Ex.: 485 nm, Em.: 520 nm). Data were always normalized to a control (dye-loaded cells without a RONS generator) of the respective time point in order to exclude an interfering fluorescence of the matrix.

4.2.6. Cellular glutathione (GSH) and glutathione disulfide (GSSG) levels

Alterations in cellular glutathione levels after Co and Ni incubation were determined with a liquid chromatography-tandem mass spectrometry method as previously described [81].

4.2.7. Caspase-3 Activity and Lactate Dehydrogenase Assay

In HepG2 cells, apoptotic cell death was assessed via caspase-3 activity, while necrotic cell death was determined by lactate dehydrogenase (LDH) release.

Caspase-3 activity

Co- and Ni-induced caspase-3 activity was determined using the cleavage of the substrate *N*-acetyl-asp-glu-val-asp-7-amino-4-trifluoromethylcoumarin (Ac-DEVD-AFC; Enzo Life Sciences) to the fluorescent form 7-amino-4-trifluoromethylcoumarin (AFC) as described before [196]. 30 µL of the lysed cells were diluted in a black 96 well plate (Lumox®, Sarstedt) containing a reaction buffer consisting of caspase buffer (50 mM PIPES, 10 mM EDTA disodium salt dihydrate, 8 mM CHAPS; pH 7.4), 9 mM dithiothreitol (DTT) and 90 µM Ac-DEVD-AFC substrate and then incubated at 37 °C for 3 h. Fluorescence was measured using a Tecan microplate reader (Tecan Infinite Pro M200; Ex.: 405 nm, Em.: 510 nm). All obtained concentrations were normalized to sample protein amount, quantified via BCA assay (Sigma-Aldrich).

Lactate dehydrogenase release

In case of necrotic cell death, LDH is released into the medium. The released LDH converts pyruvic acid to lactate while NADH is oxidized to NAD^+. The reduction in NADH levels was quantified photometrically as previously described [196]. A LDH reaction buffer (0.2 mM NADH disodium salt; 10 mM pyruvic acid; 100 mM HEPES buffer; pH 7.0) was added to the lysed cells and an aliquot of the cell culture media. Absorption was measured directly every 54 s for 50 cycles using a Tecan microplate reader (Tecan Infinite Pro M200; 355 nm). All results were normalized to sample protein amount, quantified via BCA assay (Sigma-Aldrich).

4.2.8. Statistics

Statistical analysis was performed using GraphPad Prism software 6.01 (GraphPad, La Jolla, CA, USA). Data is presented as mean ± SD with significance depicted as *$p<0.05$, **$p<0.01$ and ***$p<0.001$ compared to untreated control. The respective statistical test is stated in the figure caption of the individual experiment.

4.3. Results

4.3.1. Cytotoxicity

Since liver cells as well as brain cells are important sites of pathological changes among Co and Ni exposed human patients or *in vitro* models, HepG2 and CCF-STTG1 cells were chosen as model systems [128,199,200]. In both cell lines, the time- and concentration-dependent cytotoxic effect of Co and Ni, as well as the comparison of single and combined treatment was assessed. Therefore, two assays addressing different endpoints as metabolic activity and cell count were performed. Figure 15 shows the most sensitive endpoint (CCF-STTG1: metabolic activity; HepG2: cell count), while a summary of all cytotoxicity data is displayed in table 8. CCF-STTG1 cells showed a statistically significant decrease in metabolic activity starting at 1000 µM Co after 24 h and 750 µM Co after 48 h exposure (fig. 15A) while Ni seems to be more cytotoxic (significant decrease after 300 µM Ni; fig. 15B). In contrast, HepG2 cells are more sensitive towards Co exposure with statistically significant reduced cell survival after incubation of 50 µM Co or 300 µM Ni for 24 h (fig. 15C/D). After single Co and Ni treatment, time-dependent cytotoxicity between 24 and 48 h could be observed in HepG2 cells, and only slightly for Ni in CCF-STTG1 cells. No enhanced cytotoxic effect of the combined treatment compared to single incubation was observed in either cell line (fig. 15E and tab. 8), except for the combination of 25 µM Co with 100 and 200 µM Ni in HepG2 cells (fig. 15F) and the combination of 600 µM Ni with various Co concentrations in CCF-STTG1 cells (tab. 8).

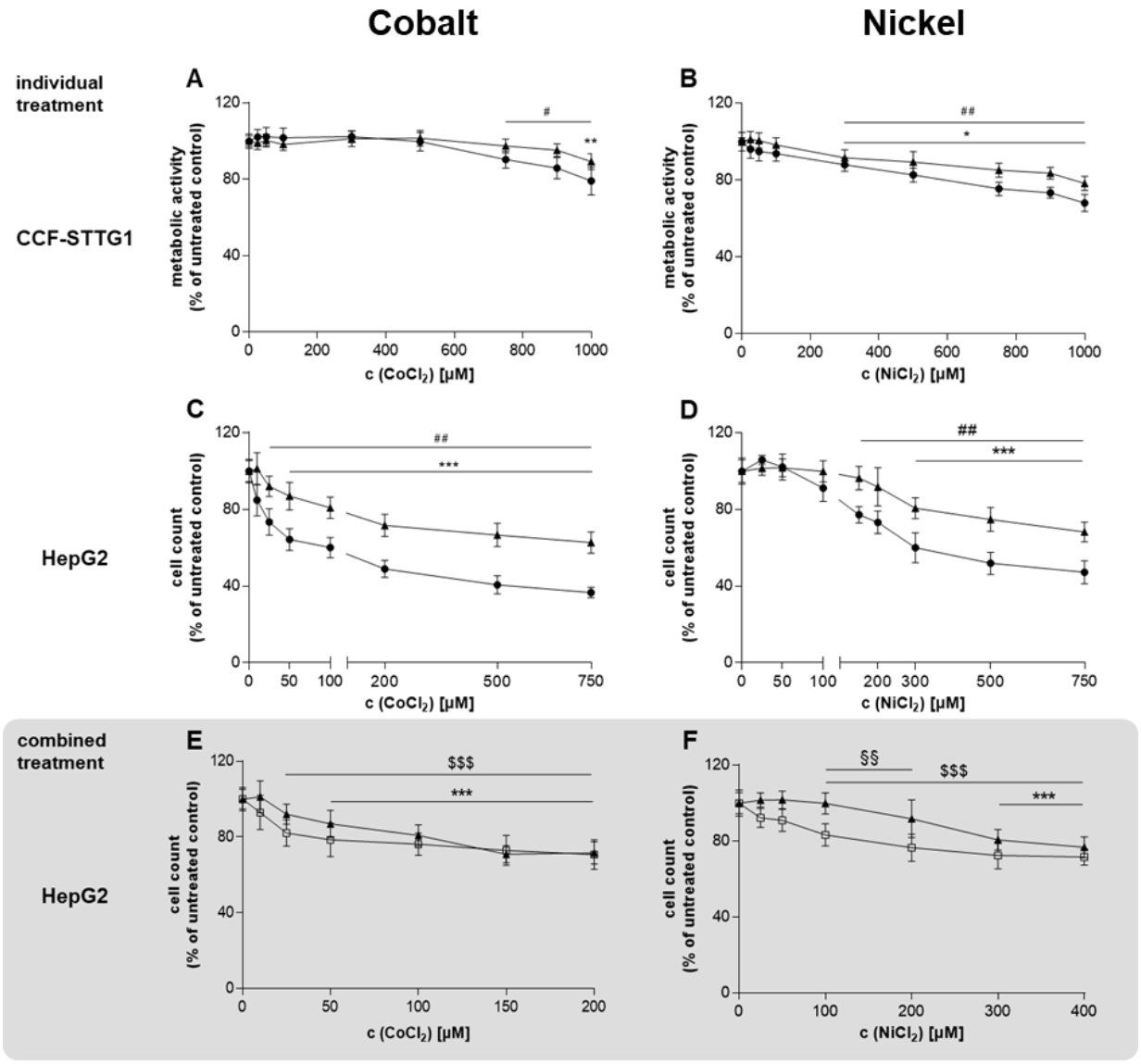

Figure 15: Cytotoxicity of Co and Ni in CCF-STTG1 and HepG2 cell lines after 24 h (▲) or 48 h (●) incubation time in single and combined (□) exposure. Metabolic activity was measured via Resazurin assay (CCF-STTG1 cells) after single exposure of 0 – 1000 µM Co (A) or Ni (B). In HepG2 cells cell count was tested using Hoechst 33258 assay after single exposure of 0 – 750 µM Co (C) or Ni (D), and after combined treatment with 150 µM Ni + varying Co concentrations (E) or 25 µM Co + varying Ni doses (F). Data is presented as mean ± SD of n ≥ 3 independent experiments. Statistical significance was tested by an unpaired t-test depicted as *p≤0.05, **p≤0.01, ***p≤0.001: 24 h treatment compared to untreated control; $^{\#}$p≤0.05, $^{\#\#}$p≤0.01: 48 h treatment compared to untreated control; $^{\$\$\$}$p≤0.001: combined treatment compared to untreated control; §§p≤0.01: combined exposure compared to single exposure.

4.3.2. Cellular bioavailability of Co and Ni

To assess the impact of different exposure scenarios on cellular Co and Ni levels, the total metal content was measured via ICP-OES. In both cell lines, a concentration-dependent increase could be observed for both metals, while there was no time dependence between 24 and 48 h. In direct comparison the bioavailability of Co and Ni (single exposure) was higher in HepG2 cells as compared to CCF-STTG1 cells. Compared to Ni, more Co was found in the cells after the same incubation time and metal concentration, but similar amounts were measured in both cell lines (CCF-STTG1: 1852 ± 188 pg Co/µg protein and 285 ± 31 pg Ni/µg protein after 24 h and 500 µM single metal exposure; HepG2: 2127 ± 214 pg Co/µg protein and 490 ± 26 pg Ni/µg protein after 24 h and 500 µM single metal exposure; fig. 16 A/B/C/D). When the HepG2 cells were incubated with both metals in combination, a higher amount of Co was observed compared to single incubation, while the Ni content decreased (fig. 16 E/F). In the higher combination of 25 µM Co and 150 µM Ni, the Co content increased by 213 % and the Ni content decreased by 66 %, while this effect was less in the lower combination of 12.5 µM Co and 75 µM Ni (Co: increased by 151 %; Ni: decreased by 14 %). The described effects are also present in the CCF-STTG1 cells but to a lesser extend (fig. 44). When shorter timepoints (2 h and 6 h) were tested, the results revealed that the described effect of elevated Co and decreased Ni levels due to combined treatment in HepG2 cells is time-dependent with significant changes starting at 6 h at the highest combination (25 µM Co + 150 µM Ni) (fig. 17 A/B). When DMT-1 blocker 2 was incubated 30 min prior to 24 h Co and Ni treatment, cellular Co levels were significantly reduced compared to treatment without the inhibitor (fig. 17 C/D). Ni was only decreased when incubated individually and not in combination with Co. The effect of increased Co levels after combined incubation could also been observed after treatment with the inhibitor, but to a lesser extent.

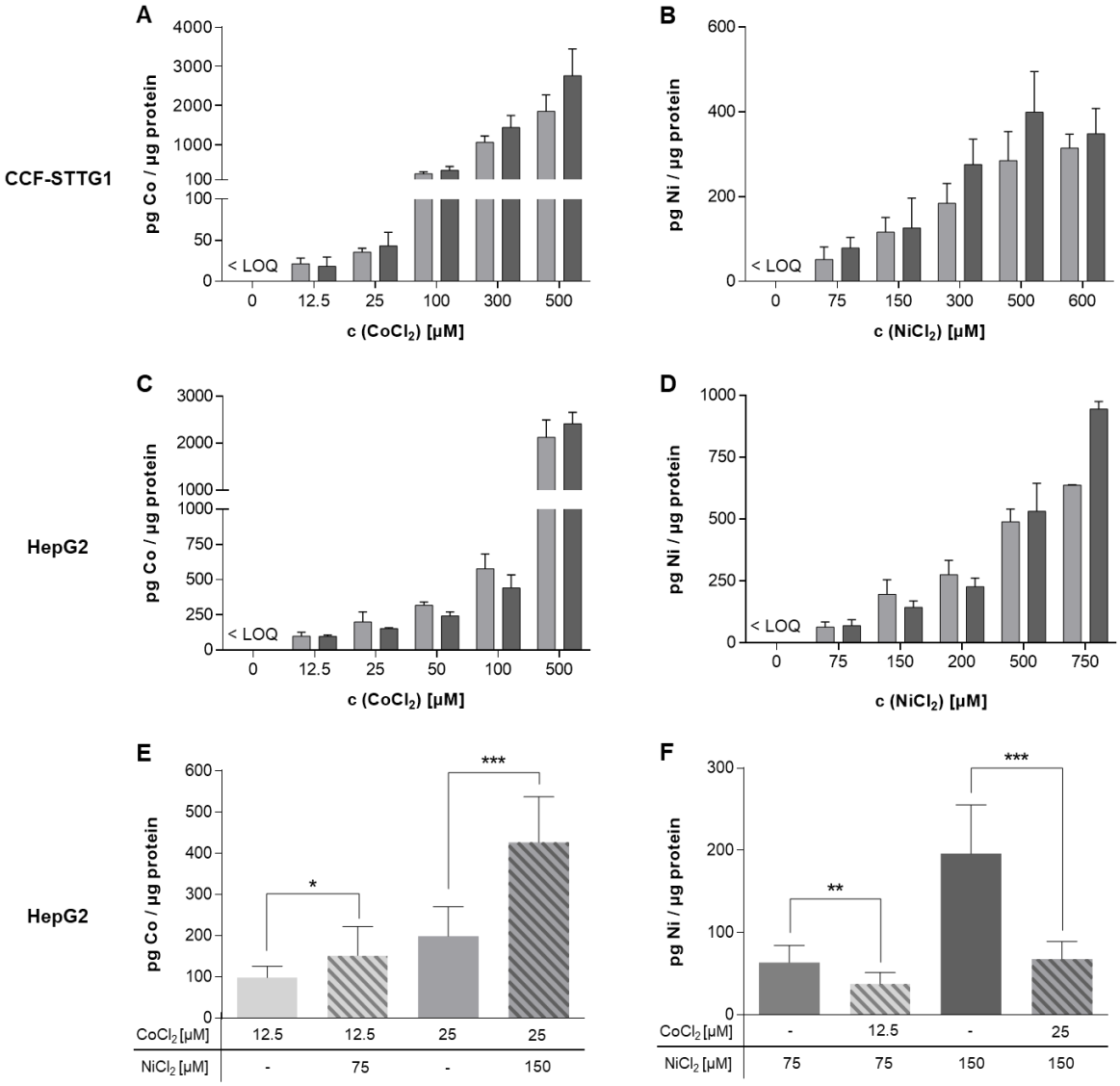

Figure 16: Bioavailability of Co and Ni in CCF-STTG1 and HepG2 cells after 24 h (light grey) or 48 h (dark grey) incubation time in single exposure and after 24 h incubation in combined exposure. Cellular metal content was measured via ICP-OES after single exposure of 0 – 500 µM Co (A) or 0 – 600 µM Ni (B) in CCF-STTG1 cells. In HepG2 cells metal amount was tested after single exposure of 0 – 500 µM Co (C) or 0 – 750 µM Ni (D) and after combined treatment with 12.5 µM Co + 75 µM Ni or 25 µM Co + 150 µM (E + F). Data is presented as mean + SD of n ≥ 3 independent experiments. Statistical significance was tested by an unpaired t-test with Welch's correction depicted as *p≤0.05, **p≤0.01, ***p≤0.001: single treatment compared to combined exposure.

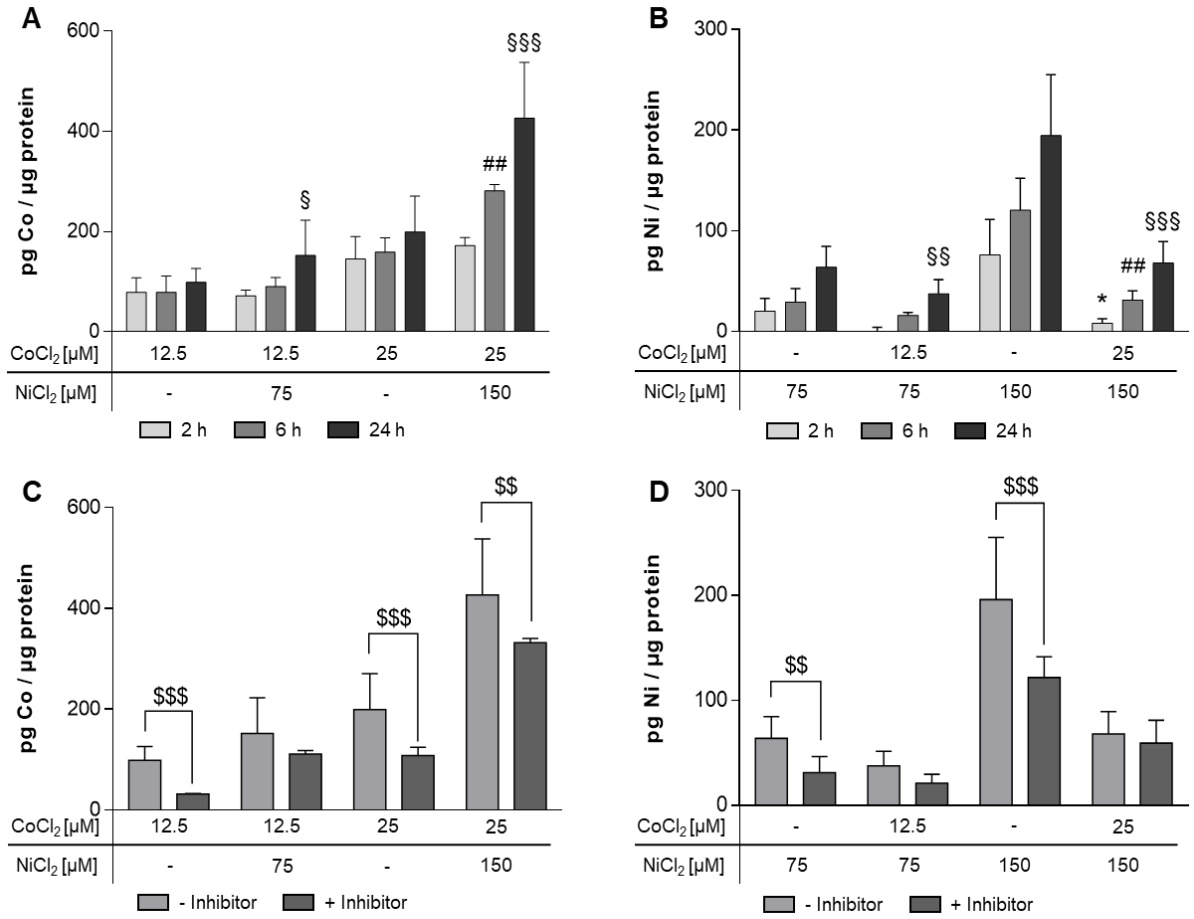

Figure 17: Bioavailability of Co and Ni in HepG2 cells after 2, 6 or 24 h incubation time in single and combined exposure and after 24 h incubation when preexposed to DMT-1 blocker 2. After 2, 6, or 24 h incubation with Co and Ni individually or in combination cellular Co (A) or Ni (B) content was measured via ICP-OES. HepG2 cells were preexposed with 3 µM DMT-1 blocker 2 for 30 min and incubated with Co and Ni individually or in combination for 24 h before measuring again cellular Co (C) or Ni (D) amount. Data is presented as mean + SD of n ≥ 3 independent experiments. Statistical significance was tested by an unpaired t-test with Welch's correction depicted as $^{*,\S}p \leq 0.05$, $^{\#\#,\S\S}p \leq 0.01$, $^{\S\S\S}p \leq 0.001$: combined treatment compared to single exposure at the same time point; $^{\$}p \leq 0.05$, $^{\$\$}p \leq 0.01$, $^{\$\$\$}p \leq 0.001$: treatment without inhibitor compared to exposure with inhibitor.

4.3.3. Oxidative stress markers

For the individual toxicity of Co and Ni, oxidative stress is an often-discussed underlying mechanism [201]. Two different assays (RONS induction and GSH oxidation) were used to investigate metal-induced oxidative stress in HepG2 and CCF-STTG1 cells. Both cell lines showed a RONS induction starting at 100 µM Co, but no significant alterations could be observed upon Ni treatment. The higher combination of both metals led to increased RONS, whereas no effects were observed compared to the single concentration (fig. 18 A/C). Similar effects were observed for GSSG, which started to be significantly altered at 100 µM Co and increased by 605 % in CCF-STTG1 and 1275 % in HepG2 cells after incubation with 500 µM Co for 24 h. Ni treatment showed no significant alterations in GSSG content tested up to 500 µM. Compared to single treatment of 25 µM Co or 150 µM Ni, the combination of both led to higher GSSG levels in both cell lines, and also the combination of 100 µM Co and 600 µM Ni resulted in elevated GSSG levels in CCF-STTG1 cells (fig. 18 B/D). Both combinations were significantly elevated compared to single Co treatment, although no significant changes were observed in comparison to single Ni treatment. The GSH content remain unaffected by Co or Ni, except after incubation of 500 µM Co or the combination of 25 µM Co and 150 µM Ni in CCF-STTG1 cells (fig. 45).

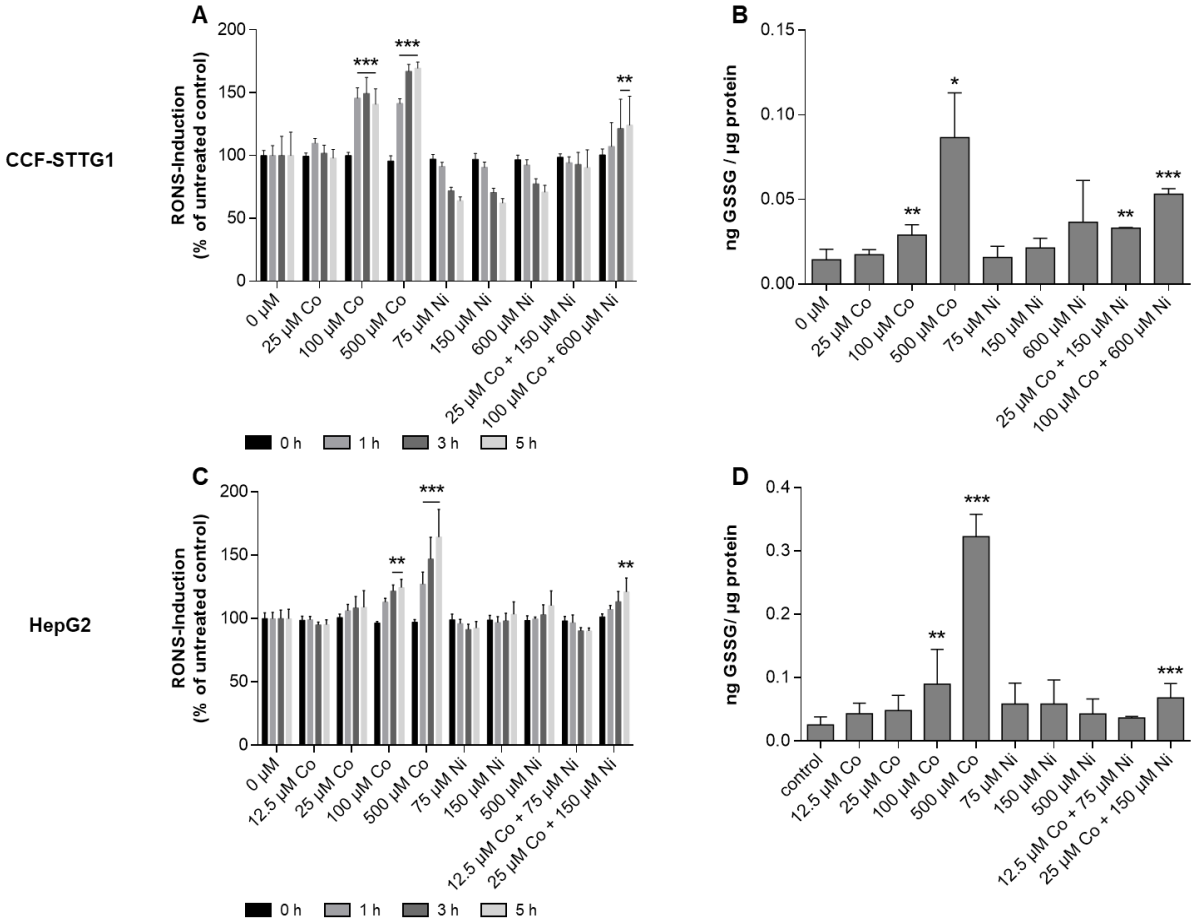

Figure 18: Oxidative stress markers after 24 h single and combined incubation of Co and Ni in CCF-STTG1 cells (A, B) and HepG2 cells (C, D). RONS induction (A, C) was investigated via Carboxy-DCFH-DA assay, measured at different time points and cellular GSSG levels (B, D) were quantified using LC-MS/MS. Data is presented as mean + SD of n ≥ 3 independent experiments. Statistical significance was tested by an unpaired t-test with Welch's correction depicted as *p≤0.05, **p≤0.01, ***p≤0.001: compared to untreated control.

4.3.4. Cell death mechanisms

To investigate possible cell death mechanisms, caspase-3 activity and LDH release were assessed after 24 h Co and Ni incubation in HepG2 cells. Both caspase-3 and LDH release were significantly induced after treatment with concentrations exceeding 100 µM Co and 500 µM Ni individually compared to untreated control. The same effect was observed with the combination of 25 µM Co and 150 µM Ni, whereas the same concentrations incubated individually showed no alterations (fig. 19 A/B). Since Co and Ni are not cytotoxic in the tested

concentration range in CCF-STTG1 cells, no significant changes were observed in caspase-3 activity and LDH release (data not shown).

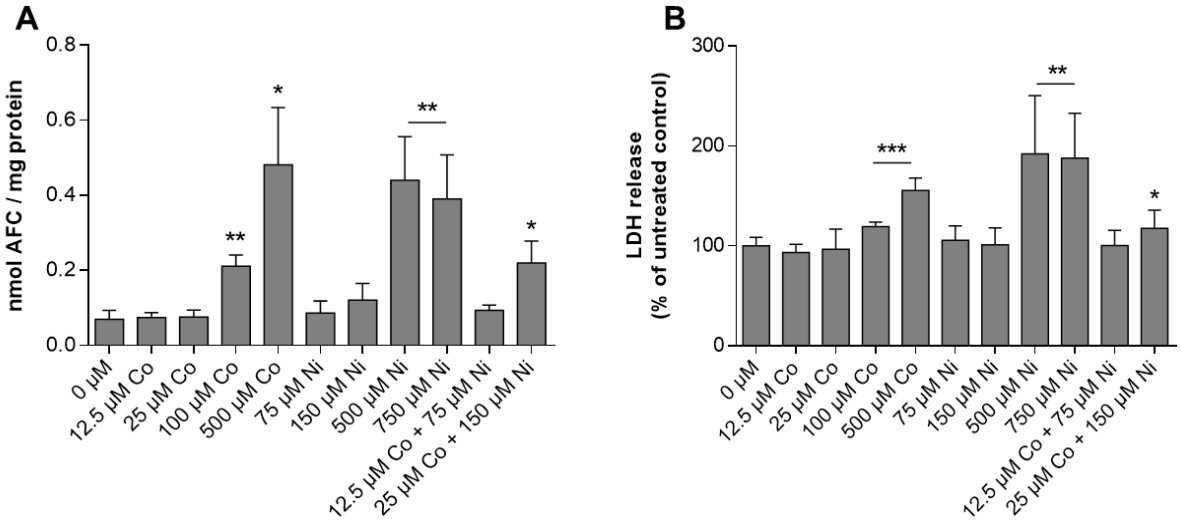

Figure 19: Caspase-3 activity (AFC cleavage) (A) and LDH release (B) after 24 h incubation of single and combined Co and Ni exposure in HepG2 cells. Data is presented as mean + SD of n ≥ 3 independent experiments. Statistical significance was tested by an unpaired t-test with Welch's correction depicted as *p≤0.05, **p≤0.01, ***p≤0.001: compared to untreated control. AFC = 7-amino-4-trifluoromethylcoumarin; LDH: lactate dehydrogenase.

4.4. Discussion and Conclusions

The high spread of products containing Co and Ni unavoidably leads to higher environmental pollution, which may result in increased ingestion by humans. Due to the reported adverse effects of Ni and Co toxicity concerns are rising. While most studies in literature focus on inhalation exposure scenarios, more data are needed upon oral exposure as it is a prominent route of exposure for the general population. Since both metals are commonly found together, identifying potential interactions in their mechanism of transport and toxicity is essential. Several studies have already investigated the effect of Co and Ni in single treatment in various human cell lines, however, to our knowledge little is known about combined exposure so far.

Therefore, in this study the effects of Ni and Co in single and combined treatment were addressed in human cell lines from tissues which are discussed as targets of toxicity, and which are relevant in an exposure setting upon oral intake. HepG2 (human liver cells) and CCF-STTG1 cells (human brain cells (astrocytes)) were chosen as model systems. In direct comparison, cytotoxicity data demonstrated a higher sensitivity of HepG2 cells to both metals than the astrocytes. This might be due to the different cellular metal content, which is almost doubled in the HepG2 cells after same concentration and incubation time compared to CCF-STTG1 cells (fig. 16). Additionally, the lower cytotoxicity compared to HepG2 cells could be due to the high production of antioxidants [202], since astrocytes are responsible for the protection of neurons, by maintaining the blood-brain barrier, scavenging of RONS, and providing neurotransmitter precursors, among other functions, making them potentially less vulnerable [130,131]. The resistance of astrocytes against Co has also been reported in a study comparing them to neuroblastoma cells [203], pointing out that astrocytes may not be a sensitive target of Co toxicity in the brain. Although Co is considered as an essential trace element, HepG2 cells appear to be more sensitive to Co than to Ni (fig. 15 C/D). This correlates with the bioavailability data, which indicates a nearly threefold higher Co concentration relative to Ni under identical incubation periods and concentrations (fig. 16 C/D). In H460 human lung epithelial cells, the amount of Co was about 8-fold higher compared to Ni content after incubation of 6 or 24 h [204]. This therefore suggests that human cells of varying organs act differently in Co and Ni homeostasis, but Co seems to be better bioavailable than Ni in human cells.

Since Co and Ni often occur together and are supposed to be transported into the cell mainly via the same transporters [4], the cellular amount of Co and Ni was assessed exposing a mixture of both metals. The chosen Ni/Co ratio of 6:1 in this study represents a ratio which is also found in industrial usage as in lithium-ion batteries and is thereby realistic [194]. Two combinations of the 6:1 ratio

(Ni:Co) were chosen, one with concentrations which showed no cytotoxic effects after single treatment (HepG2: 12.5 µM Co + 75 µM Ni; CCF-STTG1: 25 µM Co + 150 µM Ni) and a higher combination where the chosen concentrations showed a beginning (not significant) cytotoxicity in individual treatment (HepG2: 25 µM Co + 150 µM Ni; CCF-STTG1: 100 µM Co + 600 µM Ni) in the Hoechst- or Resazurin-Assay (fig. 15 C/D). Interestingly, the combined exposure led to an increase in the cellular Co amount, while the Ni content decreased compared to single treatment (fig. 16 E/F), indicating an interaction in transfer mechanisms. In literature there is to our knowledge a single study in male rats and only two *in vitro* studies (lung epithelial cells) exposing Co and Ni in parallel [190,191,205]. Regarding cytotoxicity, the studies of Cross *et al.* and Patel *et al.* carried out a synergistic cytotoxic effect after combined exposure of different Co and Ni concentrations in lung epithelial cells [190,191]. However, we could not observe this effect in our study. The three studies in literature ([190,191,205]) lack bioavailability data, limiting comparison across the studies. In other organisms (paramecia), we were recently able to identify a difference between individual Co and Ni exposure and the combination in terms of bioavailability and toxicity [206]. Regarding cellular transport in mammalian cells, for both metals DMT-1 is reported to be involved upon single exposure [30,31]. Besides the plasma membrane, DMT-1 is located intracellularly in the nucleus and on the outer mitochondrial membrane, indicating that the highest metal concentration is found there [207,208]. Substrate selectivity was observed for the H^+-coupled DMT-1, which generally transports divalent metals, but prefers Co more than Ni [32]. In a study investigating Ni uptake in competition with other divalent metals in human monocytic cells (THP-1), Ni content was decreased by Co, Mn and Zn [209]. Furthermore, a dual exposure of Co and Fe resulted in lower Fe uptake, leading to the general assumption that there is a competitive inhibition of DMT-1 [32]. However, the combination of Fe and Ni resulted in a reduced Ni uptake in Caco-2 cells [210]. Since Co stabilizes HIF-1α and HIF-2α, it is commonly used to mimic chemical hypoxia [47]. Li *et al.* demonstrated the

hypoxia-inducible nature of DMT-1 and revealed a concentration-dependent upregulation of DMT-1 expression in HepG2 cells after Co exposure, possibly leading to elevated transport [208]. By using the DMT-1 blocker 2, we clarified the involvement of DMT-1 in Co and Ni transport in HepG2 cells, with decreased metal amount when incubated in combination with the inhibitor (fig. 17). However, transport into the cells was not completely inhibited, suggesting the participation of other transporters. Co^{3+} and Ni^{2+} are also able to bind transferrin (Tf), thus making transferrin receptor 1 (TfR1) an option for cellular transport as well [33,34]. TfR1 also appears to be hypoxia-inducible, as shown by Calzolari *et al.* via incubation of Co in HepG2 cells [211]. Additionally, the Zrt- and Irt-like protein family (ZIP, SLC39A) is involved in cellular metal transport, especially of Zn [35]. Particularly ZIP8 and 14 are known to act as symporters of various divalent cations, like Co and Ni. Nebert *et al.* described a reduced Zn uptake caused by Co and Ni [37], while Co is inhibiting the transport of Fe and Mn via ZIP14 [212]. Zhao *et al.* reported that in HepG2 cells, ZIP14 is located in the plasma membrane, and mRNA levels of ZIP14 are about 10 fold higher than DMT-1 mRNA copy numbers, suggesting an important role in metal transport in HepG2 cells [213]. In addition to the above mentioned transporters, the transient receptor potential melastatin type 7 (TRPM7) is involved in Co and Ni homeostasis [38,214]. From our data we cannot point out the exact mechanism of the observed effect after dual exposure but we could indicate first involved mechanisms. Partly, DMT-1 might be involved but other mechanisms are possible. By using the DMT-1 inhibitor, the effect of increased cellular Co and lower Ni after combined treatment was observed to a lesser extent, suggesting DMT-1-independet transfer is also involved. Furthermore, Ni and Co may have different binding capacities to proteins which causes lower Ni uptake in case of combined exposure. Both metals are mostly bound to human serum albumin (HSA), where Co prefers an octahedral geometry at all three binding sites, whereas Ni forms square-planar structures by binding only at two sites [24].

Yang *et al.* reported an inhibited binding of Co to HSA by the addition of Ni, while more Ni was bound compared to single metal treatment [215].

Single Co and Ni treatment led in HepG2 cells to an increased caspase-3 activity, as well as a higher LDH release, concluding that both apoptosis and necrosis are part of the underlying cell death mechanism. This was observed even in the higher combination of both metals (25 µM Co + 150 µM Ni), with an enhanced effect compared to the respective single dose. Green *et al.* investigated the differences of Co and Ni regarding cell death in H460 cells, showing a partly p53 dependent and caspase mediated apoptosis and partly independent toxicity, while Ni-induced cell death was entirely caspase-3 driven [204]. Although Ni-induced LDH leakage, Wong *et al.* found that in this case it is due to a late event of apoptosis and not caused by necrosis [216]. In HepG2 cells, the concentration-dependent apoptosis induced by $CoCl_2$ was associated with its ability to enhance HIF-1α protein levels which negatively regulates the glypican-3 (GPC3) expression [217]. Overexpression of GPC3 was found to be important in hepatocellular carcinoma development by enhancing the resistance to apoptosis [218]. Therefore, our findings on single treatment are clearly supported by the current literature. Studies with parallel exposure are rare but their data underline the findings in lung cells [190,191]. The *in vitro* studies suggest a synergistic toxicity as for example Patel *et al.* showed an enhanced caspase-3 activity and poly(ADP-ribose) polymerase (PARP) cleavage after combined incubation of Co and Ni compared to single treatment. They further assume that this is a result of RONS induction and DSB formation [191]. In our study we could also identify increased RONS in dual exposure of Co and Ni compared to single treatment.

Lee *et al.* reported comparable effects to this study related to Co-induced RONS production starting at 300 µM Co after 24 h, also in HepG2 cells [219]. Surprisingly, we found no enhanced RONS induction by Ni, although it was reported several times before in various cell lines [179,220,221].

In U-87 MG (human astrocytoma cells), RONS production by Ni was significantly increased at 6 and 12 h exposure time, with the possibility they were scavenged by cellular antioxidants after 24 h. A comparison of Co and Ni in A549 cells showed a much lower RONS induction by Ni, compared to Co [222]. Lewis *et al.* reported in THP1 monocytic cells also no RONS production after Ni treatment, but observed a Nrf2 related redox management [223], which includes GSH metabolism, especially via inducing γ-glutamate-cysteine ligase (GCL) [224]. Both astrocytes and liver cells contain high levels of GSH, making GSH-dependent detoxification processes important for cell protection [224,225]. GSH mainly occurs in its reduced form but gets oxidized to GSSG while reducing toxins like free radicals. Additionally, GSH is able to conjugate electrophilic xenobiotics to eliminate them [81]. We observed a massive increase in GSSG levels induced by Co consistent with the enhanced RONS levels. Surprisingly, cellular GSH amount did not alter, assuming a higher GSH synthesis due to the elevated oxidation. So, in summary, oxidative stress was observed for single exposure of Co but not for Ni. Interestingly, the dual exposure of Co and Ni causes oxidative stress in terms of RONS and GSSG.

Our presented data show differences but also concurrence and synergistic potential in transport and toxicity mechanisms of Co and Ni, which also seem to be cell type specific. HepG2 cells showed higher sensitivity compared to CCF-STTG1, with Co being the more toxic metal for both cell lines. The combination of Co and Ni did not show enhanced cytotoxicity compared to single treatment, but the transport of Co into the cells is favored with subsequent lower cellular amount of Ni. The two metals also seem to differ in their toxicity mechanisms, since RONS induction and GSH oxidation were only observed with Co. The combination of Co and Ni led to enhanced effects regarding oxidative stress markers and cell death mechanisms compared to the respective single incubation, assuming this may partly result due to the increased cellular Co amount in combined treatment. Future studies are required to focus on the more

realistic exposure scenario of mixtures which is a growing concern in order to provide advanced hazard characterizations for risk assessments [226]. The risk cannot be predicted from toxicity studies with single metal treatment since we do have competition and interaction as we showed in our study, and it is always mandatory to take bioavailability into account discussing mechanisms of toxicity. We need to understand the underlying mechanisms applying mixtures, especially regarding their transport and different transporter affinity, and possible synergistic toxic potential.

4.5. Acknowledgement

This work was supported by the DFG Research Unit TraceAge (FOR 2558, BO4103/4-2) and the initiative “Metal based compounds (MeBaCo)” supported by the University of Wuppertal and the Faculty of Mathematics and Natural Sciences.

4.6. Author contribution statement

Alicia Thiel: Conceptualization, Formal analysis, Investigation, Methodology, Visualization, Writing – original draft, Writing – review & editing. **Vivien Michaelis:** Methodology, Writing – review & editing. **Marco Restle:** Investigation, Writing – review & editing. **Sabrina Figge:** Investigation, Writing – review & editing. **Martin Simon:** Writing – review & editing. **Tanja Schwerdtle:** Writing – review & editing. **Julia Bornhorst:** Writing – review & editing, Project administration, Methodology, Investigation, Funding acquisition, Conceptualization.

Abstract:

Cobalt (Co) and Nickel (Ni) are used nowadays in various industrial applications like lithium-ion batteries, raising concerns about their environmental release and public health threats. Both metals are potentially carcinogenic and may cause neurological and cardiovascular dysfunctions, though underlying toxicity mechanisms have to be further elucidated. This study employs untargeted transcriptomics to analyze downstream cellular effects of individual and combined Co and Ni toxicity in human liver carcinoma cells (HepG2). The results reveal a synergistic effect of Co and Ni, leading to significantly higher number of differentially expressed genes (DEGs) compared to individual exposure. There was a clear enrichment of Nrf2 regulated genes linked to pathways such as glycolysis, iron and glutathione metabolism, and sphingolipid metabolism, confirmed by targeted analysis. Co and Ni exposure alone and combined caused nuclear Nrf2 translocation, while only combined exposure significantly affects iron and glutathione metabolism, evidenced by upregulation of HMOX-1 and iron storage protein FTL. Both metals impact sphingolipid metabolism, increasing dihydroceramide levels and decreasing ceramides, sphingosine and lactosylceramides, along with diacylglycerol accumulation. By combining transcriptomics and analytical methods, this study provides valuable insights into molecular mechanisms of Co and Ni toxicity, paving the way for further understanding of metal stress.

Chapter 5

Transcriptomics Pave the Way into Mechanisms of Cobalt and Nickel Toxicity: Nrf2-Mediated Cellular Responses in Liver Carcinoma Cells

Based on:

Alicia Thiel, Franziska Drews, Marcello Pirritano, Fabian Schumacher, Vivien Michaelis, Maria Schwarz, Sören Franzenburg, Tanja Schwerdtle, Bernhard Michalke, Anna P. Kipp, Burkhard Kleuser, Martin Simon, Julia Bornhorst

submitted to Redox Biology

Highlights:

- Combined exposure to Co and Ni led to higher number of differentially expressed genes
- Nrf2 plays a crucial role in cellular response to Co and Ni toxicity
- Co and Ni affect the cellular sphingolipid metabolism, by increasing dihydroceramide levels and decreasing ceramides, sphingosine, and lactosylceramide
- Both metals enriched Nrf2 regulated genes related to glycolysis, iron and glutathione metabolism

Keywords:

Cobalt; Nickel; metal interactions; transcriptomic analysis; Nrf2 signaling; sphingolipid metabolism

Chapter 5 – Transcriptomics Pave the Way into Mechanisms of Cobalt and Nickel Toxicity: Nrf2-Mediated Cellular Responses in Liver Carcinoma Cells

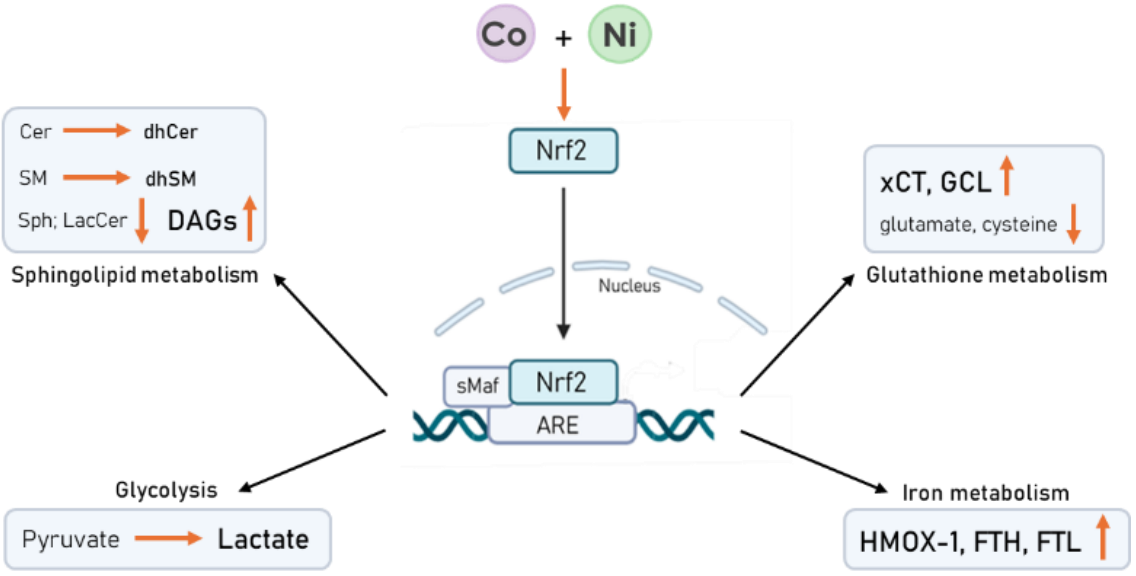

Figure 20: Graphical abstract of 'Transcriptomics Pave the Way into Mechanisms of Cobalt and Nickel Toxicity: Nrf2-Mediated Cellular Responses in Liver Carcinoma Cells'.

5.1. Introduction

Metal toxicity is a significant concern in environmental and occupational health, with cobalt (Co) and nickel (Ni) being significant contributors. Both metals find wide-ranging applications in the manufacturing of alloys, lithium-ion batteries for electric vehicles, and electronics, as well as essential components in catalysts or pigments [1,2]. Despite their industrial importance, Co and Ni seem to have a significant impact on the environmental and health, particularly in occupational settings where exposure levels can be elevated. As their usage in industrial processes continues to grow, environmental entry due to pollution rises, resulting in heightened human exposure through food sources or drinking water.

Co serves as an essential trace element primarily as a cofactor of vitamin B12 and the formation of amino acids and proteins, particularly in nerve cells. In contrast, the biological role of Ni in humans remains elusive [4]. However, concerns regarding potential adverse health effects from Co and Ni exposure are rising due to their carcinogenic potential upon inhalation, as classified by the International Agency for Research on Cancer (IARC; Co: group 2A; Ni: group 1) [43,51]. Oral exposure to these metals may lead to various risks, including neurological, cardiovascular, and thyroid dysfunction, but only limited data exist and the underlying mechanisms are still not conclusively clarified [5]. Hypotheses discussed in literature and targeted studies gave first mechanistic insights and point out the relevance of oxidative stress for both metals. Studies indicate that Co generates reactive oxygen and nitrogen species (RONS) on the cellular level via Fenton-like reactions, leading to oxidative stress, cell death and DNA damage. Similarly, Ni toxicity is associated with DNA crosslinks, inhibition of DNA repair, and mitochondrial dysfunction [7,8].

Most studies are targeted and focus on the toxicity of the individual metal. However, the combined exposure is the more realistic exposure scenario. A first study exposing liver carcinoma cells (HepG2) to the combination of Co and Ni pointed out alterations in the bioavailability, leading to heightened cellular Co levels and decreased Ni amount compared to individual treatment. Additionally, simultaneous treatment led to enhanced effects regarding RONS-induction, GSSG formation or cell death [227]. Although the relevance of combined exposure to elucidate toxicity is indicated, all former studies are focusing on specific endpoints. A transcriptomic analysis could provide a more global view of gene expression across the entire genome, allowing comparisons between alterations in individual and combined treatments. This untargeted approach will allow identifying the most relevant pathways of Co and/or Ni toxicity. The relevance of cellular responses identified by the transcriptome will be further supported by targeted analysis quantifying specific metabolites to gain a deeper

understanding of pathways affected in HepG2 cells. By examining individual cellular pathways and identifying shared and distinct responses to individual and combined Co and Ni exposure, we aim to reveal on the complex interplay between gene regulation and cellular metabolism in metal toxicity.

5.2. Materials and Methods

5.2.1. Cell culture maintenance and treatment scenario

Human hepatocarcinoma cells (HepG2) were cultured in Eagle's Minimum Essential Medium (MEM; Sigma Aldrich) to which 10 % fetal bovine serum (FBS; Sigma Aldrich), 2 % (*v/v*) penicillin/ streptomycin (Sigma Aldrich) and 1 % (*v/v*) non-essential amino acids (NEA; Sigma Aldrich) were added, as previously described [227]. Cells were incubated for 2 or 24 h with $CoCl_2$ (Thermo Fischer Scientific; 99.9 %) and $NiCl_2$ (Sigma Aldrich; 99.9 %) individually or in combination. For combined treatment of Co and Ni, two different combinations were selected, which are applied in an industrial relevant mixture of 6:1 (Ni:Co). The first combination, consisting of 12.5 µM Co + 75 µM Ni, demonstrated no cytotoxic effects when applied individually or in combination. The second, higher combination of 25 µM Co + 150 µM Ni, exhibited initial signs of cytotoxicity, though not statistically significant in individual and combined treatment. To compare the effects of combined and single treatments, cells were exposed to each concentration both together and individually. Cytotoxicity data for these treatments were published in our previous study [227].

5.2.2. Transcriptomics

For transcriptomic analysis, cells were pelletized using 0.25 % trypsin-EDTA for detaching, followed by washing with PBS and centrifugation at 2370 x g and 4 °C for 4 min. After removing the supernatant, total RNA of the cell pellet was isolated using RNeasy Plus Mini Kit which includes DNAse digestion (Qiagen). Poly-A RNA libraries were prepared using the D-Plex mRNA-seq Kit for Illumina (Hologic Diagenode) according to the manufacturer's instructions with 2.5 µg total RNA as

input for mRNA selection and 13 PCR cycles for amplification. Libraries were pooled and sequenced on the NovaSeq 6000 Illumina platform. De-multiplexing, quality trimming as well as removal of adapter-sequences and artificial poly-A-tails were performed as described by manufacturer using the cutadapt tool [228]. Resulting reads showed high quality, quantified by a mean per base quality phred score of 35.8, approx. 97 % of all reads having a quality phred score of 30 or higher (Q30) and a mean per base N content of 0.0005 % across all samples. Reads were mapped onto the human genome (hg38) using the bowtie2 plugin for Geneious Prime 2023.2 with a mean mapping ratio of approx. 85 % of reads across all samples mapping to annotated genes and gene expression levels were calculated using the “calculate expression levels” function of Geneious Prime [229]. Differences between the treatment groups were visualized by PCA on the base of transcripts per million (TPM) expression level data using the prcomp function and ggbiplot visualization function in R. Differentially expressed genes (DEGs) were calculated using the DESeq2 Plugin for Geneious Prime applying a threshold of p-value < 0.01 and $\log_2$ fold change >1/<-1 for DEG characterization [230]. Comparisons were performed between treated and untreated cells. GO Term analysis of DEGs was performed using the geneontology.org website [231,232] which uses the PANTHER tool [233]. Sequencing data are available in the ArrayExpress database (http://www.ebi.ac.uk/arrayexpress) under accession number E-MTAB-14292 [234].

5.2.3. Isolation of cell nuclei

To isolate cell nuclei, HepG2 cells were washed with ice-cold PBS and scratched from cell culture plates using lysis buffer I (10 mM HEPES, 1.5 mM $MgCl_2$, 10 mM KCl, 0.5 mM DTT, 0.5 mM PMSF, 0.1 % NP-40 alternative) as described before [235]. Samples were shaken for 3 min, 4 °C at 1300 rpm, vortexed and shaken again for further 4 min. After centrifugation for 1 min at 4 °C and 6800 x g, the supernatant containing the cytosolic fraction was removed and the remaining

pellet was resuspended in lysis buffer II (40 mM HEPES, 400 mM KCl, 10 % glycerol, 1 mM DTT, 0.1 mM PMSF) and 294 mM NaCl followed by a sonification step (12 s, cycle: 0.5, amplitude: 80 %; Hielscher UP100H) and centrifugation for 30 min at 4 °C at 20000 x g. The supernatant containing the nuclear fraction was used for protein determination, quantified via standard BCA assay (Sigma-Aldrich), and Western Blot analysis.

5.2.4. Western Blot Analysis

For Western Blot analysis, cell pellets have been processed as previously described [236]. As primary antibodies, anti-β-actin (1:2500, ab115777, Abcam), anti-FTH (1:500, D1D4, Cell Signaling), anti-FTL (1:500, ab69090, Abcam), anti-HMOX-1 (1:500, sc-136960, Santa Cruz Biotechnology), anti-Lamin A (1:10000, L1293, Sigma Aldrich) and anti-NRF2 (1:1000, D1Z9C, Cell Signaling) were used. The secondary antibodies HRP-conjugated goat anti-mouse or goat anti-rabbit (1:10000, Bio-Rad Laboratories) were incubated for 1 h at RT. Quantified protein bands were normalized to β-actin (FTH, FTL, HMOX-1) or Lamin A (NRF2).

5.2.5. Immunofluorescence staining

HepG2 cells were seeded on glass cover slips, coated with Alcian Blue 8GX® (Sigma Aldrich). For Nrf2 staining, cells were fixed and permeabilized with PBS containing 4 % formaldehyde (Carl Roth) and 0.2 % Triton-X™ (Sigma Aldrich), washed with PBS and incubated 30 min at 37 °C with 5 % normal goat serum (Life Technologies) in PBS. The primary antibody anti-NRF2 was incubated for 2 h at room temperature (1:500 in 0.5 % BSA/PBS) followed by incubation of the second antibody Alexa Fluor® 488 goat anti-rabbit (Invitrogen) for 1 h (1:400 in 0.5 % BSA/PBS). Finally, cell nuclei were stained using 1 % Hoechst 33258 in MeOH (Sigma Aldrich). Images were taken with the Leica DM6 B fluorescence microscope and processed in LAS X imaging software.

5.2.6. Iron redox speciation

To investigate the iron redox speciation, HepG2 cells were pelletized and resuspended in RIPA buffer. Cells were lysed using an ultrasonic probe (20 s, cycle: 1, amplitude: 100 %; Hielscher UP100H), centrifuged at 10000 x g for 10 min and the supernatant was transferred in a new tube. The samples were shipped on dry ice to the Helmholtz Center Munich in Germany for analysis. The speciation and quantification of Fe^{2+}, Fe^{3+}, and total iron were conducted using capillary electrophoresis inductively coupled plasma mass spectrometry (CE-ICP-MS), as previously detailed [237,238]. In brief, the analysis involved the use of a "PrinCe 706" CE system with an uncoated capillary (85 cm × 50 µm ID) and a custom-built CE-ICP-MS interface for the selective quantification of iron redox species at ICP-DRC (dynamic reaction cell)-MS. The DRC technology, using NH_3 as the reaction gas, was employed for spectral interference-free detection of the ^{56}Fe isotope. Fe^{2+}/Fe^{3+} separation and quantification were conducted in a 20 mM HCl-electrolyte at +25 kV separation voltage, with ^{56}Fe isotope detection at ICP-DRC-MS. To ensure quality control, total iron was additionally determined by ICP-sf-MS, and these values were compared to the sum of iron species quantified by CE-ICP-DRC-MS.

5.2.7. Quantification of metabolites related to glycolysis, TCA cycle and GSH metabolism by HPLC-MS/MS

Sample preparation was conducted and modified based on [239]. Cells were washed with PBS and scratched off the plate using 500 µL of 50 % methanol (MeOH) (-20 °C), containing 0.5 mM N-ethylmaleimide (NEM) and 10 mM formic acid (FA). Collected samples were sonicated for 20 s (cycle: 1, amplitude: 100 %; Hielscher UP100H) and an aliquot was taken for protein measurement. After adding 225 µL chloroform (-20 °C), samples were shaken for 10 min and then for another 2 min after adding 75 µL bidistilled water (4 °C), followed by 20 min incubation at -20 °C. They were centrifuged (4 °C, 9500 x g, 15 min) and 350 µL

of the upper layer was dried using a SpeedVac. The remaining pellet was dissolved in 50 µL 50 % ACN, centrifuged (16060 x g, 10 min) and diluted before LC-MS/MS analysis. Isotope labelled standards (sodium *L*-Lactate-3,3,3-d_3 (CDN Isotopes) and *L*-glutamic-2,3,3,4,4-d_5 acid (Sigma Aldrich)) were added as internal standards. Metabolite quantification was performed on an Agilent 1290 Infinity II LC System coupled to a Sciex QTrap 6500 + triple-quadrupole mass spectrometer with an electrospray ion source operating in both positive and negative mode. Chromatographic separation was accomplished using a Hilicon iHilic®-Fusion column (150 x 2.1 mm, 3.5 µm) complemented by the appropriate pre-column (20 x 2.1 mm, 5 µm). Parameters for the LC-MS/MS measurement and mass transitions are listed in the supplementary (tab. 9 and 10).

5.2.8. Quantification of sphingolipids and diacylglycerols by HPLC-MS/MS

HepG2 cells were pelletized, washed with ice-cold PBS, and resuspended in MeOH. Sphingolipid (SL) and diacylglycerol (DAG) extraction was performed as previously described [240]. Briefly, 1.5 mL methanol/chloroform (2:1, v:v) containing eight internal standards (all from Avanti Polar Lipids, Alabaster, USA), seven for SL and one for DAG quantification (details see supplementary tables 11 and 12), was added to the samples (~1x10^6 cells) that were then shaken overnight at 48 °C. Samples were worked up in two separate preparations, with (for SL) or without (for DAG) saponification of the lipid extract. The further procedure was analogous for both lipid classes. HPLC-MS/MS analyses were carried out under already published instrumental conditions [240,241]. The lipid extracts were chromatographically separated using a 1290 Infinity II HPLC (Agilent Technologies, Waldbronn, Germany) equipped with a Poroshell 120 EC-C8 column (3.0 × 150 mm, 2.7 µm; Agilent Technologies). Multiple reaction monitoring (MRM) was performed using a 6495C triple-quadrupole mass spectrometer (Agilent Technologies) in positive electrospray ionization mode (ESI+). The analyzed SL and DAG species, their mass transitions as well as their retention times are listed in supplementary tables 9 and 10. Analyte peak areas

were normalized to those of their corresponding internal standards followed by external calibration. Peak integration and quantification were conducted with MassHunter Quantitative Analysis Software (version 10.1, Agilent Technologies). SL and DAG quantities were normalized to cell count and expressed as "pmol/1x10^6 cells".

5.2.9. Statistics

Statistical analysis was performed with GraphPad Prism software 6.01 (GraphPad, La Jolla, CA, USA). Data are expressed as mean + SD, with significance stated as *$p<0.05$, **$p<0.01$ and ***$p<0.001$ compared to untreated control.

5.3. Results

5.3.1. Transcriptomic analysis derives the impact of Nrf2

A transcriptomic analysis was conducted to gain deeper insights into the toxicity mechanisms of Co and Ni in HepG2 cells. Both metals were exposed in subtoxic concentrations, as well as the combination of these doses, which were examined in our previous study [227]. Principal component analysis (PCA) revealed different gene expression patterns between the treatments compared to the untreated control, with PC1 explaining 38.8 % variance, indicating differences from the control, and PC2 explaining 12.7 % variance, illustrating the separation of the different exposure scenarios (fig. 21). Fig. 21B further indicates that Co and Ni in case of combined exposure result in a significantly higher number of differentially expressed genes compared to individual exposure. Subsequently, the DEGs in response to the combination (25 µM Co + 150 µM Ni) compared to the untreated control were used for Gene Ontology (GO) term enrichment (fig. 22). Combining both metals seems to influence a variety of molecular functions in HepG2 cells, including the upregulation of carbohydrate metabolism, protein binding or receptor activity. Conversely, downregulated pathways primarily involve lipid metabolism and oxidoreductase activity. Figure 23

highlights the connections between the most affected DEGs and their associated metabolic pathways in response to the combined treatment of Co and Ni. Both metals seem to have an impact on crucial cellular processes, particularly glycolysis, iron homeostasis, and glutathione metabolism. The identified target DEGs are connected to conserved cellular responses driven by the transcription factor Nrf2.

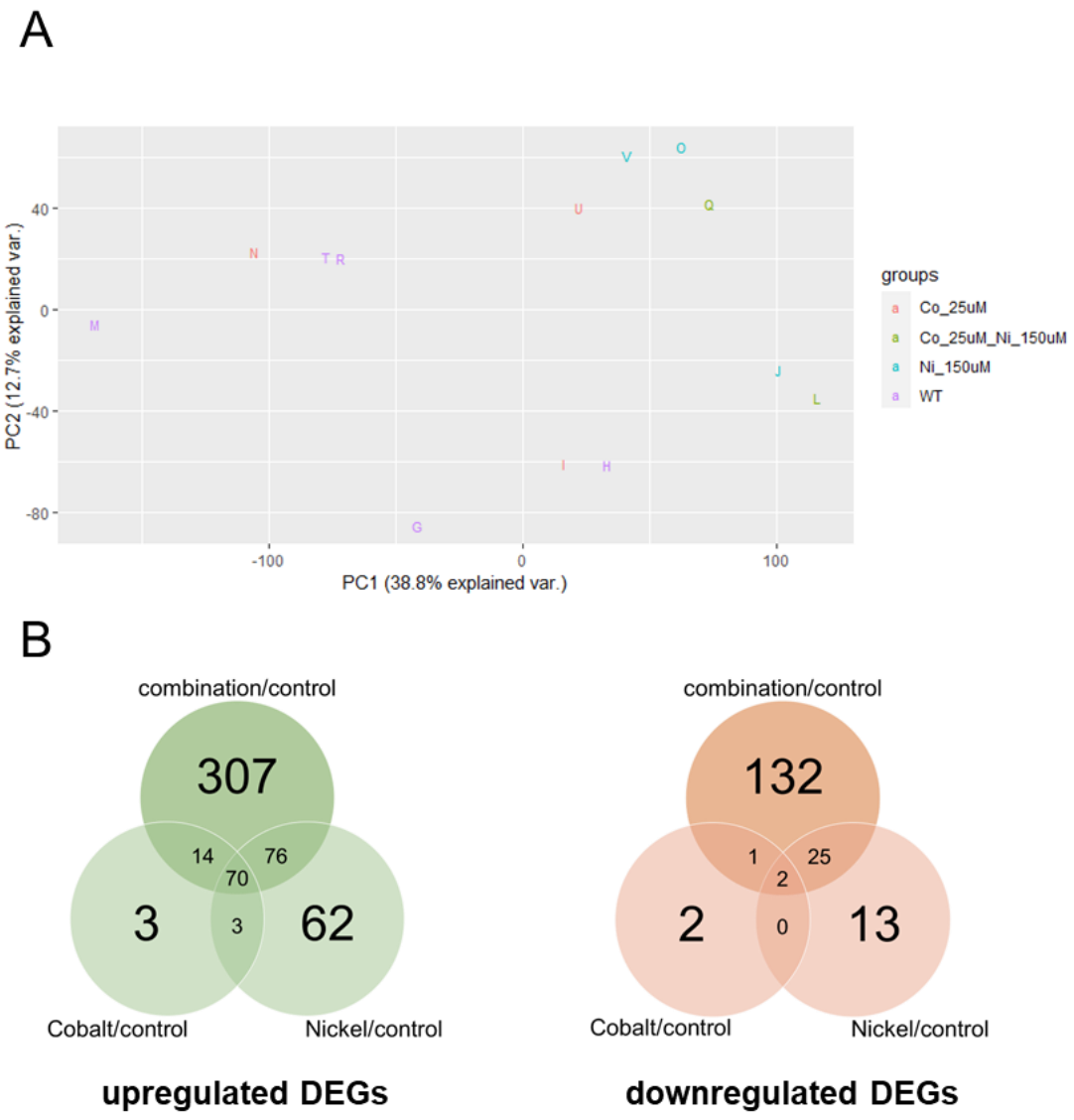

Figure 21: A) Principal component analysis (PCA plot) of PC1 and PC2, comparing the different Co(II) and Ni(II) treatments and the untreated control in HepG2 cells. Individual samples of each treatment group are highlighted by different letters. WT = untreated control. B) Venn-diagrams showing the overlap of DEGs comparing 25 µM Co(II), 150 µM Ni(II) and the combination of both treatments in HepG2 cells.

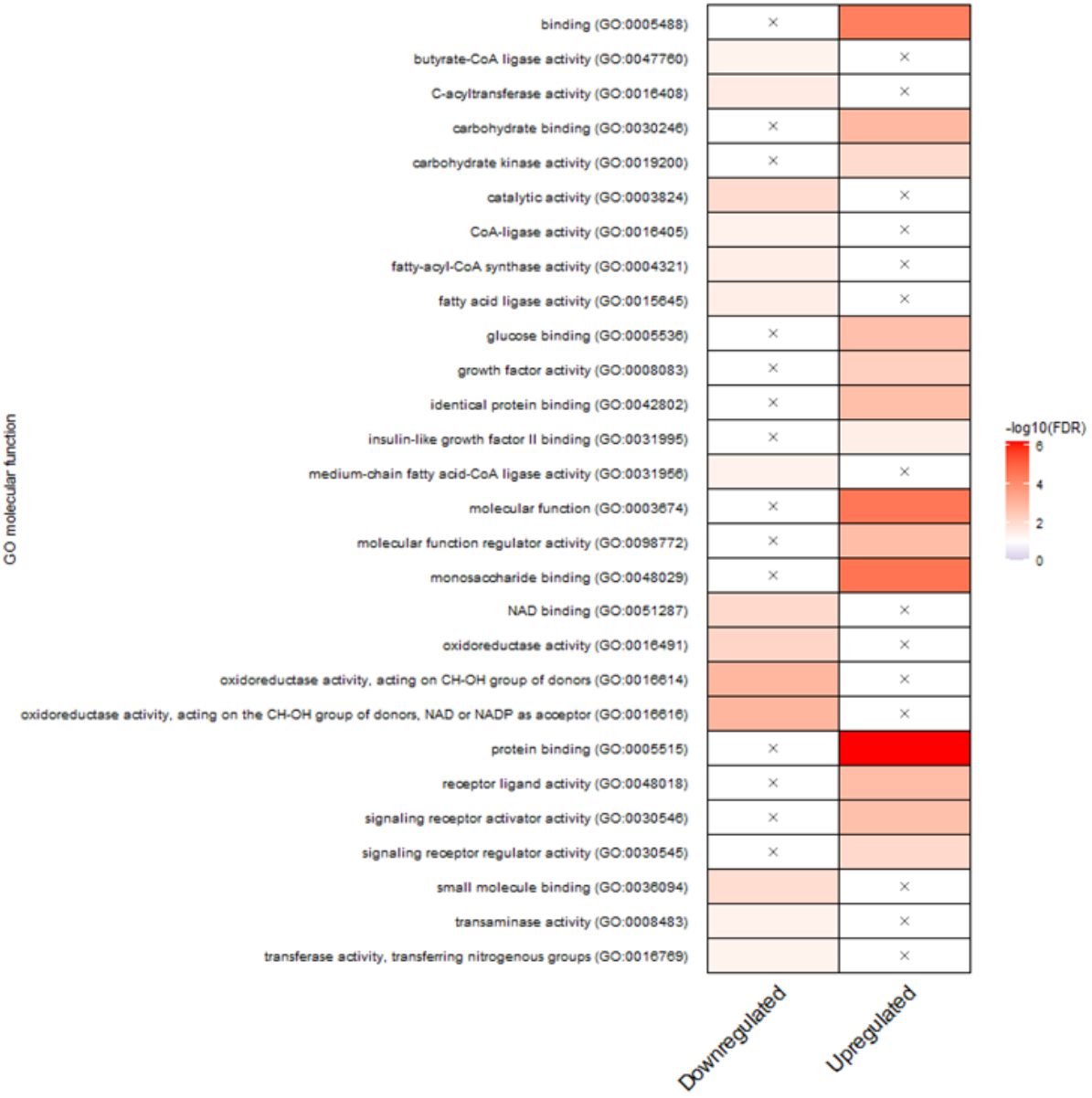

Figure 22: Summary of over-represented GO terms related to molecular function, comparing combined treatment (25 µM Co + 150 µM Ni) with untreated control in HepG2 cells. The x means no significant representation. Colors display intensity of enrichment (-log10 (FDR-corrected p-values)) with p value cutoff of 0.01. Visualization by an R-script from [242].

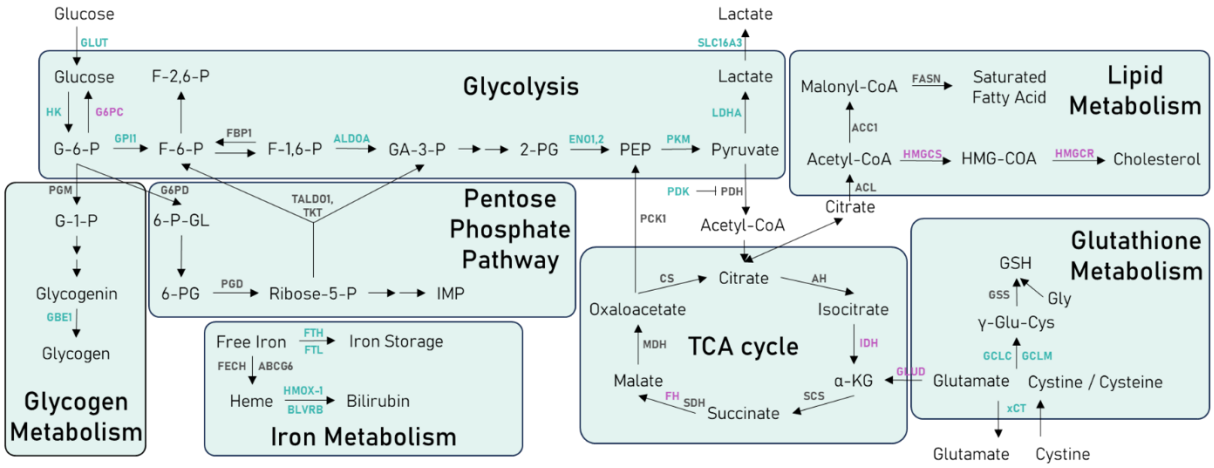

Figure 23: Affected pathways (transcriptome) by Co(II) and Ni(II) in HepG2 cells upon 24 h combined exposure (25 µM Co + 150 µM Ni). Genes in green font represent upregulation, magenta font shows downregulation, and grey font indicates no alterations compared to untreated control. More detailed data is shown in supplementary table 13. Abbreviations: GLUT glucose transporter; HK hexokinase; G6PC glucose-6-phosphatase catalytic subunit 1; GPI glucose-6-phosphatase isomerase; FBP fructose-bisphosphatase; ALDOA aldolase A; ENO enolase; PKM pyruvate kinase M; LDHA lactate dehydrogenase A; PGM phosphoglucomutase; GBE 1,4-alpha-glucan branching enzyme; G6PD glucose-6-phosphate dehydrogenase; PGD phosphogluconate dehydrogenase; TALDO transaldolase; TKT transketolase; FTH ferritin heavy chain; FTL ferritin light chain; FECH ferrochelatase; HMOX1 heme oxygenase 1; BLVRB biliverdin reductase B; PDK pyruvate dehydrogenase kinase; PDH pyruvate dehydrogenase; PCK phosphoenolpyruvate carboxykinase; CS citrate synthase; AH aconitate hydratase; IDH isocitrate dehydrogenase; SCS succinyl-CoA synthetase; SDH succinate dehydrogenase; FH fumarate hydratase; MDH malate dehydrogenase; ACL ATP citrate lyase; ACC acetyl-CoA carboxylase; FASN fatty acid synthase; HMGCS HMG-CoA-synthase; HMGCR HMG-CoA-reductase; GLUD glutamate dehydrogenase; xCT solute carrier family 7 member 11; GCL glutamate-cysteine ligase; GSS glutathione synthetase.

5.3.2. Nuclear translocation of Nrf2 induced by Co and Ni

Nuclear factor erythroid 2-related factor 2 (Nrf2) is an important transcription factor for regulating cellular defense mechanisms against environmental stressors, for detoxification of xenobiotics and for maintaining redox homeostasis [70]. The nuclear translocation and therefore activation of Nrf2 was assessed by quantifying the protein concentration in nuclear lysates after 2 h of treatment of HepG2 cells with Co and Ni individually or in combination (fig. 24A). Given the rapid activation and subsequent degradation of Nrf2, a shorter incubation time was selected compared to the other experiments investigating the consequences of Nrf2 activation [69]. Both metals, except of 75 µM Ni, led to elevated amounts of nuclear Nrf2 compared to the untreated control, with 150 µM Ni showing the strongest effect. Concurrent incubation of Co and Ni also resulted in increased nuclear Nrf2 translocation (fig. 24A). These effects could also be demonstrated by immunofluorescence staining against nuclear Nrf2 (fig. 24B).

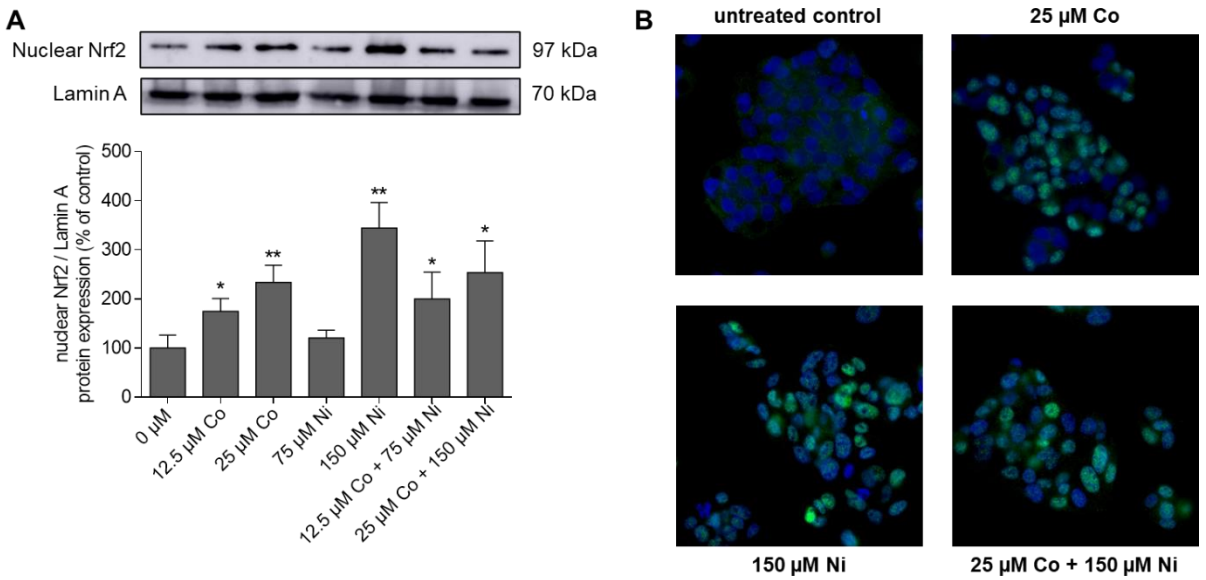

Figure 24: Nuclear Nrf2 translocation in HepG2 cells after 2 h treatment with Co(II) and Ni(II). A) Protein concentration was quantified via Western Blot and normalized to Lamin A. B) Nrf2 translocation visualized by immunofluorescence staining in 63x magnification. The pictures are processed by Leica Thunder Imager. Blue: Hoechst staining, Green: Nrf2 staining. Data is presented as mean + SD of n = 3 independent experiments. Statistical significance was tested by an unpaired t-test depicted as *p≤0.05, **p≤0.01: compared to untreated control.

5.3.3. Impact on Iron Metabolism

Based on the transcriptome data, target genes of Nrf2 connected to the iron metabolism are studied further. Transcriptomic analysis revealed an upregulation in the gene expression of *HMOX-1*, *FTL*, *FTH* and *BLVRB*, induced by the high Co and Ni combination (fig. 23). The higher combination of Co and Ni (25 µM Co + 150 µM Ni) resulted in elevated protein expression of HMOX-1 compared to control (fig. 25A). HMOX-1 plays a crucial role in metabolizing the prooxidant heme into iron and biliverdin [243]. Similarly, there was a significant effect on the expression of the iron storage protein ferritin which was more pronounced for FTL (fig. 25B), with a trend also observed for FTH (fig. 46). A shift in the Fe(II)/Fe(III) ratio towards the divalent species is an indicator for a redox imbalance caused by higher RONS formation within the cell [244]. After 24 h treatment with Co and/or Ni, there were no significant alterations in this ratio, however, a trend towards Fe(II) was observed (fig. 25C).

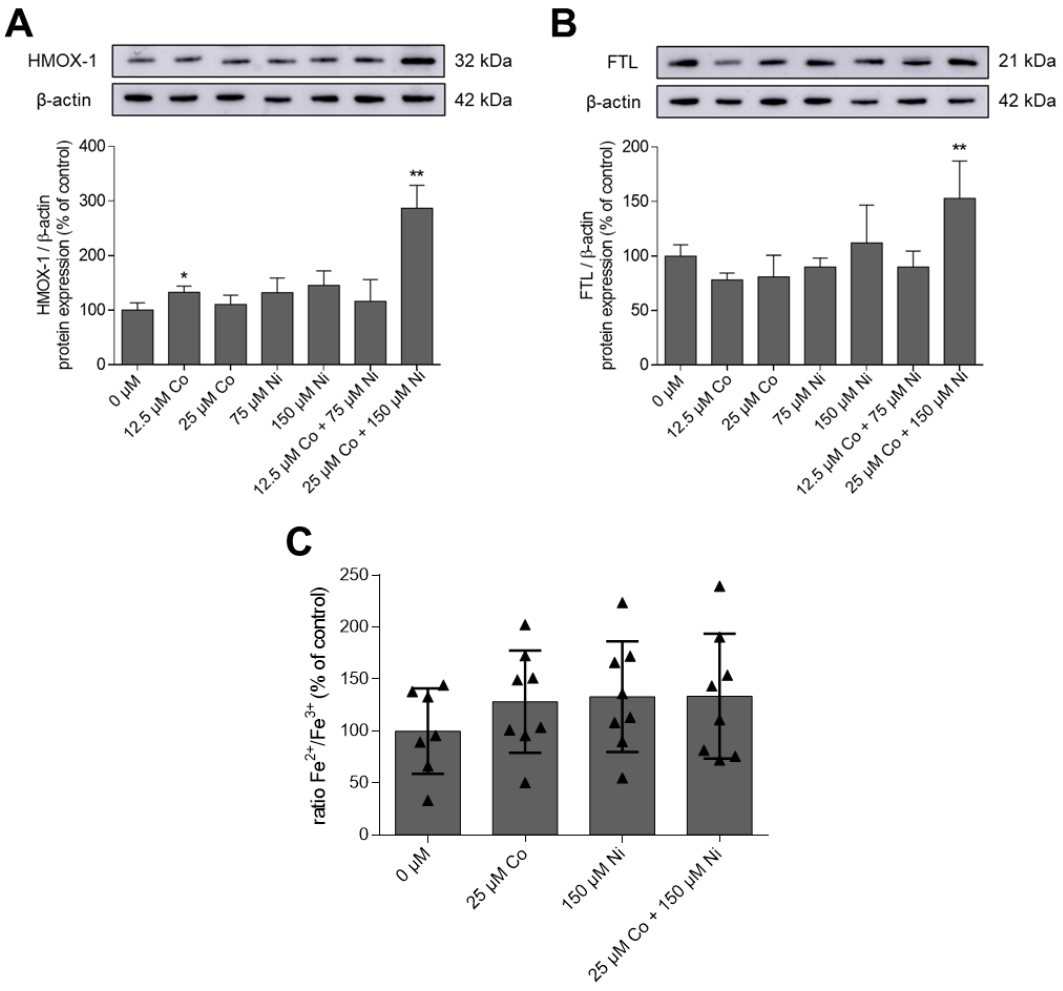

Figure 25: Impact on Fe metabolism in HepG2 cells after 24 h treatment with Co(II) and Ni(II). Protein expression of A) FTL and B) HMOX-1 were quantified via Western Blot and normalized to β-actin. C) Ratio of Fe^{2+} and Fe^{3+} normalized to protein content and untreated control. Data is presented as mean + SD of n ≥ 3 independent experiments. Statistical significance was tested by an unpaired t-test depicted as *p≤0.05, **p≤0.01: compared to untreated control.

5.3.4. Glycolysis, TCA cycle, and GSH metabolism

Nrf2 is also directing the transcription of genes encoding for enzymes involved in glycolysis, TCA cycle, and GSH metabolism, thereby influencing the synthesis of numerous metabolites [245]. LC-MS/MS analysis revealed that Co and Ni did not affect the glucose levels in HepG2 after 24 h treatment (fig. 26A). However, the pyruvate content increased significantly with the higher combination (fig. 26C), and lactate levels were enhanced across all applied Co and/or Ni concentrations (fig. 26B). TCA cycle metabolites α-ketoglutarate and succinate showed elevated

amounts only with the high combination (fig. 26D/E), while malate content increased significantly with 150 µM Ni or the combination of 12.5 µM Co + 75 µM Ni (fig. 26F). All applied concentrations except for 75 µM Ni led to decreased glutamate levels, while glutamine was enhanced by the high combination of Co and Ni (fig. 26G/H). Furthermore, the cellular cysteine amount was lower compared to control after treatment with Co or the combination of Co and Ni, whereas Ni individually did not show this effect (fig. 26I).

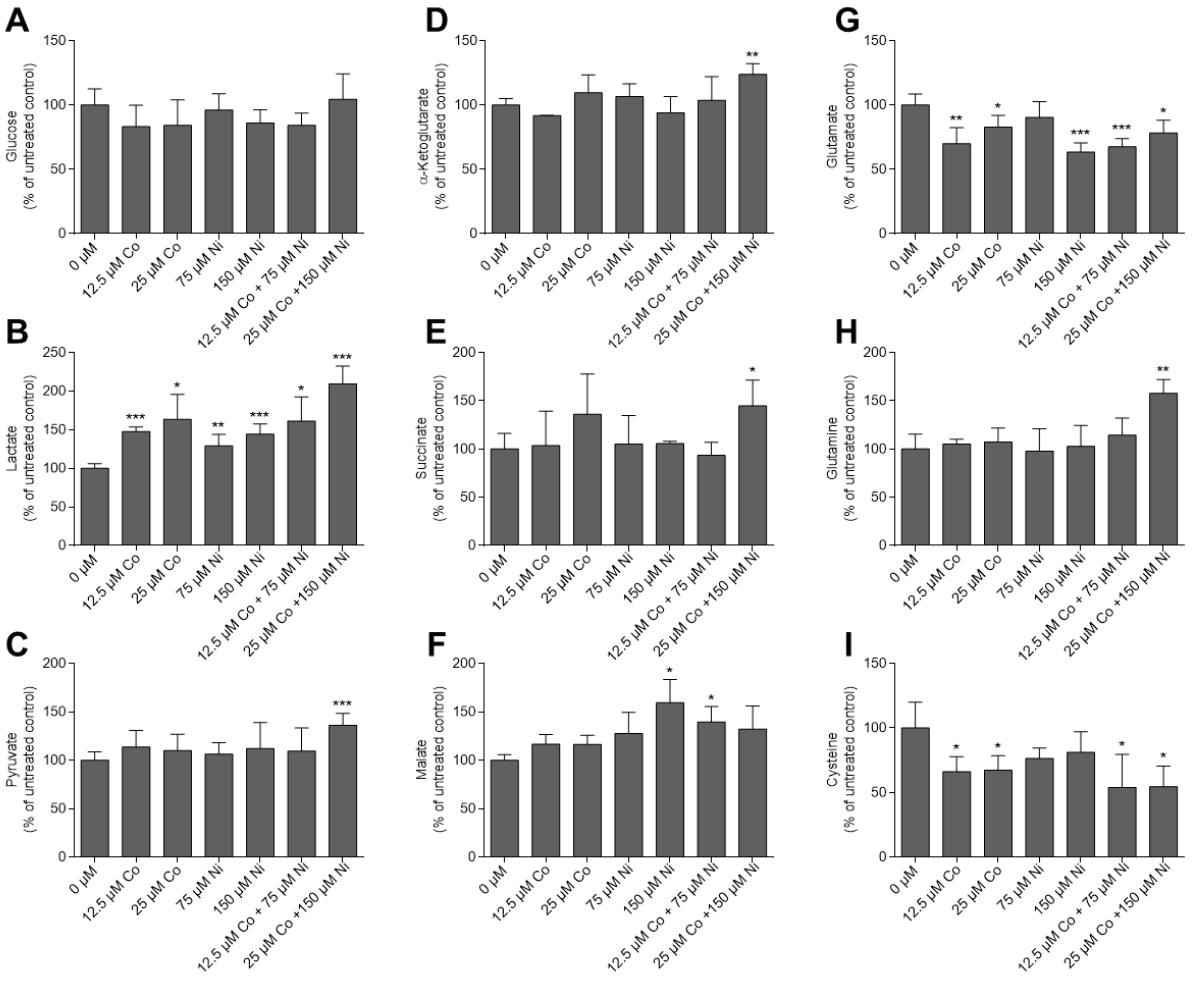

Figure 26: Levels of metabolites related to glycolysis, TCA cycle and GSH metabolism in HepG2 cells after 24 h treatment with Co(II) and Ni(II). Amount of A) glucose, B) lactate, C) pyruvate, D) α-ketoglutarate, E) succinate, F) malate, G) glutamate, H) glutamine and I) cysteine were quantified by LC-MS/MS and normalized to protein content and untreated control. Data is presented as mean + SD of n ≥ 3 independent experiments. Statistical significance was tested by an unpaired t-test depicted as *p≤0.05, **p≤0.01, ***p≤0.001: compared to untreated control.

5.3.5. Sphingolipids and diacylglycerols

Transcriptomic analysis also revealed an impact on sphingolipid metabolism and diacylglycerols (DAGs) induced by Co and Ni exposure. Specifically, the combination of both metals (25 µM Co + 150 µM Ni) led to an increased expression of *CERS1*, whose encoded protein is responsible for converting dihydrosphingosine (dhSph) to dihydroceramides (dhCer) and sphingosine (Sph) to ceramides (Cer) (fig. 27) [246]. CERS1, which belongs to a group of six isoforms, specifically forms dhCer or Cer species with a C18:0 fatty acid side chain [247]. In line with this, LC-MS/MS analysis revealed increased C18:0 dhCer levels (fig. 47A) and a trend for elevated C18:0 Cer (fig. 47B) compared to the control after treatment with Co, Ni or a combination of both. Interestingly, all other dhCer species measured were also highly elevated (fig. 47A), leading to significantly increased dhCer/Cer ratios after treatment with Ni and/or Co (fig. 28A). DhCer and Cer can be converted by sphingomyelin synthases (SGMS, fig. 27) to dihydrosphingomyelins (dhSM) and sphingomyelins (SM), respectively. Consequently, we also detected increased dhSM/SM ratios (fig. 28B, fig. 47C/D) after Co and/or Ni treatment. Furthermore, Co and Ni individually and combined resulted in a decrease in Sph (fig. 28C) as well as in lactosylceramides (LacCer) (fig. 28D). Additionally, Co and Ni caused elevated levels of various DAG species (fig. 28E). In particular, those representatives that have two saturated fatty acids in the molecule (e.g. 16:0_16:0; 16:0_18:0 and 18:0_18:0) accumulated. The effect was reduced in the case of monounsaturated DAGs (e.g. 16:0_18:1 and 18:0_18:1) and eliminated or even reversed in the case of polyunsaturated DAGs (e.g. 18:1_18:1).

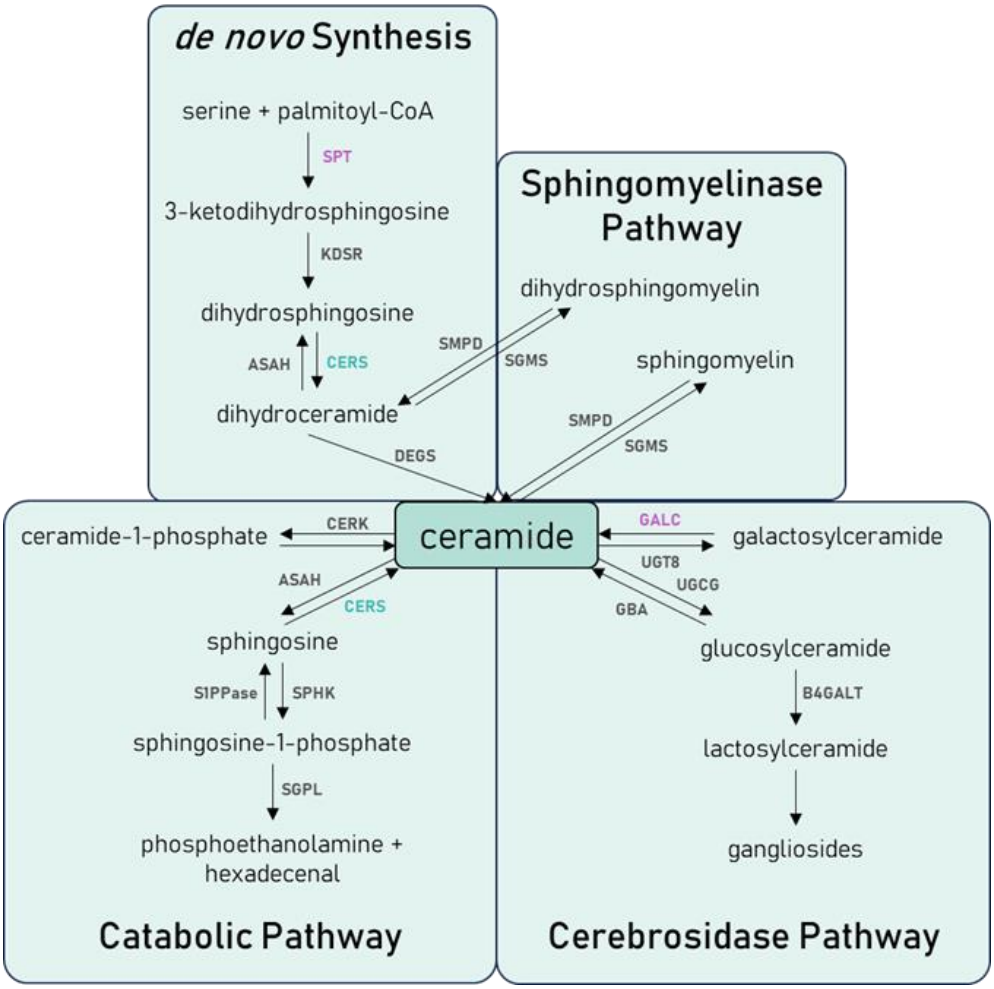

Figure 27: Effected pathways (transcriptome) related to sphingolipid metabolism by Co(II) and Ni(II) in HepG2 cells after 24 h combined exposure (25 µM Co + 150 µM Ni). Genes in green font represent upregulation, magenta font shows downregulation, and grey font indicates no alterations compared to untreated control. More detailed data is shown in supplementary table 14. Abbreviations: SPT serine palmitoyltransferase; KDSR 3-ketodihydrosphingosine reductase; CERS ceramide synthase; ASAH N-acylsphingosine amidohydrolase; DEGS sphingolipid delta 4-desaturase; SMPD sphingomyelin phosphodiesterase; SGMS sphingomyelin synthase; GALC galactosylceramidase; UGT8 UDP glycosyltransferase 8; UGCG UDP-glucose ceramide glucosyltransferase; GBA glucosylceramidase; B4GALT6 beta-1,4-galactosyltransferase 6; CERK ceramide kinase; S1PPase sphingosine-1-phosphatase; SPHK sphingosine kinase; SGPL sphingosine-1-phosphate lyase.

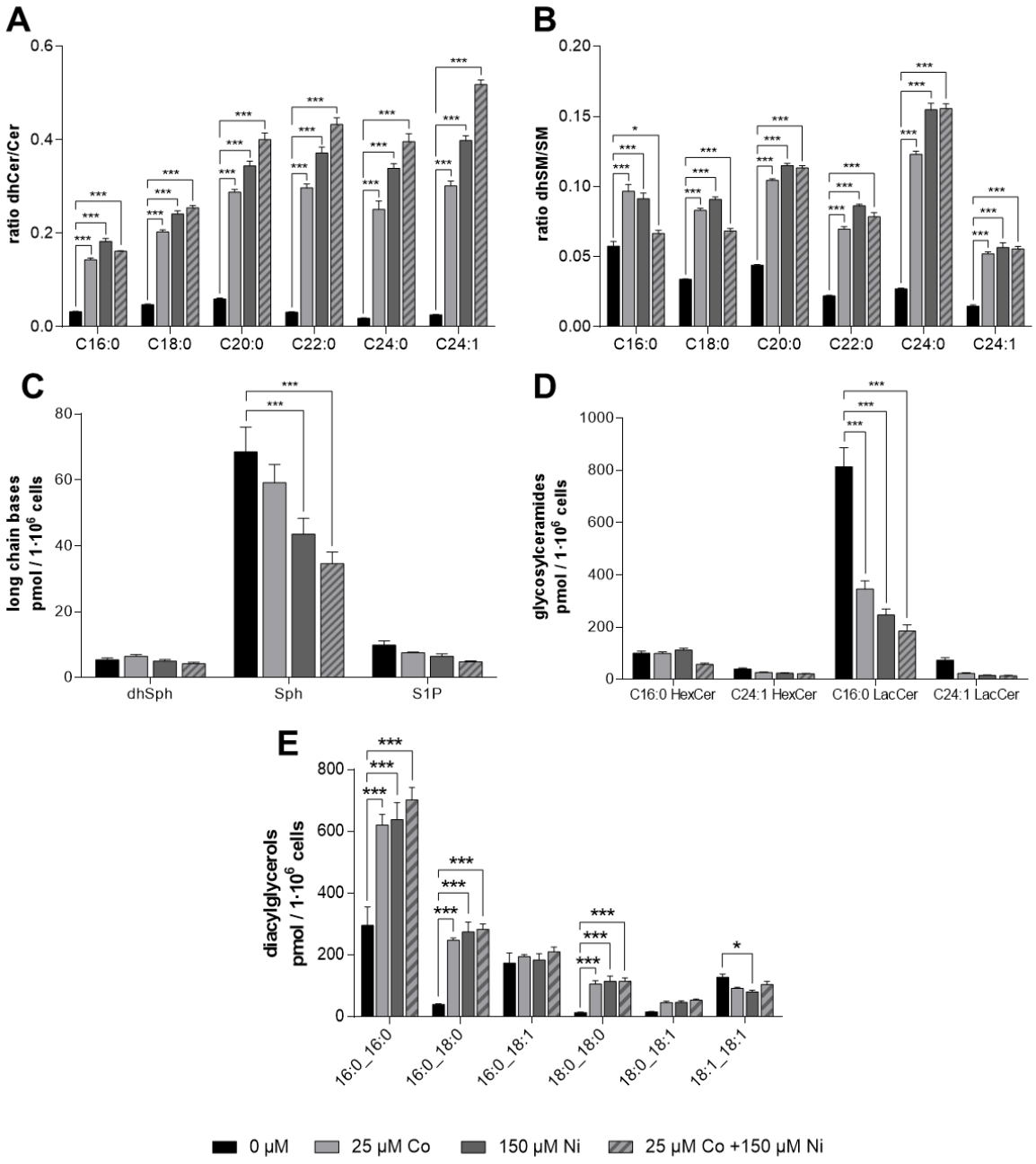

Figure 28: Quantification of A) dihydroceramides/ceramides ratio, B) dihydrosphingomyelins /sphingomyelins ratio, C) long chain bases, D) diacylglycerols, and E) glycosylceramides after individual or combined treatment with Co(II) and Ni(II) for 24 h in HepG2 cells. Sphingolipid and diacylglycerol levels were quantified using LC-MS/MS. Data is presented as mean + SD of n ≥ 3 independent experiments. Statistical significance was tested using Two-way ANOVA depicted as *p≤0.05, ***p≤0.001: compared to untreated control. Abbreviations: dhCer dihydroceramides; Cer ceramides; dhSM dihydrosphingomyelins; SM sphingomyelins; dhSph dihydrosphingosine; Sph sphingosine; S1P sphingosine-1-phosphate; HexCer hexosylceramides; LacCer lactosylceramides.

5.4. Discussion and Conclusions

This study focuses on elucidating the toxicity mechanisms of Co and Ni and exploring possible effects of their combined presence, providing insights into their environmental and public health threats. Since Co and Ni are distributed in tissues, in particular the liver and kidneys upon oral intake and hence are responsible for hepatotoxicity, human liver carcinoma cells (HepG2) are applied in this study. The untargeted transcriptomic approach allows identifying the most relevant cellular responses in case of individual or combined exposure to Co and Ni. The relevance of the pathways is validated and verified by further targeted analysis.

Both Co and Ni led to a variety of differentially expressed genes when compared to the untreated HepG2 cells, with a notable overlap in gene expression between the two metals individually. Sun *et al.* investigated the effects of single Co and Ni treatment in Japanese flounder, observing a greater number of DEGs induced by Co, contrary to the findings in HepG2 cells where Ni triggered a larger response [248]. Transcriptomic analysis following Co and Ni exposure in human cell lines are limited to lung cells and monocytes and therefore barely comparable [249,250]. In this study we demonstrated that combined treatment resulted in considerably higher number of DEGs, suggesting possible interactions between Co and Ni, leading to distinct gene regulation pathways compared to individual exposure. Interestingly, the identified target DEGs merge in cellular responses driven by the transcription factor Nrf2. Nrf2 plays a pivotal role in regulating cellular metabolism pathways, such as iron or glutathione homeostasis, glycolysis, TCA cycle, and lipid metabolism, thus underscoring its significance in cellular protection and pathogenesis [251].

Under physiological conditions, Nrf2 is degraded in the cytoplasm by Kelch like-ECH-associated protein 1 (KEAP1) and Cullin 3 [251]. Upon oxidative stress or exposure to electrophiles, this regulatory system is disrupted, leading to the

translocation of Nrf2 into the nucleus. This translocation of Nrf2 could be verified in this study upon Co and Ni exposure (alone and combined). There are only few studies reporting the Nrf2 activation in various cell lines following exposure to Co [252,253] or Ni [223,254]. However, they are primarily focusing on individual treatment, but lacking combined treatment or associated impacts of Nrf2 activation on cellular metabolism. The main mechanism triggering Nrf2 activation and subsequent translocation is oxidative stress related, by modifying the cysteine residues of KEAP1 and disrupting the KEAP1-NRF2 complex [245]. In a recent investigation involving HepG2 cells, it was observed that Co treatment led to an increase in RONS production, along with enhanced levels of oxidized glutathione (GSSG). Conversely, Ni exposure did not induce any significant alterations in these parameters [227]. Despite this, Ni led to a Nrf2 translocation, suggesting an oxidative stress independent activation of Nrf2 by Ni. It has been discussed that sequestosome 1 (SQSTM1), also known as p62, can bind to KEAP1 leading to the stabilization of Nrf2 [255]. In the present study, transcriptomic analysis revealed an upregulation of *sqstm1*, especially in response to the individual treatment of Ni or the combined exposure of Co and Ni (tab. 13). Additionally, the exposure of Ni to human lung epithelial cells resulted in a significant upregulation in SQSTM1 protein expression [256]. Given the differences in their stress induction, it is plausible that Co and Ni engage distinct mechanisms in activating Nrf2 signaling pathways.

The Nrf2-regulated pathways governing iron and GSH metabolism were affected by Co and Ni. Key proteins involved in these pathways, including HMOX-1, GCLC, and GCLM were identified as downstream targets in a human epithelial cell line using knockdown cells of *Nrf2* and *Keap1*. Furthermore, it was reported that Nrf2 expression reached its highest amount 6 h following Co treatment, while its targets reached their maximum expression levels after 24 h exposure [70,252]. From targeted studies investigating the toxicity of both metals, especially Co is associated to hypoxia-inducible factor-1 (HIF-1) and

evidence suggests an association between the HIF-1 and Nrf2 signaling pathways, with Nrf2 downstream targets potentially acting as regulators of HIF-1 [74,257]. Knockdown of *Nrf2* revealed reduced expression of HIF-1α in both human glioma cells and human colon cancer cells, even under hypoxic conditions or following Co treatment as a hypoxia-mimicking agent [258,259]. Even if Co is used as a hypoxia-mimicking agent, its toxicity mechanism seems to differ from that of physical hypoxia concerning Nrf2 signaling, particularly at transcriptional and post-transcriptional levels. Notably, Co treatment led to increased FTH mRNA expression in human erythroleukemia cells, whereas incubation under hypoxia showed no alterations in iron metabolism [260]. In our study, the combined exposure to Co and Ni resulted in elevated levels of FTL and FTH gene- and protein expression, leading to increased iron storage capacity, consequently preventing the potential for production of Fe^{3+} during Fenton reaction and radical formation. Despite Ni inducing Nrf2 activation, HMOX-1 protein expression was only increased in combined treatment with Co rather than when Ni was exposed individually. Lewis *et al.* reported similar findings in human monocytic cells treated with Ni, hypothesizing that this could result from either a sub-threshold level of activation or a form of Nrf2 incapable to promote HMOX-1 transcription [223]. Additionally, they also noted the absence of RONS induction which is consistent with the previous investigation in HepG2 cells [227]. In a human bronchial epithelial cell line, Ni caused an upregulation in HMOX-1 mRNA levels, along with elevated RONS levels. However, it is important to consider that the cells were exposed to a notably higher Ni concentration, which complicates direct comparison [261]. The two amino acids cysteine and glutamate, which are components of GSH, were decreased by Co and Ni, measured via LC-MS/MS. Transcriptomic analysis revealed an increased expression of *GCLC* and *GCLM*, induced by both Co and Ni, catalyzing the initial step of GSH synthesis. Following treatment with Co alone or in combination with Ni, HepG2 cells showed elevated GSSG levels. Notably, the GSH amount remained unchanged with both metals, indicating more GSH synthesis and direct oxidation [227]. Nrf2 also regulates

transport and metabolism of glutamine, essential for GSH synthesis as it is converted to glutamate via the catalysis of glutaminase [70]. Upon combined treatment with Co and Ni, HepG2 cells exhibited elevated glutamine levels, indicating heightened transport into the cell likely driven by increased demand for glutamate. Across various cancer cell lines, it was observed that Nrf2 activation heightened the dependency on exogenous glutamine, primarily directed towards GSH synthesis [262,263]. Notably, Nrf2 plays a role in the expression of the glutamine transporter SLC1A5, as evidenced in a study using *Keap1*-mutant cells [264]. Next to this, glutamate is also indirectly involved in GSH synthesis by serving as an exchange molecule for cystine transporter SLC7A11 (also known as xCT), which is positively regulated by Nrf2 [265]. Enhanced expression of SLC7A11 was observed after combined treatment with Co and Ni in HepG2 cells. Enhanced glutamate secretion limited its availability for the TCA cycle or other pathways [262]. The effects of Co and Ni on TCA cycle metabolites α-ketoglutarate, succinate, or malate, showed only a slight increase, indicating that this pathway may not be the main route of toxicity for Co and Ni in cellular metabolism. Nrf2 enhances glycolysis by increasing the glucose import and inducing the expression of key enzymes along the glycolytic pathway [251]. Particularly under hypoxic conditions, cells prioritize converting most of the glucose to lactate rather than utilizing it in oxidative phosphorylation [266]. Treatment with Co and Ni resulted in increased lactate levels compared to untreated HepG2 cells, indicating heightened conversion of pyruvate to lactate, thus ensuring cellular energy supply. Lactate production is catalyzed by lactate dehydrogenase A (LDHA), which is notably enhanced in tumor growth and increased cell proliferation. Knockdown of *Nrf2* in breast cancer cells led to a decrease in LDHA protein expression, correlating with reduced expression of HIF-1α [267].

Cellular metabolism of bioactive sphingolipids is highly regulated by a variety of enzymes, contributing to essential cellular functions such as cell growth, cell cycle regulation, cell death, inflammation, response to stress stimuli, and autophagy [268]. A previous metabolomic study in liver cells pointed out an impact especially of Co on the sphingolipid metabolism and synthesis [269]. The accumulation of dhCer, an intermediate in the *de novo* synthesis of Cer, is discussed to be stimulated by hypoxia or oxidative stress [270]. In mouse embryonic fibroblasts, knockdown of dihydroceramide desaturase 1 (DEGS1) resulted in elevated levels of dhCer and dhSM, while Cer, SM, Sph, and LacCer were decreased [271]. Similar results were observed in this study in HepG2 cells following treatment with Co and Ni in HepG2 cells, with more intense effects after combined incubation. Exposing different breast cancer cell lines to hypoxia resulted in DEGS1 inhibition with concurrent increase of dhCer [272], suggesting that Co and Ni may inhibit DEGS1 through their hypoxia-mimicking properties. The accumulation of dhCers is associated with altered bioenergetics, notably evidenced by decreased ATP/AMP ratios [271]. This alteration is believed to activate AMPK, which in turn stimulates autophagy through the activation of ULK1/2 [273]. Hernández-Tiedra *et al.* revealed the link between an increased dhCer/Cer ratio and autophagy-mediated apoptosis in human glioma cells [274]. An association between AMPK and Nrf2 signaling pathways is, among others, given by the earlier mentioned p62, which interacts with KEAP1 to activate Nrf2. Elevated levels of p62, in turn, facilitate AMPK-mediated activation of ULK [275]. Both ULK1/2 and p62 are overexpressed in HepG2 cells treated with Ni individually or in combination with Co (tab. 13). In contrast to their less abundant saturated analogs (dhSM), SM are major components of biological membranes. Both sphingolipid subclasses have different effects on membrane fluidity; SM favors it, while dhSM increases membrane rigidity [276]. An increase in the cellular dhSM/SM ratio, as observed in this study after Co and/or Ni treatment, could facilitate the formation of assemblies in SM-rich lipid domains, which could play an important role in membrane-related biological processes [277].

Various pathways facilitate the intracellular formation of DAGs, including their production during triacylglycerol and phospholipid biosynthesis, or as a byproduct in the SM synthesis using Cer and phosphatidylcholine catalyzed by sphingomyelin synthase [278,279]. Exposure of Co and Ni individually and combined to HepG2 cells resulted in an increase of intracellular DAG levels. Lakatos *et al.* demonstrated in mesenchymal stromal cells that DAG content was elevated under hypoxic conditions and in the presence of Co as a hypoxia-mimicking agent. Inhibiting phosphatidylcholine-specific phospholipase C and sphingomyelin synthase reduced DAG levels under hypoxia, suggesting that increased DAGs result from enhanced enzyme activity [280]. Accumulation of DAGs is associated with the activation of protein kinase C (PKC) and their translocation to membranes [279]. This activation leads to the phosphorylation of various enzymes, including Nrf2, which is subsequently stabilized for translocation into the nucleus [281].

In conclusion, this study delves into the toxicity mechanisms of Cobalt (Co) and Nickel (Ni), shedding light on their individual and combined effects on cellular metabolism. Transcriptomic analysis provided a comprehensive understanding of gene regulation pathways impacted by both metals in HepG2 cells, revealing both shared and distinct responses. Notably, Co and Ni showed a synergistic effect, resulting in a significantly higher number of differentially expressed genes compared to individual exposure. Especially the activation of the Nrf2 signaling pathway seems to play an important role in cellular response to Co and Ni exposure. Additionally, alterations in sphingolipid metabolism and diacylglycerol accumulation underscore the complex cellular responses induced by these metals. Combining transcriptomic analysis and analytical methods provide an important and unconventional approach to gain insights into the intricate interplay between gene regulation and cellular metabolism underlying metal toxicity.

5.5. Acknowledgement

This work was supported by the DFG Research Unit TraceAge (FOR 2558, BO4103/4-2), the initiative “Metal based compounds (MeBaCo)” supported by the University of Wuppertal and the Faculty of Mathematics and Natural Sciences and by the DFG Research Infrastructure NGS_CC (project 407495230) as part of the Next Generation Sequencing Competence Network (project 423957469). NGS analyses were carried out at the Competence Centre for Genomic Analysis (Kiel). The authors thank Daniel Herrmann for excellent technical assistance with LC-MS/MS analyses of sphingolipids and DAGs.

5.6. Author contribution statement

Alicia Thiel: Conceptualization, Methodology, Visualization, Formal analysis, Investigation, Writing – Original Draft, Writing – Review & Editing; **Franziska Drews:** Formal analysis, Visualization, Writing – review & editing; **Marcello Pirritano:** Formal analysis, Visualization, Writing – review & editing; **Fabian Schumacher:** Formal analysis, Investigation, Writing – review & editing; **Vivien Michaelis:** Conceptualization, Methodology, Writing – review & editing; **Maria Schwarz:** Methodology, Writing – review & editing; **Sören Franzenburg:** Investigation; **Tanja Schwerdtle:** Writing – review & editing**; Bernhard Michalke:** Investigation, Methodology; **Anna P. Kipp:** Writing – review & editing; **Burkhard Kleuser:** Writing – review & editing; **Martin Simon:** Writing – review & editing; **Julia Bornhorst:** Writing – review & editing, Project administration, Methodology, Investigation, Funding acquisition, Conceptualization.

Abstract:

The usage of Cobalt (Co) and Nickel (Ni) in numerous commercial, industrial, and military applications causes a widespread exposure nowadays, and concerns are rising about adverse impacts on human health. Emphasis is on the respiratory system with both metals classified as (possibly) carcinogenic upon inhalation by the International Agency for Research on Cancer (IARC), but limited data are available upon oral exposure. Therefore, this study aims to evaluate the *in vitro* genotoxicity of Co and Ni and their combination in HepG2 cells, since exposure of those environmental pollutants occurs realistically in concert and. Here, Co exposure led to the induction of single-strand breaks and oxidative DNA damage detected by Comet assay as FPG-sensitive sites, while Ni increased the expression of γ-H2AX, an indicator for double-strand breaks. Notably, combined exposure to Co and Ni resulted in enhanced DNA damage especially on the chromosomal level with an increased formation of micronuclei as well as polynucleated cells, indicating a synergistic effect. Furthermore, both metals induced the DNA damage response pathway PARylation. As this process involves the consumption of large amounts of cellular NAD^+ after DNA damage, the energy state was assessed upon exposure with Co and Ni. Current data indicate that especially Co altered the cellular energy state. This study reveals distinct mechanisms of DNA damage exhibited by Co and Ni, which were enhanced after combined treatment. This highlights the need for further research to estimate the genotoxic potential to target cells upon oral intake with their increasing environmental entry.

Chapter 6

Genotoxicity Assessment of Co(II) and Ni(II) in HepG2 Cells: Insights into Combined Metal Exposure

Based on:

Alicia Thiel, Sarah Heider, Kira Bieck, Tanja Schwerdtle, Franziska Ebert, Julia Bornhorst

submitted to Toxicological Sciences

Keywords:

Cobalt; Nickel; metal interactions; DNA damage; PARylation; metal genotoxicity

Chapter 6 – Genotoxicity Assessment of Co(II) and Ni(II) in HepG2 Cells: Insights into Combined Metal Exposure

6.1. Introduction

Cobalt (Co) and Nickel (Ni) are trace elements with significant industrial applications, ranging from the production of lithium-ion batteries to their use in alloys, catalysts, and pigments [11,12]. Despite their utility, both metals pose environmental and human health threats, especially in occupational settings. Due to the increasing industrial use of Co and Ni, their environmental presence has heightened, subsequently increasing human exposure through food and drinking water. Upon inhalation, both metals have been classified by the IARC as carcinogenic (Co: group 2A, Ni: group 1) [43,282]. While their carcinogenic potential through inhalation is well-documented, their genotoxic potential upon oral exposure remains less explored, although bioavailability has been shown [227]. Given that Co and Ni may enter the human body via ingestion, understanding their genotoxic potential is crucial.

Co serves as a cofactor for vitamin B12 and is important for the formation of amino acids and proteins, particularly in nerve cells, turning it into an essential trace element in the human body [23]. Conversely, the biological role of Ni in humans is not clearly established, even if it is often discussed [4]. Exposure to both metals is associated with the development of various adverse health effects, including neurological, cardiovascular, and thyroid dysfunctions [2,179]. Co exerts its health effects through several cellular processes, primarily due to its ability to generate reactive oxygen species (ROS) via Fenton-like reactions, leading to oxidative stress and an imbalance in cellular glutathione metabolism [227]. This in turn may lead to damage to DNA, proteins, and lipids [45]. There is strong evidence that Co(II) ions caused DNA damage after *in vitro* exposure in human cells. DNA damage, like strand breaks, was reported after cobalt chloride treatment in several human cell lines including diploid

fibroblasts, mononuclear leukocytes, HepG2 cells, H460 lung epithelial cells, and T-cells. Further evidence that Co compounds cause chromosomal damage comes primarily from studies using human lymphocytes or lung fibroblast cells (summarized in [283]). Additionally, genotoxic effects of Co may arise from an inhibition of DNA repair mechanisms [8]. Excessive uptake of Ni is linked to mitochondrial dysfunction by altering the membrane potential, decreasing ATP and mitochondrial DNA concentrations [57]. The published genotoxicity data confirm that Ni(II) ions induce DNA damage *in vitro* as DNA strand breaks, particularly single-strand breaks. However, the genotoxicity of Ni is likely due to indirect effects including inhibition of DNA repair and ROS production. In addition, chromatin changes may occur following dysregulation of signaling pathways and alteration of the epigenetic landscape [6].

Most research to date has focused on the individual toxicity of Co and Ni, primarily using human lung cell lines and human lymphocytes [284–286]. However, combined exposure represents a more realistic scenario, as both metals are frequently occurring together in the environment and in industrial products. Furthermore, the oral route of exposure is relevant for the general population with the liver as target organ. Preliminary studies have shown that simultaneous exposure to Co and Ni in liver carcinoma cells (HepG2) results in altered cellular metal amount combined with enhanced effects regarding oxidative stress markers and cell death mechanisms compared to single metal incubation [227]. These findings suggest interactions between these metals which need to be further investigated. Therefore, this study aims to evaluate the genotoxic potential of Co and Ni (single and combined) using HepG2 cells, by examining the nuclear metal uptake, the DNA damage pattern and damage response. Understanding these interactions will provide crucial insights into potential health risks associated with environmental and occupational exposure to these metals.

6.2. Materials and Methods

6.2.1. Cell culture maintenance and treatment scenario

Human hepatocarcinoma cells (HepG2) were grown in Eagle's Minimum Essential Medium (MEM; Sigma Aldrich) containing 10 % fetal bovine serum (FBS; Sigma Aldrich), 2 % (v/v) penicillin/streptomycin (Sigma Aldrich) and 1 % (v/v) non-essential amino acids (NEA; Sigma Aldrich) as described earlier [227]. Sub-culturing was carried out every second day and growth conditions were maintained at 37 °C, 100 % humidity and 5 % CO_2. Cells were treated with $CoCl_2$ (Thermo Fischer Scientific; 99.9 %) and $NiCl_2$ (Sigma Aldrich; 99.9 %), dissolved in water, individually or in combination.

6.2.2. Isolation of cell nuclei and cytosolic fraction

To extract cell nuclei from cytosolic fraction, HepG2 cells were detached from culture plates using lysis buffer I, which consists of 10 mM HEPES, 1.5 mM MgCl2, 10 mM KCl, 0.5 mM DTT, 0.5 mM PMSF, and 0.1% NP-40 alternative, following a previously described protocol [235]. Samples were shaken for 3 min at 1300 rpm and another 4 min after being vortexed. Cytosolic and nuclear fraction were separated by centrifugation (6800 x g, 1 min, 4 °C) and the cytosolic fraction (supernatant) was collected in a new tube. The remaining pellet was resuspended in lysis buffer II (40 mM HEPES, 400 mM KCl, 10% Glycerol, 1 mM DTT, 0.1 mM PMSF) with additional 294 mM NaCl, sonicated for 12 s (cycle: 0.5, amplitude: 80%, Hielscher UP100H) and centrifuged again (20000 x g, 30 min, 4 °C). The resulting supernatant contains the nuclear fraction. An aliquot from both fractions was collected for protein quantification via standard BCA assay (Sigma-Aldrich).

6.2.3. Quantification of metal amount

Quantification of metal amount in cytosolic and nuclear fraction was assessed using inductively coupled plasma-optical emission spectrometry (ICP-OES; Avio 220 Max, PerkinElmer). Samples were prepared and measured as previously described [227].

6.2.4. Measurement of single-strand breaks via alkaline unwinding

To assess DNA damage in terms of single-strand breaks, the alkaline unwinding assay was utilized as described before [287]. HepG2 cells were exposed to Co and Ni, followed by treatment with 1.5 mL of alkaline unwinding buffer (0.9 M NaCl, 0.01 M Na_2HPO_4, 0.03 M NaOH) for 30 min. This process was stopped by adding 0.1 M HCl to neutralize the solution to pH 6.8. Samples were then sonicated for 15 s (cycle: 1, amplitude: 100%, Hielscher UP100H), and SDS was added to a final concentration of 0.075 %. Single- and double-stranded DNA were separated at 60 °C using a hydroxyapatite column. Single-stranded DNA eluted with 0.15 M potassium phosphate buffer, while double-stranded DNA was eluted using 0.35 M potassium phosphate buffer. The amount of DNA in each fraction was quantified by Hoechst 33258 staining (7.5×10^{-7} M) and fluorescence measurement using a Tecan microplate reader (Tecan Infinite Pro M200; Ex.: 355 nm, Em.: 460 nm).

6.2.5. Measurement of double-strand breaks (γ-H2AX)

γ-H2AX were measured by Western Blot analysis. The principle is described in [236] with slight modifications. After 24 h Co and Ni exposure, cells were pelletized and lysed in ice cold RIPA buffer in combination with sonification using an ultrasonic probe (6 s, amplitude: 100 %, cycle: 0.5). Protein amounts from 10 µg were denaturized with 5x Laemmli buffer (12.5 % β-mercaptoethanol (v/v), 10 % SDS (w/v), 50 % Glycerol (v/v), 0.2 M Tris (pH 6.8), 0.625 % bromophenol blue) were applied for SDS-PAGE. Protein transfer on a PVDF blotting membrane (0.45 PVDF Amersham™ Hybond™, GE Healthcare life science) via

tank blotting (Bio-Rad Laboratories Inc.) was verified using 0.2 % Ponceau staining. After blocking membranes in 3 % (w/v) BSA in 1x Tris buffered saline containing 0.1 % (v/v) Tween® 20 (T-TBS) for 1 h at RT, primary antibodies diluted in blocking solution were incubated at 4 °C over night. Recombinant anti-β-actin (1:25000, anti-ß-Actin-Peroxidase antibody, mouse monoclonal, A3854, Sigma Aldrich), anti-phospho-Histone H2AX (Ser139) antibody, clone JBW301 (1:2000, Sigma Aldrich) were used as primary antibodies. Horseradish peroxidase (HRP)-conjugated goat anti-mouse antibody (1:1000, Bio-Rad Laboratories Inc.) was incubated as secondary antibodies for 1 h at RT. Chemiluminescence detected with Clarity™ Western ECL Substrate (Bio Rad Laboratories Inc.). Protein bands were quantified using Bio-Rad Image Lab software and normalized to β-actin as loading control.

6.2.6. Alkaline comet assay

Alkaline Comet Assay was performed as described previously [158]. In particular, cells were seeded in a 12 well plate (3.66 cm^2 per well). After 24 h incubation, cells were trypsinised and counted with an automatic cell counter (Casy TTC). 20 mL of a cell solution containing 2 x 10^6 cells per mL were mixed with 180 mL of 0.5 % (w/v) low melting point agarose and 45 mL of the mixture were subjected on a slide pre-coated with 1.5 % of normal melting point agarose. Cell suspension was covered with a cover glass and was kept at 4 °C. After removal of the cover glass, slides were kept in a lysis solution (0.1 % Triton X-100), dimethyl sulfoxide and 89 % of the lysis buffer (10 mM Tris, 2.5 M NaCl and 100 mM Na_2EDTA; pH 10) for 1 h at 4 °C. In case for Fpg sensitive sites, slides were washed 3 times in cold Fpg buffer (40 mM Hepes, 100 mM KCl, 0.5 mM EDTA, 0.2 mg/mL BSA, pH 8) and were incubated with the Fpg enzyme (LOT 110240L, New England Biolabs) diluted 1:10,000 for 30 min at 37 °C. Afterwards, slides were placed into the electrophoresis chamber (electrophoresis buffer: 300 mM NaOH and 1 mM Na_2EDTA; pH 13) for DNA unwinding at 4 °C. After exactly 20 min, electrophoresis was started for 20 min at 25 V and 300 mA at 4 °C. Slides were

neutralized with 0.4 M Tris buffer (pH 7.5) for 5 min and then fixed for 5 min in ice cold methanol. Slides were stained with 20 µL of Gel red/Dabco solution and blinded before analyzing with the fluorescence microscope (Leica DM 2000 LED, Wetzlar, Germany). Two hundred randomly selected cells (100 per replicate slide) for each incubation were observed by semi-automated image analysis software (Comet IV^{TM}, Perceptive Instruments, UK). Percentage of DNA in tail was used to quantify DNA damage.

6.2.7. Micronucleus analysis

As biological marker of chemical-induced genotoxicity on chromosomal level the micronucleus assay was shown to be suitable and is recently fixed as OECD guideline as SOP [288]. To investigate the induction of micronuclei and multinucleated cells, in this study HepG2 cells were seeded in 12 well plates (3.66 cm^2 per well) on Alcian blue coated glass coverslips. Cytochalasin B was not used, due to its toxicity on the cells and due to possible interferences with incubated test compound. After 24 h, cells were incubated with the respective $CoCl_2$ alone or in combination with $NiCl_2$ for 24 h. Then cells were directly fixed on those coverslips with an ice-cold fixation solution (90 % methanol/10 % PBS, −20°C) for 10 min and air-dried at room temperature. Staining was proceeded with acridine orange (125 mg/L in PBS) for 90 s, and finally analyzed by fluorescence microscopy (Leica DM5500 B). Slides were blinded and, at least 1000 cells were counted and categorized in mononucleated, binucleated, and multinucleated cells as well as cells with and without micronuclei.

6.2.8. Quantification of poly(ADP-ribosyl)ation (PAR) levels via LC-MS/MS

Briefly, HepG2 cell pellets were dissolved in 225 µL 0.5 M KOH, incubated at 37 °C for 50 min using a thermoshaker and centrifuged for 10 min at 13300 x g. Samples were neutralized with 50 µL 4.8 M MOPS and an aliquot was collected for DNA measurement via Hoechst assay. Further sample preparation was carried out as described previously [120]. Quantification of PAR levels were

conducted on an Agilent 1290 Infinity II LC System coupled to a Sciex QTrap 6500+ triple-quadrupole mass spectrometer with an electrospray ion source operating in positive mode and method parameters as described before [120].

6.2.9. Cellular nucleotide levels

For quantification of cellular energy related nucleotides (AMP, ADP, ATP, NAD^+, NADPH), cells were pelletized and directly prepared for HPLC-DAD (Agilent 1260 System) analysis as described before [289].

6.2.10. Statistics

Statistical analysis was performed using GraphPad Prism software 6.01 (GraphPad, La Jolla, CA, USA). Data are presented as mean + SD, with significance stated as *$p<0.05$, **$p<0.01$ and ***$p<0.001$ compared to untreated control.

6.3. Results

6.3.1. Metal content in cell nucleus

The content of Co and Ni in the nucleus and cytosol was measured after 24 h treatment, both individually and in combination, via ICP-OES. Both metals are transferred into the nucleus, though to a lesser extent than in the cytosolic fraction (fig. 29). In both fractions, treatment with the higher combination (25 µM Co + 150 µM Ni) resulted in elevated Co levels compared to the single treatment (fig. 29A). This combination also caused a decrease in Ni levels in the nuclear fraction compared to individual exposure. Additionally, the combination of 12.5 µM Co and 75 µM Ni led to a lower Ni concentration in the cytosolic fraction only (fig. 29B). The cytotoxicity of Co and Ni, both individually and combined, is summarized in table 7. Data are derived from our previously published study [227].

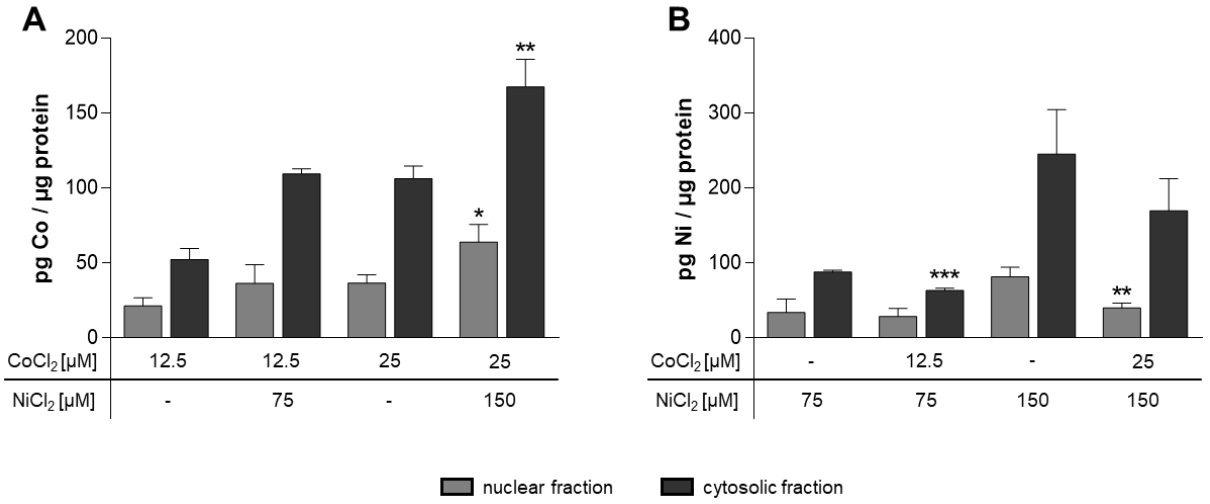

Figure 29: Cellular metal content of Co(II) and Ni(II) in nuclear and cytosolic fraction after 24 h treatment in HepG2 cells. Quantification of intracellular A) Co(II) and B) Ni(II) amount was performed via ICP-OES. Data is presented as mean + SD of n ≥ 3 independent experiments. Statistical significance was tested using an unpaired t-test depicted as *p ≤ 0.05, **p ≤ 0.01, ***p ≤ 0.001: single treatment compared to combined exposure.

Table 7: Cytotoxicity in HepG2 cells after 24 h incubation with Co(II) and Ni(II) in single and combined exposure. EC_{70}= effect concentration 70 % compared to the non-treated control. Adapted from [227].

HepG2	significant at	EC_{70}
Co(II)	50 µM	150 µM
Ni(II)	300 µM	500 µM
150 µM Ni(II) + variable Co(II)	25 µM	150 µM
25 µM Co(II) + variable Ni(II)	100 µM	300 µM

6.3.2. Comet assay

The comet assay was performed firstly in order to detect Co or Ni induced DNA damages since the comet assay helps to measure the single- and double-strand breaks, alkali labile sites (apurinic/ apyrimidinic sites), DNA cross-links, base/ base-pair damages and apoptotic nuclei in cells. For both metals, no changes in DNA in tail were observed in the alkaline comet assay (fig. 30A/B; fig. 48). However, higher concentrations of Co (100 µM and 500 µM) significantly increased the formation of FPG-sensitive sites, indicating oxidative DNA

damage (fig. 30A). Additionally, the combination of 25 µM Co with 150 µM Ni resulted in enhanced FPG-sensitive sites in HepG2 cells compared to the individual metal treatments (fig. 30B). Ni alone did not show any alterations in the FPG comet assay (fig. 48).

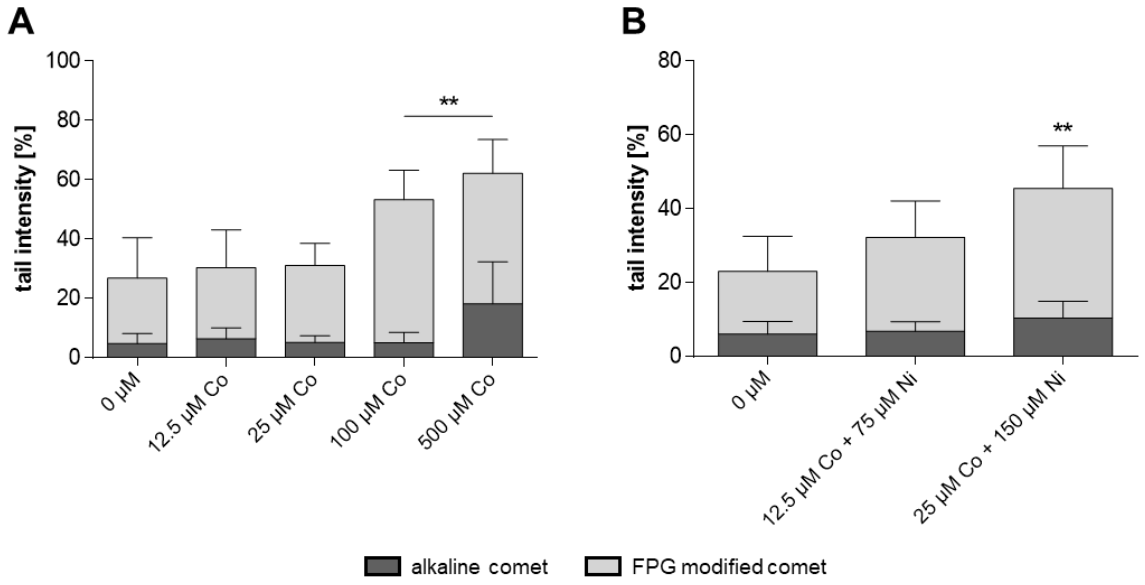

Figure 30: Genotoxic effects of Co(II) and Ni(II) assessed by comet assay analysis. HepG2 cells were treated with Co(II) for 24 h alone (A) and in combination with Ni(II) (B). Bottom bar: alkaline comet assay, top bar: FPG modified comet assay. Data is presented as mean + SD of n ≥ 3 independent experiments. Statistical significance was tested using an 2way ANOVA depicted as **p ≤ 0.01: compared to untreated control.

6.3.3. DNA single- and double-strand breaks

To distinguish the possible type of DNA damage caused by Co and Ni, the occurrence of DNA single- and double-strand breaks was assessed. Elevated levels of cellular lesions and decreased double-stranded DNA were observed only after 24 h treatment with 500 µM Co (fig. 31A). Incubation with Ni and the combination of both metals showed no alterations (fig. 49). Additionally, the expression of γ-H2AX was not affected by Co or the combination of Co and Ni. A tendency towards strand break induction was observed after treatment with 100 µM Co and the higher combination (25 µM Co + 150 µM Ni). However, the incubation with 500 µM and 750 µM Ni resulted in a significantly elevated protein expression of γ-H2AX (fig. 31B).

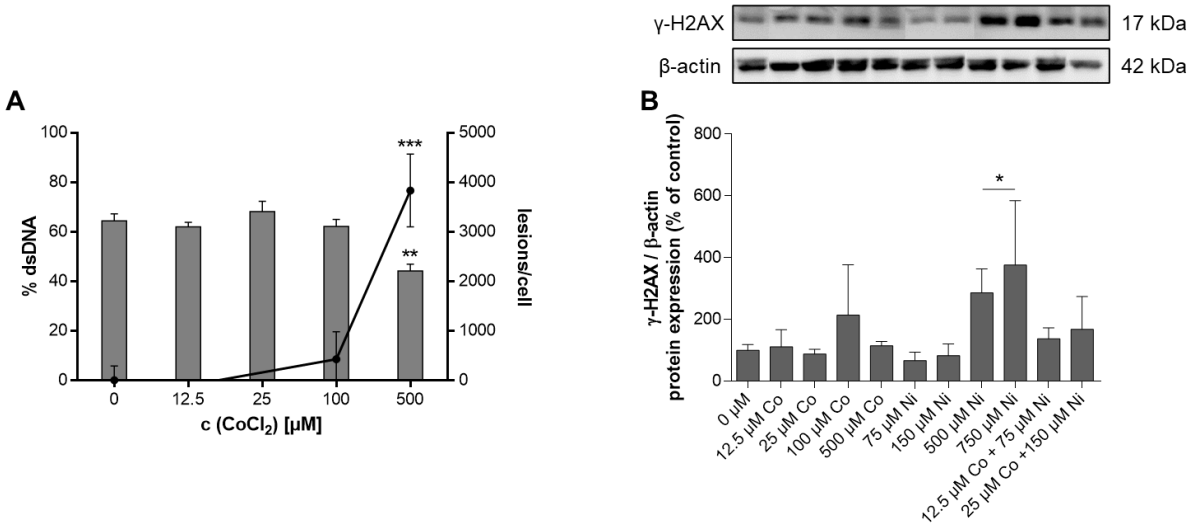

Figure 31: DNA strand breaks after 24 h of treatment with Co(II) and Ni(II) in HepG2 cells. A) The amount of dsDNA and lesions/cell were determined via alkaline unwinding. B) Protein expression of γ-H2AX was quantified via Western Blot and normalized to β-actin, with one exemplary blot. Data is presented as mean + SD of n ≥ 3 independent experiments. Statistical significance was tested by an unpaired t-test depicted as *p ≤ 0.05, **p ≤ 0.01, ***p ≤ 0.001: compared to untreated control.

6.3.4. Formation of micronuclei and polynucleated cells

To assess the genotoxicity of Co and Ni on chromosomal level, micronuclei and polynucleated cells were counted. The highest concentrations of Co and Ni, as well as the combination of 25 µM Co and 150 µM Ni showed a significant increase in micronuclei number (fig. 32A). Additionally, both metals led to the formation of polynucleated cells (fig. 32B).

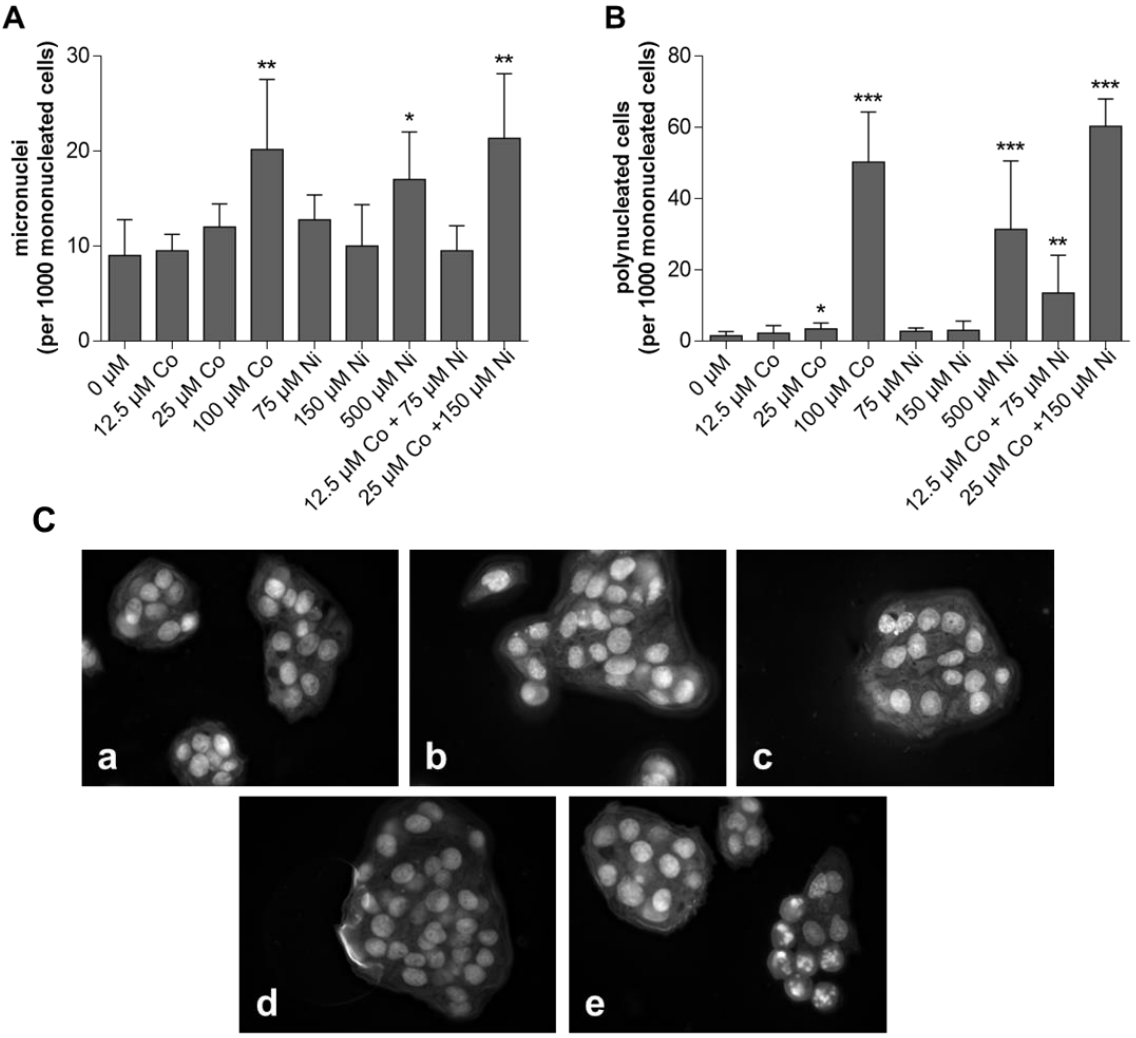

Figure 32: Induction of A) micronuclei and B) polynucleated cells after 24 h treatment with Co(II) and Ni(II) in HepG2 cells. C) shows representative microscopy pictures in 63x magnification. a) untreated control, b) 100 µM Co, c) 500 µM Ni, d) 12.5 µM Co + 75 µM Ni, e) 25 µM Co + 150 µM Ni. The pictures are processed by Leica Thunder Imager. Data is presented as mean + SD of n ≥ 3 independent experiments. Statistical significance was tested using an unpaired t-test depicted as *p ≤ 0.05, **p ≤ 0.01, ***p ≤ 0.001: compared to untreated control.

6.3.5. PARylation

For the assessment of DNA damage response, PAR levels were quantified via LC-MS/MS. Both Co and Ni led to increased PAR levels after 24 h treatment across all tested concentrations, except for 500 µM Co. Additionally, both combinations of the two metals resulted in significantly elevated PAR levels compared to the untreated control (fig. 33).

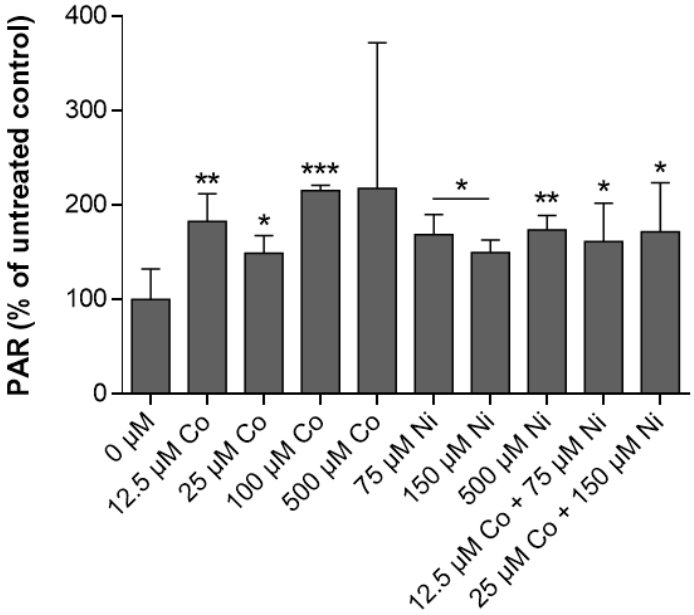

Figure 33: Quantification of PAR levels in HepG2 cells after 24 h treatment with Co(II) and Ni(II) via LC-MS/MS. Data is presented as mean + SD of n ≥ 3 independent experiments. Statistical significance was tested using an unpaired t-test depicted as *p ≤ 0.05, **p ≤ 0.01, ***p ≤ 0.001: compared to untreated control.

6.3.6. Energy related nucleotides

The impact of Co and Ni on energy-related nucleotides was determined using LC-DAD. Incubation with 500 µM Co resulted in increased AMP levels, while the amount of ATP was decreased (fig. 34A). The lower concentrations of Co (12.5 µM and 25 µM) as well as 150 µM Ni led to an increase in the cellular ATP levels, an effect has been also observed with both combinations (fig. 34B). The cellular amount of ADP remained unchanged for both metals (fig. 50). All Co concentrations, except 500 µM Co, as well as 150 µM Ni and both combinations, resulted in significantly elevated NAD^+ levels (fig. 34C). Additionally, the NADPH content increased after 500 µM Co treatment (fig. 34D).

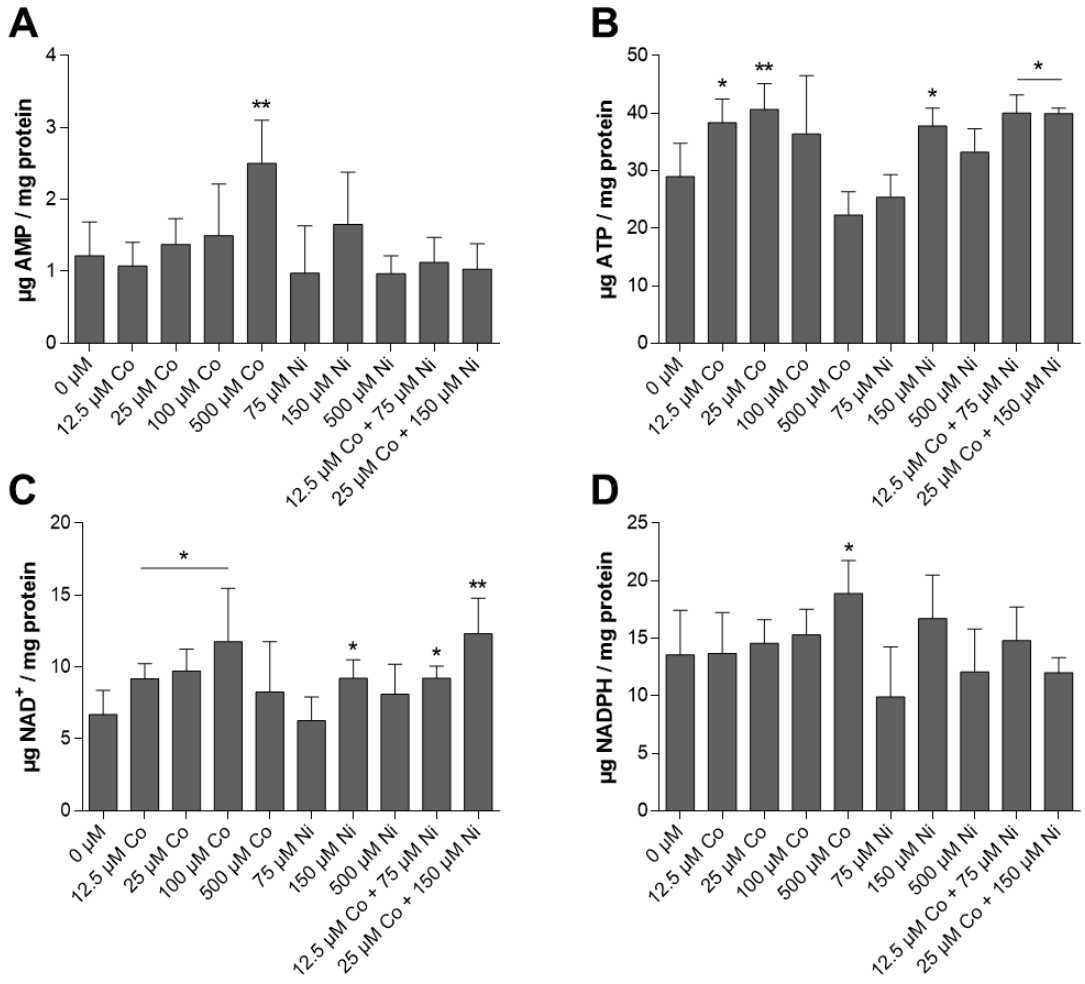

Figure 34: Energy related nucleotides measured after 24 h incubation of Co(II) and Ni(II) individually and combined in HepG2 cells. The amount of AMP (A), ATP (B), NAD^+ (C) and NADPH (D) was quantified via HPLC-DAD. Data is presented as mean + SD of n ≥ 3 independent experiments. Statistical significance was tested by an unpaired t-test depicted as *p ≤ 0.05, **p ≤ 0.01: compared to untreated control.

6.4. Discussion and Conclusion

The two trace elements Co and Ni are classified by the IARC as (possibly) carcinogenic to humans (Co: group 2A; Ni: group 1), particularly upon inhalation [43,282]. Oral exposure data is limited, but current evidence suggests it is unlikely to cause cancer. However, their genotoxic potential is evident and needs to be addressed to understand their toxicity and risk. Genotoxicity studies have been performed in bacteria, non-mammalian eukaryotes, and mammalian cells, including rodent and human cells (for Co summarized in [283] and for Ni

in [6]). Data in human cells is essential to understand the genotoxic potential of Co and Ni upon oral intake via food and drinking water. Previous studies focused on human lung cell lines and lymphocytes [191,284,285]. However, the liver is another important target upon oral intake since Co and Ni accumulate there and exert toxic effects [26,185]. Therefore, we characterized their genotoxic potential in liver carcinoma cells (HepG2). Additionally, due to increased usage and release, Co and Ni are often exposed in concert, underlining the importance of evaluating their combined genotoxic potential.

Firstly, we addressed intracellular metal localization of Co and Ni to determine their nuclear transfer. When incubated combined, an increased Co amount and decreased Ni content were observed inside the nucleus compared to single treatments. This effect was also noted in our previous study, measuring the metal amount within the entire cell [227]. One of the primary cellular transporters for both metals is the divalent metal transporter 1 (DMT-1), located mainly at the cell membrane and also in the nucleus [290]. While DMT-1 transports a variety of divalent metals, it has been reported to preferentially transport Co over Ni [32]. These findings suggest that Co and Ni influence each other in their cellular uptake, specifically into the nucleus, possibly altering their combined impact on the DNA. Higher Co concentrations (100 and 500 µM), which are already cytotoxic, induced FPG-sensitive sites and single-strand breaks in HepG2 cells. In literature, several studies confirmed the genotoxic activity of Co(II) ions, often associated with moderate or low cytotoxicity [49]. FPG-sensitive sites indicate oxidatively altered purines, such as 8-oxo-7,8-dihydro-2'-deoxyguanosine (8-oxodG) [291]. A study from Kirkland *et al.* corroborates our finding in lung adenocarcinoma cells with DNA strand breaks being significantly aggravated in the Comet assay when treated with hOGG1 [292]. This damage results from extensive formation of reactive oxygen species (ROS), which has been observed with Co in our previous study in HepG2 cells [227]. In contrast, Ni does not enhance ROS formation, correlating with the absence of FPG-sensitive sites.

However, the combination of 25 µM Co and 150 µM Ni significantly enhanced oxidative DNA damage compared to individual treatment, possibly due to the higher nuclear Co amount. Uboldi *et al.* demonstrated a significant induction of DNA damage after 2 h Co treatment assessed by Comet assay, whereas 24 h incubation showed no alterations, assuming that the possible DNA damage may be repaired during longer exposure of non-cytotoxic Co concentrations [293]. While Co treatment resulted in single-strand breaks, high Ni concentrations caused elevated γ-H2AX expression, a marker for double-strand breaks [294]. In the current study y-H2AX was not measured on cellular level thus counter-staining for S phase was not applicable and consequently an over-estimation of cells stuck in the S phase could be the reason for high y-H2AX signal. Our data are in contrast to a study, in which HepG2 cells were exposed to Ni in a similar dosage range for 24 h, as they found no induction of double-strand breaks [295]. Ni may inhibit DNA repair mechanisms, especially homology-directed DNA double-strand break repair by downregulating involved genes [296]. This inhibition possibly leads to increased incidence of double-strand breaks induced by Ni in our study. In human lung epithelial cells, treatment with both Co and Ni resulted in enhanced γ-H2AX expression, however, at concentrations that were highly cytotoxic [191]. Additionally, 100 µM Co and 500 µM Ni resulted in nuclear alterations characterized by an enhanced number of micronuclei. This effect was also observed with the combination of both metals at lower concentrations (25 µM Co + 150 µM Ni), whereas these concentrations individually showed no significant alterations compared to untreated controls. Colognato *et al.* compared genotoxic effects of $CoCl_2$ and Co nanoparticles in human peripheral leukocytes, reporting that $CoCl_2$ caused a higher number of micronuclei but fewer strand breaks than nanoparticles [297]. Additionally, in human lung fibroblasts and urothelial cells, Co caused chromosomal instability, primarily manifested as chromatid lesions [284,298]. A study from Kirkland *et al.* corroborate our findings pointing out the clastogenic potential of Co(II) in mouse lymphoma cells [292]. Ni induced micronuclei formation in HepG2 cells only at highly cytotoxic

concentrations, while a significant increase in micronuclei was observed in mouse embryo fibroblasts at non-cytotoxic Ni concentrations [299]. A higher frequency of micronuclei was also observed in human bronchial epithelial cells (BEAS-2B) following Ni exposure for 48 h [300]. Both metals, individually and combined, induced multinucleated cells, mainly resulting from defective cell division [301]. Both Co and Ni support G2/M cell cycle arrest, primarily through the activation of p53 and p21 [302,303]. This arrest inhibits cytokinesis, resulting in the formation of multinuclear cells, associated with an enhanced apoptotic rate [304]. In our previous study in HepG2 cells, we observed an increased caspase- 3 activity with concentrations exceeding 100 µM Co and 500 µM Ni. This effect was also observed for the combination of 25 µM Co and 150 µM Ni, while the respective single incubation showed no alterations [227]. Both metals activated poly(ADP-ribosyl)ation (PARylation), a response mechanism to DNA damage mainly catalyzed by poly(ADP-ribose) polymerase-1 (PARP-1), indicating their potential to compromise genomic integrity. Under highly cytotoxic conditions, PARP-1 is cleaved by caspase-3, reducing its ability for DNA repair and leading to the induction of apoptotic cell death [305]. PARP-1 cleavage was observed in human lung epithelial cells treated with high Co and Ni concentrations, with a synergistic effect seen after combined treatment [191]. In HepG2 cells, 500 µM Co showed no alterations in PARylation, and this concentration induced the highest caspase-3 activity, indicating an apoptotic cell death [227]. Despite the significant amount of NAD^+ required as a precursor of poly(ADP-ribose) during PARylation [306], treatment with Co and its combination with Ni led to increased cellular NAD^+ levels in HepG2 cells. Although PARylation is a major consumer of NAD^+, it is synthesized and recovered through various cellular mechanisms, suggesting that Co particularly enhances these pathways [307]. The main pathway for NAD^+ regeneration involves the conversion of pyruvate to lactate, catalyzed by lactate dehydrogenases (LDH). Co is known to induce hypoxia by stabilizing the transcription factor hypoxia-inducible factor 1 alpha (HIF-1α), activating the expression of related genes [47].

Under these hypoxic conditions, increased expression of LDH and resulting higher concentration of NAD^+ were observed in endothelial progenitor cells, indicating that Co may induce a similar effect [308]. Low Co concentrations and the combination with Ni increased ATP levels, while 500 µM Co elevated cellular AMP. An increase in the AMP/ATP ratio activates the AMP-activated protein kinase (AMPK), which regulates the intracellular energy homeostasis and supports DNA damage repair mechanisms [309]. In HepG2 cells it was reported that Co treatment is resulting in phosphorylation of AMPK, which can be attributed to the hypoxia-mimicking properties of Co [310].

In conclusion, this study highlights the genotoxic potential of Co and Ni upon oral exposure, emphasizing their distinct mechanisms for inducing DNA damage. Thereby the genotoxic activity of Co(II) ions is associated with cytotoxicity. The induced oxidative damage and single-strand breaks probably result from oxidative stress. Additionally, we point out a genotoxic effect on the chromosomal level at cytotoxic Co concentrations. For Ni, cytotoxicity is accompanied with increased double-strand break induction and genotoxic insults on chromosomal level (micronuclei induction). Interestingly, combined Co and Ni induce oxidative DNA damage, single-strand breaks, and micronuclei at moderate cytotoxicity. This underlines the importance to study metal combinations due to their concurrent exposure. All tested conditions activated PARylation, linked to hypoxia and altered energy metabolism. Further research is essential to elucidate these mechanisms as well as the effect of Co and Ni on DNA repair pathways in liver cells more detailed to identify potential genotoxic risks with increased uptake of Co and Ni from environmental sources.

6.5. Acknowledgement

This work was supported by the DFG Research Unit TraceAge (FOR 2558, BO4103/4-2) and the initiative “Metal based compounds (MeBaCo)” supported by the University of Wuppertal.

Abstract:

Cobalt (Co) and Nickel (Ni) are increasingly found in our environment. We analysed their combined toxicity and uptake mechanisms in the early food chain by studying bacteria and the bacterivorous ciliate *Paramecium* as a primary consumer. We exposed both species to these metals to measure the toxicity, uptake and transfer of metals from bacteria to *Paramecium*. We found that Ni is more toxic than Co, and that toxicity increases for both metals when (i) food bacteria are absent and (ii) both metals are applied in combination. The cellular content in bacteria after exposure shows a concentration dependent bias for either Ni or Co. Comparing single treatment and joint exposure, bacteria show increased levels of both metals when these are both exposed. To imitate the basic level of the food chain, we fed these bacteria to paramecia. The cellular content shows a similar ratio of Nickel and Cobalt as in food bacteria. This is different to the direct application of both metals to paramecia, where Cobalt is enriched over Nickel. This indicates that bacteria can selectively pre-accumulate metals for introduction into the food chain. We also analysed the transcriptomic response of *Paramecium* to sublethal doses of Nickel and Cobalt to gain insight into their toxicity mechanisms. Gene ontology (GO) analysis indicates common deregulated pathways, such as ammonium transmembrane transport and ubiquitine-associated protein degradation. Many redox-related genes also show deregulation of gene expression, indicating cellular adaptation to increased RONS stress. This suggests that both metals may also target the same cellular pathways and this is consistent with the increased toxicity of both metals when used together. Our data reveal complex ecotoxicological pathways for these metals and highlights the different parameters for their fate in the ecosystem, in the food chain and their ecotoxicological risk after environmental contamination.

Chapter 7

Microbial impact to environmental toxicants Ni(II) and Co(II): Joint toxicity and cellular response in *Paramecium*

Based on:

Diana Laura Garza Amaya*, **Alicia Thiel***, Melanie Möller, Gilles Gasparoni, Marcello Pirritano, Franziska Drews, Julia Bornhorst, Martin Simon

*These authors contributed equally.

Chemosphere, 2023, 140434.

DOI: 10.1016/j.chemosphere.2023.140434

Highlights:

- We investigated uptake and toxicity of Ni and Co in bacteria and the ciliate Paramecium.
- Klebsiella bacteria accumulate more of both metals when these are co-exposed.
- Co affects the bioavailability of Ni in *Paramecium*.
- Joint exposure of Ni and Co causes increased toxicity in dixenic systems with bacteria and *Paramecium*.
- Bacteria show biased uptake and deliver metals to paramecia.

Keywords:

Metal induced toxicity; Joint toxicity; Bacteria; Ciliate; Food chain; Transcriptomics

Chapter 7 – Microbial impact to environmental toxicants Ni(II) and Co(II): Joint toxicity and cellular response in *Paramecium*

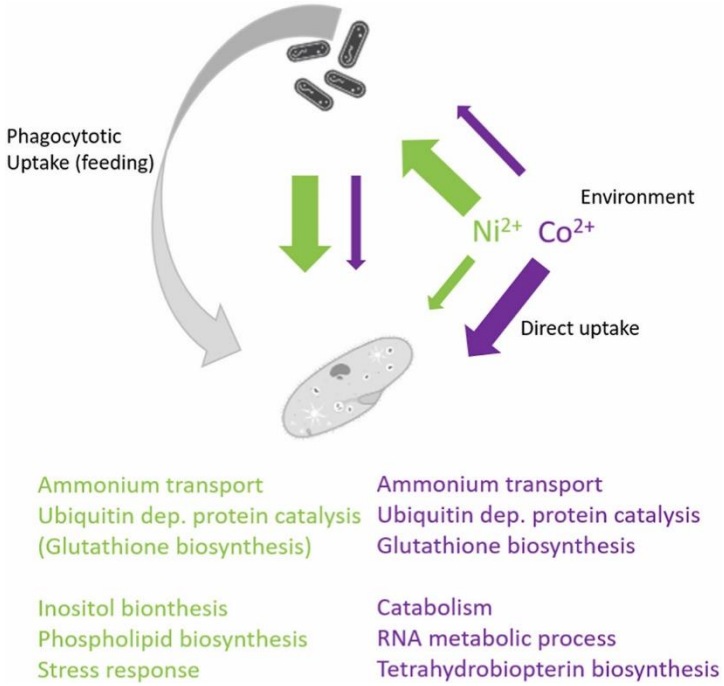

Figure 35: Graphical abstract of 'Microbial impact to environmental toxicants Ni(II) and Co(II): Joint toxicity and cellular response in Paramecium'.

7.1. Introduction

The need for decarbonization of transportation and the general need for short time storage of electric energy moves Lithium Ion Batteries (LIBs) into the recent focus of industry and into our daily life. In addition to the pollution associated with recycling, the classic problems of illegal dumping and, most importantly, an increasing rate of battery incineration are causing massive inputs of metals into our air, water and soil. Many electric vehicles now use lithium nickel manganese cobalt (NMC) oxide composite cathode materials Li(NixCoyMn1-x-y)O2 that combine optimised performance and reduced cost. NMC composite cathodes have higher capacities and longer life cycles of around 1000–2000 cycles [311] which makes them also attractive by a higher sustainability. However, chemical

and structural instabilities [312] cause difficult to assess environmental risks. It seems clear that Nickel and Cobalt, in particular, are highly toxic metals that are now being released into the environment in increasing quantities.

We approach this problem from the perspective of microbial ecotoxicology, which characterises the interaction of pollutants with microorganisms. There is a growing awareness that pollutants strongly influence microbes, their diversity and metabolism in ecosystems. Conversely, microbes respond to pollutants not only by adapting to their presence, but also by transforming them and thus affecting their bioavailability; metals in particular have become the focus of recent research as major drivers of microbial community structure and diversity [132]. Since we know that different contaminants and other biotic and abiotic factors must be considered to influence the capacity of an ecosystem to cope with environmental contaminants, there is a clear need for mechanistic approaches to characterize the response of microbial communities to environmental metal contaminants [132]. Ciliates are unicellular eukaryotic protists which can be found in pelagic, benthic and soil environments. These heterotrophic cells feed on bacteria and represent therefore an important primary component of the food web as a major consumer and by transfer of organic matter to higher trophic levels [313]. Ciliates have been used to assess aquatic ecosystems for decades using both, community assessment and toxicological tests [314]. For both approaches, ciliates have particular advantages over other organisms. One quite evident is the lack of a cell wall, causing quite fast responses to pollutants compared to bacteria and fungi [315]. Second, several ciliate species have been model organisms in genetics, epigenetics and molecular biology for almost hundred years [316]. There is an enormous amount of knowledge about the molecular mechanisms that contribute to genetic and phenotypic adaptation [317] and their detailed genome databases allow for genomic and post-genomic analyses [318,319]. Among the omics analyses, transcriptomics in particular is considered an emerging tool to analyse the cellular response to toxicants and

has gained acceptance in risk and safety assessment through the definition of transcriptional biomarkers associated with cell death, cellular injury or carcinogenic transformation [320]. In ecotoxicology, the transriptomics interpretation of the cellular response to pollutants contributes to a wide range of tools to characterize the responses at different levels [321].

Here, we investigated the joint toxicity of Ni and Co representing the main toxic compounds in NMC-LIBs. Especially for joint toxicity of these metals and also many other combinations, the literature reveals a huge gap: with regard to their increasing environmental pollution, we analysed their individual and combined toxicity in *Paramecium tetraurelia*. To further include different trophic levels, we also included the feeding bacteria in these analyses to get a preliminary insight in the first stages of the food chain.

7.2. Materials and Methods

7.2.1. Toxicity assays

P. tetraurelia stock cultures of strain 51 were maintained in WGP (wheat grass powder) medium inoculated with *Klebsiella planticola* described before [322,323]. For toxicity tests, paramecia were cultured at 31 °C, washed and starved at room temperature for 60 min. To exclude autogamy, nuclear staining with DAPI was carried out to guaranty for vegetative cultures as described before [324].

All toxicity tests used the same number of paramecia in the same volume. Time and temperature were also kept constant for all tests unless otherwise stated. We used 2 h for all toxicity tests and treatments to limit the influence of cell division. Under these conditions, paramecia divide every 4–5 h. For a single test, 30 cells were placed in one well of a 96-well plate. For treatments involving bacteria, the bacterial density should be comparable between all treatments. Exponentially growing bacteria were diluted from a stock solution in fresh WGP medium to a final OD (600 nm) of 0.2. The OD of this dilution was checked again prior to treatment. The individual metals were then added at the indicated

concentrations. For experiments without bacteria, starved paramecia were used without the addition of *Klebsiella*. Plates were incubated at room temperature for 2 h. Cell viability was calculated by counting swimming and non-swimming cells. Cells lying on the bottom were counted first. All non-swimming cells were considered as dead cells. Then 10 µl of (4 %) paraformaldehyde solution was added to the wells to rapidly kill the remaining living cells. The total number of cells at the bottom of the well was then counted again. Dead cells were subtracted from the total cells to give a percentage of dead cells. LC50 concentrations were calculated from data by equation of the best fit line using the LD50 calculator tool [325].

7.2.2. Sampling paramecia and bacteria for element analysis

For metal uptake by bacteria, *Klebsiella* was grown in a total volume of 14 ml LB-medium. When the cultures reached an optical density of 1 (OD 600nm), the individual metals were added at the indicated concentrations and the cultures were incubated for 2 h at 37 ◦C while shaking. Afterwards, bacteria were washed three times by centrifugation at 4200 rpm for 15 min and re-suspended in 600 µl of double distilled water. For the analysis of metal uptake by *Paramecium*, samples containing 100,000 cells were prepared. These cells were starved for 1 h before the addition of *Klebsiella* to a final OD of 0.2 and the addition of Co or Ni as described above. *Paramecium* cells with or without bacteria were incubated for 2 h at room temperature and then washed three times with Volvic water by centrifugation at 2000 rpm for 3 min. The cells were resuspended in 600 µl of double-distilled water. For the analysis of metal uptake by *Paramecium* through phagocytosis, *Klebsiella* were pre-incubated with Co or Ni for 2 h at 37 ◦C while shaking in LB medium. The bacteria were then washed three times by centrifugation at 4200 rpm for 15 min and resuspended in WGP medium. This bacterial suspension was added to a final OD of 0.2 to *Paramecium* cultures containing 100,000 cells in 100 ml. This culture was incubated for 2 h at room temperature and then washed three times by centrifugation at 2000 rpm for

3 min. Finally, the cells were resuspended in 600 µl of double-distilled water. Controls represent bacteria and paramecia not treated with metals.

7.2.3. Analysis of bio-availability by ICP-OES

Samples from all treatments were homogenized with an ultrasonic homogenizer for 30 s set at maximum power and 30 percent cycles (Sonopuls HD 60, BANDELIN, Berlin, Germany). Then the samples were centrifuged at 10,000 rpm for 5 min. In all cases, an aliquot (30 µl) was separated for protein quantification following the Bradford assay (SERVA). The remaining samples (570 µl) were dried at 70 ◦C overnight and processed for ICP-OES. Dried pellets were digested in 500 µL of a 1:1 mixture of 65 % nitric acid (Suprapur®, VWR) and 30 % hydrogen peroxide (Sigma Aldrich) at 90 ◦C overnight. Ashed samples were dissolved and diluted in 2 % nitric acid to a final volume of 3.6 ml. All samples were spiked with 100 µg/L Yttrium (Y) (ICP-Standard-Solution ROTI®Star, Carl Roth) as an internal standard before digestion. Total metal content was determined using inductively coupled plasma-optical emission spectrometry (ICP-OES; Avio 220 Max, PerkinElmer) with measurement parameters displayed in Appendix Fig. 51. Each measurement was verified using Standard Reference Material® 1643f (National Institute of Standards and Technology) and Certified Reference Material BCR®-274 (single cell protein, Institute for Reference Materials and Measurements). The obtained metal content was normalized to sample protein amount.

7.2.4. Statistics

To compare the respective dose-response curves, a two-way ANOVA was performed using GraphPad Prism (GraphPad Software Inc.) version 6.01. Data represent mean ± SEM of three biological replicates. All data for ICP-OES were analysed in Prism and represent mean ± SEM of three biological replicates with statistical significance tested by unpaired *t*-test as shown.

7.2.5. Transcriptomics

For RNA isolation and sequencing, we followed the procedure described in [326]. Briefly, total RNA was isolated from washed and pelleted cells using TriReagent (Sigma-Aldrich, Seelze, Germany). For further purification involving DNAse digestion, samples were cleaned with the RNA clean and concentrator Kit (Zymo, Freiburg, Germany). RNA integrity was checked using Agilent Bioanalyzer 2100 RNA Pico Chips®. 2.5 µg total RNA each was used for poly-A enrichment using the D-Plex mRNA capture module with the D-Plex mRNA-seq Library Preparation Kit (Diagenode) for Illumina® for library preparation with amplification using 13 PCR cycles. Libraries were pooled and sequenced on an Illumina HiSeq2500 platform in 100 nt SE High output mode.

7.2.6. Bioinformatics, GO-enrichment and visualization

At least 10 million reads were obtained for each replicate of each treatment, the numbers of reads were assessed with MultiQC Version 1.14. Adapters, polyA tails, UMI sequences and template switch motifs were trimmed using Cutadapt V3.4 using the recommended commands in the D-Plex mRNA-seq Kit manual from Diagenode (Liege, Belgium). Reads were mapped to the macronuclear genome of *Paramecium* strain 51 Version 2 obtained from ParameciumDB (2022) [318] using the plugin Bowtie2 [229] in Geneious Prime® 2023.0.4. Gene expression levels were calculated using the Geneious Prime® 2023.0.4 expression analysis tool with the default parameters. Differentially expressed genes between the control group and those groups exposed to Ni or Co were normalized and compared using the DESeq2 [327] plugin in Geneious Prime® 2023.0.4. Differential expression log2 ratio and p-values were obtained. A principal component analysis plot which is a distance matrix showing normalized differences in expression patterns between samples was automatically generated by comparing expression levels using DESeq2. Genes with a differential expression p-value below 0.05 and a fold change log2 of at

least 2 were extracted for gene ontology enrichment. Predicted GO terms from *Paramecium* strain 51 were obtained from *Paramecium*DB database (2023), using the Sherlock tool. GO Enrichment Tool in usegalaxy.org (Galaxy version 23.0.rc1 [328]) was used to generate a list of GO enriched DEGs. GO-enrichments were visualized by the R-package published in [242] without reduction of redundant terms. TPM values were extracted from Geneious and plotted into a heatmap using R heatmap2 tool in Galaxy Europe version 23.0.rc1 [328]. TPM values were log2 (+1) transformed, and the Euclidean distance method which measures the proximity between vectors was used without scaling.

7.3. Results

7.3.1. Toxicity of Ni and Co: influence of joint exposition and starvation

To assess toxicity at overexposure, Ni and Co were applied to paramecia in feeding medium together with feeding bacteria (*K. planticola*) for 2 h. Fig. 36A shows that Ni is significantly more toxic than Co: the LC50 for Ni is 320 µM and for Co 1509 µM. To investigate the extent to which bacteria could influence metal-induced toxicity, we compared fed cultures (with feeding bacteria) with cultures without bacteria. Fig. 36B shows that both metals show significantly increased toxicity in the absence of bacteria (LC50 for Ni 186 µM and for Cobalt 1328 µM). This effect is more pronounced for Ni than for Co. This effect also demonstrates that paramecia are capable of ingesting the metals by phagocytosis independent pathways as during starvation, no phagosomes are by the cells. Fig. 36C shows the analysis of joint toxicity in which we added a sublethal dose of Ni (150 µM) to the Co series and a sublethal dose of Co (600 µM) to the Ni dilution series. In both cases, this significantly increases toxicity: for this joint exposure we calculate a LC50 for Ni 128 µM and for Co 1118 µM. Finally, Fig. 36D shows the same analysis of joint toxicity in comparison with and without food bacteria. A significantly increased joint toxicity can be observed for Co without bacteria. However, this effect cannot be observed for Ni in combination with a sublethal dose of Co. Fig. 37 summarises the LC50 values from these experiments.

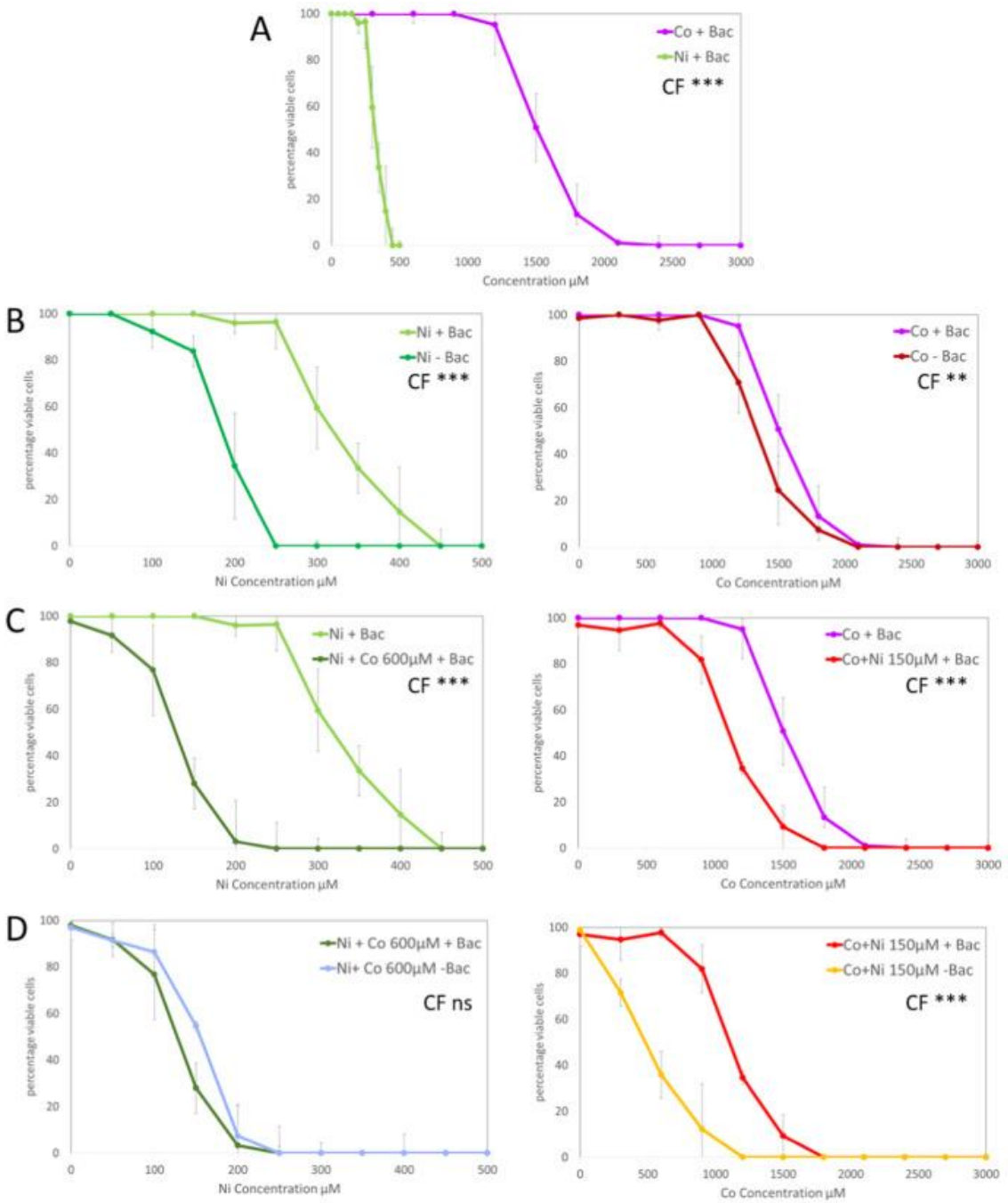

Figure 36: Toxicity assays with Ni and Co with vegetatively growing paramecia. A. Varying Ni and Co concentrations were applied to paramecia together with food bacteria for 2 h. B-D show toxicity assays separated for Ni (left) and Co (right). Please note the different range of concentrations on the axes. B compares toxicity of both metals in paramecia with and without food bacteria. C compares joint-toxicity when the respective other metal is added in a sublethal dose (Ni 150 µM or Co 600 µM) in the presence of food bacteria. D shows the same comparison without food bacteria. Data represents the mean of three biological replicates; error bars represent the standard deviation. Statistical comparison of the shown curves using TWO-WAY ANOVA for the individual comparison is indicated in the graphs by comparing the treatment group; ***p ≤ 0.0001, **p≤ 0.001, ns = non significant.

	+ Bac	-Bac	+ 600Co + Bac	+ 600Co - Bac
LC50 Nickel (µM)	320	186	128	155
	+ Bac	-Bac	+ 150Ni + Bac	+ 150Ni - Bac
LC50 Cobalt (µM)	1509	1328	1118	476

Figure 37: Summary of the calculated LC50 values of Paramecium from different treatments. Data is µM.

7.3.2. Klebsiella bacteria accumulate more Co than Ni in paramecium

We started the analysis of metal uptake in our system with the *Klebsiella* bacteria. These were exposed to Ni and Co at 100 µM each or in combination (Fig. 38A) for subsequent multi-element analysis, and we made a second set at higher concentrations of 600 µM of both metals and their various combinations (Fig. 38B). Please note that these concentrations are not toxic for the bacteria (Data not shown). Comparison of Fig. 38A and B shows that bacteria are biased towards Co at lower concentrations, but biased towards Ni at higher concentrations. Most interestingly, we can observe increased levels of the individual metals when their combination is applied, except for the lower doses of Ni: when the concentration of one metal is the same, its uptake increases as the concentration of the other metal increases.

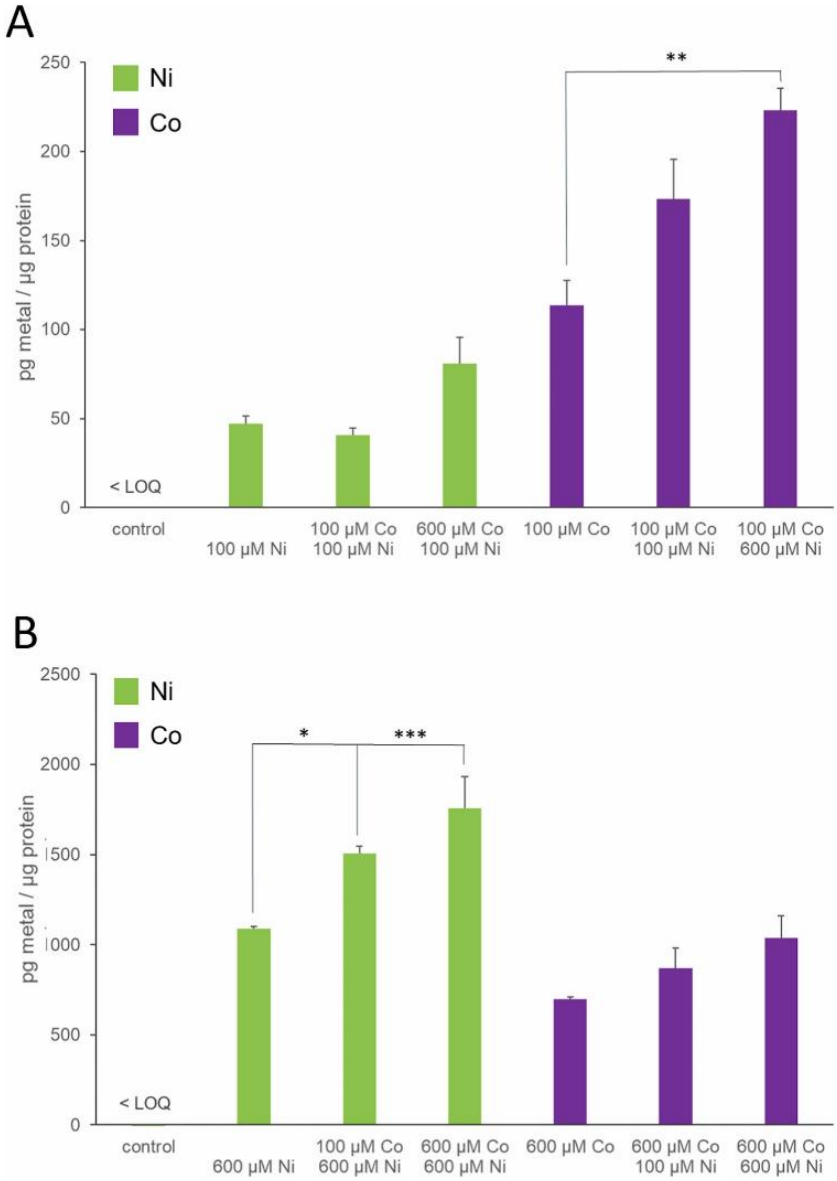

Figure 38: Cellular content of Ni and Co in bacteria. A. Klebsiella bacteria were exposed to Ni and/or Co at 100 µM (X-axis) alone or on different combinations. B. Klebsiella bacteria were exposed to Ni and/or Co at 600 µM (X-axis) alone or on different combinations. Data is normalized to protein content of samples and represents the mean of three biological replicates; Statistical significance was tested by an unpaired t-test depicted as *p≤ 0.05, **p≤ 0.01, ***p≤ 0.001: combined treatment compared to the respective single exposure. LOQ = Limit of quantification.

7.3.3. Ni and Co uptake in paramecium

We further investigated the cellular content of both metals when applied to paramecia. To correlate toxicity data to uptake and bio-availability of both metals, we applied sublethal doses to paramecia with and without feeding bacteria. Fig. 39A shows the data for Co, Fig. 39B shows the data for Ni. Paramecia show a higher cobalt content at 600 µM exposure in the starved condition - this may explain the higher toxicity of Co in the starved cultures. This effect is not apparent at lower concentrations of 100 µM Co. Furthermore, the Co content in paramecia does not seem to be influenced by Ni, at least in this experimental setup. The latter aspect is different for Ni, as shown in Fig. 39B. The equimolar application of Co does not seem to alter the Ni uptake at 100 µM. Higher Co concentrations (600 µM) result in lower Ni content, lower Co concentrations (16 µM) result in higher Ni uptake, but only in the starvation condition.

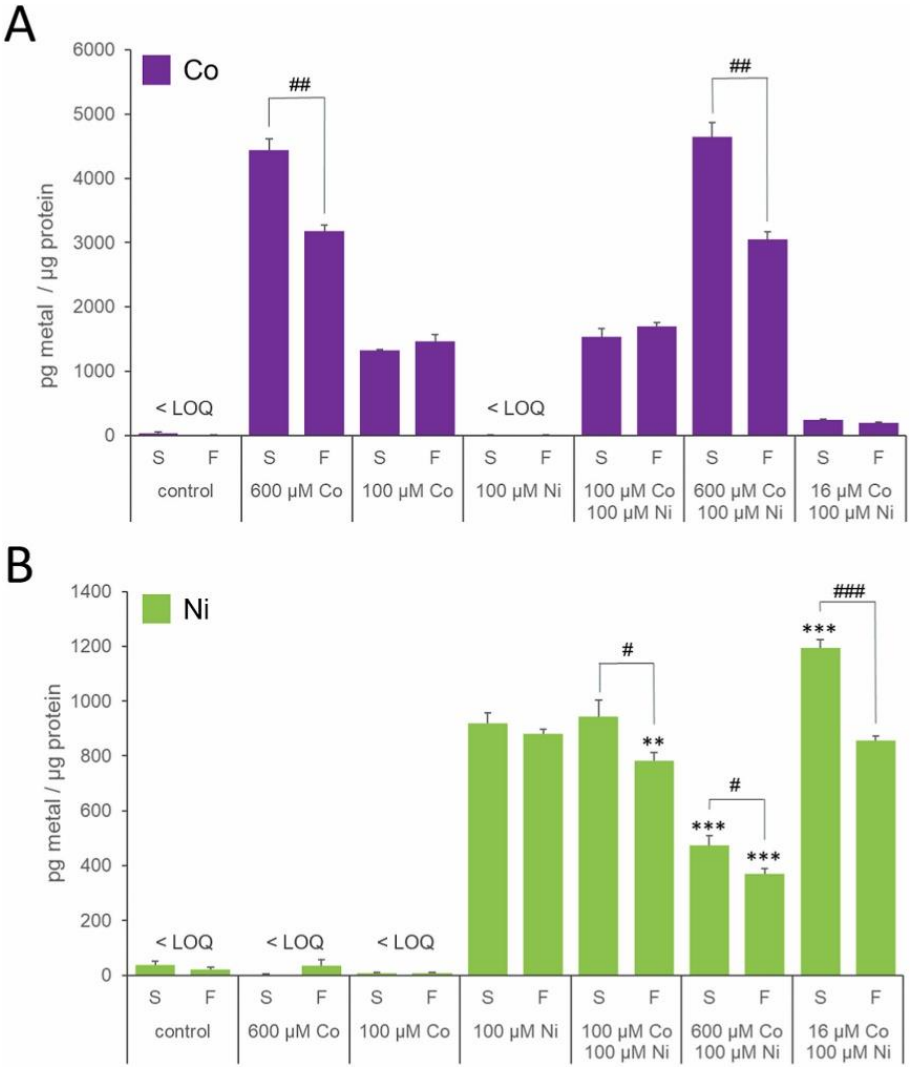

Figure 39: Cellular content of Ni and Co in Paramecium by ICP-OES. "S″-means starved, "F″-means fed, including bacteria. paramecia were exposed to the indicated combinations of metals and for 2 h, washed and analysed. A. Data for Co. B. Data for Ni. Data represents the mean of three biological replicates; error bars represent the standard deviation. Data represent the mean + SEM of n = 3 independent experiments. Statistical significance was tested by an unpaired ttest depicted as **p≤ 0.01, ***p≤ 0.001: combined treatment compared to the respective single exposure; #p≤ 0.05, ###p≤ 0.001: comparison of fed and starved paramecia.

7.3.4. Bacterial delivery to paramecium

We then asked whether metal-loaded bacteria could transfer their metal content to paramecia. Fig. 40A shows the elemental analysis of bacteria incubated with 600 µM Ni or Co each and in combination. Note that the co-exposed bacteria already accumulated significantly more Ni and also more Co. These bacteria were washed and then fed to paramecia according to the experimental

parameters of the previous experiments. Fig. 40B shows the ICP-OES data of the paramecia, which is very similar to the pattern of the bacteria. Paramecia show significantly more of both metals after feeding with co-applied bacteria. For comparison, Fig. 40C shows ICP-OES data of paramecia (starved) and with food bacteria to which both metals are directly applied. While the paramecia have a bias for Co, the feeding of pre-exposed bacteria causes a bias for Ni.

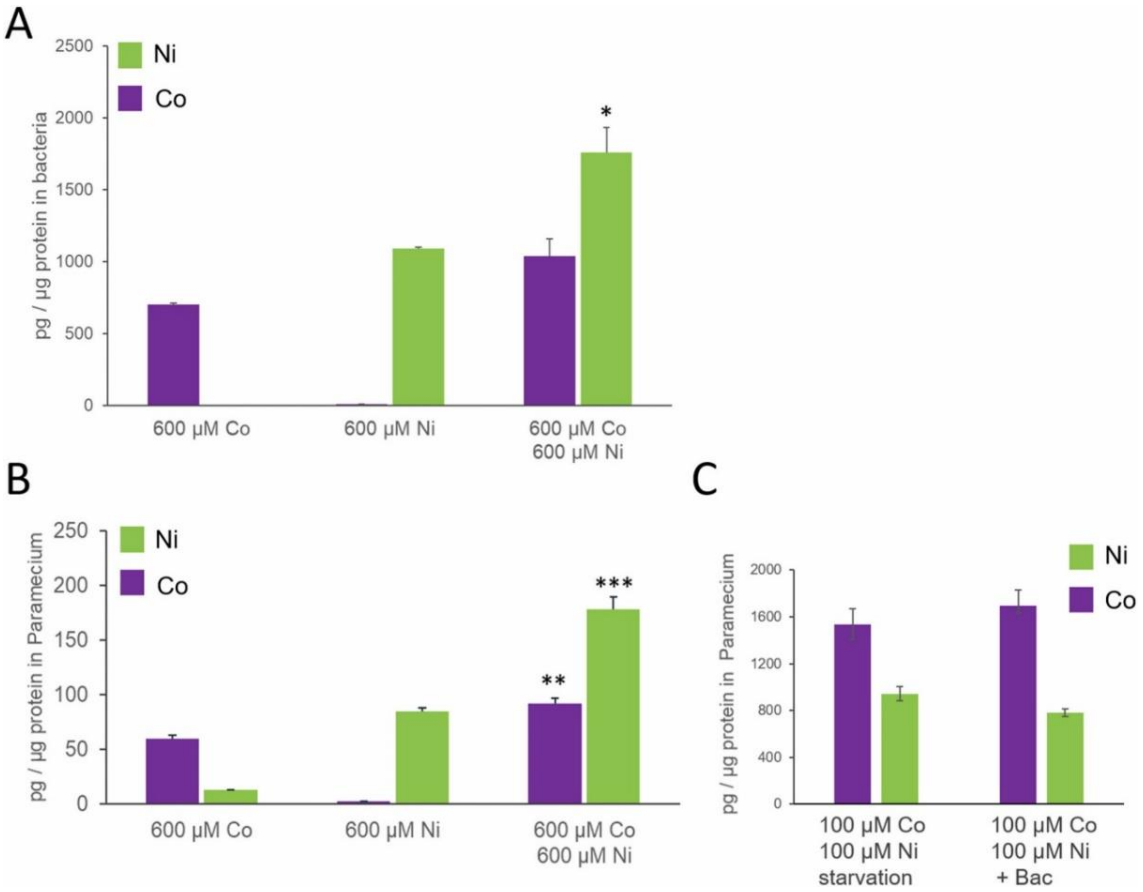

Figure 40: Element analysis of bacteria and paramecia in a feeding experiment. A. bacteria exposed to 600 µM Co and Ni alone and in combination. B. shows the ICP-OES data of these paramecia fed with bacteria from (A). C. shows the data of paramecia with Ni and Co directly added to the ciliate culture at 100 µM each with and without bacteria. Data represent the mean + SEM of n = 4 independent experiments. Statistical significance was tested by an unpaired t-test depicted as *p≤ 0.05, **p≤ 0.01, ***p≤ 0.001: combined treatment compared to the respective single exposure.

7.3.5. Transcriptomics of Ni and Co induced cellular responses

We then aimed to get insights in the toxicity mechanisms. Sublethal doses of both metals were applied individually and in combination before isolation of RNA. For transcriptomic analysis, we chose the highest sublethal concentrations where we did not observe lethality in the individual treatments (1141 µM Co and 160 µM Ni) to avoid induction of cell death. For the joint application transcriptomics, we had to reduce these concentrations even further to concentrations that did not cause cell death because of the accumulated toxicity. We used Co 600 µM/124 µM Ni and Ni 150 µM/Co 245 µM for these experiments.

Fig. 41A shows the PCA plot where PC1, explaining 58% variance, mainly dissects the untreated control to the batch of metal treated samples, indicating that control and treatments are indeed quite different. The individual treatments are then dissected by PC2 explaining 17% variance. Individual treatments of Ni and Co are clearly separated from each other. Joint treatments of both metals in different proportions can still be separated from each other, lying between the individual treatments. This could indicate a mixed response in the joint exposures. In support of this, a clustering heatmap in Fig. 41B shows the clear separation of untreated controls from all treatments. However, we were unable to find a correlation or distance based method that could separate the individual single and combined treatments. The dendrogram in principle separates the high Co treatments (1141 µM and 600 µM in combination with Ni) from the high Ni treatments (160 µM and 150 µM/Co 245 µM). The transcriptomic response to 600 µM Co seems to dominate the transcriptome in the co-exposure with 150 µM nickel, as these samples cluster with the 1141 µM Co single exposure. Samples with almost the same Ni concentration of 150 µM but with drastically lower Co (245 µM) cluster to the single Ni treatment. These data support the idea, that common pathways are activated, not only in the combined treatments compared to the single treatments, but also in each treatment compared to the control.

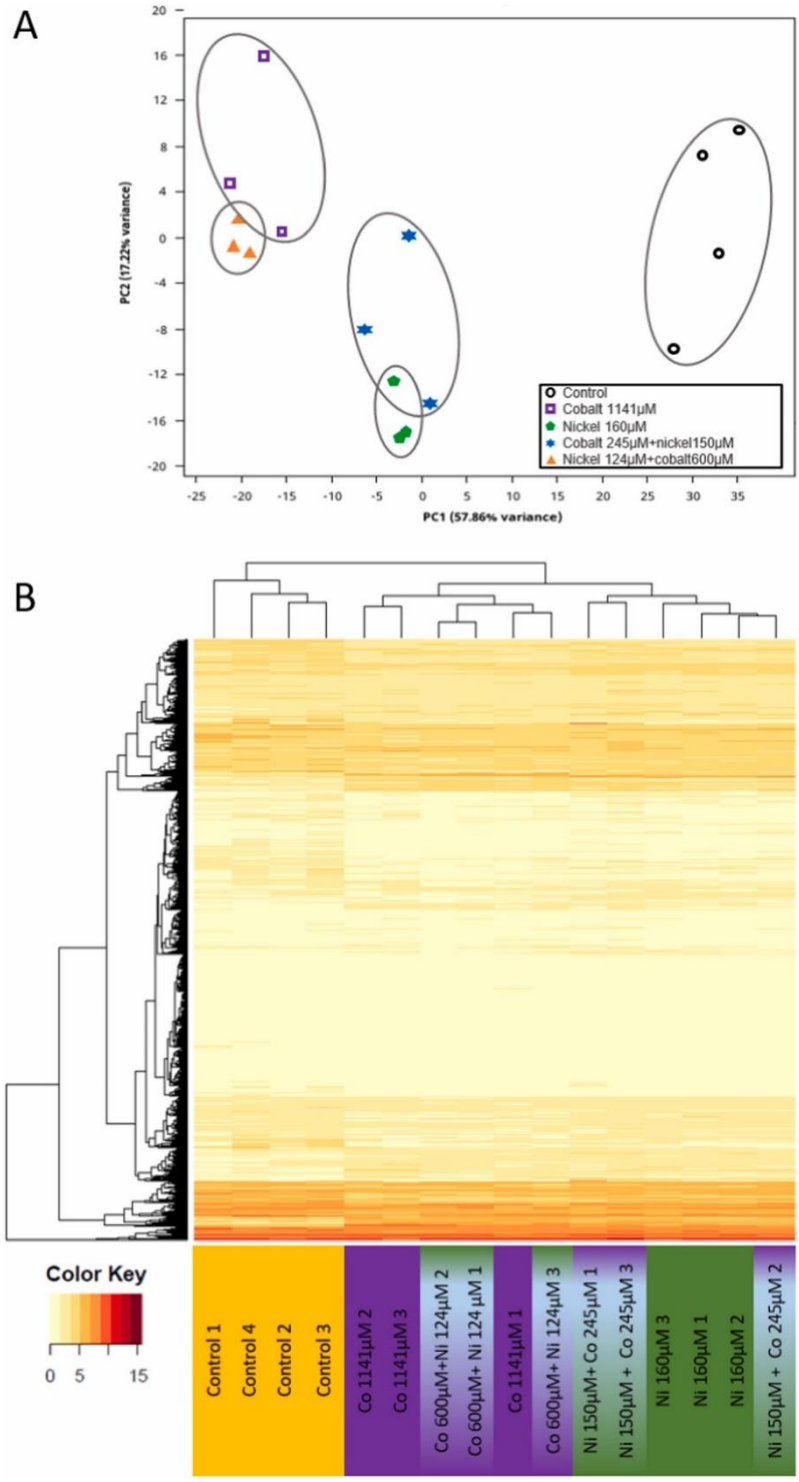

Figure 41: Relationship between transcriptomes of the individual samples and replicates. A. Principal Component Analysis (PCA score plot) of the first two principal components of the analysed transcriptomic profiles thus indicating how samples are related to each other. B. Clustering heatmap indicating expression levels (TPM) according to the color key beneath. The dendrogram on the left shows clustering of genes with similar regulation pattern and the dendrogram on top is based on the global similarity of transcriptomic profiles using Euclidean distance.

7.3.6. GO-enrichments indicate specific and common responses

Up- and down-regulated DEGs were used separately for GO term enrichment. Fig. 42 shows the comparison of all analysed states, separating up- and down-regulated GO terms. Note that boxes marked with an X represent GO terms that do not fall within our relatively strict cutoff of FDR 0.01.

Some GO terms are specific to a single metal, and some GOs are shared between states: mostly between the corresponding single and joint treatments, but some interestingly also between single Ni and single Co. The joint treatment shows many specific GOs. These include for example *GO:*0016070 RNA *metabolic process* and *GO:*0006418 tRNA *aminoacylation*, both of which are enriched in upregulated DEGs. This may be related to the enriched *GO:0006620 cellular amino acid metabolism*, which is only significant in upregulated DEGs of high cobalt treatment, and also to *GO:0006729 tetrahydrobiopterin biosynthesis*: Three DEGs of this GO term, which summarises components involved in the formation of reduced biopterin, a co-factor of many enzymatic processes, are differentially regulated. Tetrahydrobiopterin is a component of a complex redox system active in the oxidation of aromatic rings, e.g. in the biosynthesis of tyrosine and phenylalanine. To interpret and summarise these GO data, the cell seems to be altering translation and amino acid metabolism, while in parallel *GO:0006511 ubiquitine-dependent protein catabolic process* is positively enriched. This could indicate a massive reorganisation of the proteome. The down-regulated *GO:0072488 ammonium transmembrane transport* could be related to this, if the cell wants to retain components of degraded proteins instead of releasing them to the outside. In addition to these GO terms associated with amino acid metabolism, *GO:0009056 catabolic process* appears to be specifically up-regulated by Co treatment, suggesting a further effect on the genome and DNA turnover metabolism, while in parallel also *GO:0006511 ubiquitine dependent protein catabolic process* is positively enriched. This could speak for a massive re-organization of the proteome. The down-regulated

GO:0072488 ammonium transmembrane transport could be related to this, if the cell would like to maintain components of degraded proteins instead of releasing to the outside. Next to these GO-terms associated with amino acid metabolism, *GO:0009056 catabolic process* appears up-regulated specifically in Cobalt-treatments, suggesting another effect to the genome and the DNA turnover. Ni reveals many regulated GOs. One is the down-regulation of *GO:0006021 inositol synthetic process*. This GO term may be related to *GO:0008664 phospholipid biosynthetic process*, which is also down-regulated in the same Ni treatments. Both imply that the synthesis of phosphatidylinositol, a component of biological membranes, is down-regulated, which could be an indicator of altered membrane composition or also altered signalling, as phosphatidylinositol is involved in the transmission of extracellular signals through cleavage by phospholipase C into second messengers, which have also been described in *Paramecium* [329,330]. More biochemical data are available for the ciliate *Tetrahymena*, where detailed analysis of various phosphatidylinositols has been characterised for different functions involving the secretion of lysosomal enzymes and phagosomal trafficking [331,332]. Regulation of these GO terms could indeed indicate altered signalling, and the enrichment of *GO:0050896 response to stimulus* on Ni treatment would support the latter idea, but the term is enriched in up-regulated DEGs. Assuming an alteration or disruption of signalling pathways based on phosphoinositol metabolism, *GO:0050896 response to stimulus* may attempt to counteract this. Ni treatment also exclusively shows the appearance of the *GO:0006950 response to stress*, which may involve heat shock chaperones. In our data, Ni treatment seems to alter the proteomic state more by these chaperones compared to Co treatment, which shows a substantial alteration in amino acid metabolism.

In terms of common GO terms, the down-regulation of *GO:0072488 ammonium transmembrane transport* is apparent in all states. This may be related to the up-regulation of ubiquitin-dependent protein catalysis, which is seen in all states

except Ni 150 µM/Co 245 µM. Also interesting is the term glutathione biosynthetic response, which could be an indicator of redox stress: its GO term appears up-regulated here in Ni and Co treatments, including the Co 600 µM/Ni 124 µM samples, but not in the Ni 150 µM/Co 245 µM samples. As redox stress would be a prime candidate to be involved in the toxicity of both metals, we analysed this in more detail.

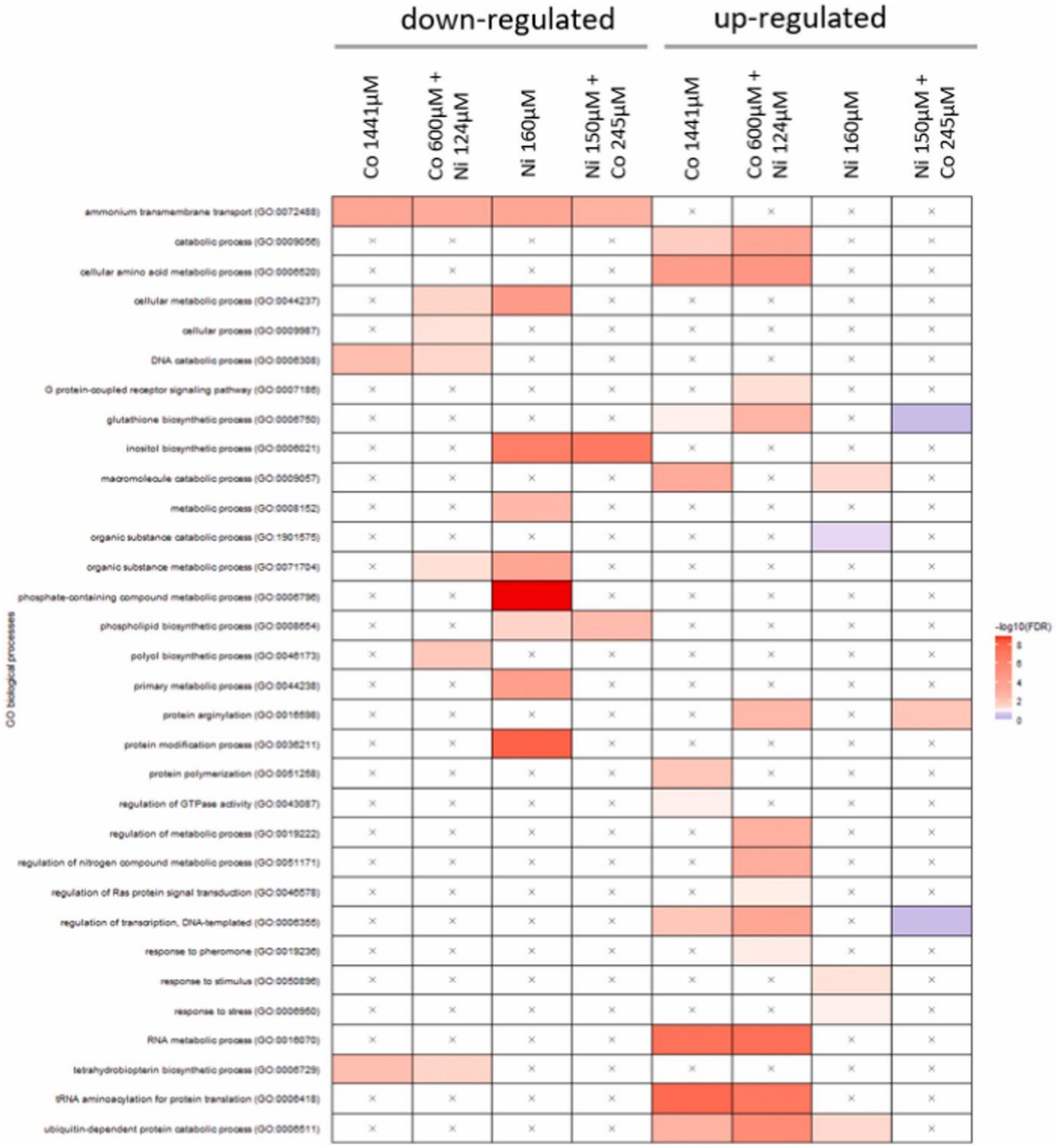

Figure 42: Plot of over-represented biological processes in up- and down-regulated DEGs. Colors indicate significance of enrichment (-log10 (FDR-corrected p-values) with a p value cutoff 0.01. An X means that the term is not significantly represented in a condition. Visualization by an R-script from [242].

7.3.7. Altered gene expression suggests global downregulation of ammonium transport and upregulation of glutathione

GO:0008519 ammonium transmembrane transport is associated with 19 genes in the Mac genome of *P. tetraurelia* stock 51, mainly consisting of genes annotated as ammonium transporters. Appendix Fig. 52A shows all of these gene's fold change of expression in relation to control (not only the significant DEGs). If the annotation of these transporters is correct, ammonium transport is apparently down-regulation. For many metal intoxications, redox systems have been reported to be involved. Indeed, the GO term glutathione biosynthetic process is significantly enriched in all conditions except the single Ni treatment (with our chosen thresholds). Glutathione is a main antioxidant component of the phase 2 biotransformation of heavy metals. Glutamate-Cysteine ligases activity producing y-glutamylcysteine, the first step to produce glutathione, which mainly determines the cellular glutathione level [333]. Appendix Fig. 52B shows the regulation of the three genes associated with this GO term. A putative glutathione synthase and two genes encoding putative glutamate-cysteine ligases. All of them show up-regulation, also in the single Ni treatment, suggesting a redox effect of both metals. Interestingly, two genes reveal an even higher up-regulation in co-exposure: this may be a hint to explain the increased toxicity in joint exposure of both metals, assuming that both target the redox system for detoxification.

7.3.8. Complex regulation of gene expression associated with Cell Redox homeostasis and DNA repair

We also had a deeper look for GO terms which are not among the enriched with strongest significance but appear to be relevant in relation to the literature. These concern redox homeostasis and DNA repair because Ni and Co have been reported to cause redox stress and have also the ability to interfere with chromatin and thus e.g. with DNA repair mechanisms. We first had a closer look

for the 102 annotated genes associated with *GO:0045454 Cell Redox homeostasis*. This GO term does not appear to be significantly enriched in our analysis e.g. in the Ni treatment its p-value is 0.12 (not shown) and therefore slightly below our set threshold of 0.1. Analyzing the 102 genes of this GO term, Fig. 43A shows a scatter plot of their individual fold-change in Ni 160 µM and Co 1140 µM treatment. The plot reveals non uniform regulation of these genes in both directions. This may be the reason why the GO term is not significant in our analysis, because we separated first up- and down-regulated DEGs before the GO enrichment. The data dissects also for genes showing regulation in with a single metal, only, and those reacting uniformly to both. We can conclude that there is indeed a regulation of Redox associated genes occurring and that a large number of genes is co-regulated by both Ni and Co. We can confirm this also for the co-exposure experiments. Appendix Fig. 53 shows bar plots of the TPM fold-change of individual genes of this GO term. Many of them indeed show a even higher regulation on the co-exposure than the single exposure. This may be another hint to explain the increased toxicity in joint applications. This may also be true for the second interesting *GO:0006281 DNA repair* with 45 genes associated in the current annotation. Genes of this GO term show weak significant enrichment only in the Ni 160 µM cultures (p-value 0.08, thus below our threshold), and not in any other treatment. Fig. 43B dissects this parental GO into the individual DNA repair mechanisms. Several genes show up-regulation in both, Co and Ni treatment including two putative isoforms of DNA ligase 4, a component of the non homologous end joining repair. Two genes show stronger up-regulation in Ni treatment compared to Co: a putative ERCC3/RAD25/XPB C-terminal helicase, a putative DNA mismatch repair protein Mlh1. This may indicate a stronger activation of some DNA repair mechanisms in the Ni treatment.

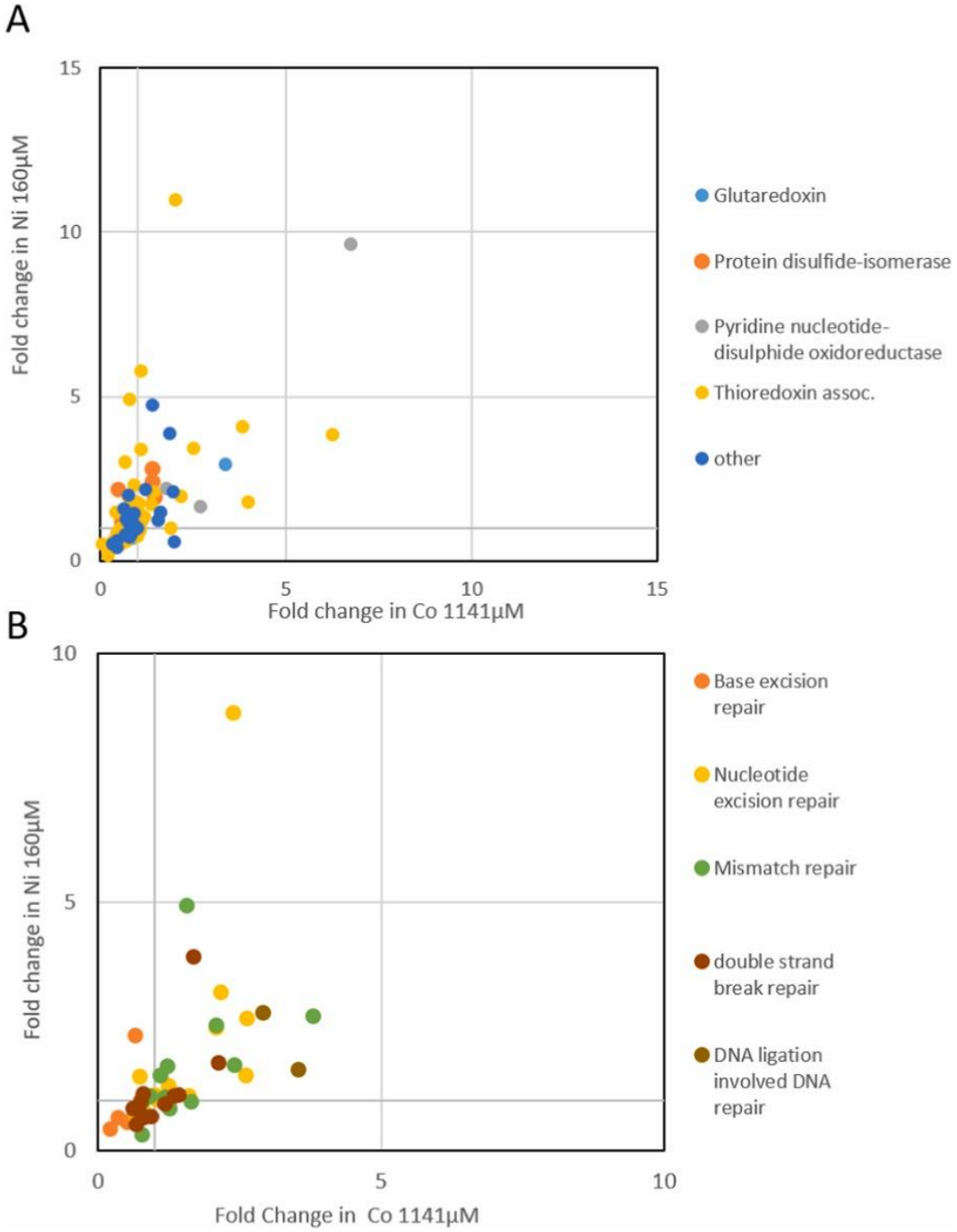

Figure 43: A. Scatter plot for the fold change of 102 genes associated with GO:0045454 Cell Redox Homeostasis. B. Scatter plot for the fold change of 45 genes associated with GO:006281 DNA repair dissected into the subGOs indicated in the legend. Genes with Fold-change below 1 are down-regulated, genes with a Fold-change above 1 are up-regulated.

7.4. Discussion

7.4.1. The relationship between bacteria and paramecia in the food web

Our data indicates that paramecia can take up Ni an Co by phagocytosis-independent mechanisms as well as by phaygocytosis. The latter appears to be due to the capacity of bacteria themselves to accumulate both metals. Bio-accumulation of many different metals in bacteria was known for a long time. For instance, in Gram-negative species, such as *Klebsiella*, metal deposition was shown to occur mostly at polar head groups along the two membranes or along the peptidoglycan layer [334]. Our data show a higher Ni content compared to Co, interestingly both are drastically increased when applied in combination. Given the constant binding capacity of the cell wall, the increased binding in the combined application could be due to an adaptation of the bacteria in response to metal stress. Such responses include morphological changes in the cell wall for increased extracellular binding or activation of metallothioneins for intracellular binding [335]. Another interesting aspect is that *Klebsiella* biases for either Ni or Co, depending on the concentration and this is a clear argument to spent attention to the food bacteria as they could heavily affect uptake into the ciliates. Firstly, both metals show less toxicity when applied together with food bacteria. This could be due to the different uptake mechanism, but it seems more likely that the presence of bacteria reduces the available metal concentration for *Paramecium*. Our data suggest that reduced toxicity is associated with reduced metal accumulation in *Paramecium*, and this is supported by the high levels of metal accumulation in bacteria. However, bacteria cannot only be considered as a sink, because feeding pre-exposed bacteria to *Paramecium* shows that bacteria can also introduce metals into the food chain: importantly, they can pre-select for individual metals, because they transfer the enrichment of Ni over Co to the prey organisms. In nature, this could indeed lead to accumulation processes along the food chain. In this context, the microbial loop concept addresses the non-linear food chain by bacteria which grow on the extrusions of

higher trophic levels [336]. Since the definition of the term, there has been an ongoing debate about the fate of this bacterial biomass: (i) a loss of fixed biomass (sink) due to bacterial sedimentation. This would represent a removal of biomass from the food web. (ii) introduction into the food chain (link), which would mean the transfer of biomass to higher trophic levels. The current perspective goes more into the direction of a sink but the relative role of the microbial loop is variable and depends on the individual temporal characteristics of an ecosystem [337]. It is well known in marine and limnic systems, the occurrence of microbial loops has also been characterised in soil microfauna-plant interactions, revealing a complex situation in which plants benefit from protists and nutrients released from bacterial biomass growing on plant exudates [338]. Taking into account the variable influence of the microbial cycle, the link or sink discussion can also be applied to metal toxicity in the environment. Our data show that bacteria can indeed be a sink, not only for biomass but also for accumulated metals. However, they can also be the entry point into the food chain and they could be biased towards highly toxic metals and efficiently deliver them to higher trophic levels.

7.4.2. Ni and Co toxicity in paramecium

Our data show, that *Paramecium* is more insensitive to Co compared to Ni. This is in contrast to what has been published e.g. for mammals. PubChem reports the LD50 by intraperitoneal injection for Ni(II) with 250 mg/kg and for Co(II) with 100 mg/kg body weight. This is certainly a simplified measurement of the whole organism, in this case rats. The individual sensitivity of different cell types is likely to vary. However, it may be a good comparison with *Paramecium* from the point of view of the single cell as an organism. Co is an essential element in mammals as the central ion of cobalamin (vitamin B12), which is produced by certain bacteria. Animals cannot produce cobalamin themselves, but obtain it from bacterial cobalamin (intestinal symbionts) or by eating meat. Little is known about Co and especially about cobalamin-dependent enzymes in *Paramecium*, but the simple fact that the receipt for axenic cultivation of *Paramecium tetraurelia* strain

51 (exactly the strain we used for our experiments) does not contain any cobalamin derivative or Co in the trace elements [339] suggests that both, cobalamin biosynthesis as well as cobalamin dependent enzymes are missing in this species. Comparing with the literature, the mechanisms reported for cellular toxicity differ between Ni(II) and Co(II), however they may also target similar pathways. In *E.coli*, both were demonstrated to cause elevated DNA damages: interestingly not by oxidative stress but by blocking the SOS DNA repair pathways and also both inhibit the RecBCD enzymes [340]. Co(II) is supposed to generate reactive oxygen and nitrogen species (RONS), superoxides and hydroxy radicals from O_2 and H_2O_2 through Fenton reactions in pro- and eukaryotes [65]. Also for Ni(II) overdoses, redox-stress was also reported in mammals, however the background seems less clear: mitochondrial damage was reported which could increase ROS. Thus, oxidative stress appears to account for the toxicity of both metals, and this would fit to our data suggested by the transcriptomics analysis in *Paramecium*.

In literature, the main target for Ni was by inhibition of histone-deacetylation resulting in alteration of gene expression and inhibition of DNA repair. Ni is therefore considered to be carcinogenic [341]. Also Co is directly interacting with the chromatin by interaction with cellular zinc finger motifs which involve Zn(II) bound by cysteine thiols or histidine imidazole groups to realize their affinity to chromatin and DNA (reviewed in [49]). In our experiments, both toxicants appear to cause similar transcriptomics changes to the same genes annotated for DNA repair mechanisms, suggesting a common effect of both metals. Could there be an organismal background for the higher Ni sensitivity of *Paramecium*? At first glance, one might think that the ciliate might have some buffers against chromatin damage by Ni, because the polyploidy in the macronucleus could accept some DNA damage while still maintaining enough intact alleles, and any DNA damage in the diploid micronucleus will only become apparent during recombination. Could the cell cycle be the Achilles' heel? The S phase of the Mac extends to

more than half of the cell cycle: this means that most individuals in the culture replicate their DNA [317,342] and this is a much higher number than in mammalian cell cultures. If we assume that Ni interferes with the replication machinery, this may explain the increased sensitivity to Ni.

7.4.3. Nickel and Cobalt uptake in paramecium

We measured the uptake of both metals into *Paramecium* and were able to dissect between ingestion of metal loaded bacteria by phagocytosis and uptake during starvation by phagocytosis independent mechanisms. A dynamic change in the uptake mechanism must be taken into account during the 2 h exposure. Immediately after the mixing of (i) *Paramecium*, (ii) bacteria and (iii) metals, the metal concentration in the medium is high and the preferential uptake for *Paramecium* at this time is likely to be through channels. With increasing time, we hypothesise that increasing amounts of metal ions are bound by bacteria, resulting in two effects: The concentration decreases and more metals are taken up by the paramecium via the phagocytotic pathway. This scenario seems quite likely and future research will need to clarify the dynamics of these processes and also discriminate between different toxic effects between the two uptake mechanisms. In fact, these future experiments would even have to consider a third uptake mechanism, namely nanoparticles. Enzymatic catalysed reduction contributes to nanoparticle formation, e. g. in fungi, where extra- and intracellular enzymes have been shown to be involved [343] e.g. NADH dependent reductase, nitrate reductase [344,345]. Also protists have quite recently been described for nanoparticle formation, e.g. *Tetrahymena* producing Gadolinium particles [346] or silver nanoparticels produced by the marine bacterium *Marinomonas* associated with the ciliate *Euplotes* [347]. The authors speculate that the formation of nanoparticles may fulfil two different roles, detoxification of free silver ions and protection against other pathogens; interestingly, bacterially synthesised nanoparticles showed higher antibacterial activity compared to chemically synthesised ones [348], however they can also harm the ciliate [349].

Also for our system, transformation of metals by bacteria could explain some finding, e.g. the fact that we cannot identify any relation between uptake and toxicity. It seems likely that bacteria are not a simple sponge for metals but they could also transform them into more or less toxic derivates or by detoxification by protein binding as known for other divalent metals like Cu, Fe or Zn. Importantly, our experiments show that the metal content in bacteria is higher when both metals are present. Although the reason for this is unclear, this means that environmental pollution with Ni and Co, which is not a rare scenario due to their usage in LIBs may lead to self enforcing effects in terms of increased uptake, increased toxicity and increased accumulation in the food chain.

7.5. Conclusions

In mammals, Ni and Co are believed to cause toxicity mainly by either chromatin interaction or, for Co, redox stress. The results of our study reveal increased toxicity of Ni and Co in joint exposure in *Paramecium* and the transcriptomic data suggest that this could be due to several common metabolic pathways to be involved. Therefore the dual use and the combined environmental pollution of Co and Ni by damaged LIBs needs to be considered carefully, not only with regard to their individual toxicity, but also with regard to a possible accumulation in the food web. This factor becomes even more important as our experiments reveal increased uptake of both metals when co-exposed: in bacteria and *Paramecium*. Hypothesizing that in nature, the role of bacteria in food chain can be both: a sink, because they could clear the environment from free metals, but also a link, delivering Ni and Co to higher trophic levels. Bacteria could therefore be a crucial component responsible for enrichment of metals along the food chain. More research is needed especially in characterizing effects of combined metal exposure since they may behave differently in comparison to individual exposure, as in our study.

7.6. Acknowledgements

This study was supported by the initiative *Metal based compounds MeBaCo* supported by the University of Wuppertal/Faculty of Mathematics and Natural Sciences. M.P. is recipient of a doctoral scholarship of the Studienstiftung des deutschen Volkes. This work was also supported by the DFG Research Unit TraceAge (FOR 2558, BO4103/4-2). The graphical abstract was in parts created with BioRender.com.

Chapter 8

Final discussion and future perspectives

Chapter 8 – Final discussion and future perspectives

Metal toxicity is a critical concern in environmental, occupational, and general human health, arising from the extensive use of metals in various industrial applications. The interactions between different metals can intensify their toxic effects, thus it is essential to investigate their combined impact. Among the metals of concern are cobalt (Co) and nickel (Ni), which are extensively used in the production of alloys, lithium-ion batteries for electric vehicles, as well as components in catalysts and pigments [11,12]. As their usage in industrial processes continues to grow, environmental contamination increases, resulting in heightened human exposure through food sources and drinking water. Despite their utility, Co and Ni pose substantial environmental and human health threats [4].

Co serves as an essential trace element in humans, primarily as a cofactor of vitamin B12, which is crucial for the formation of amino acids and proteins [23]. Conversely, the biological role of Ni remains elusive, although it is often discussed [4]. Concerns are rising regarding potential adverse health effects from Co and Ni since oral exposure to both metals is associated with health risks such as neurological, cardiovascular, and thyroid dysfunctions [2,179]. However, only limited data exist on the underlying mechanisms of toxicity. The carcinogenic potential upon inhalation is well-documented for both metals and classified by the IARC (Co: group 2A; Ni: group 1) [43,51].

The majority of past studies have focused on individual toxicity of Co and Ni, often using human lung cell lines to model exposure via inhalation [284–286]. However, as both metals frequently occur together in the environment, combined exposure represents a more realistic scenario to investigate the underlying toxicity mechanisms. This thesis aims to address this gap by exploring the impact of Co and Ni on two different cell lines, liver carcinoma cells (HepG2) and

astrocytoma cells (CCF-STTG1), simulating oral exposure. Various methodical approaches were employed, including non-targeted transcriptomic analysis, enzymatically based dye-assays and analytical techniques with prior method development. These methods allowed for the assessment of alterations in cellular mechanisms, including oxidative stress, activation of transcription factors and their consequences on cell metabolism, genotoxic effects, and cell death mechanisms, focusing on the comparison of combined and individual treatment. Additionally, the model organism *Paramecium tetraurelia*, was used to clarify the potential implications of Co and Ni contaminations on the ecosystem.

8.1. Development of a LC-MS/MS method for simultaneous quantification of reduced and oxidized glutathione

Glutathione (GSH) plays a fundamental role in maintaining cellular health through its involvement in redox homeostasis and phase II metabolism. Under normal conditions, GSH exists predominantly in its reduced form, however, oxidative stress can lead to the formation of the oxidized form glutathione disulfide (GSSG). With physiological intracellular concentrations in the millimolar range, GSH is a key player in cellular response to free radicals. The NADPH-dependent enzyme glutathione reductase (GR) converts GSSG back to GSH, maintaining a typical GSH/GSSG ratio of about 100:1 under physiological conditions in mammalian cells [138]. The ability to conjugate with electrophilic xenobiotics, catalyzed by GSH S-transferases further underscores the role of GSH in detoxification processes [136].

Alterations in GSH and GSSG levels as well as a low GSH/GSSG ratio are common biomarkers for oxidative stress and cellular injury in toxicological studies, hence it is crucial to quantify both accurately in different biological matrices. This quantification is essential for monitoring the oxidative status of cells and tissues and offers the possibility to evaluate the effectiveness of antioxidative treatments [94]. Over the last years, numerous techniques have been developed for this purpose, each with its own advantages and limitations.

One commonly used method is the enzymatic recycling assay, which relies on a spectrophotometric measurement [93]. This method only allows to determine GSH and indirectly GSSG, thus it is less specific and sensitive compared to analytical techniques. The sensitivity is especially important for small sample sizes or low GSSG amounts, which physiologically occurs in cells in a 1:100 ratio compared to GSH [138]. To overcome these limitations, chromatography-based methods have been developed, including HPLC-UV, -FD, -ECD, and -MS/MS. However, UV- and FD-based methods often require a time-consuming derivatization, and ECD is mostly inadequate for simultaneous measurement due to lack of sensitivity [136,146].

To address the need for a suitable and sensitive method for exactly our application, we developed a new LC-MS/MS method, focusing on the simultaneous quantification of GSH and GSSG in small sample sizes and biological matrices. Mass spectrometric detection offers the advantage of a high specificity by distinguishing between GSH, GSSG, and other similar compounds based on their unique mass-to-charge ratios, reducing the risk of interferences in complex biological matrices. This method does not require derivatization, simplifying the sample preparation process and ensuring rapid analysis, which is crucial due to the fast oxidation of GSH and the risk of overestimating GSSG [350]. The rapid measurement time of 5 min allows for high-throughput analysis, which is beneficial for time-sensitive experiments with a large number of samples. The method's reproducibility was optimized using NEM as a thiol group conjugator, providing a better stability of GSH throughout the whole process of sample preparation and analysis. To compare the GSH and GSSG contents of different biological matrices amongst each other, the method was validated in mammalian cells, the nematode *C. elegans*, and mouse liver tissue, with only minor adaptions in sample preparation. With this ability, the developed method was used for a variety of other research projects within our working group [351].

To further enhance the accuracy and minimize variation, the quantification method could be refined by incorporating an isotope-labeled internal standard instead of external calibration. This approach would compensate for variations in sample preparation, injection, and analysis, as well as account for potential matrix effects [352]. The stability issues for isotope-labeled GSH could be mitigated by using NEM also for the internal standard, as described before [151,152]. Additionally, the method could be expanded to include the simultaneous determination of several other compounds related to the GSH cycle. This expansion is valuable as toxins are also able to alter the GSH synthesis or other key pathways in which GSH is involved. Relevant compounds would be the biosynthesis intermediate γ-glutamylcysteine, the amino acids cysteine, cystine, glutamic acid, and serine or the precursor N-acetylcysteine. Recently, two new methods were developed to quantify the GSH pathway metabolites in different cell lines using an UPLC-MS/MS system [353,354]. Since reversed phase columns did not provide sufficient retention of the polar amino acids, an expanded method has to be evaluated using another type of column. Serafimov *et al.* considered hydrophilic interaction liquid chromatography (Hilic) columns as the best for this application [355]. Combining this analysis with the determination of gene or protein expression of involved enzymes could provide a broader overview of GSH regulation. In addition, preliminary tests indicated that the method is also suitable for determination of GSH and GSSG in serum and plasma samples (data not shown). However, it must first be validated for these matrices to ensure reliable results. Accurately measurement of the GSH/GSSG status in human serum or plasma is crucial, as it serves as a clinical marker for various diseases, including diabetes, HIV, cancer, and aging. For those diseases, GSH imbalance represents a critical target for medical intervention [140].

In conclusion, GSH is a pivotal molecule in maintaining cellular health and protecting against oxidative damage. Developing stable and reliable methods for the quantification of GSH and molecules related to its metabolism is essential for

understanding the impact of environmental and dietary factors on the antioxidant status and evaluating therapeutic strategies for diseases related to oxidative stress.

8.2. Impact of Co and Ni on the cellular mechanisms of human cell lines

Co and Ni, extensively used in industrial applications such as lithium-ion batteries, pose increasing environmental and human health risks. Both metals are known to be (potentially) carcinogenic upon inhalation, and an overexposure is associated with a variety of diseases like neurological and cardiovascular disorders [2,6]. Despite their widespread use, the underlying mechanisms of toxicity remain poorly understood, especially regarding their combined exposure. This comprehensive research investigated the individual and combined effects of Co and Ni on human liver carcinoma cells (HepG2) and astrocytoma cells (CCF-STTG1), focusing on stress mechanisms, alterations in cellular metabolism, cell survival, and genotoxic effects.

Given that both metals are utilized in similar industrial applications, combined exposure is a realistic scenario. For instance, in lithium-ion batteries, a ratio ranging from 3:1 to 8:1 (Ni:Co) is common, hence a 6:1 ratio was chosen for this studies [194]. In the literature, divalent metals such as Co and Ni are reported to be transported into cells particularly via similar transporters, thus the investigation of metal interactions is of crucial importance. While the cellular effects of these metals upon inhalation are well-documented, their impact following oral exposure is less understood. This knowledge gap is of significant concern given the increasing environmental entry of Co and Ni. The liver, a primary organ for distribution, storage, and detoxification, and the brain, central to nervous system functions, are critical targets for Co and Ni toxicity upon oral intake [26,185,192]. Therefore, this study compared the impact of Co and Ni on two different human cell lines, HepG2 liver carcinoma cells and CCF-STTG1 astrocytoma cells. The findings revealed that HepG2 cells are more sensitive to Co and Ni compared to

CCF-STTG1 cells, with higher metal content observed in HepG2 cells comparing the same incubation time. One of the main responsibilities of astrocytes is the protection of neurons, due to the neurons' post-mitotic and non-regenerative nature. For this, astrocytes show a high Nrf2 activity and consequently enhanced production and storage capacity of antioxidants and their precursors, providing them to neurons [202]. Astrocytes have been found to exhibit resistance to Co toxicity, as demonstrated in a study comparing them to neuroblastoma cells, suggesting that astrocytes may not be a particularly sensitive target for Co toxicity in the brain [203]. Therefore, expanding research to investigate Co and Ni toxicity in neuronal cell lines, such as LUHMES human mesencephalic cells or SH-SY5Y human neuroblastoma cells is essential for further studies. These cell lines are widely used as model systems for studying neurotoxicity and could provide further insights into the effects of Co and Ni on the nervous system. HepG2 cells exhibit a higher vulnerability to Co than to Ni, corresponding to a higher cellular Co content. We demonstrated an involvement of DMT-1 as a primary transporter for both metals using the DMT-1 blocker 1. However, other transporters are also implicated. Next to the cell membrane, DMT-1 is present in nuclei and the outer mitochondrial membrane, suggesting these are the main targets for Co and Ni toxicity [207,290]. Other Co and Ni transporters, such as Tfr1, ZIP8 and 14, and DMT-1 are known to exhibit preferences for certain metals [4]. For example, DMT-1 favors Co over Ni, explaining the increased Co and decreased Ni levels in HepG2 cells when both metals are incubated combined compared to individual treatment. This effect was also observed within cell nuclei, resulting in elevated nuclear Co levels and reduced Ni amount., indicating that both metals also interact during nuclear transport. Future studies should aim to uncover the detailed cellular transport mechanisms of both metals to understand the exact contribution of various transporters and the metal interactions. In HepG2 cells, an increase in DMT-1 protein expression was observed after a 4 h incubation with Co, which has been linked to an enhanced expression of HIF-1α [208]. These findings could be extended by analyzing the mRNA and protein expression

of relevant metal transporter proteins following combined administration of Co and Ni, using techniques such as qRT-PCR and Western blot analysis. Since DMT-1 is reported to transport other divalent metals, including Zn, Fe, Mn, and Cu, it is important to investigate the potential effects when these metals are combined with Co and Ni to gain deeper insights into the complexity of metal interactions [209]. To further understand the involvement of DMT-1 and to overcome limitations related to the specificity and sensitivity of the used DMT-1 blocker 2, utilizing DMT-1 knockdown cells would be a valuable approach [356,357]. Additionally, comprehensive knowledge of cellular homeostasis for Co and Ni is still elusive. It is crucial to identify potential storage proteins and cellular exporters of both metals in future studies. The observed higher Co amount and decreased Ni levels after combined exposure, compared to the single treatment, necessitate further investigation to determine if this effect is due to differences in uptake, storage, or export mechanisms. This metal homeostasis should be further explored by assessing the metal content in cellular sub-compartments. In these studies, the isolation of cell nuclei was included, and this should be expanded to isolation of mitochondria and subsequent metal content analysis using ICP-OES or ICP-MS following Co and Ni treatment. Various advanced techniques are available for visualizing metal ions in biological samples for defining metal distribution, such as secondary ion mass spectrometry (SIMS), laser ablation inductively coupled plasma mass spectrometry (LA-ICP-MS), and X-ray fluorescence microscopy (XRFM) [358]. Additionally, fluorescent probes have been developed for live-cell imaging of specific metals, including Co and Ni [359,360].

Based on the observed interactions among Co and Ni in their transport into the cell, it is likely that there are also differences in their toxicity mechanisms compared to single metal incubation. Elucidating these mechanisms was the further focus of this thesis, primarily using the more sensitive HepG2 cells. To identify the most relevant pathways in response to Co and Ni exposure, the non-

targeted transcriptomics approach was chosen. Transcriptome analysis offers comprehensive insights into the complete set of RNA transcripts produced by the genome, allowing for a comparative examination of gene expression patterns across specific samples [361]. This detailed gene expression profile can then be used to study and verify the affected pathways more targeted. In HepG2 cells, we observed a higher number of DEGs after treatment with the combination of Co and Ni compared to individual exposures, suggesting a synergistic effect with additional responses. For both metals, especially when combined, the target DEGs were associated with the transcription factor Nrf2. Nrf2 is primarily activated by ROS, which react with the cysteine residues of KEAP1, the protein that complexes with Nrf2 under physiological conditions. Newly synthesized Nrf2 is then able to translocate into the nucleus and activate the expression of various cytoprotective and antioxidative genes [245]. Both Co and Ni, individually and combined, resulted in elevated amounts of nuclear Nrf2, corresponding with the increased formation of ROS induced by Co and its combination with Ni. In contrast, Ni alone did not induce ROS in HepG2 cells, indicating a ROS-independent activation of Nrf2. This can be attributed to a cysteine-independent mechanism, by interfering with the Nrf2-KEAP1 complex [245]. Notably, individual treatment with Ni resulted in the upregulation of *sqstm1*, revealed in the transcriptome analysis. Sqstm1, also known as p62, is a multifunctional protein important in various cellular processes, such as autophagy and cell signaling. Additionally, p62 can interact with KEAP1, leading to the activation of the Nrf2 signaling pathway [362]. Future studies should aim to clarify the mechanisms of Nrf2 activation by Co and Ni to further understand the differences between these metals. Other transcription factors connected with Nrf2, such as NF-κB, ATF4, and HIF-1, are known to activate each other and overlap in their pathways [245]. It was reported that Nrf2 is activated as response to hypoxia, which can be induced by Co [74,303]. Additionally, in Nrf2-deficient primary murine kidney tubular epithelial cells, the hypoxia-stimulated HIF-1α activation was impaired, and Nrf2-knockdown PC12 cells showed an increased sensitivity

towards Co toxicity [363,364]. Therefore, it can be concluded that the Nrf2 signaling pathway plays a crucial role in response to the combination of Co and Ni metals in HepG2 cells. Further studies should address the involvement of other transcription factors in response to Co and Ni treatment, to fully elucidate this complex interplay.

Our next aim was to investigate the Nrf2-regulated pathways in greater detail following Co and Ni treatment. The combination of both metals led to alterations in cellular iron metabolism, increasing the gene and protein expression of HMOX-1 and FTL. HMOX-1 degrades the pro-oxidant heme into biliverdin, carbon monoxide, and free iron, which in turn can be bound by FTL to prevent the cells from ROS formation through Fenton reactions. Thus, an increase in iron metabolism helps the cell mitigate oxidative stress and has cytoprotective properties [365]. One of the main Nrf2-targeted pathways is the glutathione metabolism, crucial for cellular antioxidative defense [366]. The combination of Co and Ni resulted in increased gene expression of GCLC and GCLM, which catalyze the initial step of GSH synthesis. Both metals did not affect the cellular GSH amount, indicating the direct oxidation of newly synthesized GSH. This is consistent with the increased levels of GSSG observed after treatment with Co alone and in combination with Ni. GSH and GSSG levels were quantified using our newly developed LC-MS/MS method. The enhanced GSSG levels indicate oxidative stress induced by Co and the combined treatment, whereas Ni alone did not show alterations, aligning with the lack of ROS induction mentioned earlier. GSH is composed of three amino acids: glutamate, cysteine, and glycine [367]. Glutamate is provided through glutamine, catalyzed by glutaminase. Combined treatment with Co and Ni resulted in elevated glutamine levels, necessary for the heightened GSH synthesis. Conversely, glutamate levels decreased with Co and Ni treatment, both individually and combined, potentially due to cellular export via the cystine/glutamate antiporter SLC7A11. This transporter is positively regulated by Nrf2, and its gene expression was

enhanced by the combination of Co and Ni in HepG2 cells, supporting the increased need for GSH in response to oxidative stress. We also investigated the cellular pathways glycolysis and TCA cycle following treatment with Co and Ni. For this, we developed a novel LC-MS/MS method capable of simultaneously quantifying 11 different analytes, including glucose, lactate, pyruvate, citrate, α-ketoglutarate, succinate, malate, glutamine, glutamate, cysteine, and serine. Separation was achieved using a Hilic column, with a total analysis time of 20 min. The sample preparation protocol was adapted and validated for use with mammalian cells and the nematode *C. elegans*, with the potential for extension to various other biological matrices in the future. Additionally, the method can be expanded to include several other analytes and we started to combine it with our previously developed LC-MS/MS method for the quantification of GSH and GSSG. After treatment with the combination of Co and Ni, only glycolysis was significantly affected, leading to a higher gene expression of key enzymes involved in glucose import and metabolism and an enhanced intracellular lactate concentration, while the TCA cycle seems not to be affected by Co and Ni. The elevated expression of glucose transporter GLUT1 has been observed previously in nucleus pulposus cells under hypoxic conditions induced by Co [368]. These hypoxic conditions are also known to increase the lactate production by enhancing the expression of LDHA, as seen in Sertoli cells [369]. Both genes encoding for GLUT1 and LDHA contain hypoxia response element (HRE) sequences in their promotors [370,371]. During the conversion of pyruvate to lactate, LDHA catalyzes the oxidation of NADH to NAD^+ under anaerobic conditions [372]. Both Co and Ni, individually and combined, led to increased cellular lactate amount, which corresponded with increased LDHA gene expression and NAD^+ levels in HepG2 cells. This higher glucose uptake rate and lactate production is characteristic for hypoxic cancer cells, supporting tumor growth and cell proliferation [373]. Both metals, especially in combination, activate the Nrf2 response pathway. This is consistent with the tested concentrations, which are non-toxic in HepG2 cells and only the combination of

25 µM Co and 150 µM Ni leads to higher rates of apoptosis and necrosis, suggesting the cells are able to counteract the effects caused by Co and Ni under certain conditions. To verify the significance of Nrf2 in Co and Ni toxicity, it would be essential to utilize Nrf2 knockdown HepG2 cells. This approach would allow for the investigation of Nrf2-related pathways following Co and Ni treatment, facilitating a comparison with the findings from these studies.

Sphingolipids play crucial roles in cellular processes, such as influencing cellular membrane structures, interacting with the extracellular matrix and acting as second messengers in cellular signaling [374]. A metabolomic study in HepaRG cells revealed significant alterations in sphingolipid biosynthesis and metabolism, particularly due to Co exposure [269]. Additionally, transcriptomic analysis showed that the combination of Co and Ni impacted the lipid metabolism of HepG2 cells. This prompted us to investigate key intermediates and metabolites of sphingolipid metabolism. Exposure to Co and Ni, both individually and in combination, resulted in increased formation of dhCer across all species, consistent with the elevated gene expression of Cers1, which specifically forms C18:0 dhCer [247]. Next to this, Co and Ni exposure led to increased dhSM formation but decreased levels of Sph and LacCer. Similar results were observed under hypoxic conditions in mouse embryonic fibroblasts with DEGS1 knockdown. DEGS1 catalyzes the formation of Cer from dhCer, suggesting that Co and Ni may inhibit this enzyme. These effects were associated with altered mitochondrial morphology, lower oxygen consumption rates, and impaired ATP synthesis, underscoring the importance of sphingolipids as essential membrane components [271]. DEGS1 deficiency is also linked to changes in cholesterol metabolism, phospholipid metabolism, and biogenesis of lipid droplets [375]. To our knowledge, this study is the first to investigate sphingolipid metabolism in relation to Co and Ni toxicity, and sphingolipids are rarely targeted in toxicological studies of other metals. Therefore, it is crucial to clarify these mechanisms, as sphingolipid metabolism appears to be a sensitive endpoint for Co and Ni toxicity,

even at the lowest applied concentrations. Given the important impact of sphingolipids on mitochondrial health, further elucidation of Co and Ni toxicity effects is necessary, as these metals are implicated in mitochondrial dysfunction [54,376]. There are several possibilities to study mitochondrial activity in cells. The first endpoint is the mitochondrial membrane potential, crucial for ATP production, which can be measured using fluorescent dyes such as JC-1 or tetramethylrhodamine methyl ester (TMRM) [377,378]. Mitochondrial respiration can be assessed by measuring the oxygen consumption rate using a Seahorse Analyzer or Oroboros instrument. Oroboros combines this with monitoring ROS production, mitochondrial membrane potential, ATP production, Ca^{2+} concentration, and pH measurement [379]. Additionally, assessing the integrity and quantity of mitochondrial DNA (mtDNA), for example by measuring mtDNA copy number, is important [380]. Electron microscopy can provide insights into mitochondrial health by comparing mitochondrial shape and network structure [381]. Furthermore, sphingolipids play an essential role in brain function and development by supporting neuronal differentiation, myelin stability, and synaptic transmission within neuronal-glial connections. Alterations in sphingolipid metabolism are implicated in the development of various neurological diseases [382]. Therefore, it is essential to investigate sphingolipid alterations following Co and Ni exposure in astrocytes or neuronal cells to elucidate potential neurotoxic effects.

Diacylglycerols (DAGs) act as second messengers, and alterations in their occurrence can significantly impact cellular health. Exposure to Co and Ni, both individually and in combination, resulted in increased cellular DAG concentrations, particularly those with two saturated fatty acids. This increase is associated with the activation of PKC, which has been shown to enhance the cellular glucose uptake [383]. In HeLa cells, hypoxia induced an accumulation of DAGs, mainly driven by the activity of phosphatidylcholine phospholipase C and sphingomyelin synthase (PC-PLC/SMS) activity [384]. Similarly, in mesenchymal

stem cells, hypoxia-induced DAG accumulation was also reported, along with increases in triglycerides and fatty acids, suggesting Co and Ni may impact other lipid classes as well [280].

Both Co and Ni were extensively transferred into the nucleus, suggesting that both metals may have a genotoxic potential. We investigated their impact on the DNA, identifying significant effects mainly at high concentrations, which were already cytotoxic to HepG2 cells. However, the combination of 25 µM Co and 150 µM Ni also led to notable alterations compared to their single incubation. Treatment with the ROS-inducing Co and its combination with Ni resulted in an induction of FPG-sensitive sites, indicating the occurrence of oxidatively altered purines like 8-oxodG. Ni, which did not induce ROS formation or GSH/GSSG alterations, showed no effect in the alkaline or FPG-modified comet assay. In mammalian cells, 8-oxodG is removed via the base excision repair pathway, initiated by 8-oxoguanine DNA glycosylase-1 (OGG1) [385]. Nrf2 knockdown in HEK293 cells showed a significant decreased OGG1 protein expression, confirming that Nrf2 plays a crucial role in regulating OGG1 activity [386]. This suggests that the Co- and Ni-induced Nrf2 activation protects cells against oxidative DNA damage by enhancing the antioxidative capacity and activating repair mechanisms. To verify this hypothesis, future studies should employ Nrf2 knockdown cells to investigate the genotoxic effects of Co and Ni in absence of Nrf2. However, these protective pathways can be exhausted, leading to the formation of 8-oxodG after treatment with higher Co concentrations starting at 100 µM and the combination of 25 µM Co and 150 µM Ni. Exposure to 500 µM Co led to the formation of single-strand breaks, while high Ni concentrations increased the γ-H2AX expression, indicating cellular double-strand breaks. In human colon cancer cells, treatment with sub-lethal doses of Ni did not alter the expression of γ-H2AX compared to control [387]. However, in these cells but with a Nrf2 knockdown, the same concentrations significantly increased double-strand breaks compared to the normal cells. It was also reported that the exposed

Nrf2 knockdown cells showed an upregulation of genes associated with oxidative stress and inflammation and downregulation of DNA repair-related genes [387]. This leads to the assumption that Nrf2 also acts protective at DNA strand breaks, and this should be further investigated regarding Co and Ni toxicity by using Nrf2 knockdown cells. The downregulation of DNA repair genes was observed for Ni in different cancer cell lines, particularly those genes involved in the homology-directed DNA double-strand break repair, but only for highly cytotoxic Ni doses [296]. Both Co and Ni induced chromosomal damage, as evidenced by the increased number of micronuclei. This effect was predominantly observed following exposure to highly cytotoxic concentrations of Co and Ni individually. However, enhanced micronuclei formation was also detected after combined exposure to 25 µM Co and 150 µM Ni, concentrations that exhibited only a beginning cytotoxicity in HepG2 cells. Notably, single treatment with 25 µM Co or 150 µM Ni did not induce significant formation of micronuclei, indicating a synergistic effect of the combined metal exposure. Specifically, Co has been reported to cause chromosomal instability in different cell lines by inducing chromatid lesions [284,298]. Treatment with Co and Ni also resulted in the increased formation of multinucleated cells, even at non-cytotoxic concentrations, indicating a defective cell division or an enhanced cell fusion [388]. Both metals were associated with an altered cell cycle, primarily causing a G2/M phase arrest [60,303]. This arrest likely inhibits cytokinesis, the final stage of cell division [304]. A functional lipid metabolism is essential for cytokinesis, which was altered by Co and Ni as mentioned earlier. The inhibition of cholesterol biosynthesis is linked to a cytokinesis failure, and sphingolipids were also observed to regulate multinuclear cell formation by inhibiting cytokinesis [389,390]. An overexpression of PKC, induced by elevated DAG levels, resulted in the accumulation of cells in the G2/M cell cycle phase, inhibition of cytokinesis, and enhanced multinucleation [391,392]. This suggests a connection between the enhanced DAG levels and increased multinucleated cells, both caused by Co and Ni, with altered sphingolipid metabolism also

playing a key role in the affected cell cycle. Future studies should explore these interconnections in response to Co and Ni treatment, especially focusing on the cell cycle phases and cell fusion.

Both Co and Ni, individually and in combination, activated the DNA damage response pathway PARylation. This activation indicates a DNA damaging potential for both metals, even at the lowest concentrations tested. In BEAS-2B cells, treatment with Co significantly induced DNA damage after 2 h incubation, while no alterations were observed after 24 h [293]. This suggests that the induced DNA damage might be repaired during the long-term exposure and future studies should address a shorter exposure scenario to compare them with the results of this work. Additionally, PARP-1 is reported to be activated under hypoxic conditions, subsequently leading to HIF-1α stabilization [393]. Hypoxia is known to promote genomic instability without causing direct DNA damage, but by downregulating repair pathways, suggesting this as a possible mechanism for Co and Ni [394]. PARP-1 plays a crucial role in apoptotic cell death, as it gets cleaved by caspase-3 under highly cytotoxic conditions, which diminishes its ability for DNA repair [305]. In HepG2 cells, caspase-3 was induced following treatment with high Co and Ni concentrations starting at 100 µM Co and 500 µM Ni, but also with the combination of both metals. Apoptosis is a process requiring energy, leading to a higher consumption of ATP, as observed after exposure to 500 µM Co, which led to the highest caspase-3 activity [395]. At this concentration, no PARylation was observed in HepG2 cells, assuming that PARP-1 was cleaved by caspase-3. Future studies should verify this hypothesis by quantifying the resulting fragments via western blot analysis [396]. The corresponding decrease in ATP levels and increase in AMP suggests that Co may activates the AMP-activated protein kinase (AMPK), leading to autophagy [309]. Another ATP consuming process is the GSH synthesis, which is enhanced by Co and Ni, as mentioned earlier. GSH metabolism is known to be involved in the activation of autophagy, as well as promoting apoptosis [397].

In conclusion, this research provides new insights into the toxicity mechanisms of Co and Ni in mammalian cells, especially focusing on their combined effects. A significant limitation of these studies is the use of cancer cell lines, since they mostly exhibit aberrant cellular functions and altered gene expression profiles [398]. This deviation from normal cellular physiology necessitates the investigation of Co and Ni toxicity in primary cells to validate and compare our findings. However, cancer cell lines offer notable advantages, including high reproducibility and ease of use, thereby providing valuable insights into metal toxicity mechanisms. The results demonstrated a complex interaction between Co and Ni during combined exposure, leading to altered cellular metal content, a greater number of differentially expressed genes, and increased toxicity compared to individual treatments. Both metals, individually and combined, activated the Nrf2 signaling pathway, impacting GSH and iron metabolism, as well as glycolysis. Notable alterations were observed in sphingolipid and DAG metabolism, which have significant implications for mitochondrial function. At high concentrations, Co and Ni exhibited genotoxic potential, but through different mechanisms. Co exposure induced RONS, altered the GSH/GSSG ratio, and caused oxidative DNA damage. In contrast, Ni exposure primarily led to DNA double-strand breaks. Both metals contributed to chromosomal instability, multinucleation, and increased apoptosis rates. Future research should aim to elucidate the detailed transport mechanisms of Co and Ni to better estimate the risks associated with combined exposure. Understanding the effects of combined toxicity is particularly crucial, since the higher number of differential expressed genes compared to the single treatment indicates a complex mechanism. Additionally, further investigation to the impact on mitochondrial function and DNA damage repair pathways, including the role of Nrf2, is essential to expand on the findings of this thesis and fully understand the complex interplay of Co and Ni in cellular toxicity upon oral exposure. Given that Co is an essential component of vitamin B12, which is widely supplemented, it would be interesting to investigate the effects of vitamin B12 on human cells for comparison with our findings.

8.3. Impact of Co and Ni on the cellular mechanisms of *Paramecium tetraurelia*

Given that both Co and Ni are environmental pollutants, investigating their toxicological risks on organisms of the aquatic ecosystem is crucial. Therefore, we examined the uptake and toxicity mechanisms of Co and Ni using the ciliate *Paramecium*, comparing individual and combined treatment. Additionally, their feeding bacteria *Klebsiella planticola* were included, to gain insights into the initial stages of the food chain.

Paramecia exhibited higher sensitivity towards Ni than to Co, despite similar cellular metal levels with both metals. This contrasts with the mammalian cells, where Co induced greater cytotoxic effects with concurrent enhanced cellular levels compared to Ni. The toxicity of both metals increased in starved paramecia, correlating with higher metal uptake in the absence of food. In *Klebsiella* the cellular amount of both metals was dependent on the incubated concentration. Lower concentrations (100 µM) led to a higher uptake of Co, while higher concentrations (600 µM) favored Ni uptake. After feeding incubated *Klebsiella*, paramecia showed increased metal amount and alterations following combined treatment, indicating that food bacteria affect the metal uptake inside the food chain. This suggests that Co and Ni uptake in paramecia occurs through both phagocytotic and phagocytosis-independent mechanisms. Joint treatment of Co and Ni in paramecia resulted in increased toxicity compared to single metal exposure, without alterations in cellular Co amount. Interestingly, Ni levels were decreased when combined with 100 µM and 600 µM Co. This effect was also observed in mammalian cells, but in this case the Ni deprivation was constant with increased cellular Co amount. Previous studies on various ciliate protozoa strains have shown that the combined treatment of the metals Cd and Zn influences their toxic effects and bioaccumulation compared to the single incubation. It is known that ciliates possess specific metallothioneins which mediate the transport of these metals [399]. A genomic analysis of *P. tetraurelia*

has identified several transport proteins involved in various metabolic processes, but these proteins have not been characterized for specific metals [400]. To our knowledge, the exact transport mechanism of Co and Ni in paramecia is still elusive, thus further research should focus on identifying these pathways.

Transcriptomic analysis was employed to identify pathways specific for single metal exposure and to understand the alterations following combined treatment with Co and Ni in paramecia. Exposure to Co, both individually and the combination of Ni and high Co concentration, resulted in the upregulation of the GO term ‘cellular amino acid metabolism’ and a downregulation of the GO term ‘tetrahydrobiopterin biosynthesis’. Additionally, genes associated with the GO term ‘ammonium transmembrane transport’ were downregulated following treatment with both metals, either alone or in combination. These findings suggest alterations in amino acid-related pathways, primarily induced by Co exposure. Amino acids are essential not only for protein synthesis but also play vital roles in glycolysis, the TCA cycle, ATP generation, and as precursors for compounds like GSH [401]. Tetrahydrobiopterin functions as a cofactor involved in the conversion of amino acids to precursors of neurotransmitters and is required for the production of nitric oxide (NO) [402]. Therefore, future studies should focus on clarifying specific altered amino acids to better understand the pathways affected by Co and Ni. Our newly developed LC-MS/MS method, which includes analytes of glycolysis, the TCA cycle, and GSH metabolism, could be adapted for paramecia to facilitate this research. Ni exposure mainly led to the downregulation of genes related to the GO terms ‘inositol synthetic process’ and ‘phospholipid biosynthetic process’. Inositol compounds, including the phospholipid phosphatidylinositol, are important for membrane biogenesis, signal transduction, DNA repair, and energy metabolism [403]. Disruption in the synthesis and homeostasis of these compounds can lead to a wide range of cellular disorder, suggesting that Ni exposure may alter membrane composition and associated signaling pathways. For both metals, an effect in the GO term

‘glutathione biosynthetic stress’ was observed, mainly caused by an upregulation of the glutamate-cysteine ligase, an enzyme taking part in the GSH synthesis [79]. This indicates that both metals are causing redox stress in paramecia, which was also observed in the mammalian cells, especially after Co exposure. In HepG2 cells, combined exposure to Co and Ni resulted in the upregulation of the glutamate-cysteine ligase. Further transcriptomic changes were noted in genes related to glutaredoxin, pyridine nucleotide disulfide oxidoreductase, and thioredoxin, which are pivotal systems for maintaining cellular redox state [404]. Both metals seem to cause transcriptomic changes in genes related to DNA repair mechanisms, consistent with previous literature suggesting that especially Ni inhibits DNA repair [60]. This points to potential genotoxic effects of Co and Ni exposure. To gain a deeper understanding of the pathways affected by Co and Ni, which were revealed via transcriptomic analysis, further detailed studies are necessary. This should specifically include redox stress endpoints, glutathione metabolism, and genotoxic effects. For this, methods and techniques used in the HepG2 cells, such as the developed LC-MS/MS method for GSH and GSSG quantification and the method addressing the glycolysis and TCA cycle, should be adapted for use in paramecia. This will facilitate a comprehensive comparison of results across different testing systems and provide insights into the similarities and differences in metal toxicity mechanisms between these models.

In conclusion, paramecia exhibited higher sensitivity to Ni than to Co, despite similar cellular metal levels. This finding contrasts with observations in mammalian cells, where Co induced greater cytotoxic effects. This highlights the differential impacts of metal toxicity on mammals and the ecosystem, underlining the necessity of investigating both to comprehensively understand the effects on human health and the environment. Combined Co and Ni treatment led to higher toxicity in paramecia without altering cellular Co levels but decreased Ni levels, suggesting an interaction in their bioaccumulation. Transcriptomic analysis

revealed both distinct and shared pathways affected by Co and Ni, primarily involving redox stress and DNA repair mechanisms. Additionally, bacteria can take up both metals, facilitating their entry into the food web and subsequent accumulation in organisms such as paramecia. Further research is needed especially to characterize the effects of combined Co and Ni exposure, as this represents a realistic environmental scenario.

Appendix

Supplementary Material

Appendix – Supplementary Material

Supplementary Material for Chapter 4: Single is not combined: the role of Co and Ni bioavailability on toxicity mechanisms in liver and brain cells

Table 8: Detailed data of cytotoxicity tests in HepG2 and CCF-STTG1 cells after incubation with Co and Ni in single and combined exposure. All results are compared to untreated control.

HepG2	Hoechst				Resazurin			
	significant at		EC_{70}		significant at		EC_{70}	
	24 h	48 h	24 h	48 h	24 h	48 h	24 h	48 h
Co(II)	50 µM	25 µM	150 µM	25 µM	200 µM	50 µM	750 µM	300 µM
Ni(II)	300 µM	150 µM	500 µM	200 µM	300 µM	300 µM	1000 µM	750 µM
150 µM Ni(II) + variable Co(II)	25 µM		150 µM		150 µM		-	
25 µM Co(II) + variable Ni(II)	100 µM		300 µM		500 µM		1000 µM	

CCF-STTG1	Hoechst				Resazurin			
	significant at		EC_{70}		significant at		EC_{70}	
	24 h	48 h	24 h	48 h	24 h	48 h	24 h	48 h
Co(II)	-	900 µM	-	900 µM	1000 µM	750 µM	-	-
Ni(II)	750 µM	900 µM	-	900 µM	300 µM	300 µM	-	900 µM
600 µM Ni(II) + variable Co(II)	1000 µM		-		25 µM		-	
100 µM Co(II) + variable Ni(II)	-		-		750 µM		-	

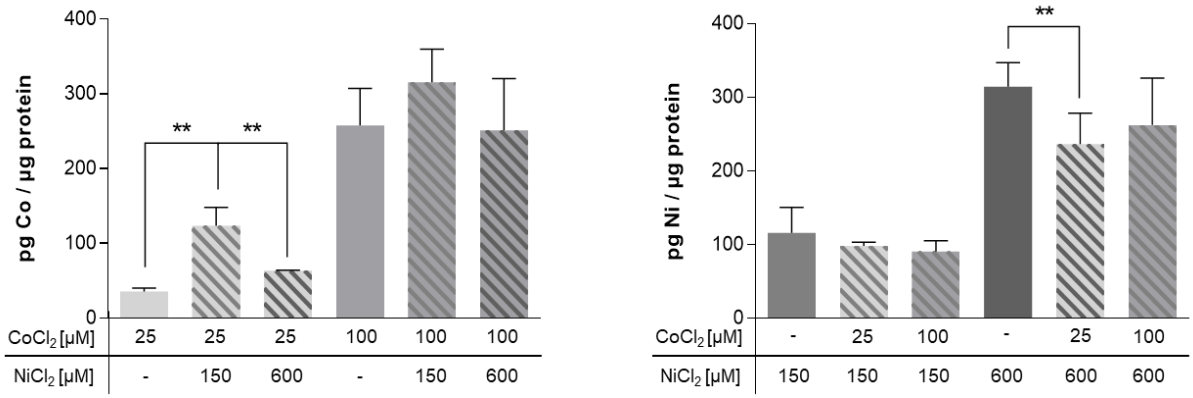

Figure 44: Bioavailability of Co and Ni in CCF-STTG1 cells after 24 h incubation in combined exposure compared to single treatment. Cellular metal content was measured via ICP-OES after single or combined treatment with Co and Ni. Data is presented as mean + SD of n ≥ 3 independent experiments. Statistical significance was tested by an unpaired t-test with Welch's correction depicted as **p≤0.01: single treatment compared to combined exposure.

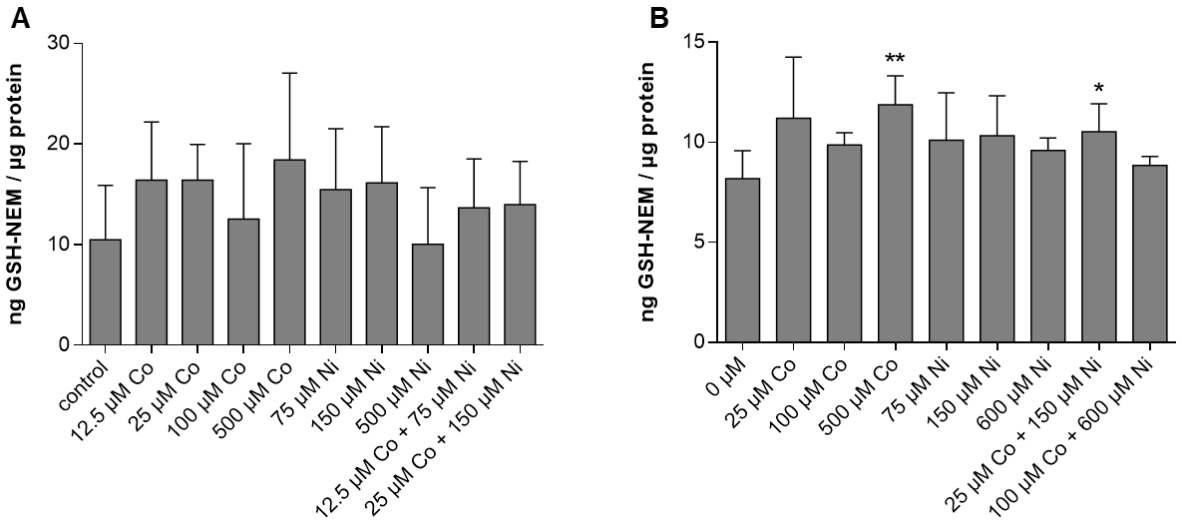

Figure 45: Cellular GSH level after 24 h single and combined incubation of Co and Ni in HepG2 cells (A) and CCF-STTG1 cells (B). GSH amount was quantified using LC-MS/MS. Data is presented as mean + SD of n ≥ 3 independent experiments. Statistical significance was tested by an unpaired t-test with Welch's correction depicted as *p≤0.05, **p≤0.01: compared to untreated control.

Supplementary Material for Chapter 5: Transcriptomics Pave the Way into Mechanisms of Cobalt and Nickel Toxicity: Nrf2-Mediated Cellular Responses in Liver Carcinoma Cells

Quantification of metabolites related to glycolysis, TCA cycle and GSH metabolism by HPLC-MS/MS

LC-MS/MS parameters

Eluent A comprised bidistilled water with 10 mM ammonium bicarbonate and 10 mM formic acid (FA) (LC-MS grade, fisher chemicals), while eluent B consisted of acetonitrile (LC-MS grade, VWR) with 10 mM FA. After injecting 2 µL of the sample, the gradient started at 90 % - 40 % eluent B for 10 min, followed by a return to 90 % eluent B in 0.5 min and additional 9.5 min at 90 % eluent B for column equilibration. At a flow rate of 0.25 mL/min the total run time was 20 min. Ion source parameters were conducted as follows: entrance potential (EP) 10.0 V; curtain gas (CUR) 40.0 psi; collision gas (CAD) medium; ion spray voltage (IS) 3000.0 V; temperature (TEM) 500 °C; ion source gas 1 and 2 (GS1 and 2) 40.0 psi and 50.0 psi for analytes in positive mode and entrance potential (EP) 10.0 V; curtain gas (CUR) 40.0 psi; collision gas (CAD) 6.0; ion spray voltage (IS) -4500.0 V; temperature (TEM) 550 °C; ion source gas 1 and 2 (GS1 and 2) 70.0 psi for analytes in negative mode. The dwell time was set at 35 ms for all analytes. All mass transitions and the optimized collision energy (CE), collision cell exit potential (CXP) and declustering potential (DP) for each analyte are displayed in table 9 and 10.

Table 9: Mass spectrometry parameters of analytes measured in negative ion mode. Shown are the quantifier (*) and qualifiers for analyte identification.

Analyte	Fragmentation [*m/z*]	Collision energy [V]	Collision cell exit potential [V]	Declustering potential [V]
Glucose	179 > 89*	-14	-13	-30
	179 > 119	-10	-13	-16
	179 > 59	-23	-9	-52
	179 > 71	-29	-8	-52
Lactate	89 > 43*	-14	-18	-31
	89 > 71	-15	-10	-42
Pyruvate	87 > 32*	-11	-5	-12
	87 > 43	-10	-6	-16
α-Ketoglutarate	145 > 57*	-15	-22	-33
	145 > 101	-11	-11	-26
	145 > 73	-15	-39	-21
	145 > 83	-18	-14	-17
Succinate	117 > 73*	-16	-16	-16
	117 > 99	-14	-14	-24
	117 > 59	-14	-7	-12
Malate	133 > 115*	-14	-8	-22
	133 > 71	-16	-12	-21
	133 > 89	-17	-12	-13
	133 > 43	-29	-21	-13

Table 10: Mass spectrometry parameters of analytes measured in positive ion mode. Shown are the quantifier (*) and qualifiers for analyte identification.

Analyte	Fragmentation [*m/z*]	Collision energy [V]	Collision cell exit potential [V]	Declustering potential [V]
Glutamate	148 > 84*	16	19	27
	148 > 102	14	10	20
	148 > 130	21	10	22
Glutamine	147 > 130*	15	21	33
	147 > 84	22	13	16
	147 > 101	14	10	23
	147 > 59	18	6	10
Cysteine-NEM	247 > 230*	18	10	25
	247 > 201	18	18	36
	247 > 212	22	11	41
	247 > 184	27	9	42

Quantification of sphingolipids and diacylglycerols by HPLC-MS/MS

Table 11: HPLC-MS/MS parameters for quantification of sphingolipids.

Sphingolipid	Precursor ion (*m/z*)	Product ion (*m/z*) [a]	Retention time (min)	Calibration Reference Compound	Internal Standards
d_7-Sph (ISTD)	307.3 $[M+H]^+$	**289.3** / 259.3	5.4	-	-
d_7-dhSph (ISTD)	309.4 $[M+H]^+$	**291.3** / 261.3	5.7	-	-
d_7-S1P (ISTD)	387.3 $[M+H]^+$	**271.3** / 82.1	6.7	-	-
Sph	300.3 $[M+H]^+$	**282.3** / 252.3	5.4	-[b]	d_7-Sph
dhSph	302.3 $[M+H]^+$	**284.3** / 254.3	5.7	-[b]	d_7-dhSph
S1P	380.3 $[M+H]^+$	**264.3** / 82.1	6.7	-[b]	d_7-S1P
C16:0 dhCer	540.5 $[M+H]^+$	**522.6** / 284.3	13.7	C16:0 dhCer	C17:0 Cer
C18:0 dhCer	568.5 $[M+H]^+$	**550.5** / 284.3	15.6	C18:0 dhCer	C17:0 Cer
C20:0 dhCer	596.6 $[M+H]^+$	**578.6** / 284.3	17.9	C18:0 dhCer	C17:0 Cer
C22:0 dhCer	624.6 $[M+H]^+$	**606.6** / 284.3	20.7	C24:0 dhCer	C17:0 Cer
C24:0 dhCer	652.7 $[M+H]^+$	**634.6** / 284.3	24.0	C24:0 dhCer	C17:0 Cer
C24:1 dhCer	650.7 $[M+H]^+$	**632.7** / 284.3	21.0	C24:1 dhCer	C17:0 Cer
C17:0 Cer (ISTD)	534.5 $[M-H_2O+H]^+$	**264.3** / 282.3	14.0	-	-
C16:0 Cer	520.5 $[M-H_2O+H]^+$	**264.3** / 282.3	13.2	C16:0 Cer	C17:0 Cer
C18:0 Cer	548.5 $[M-H_2O+H]^+$	**264.2** / 282.3	14.9	C18:0 Cer	C17:0 Cer
C20:0 Cer	576.6 $[M-H_2O+H]^+$	**264.3** / 282.3	17.1	C20:0 Cer	C17:0 Cer
C22:0 Cer	604.6 $[M-H_2O+H]^+$	**264.3** / 282.3	19.8	C22:0 Cer	C17:0 Cer
C24:0 Cer	632.6 $[M-H_2O+H]^+$	**264.3** / 282.3	22.9	C24:0 Cer	C17:0 Cer
C24:1 Cer	630.6 $[M-H_2O+H]^+$	**264.3** / 282.3	20.0	C24:1 Cer	C17:0 Cer
C16:0 dhSM	705.6 $[M+H]^+$	**184.0** / 86.1	12.9	C16:0 SM	d_{31}-C16:0 SM
C18:0 dhSM	733.6 $[M+H]^+$	**184.0** / 86.1	14.6	C18:0 SM	d_{31}-C16:0 SM
C20:0 dhSM	761.6 $[M+H]^+$	**184.0** / 86.1	16.7	C20:0 SM	d_{31}-C16:0 SM
C22:0 dhSM	789.7 $[M+H]^+$	**184.0** / 86.1	19.3	C22:0 SM	d_{31}-C16:0 SM
C24:0 dhSM	817.7 $[M+H]^+$	**184.0** / 86.1	22.5	C24:0 SM	d_{31}-C16:0 SM
C24:1 dhSM	815.7 $[M+H]^+$	**86.1** / 184.0	19.4	C24:1 SM	d_{31}-C16:0 SM
d_{31}-C16:0 SM (ISTD)	734.6 $[M+H]^+$	**184.0** / 86.1	12.2	-	-
C16:0 SM	703.6 $[M+H]^+$	**184.0** / 86.1	12.3	C16:0 SM	d_{31}-C16:0 SM
C18:0 SM	731.6 $[M+H]^+$	**184.0** / 86.1	13.9	C18:0 SM	d_{31}-C16:0 SM
C20:0 SM	759.6 $[M+H]^+$	**184.0** / 86.1	16.0	C20:0 SM	d_{31}-C16:0 SM
C22:0 SM	787.7 $[M+H]^+$	**184.0** / 86.1	18.1	C22:0 SM	d_{31}-C16:0 SM
C24:0 SM	815.7 $[M+H]^+$	**184.0** / 86.1	21.0	C24:0 SM	d_{31}-C16:0 SM
C24:1 SM	813.7 $[M+H]^+$	**86.1** / 184.0	18.2	C24:1 SM	d_{31}-C16:0 SM
C17:0 Glucosyl-Cer (ISTD)	714.6 $[M+H]^+$	**264.2** / 696.6	12.7	-	-
C16:0 Hexosyl-Cer	700.6 $[M+H]^+$	**264.2** / 682.6	12.0	C16:0 Hexosyl-Cer	C17:0 Glucosyl-Cer
C24:1 Hexosyl-Cer	810.7 $[M+H]^+$	**264.2** / 792.7	17.6	C24:1 Hexosyl-Cer	C17:0 Glucosyl-Cer
C17:0 Lactosyl-Cer (ISTD)	876.6 $[M+H]^+$	**264.3** / 534.5	12.2	-	-
C16:0 Lactosyl-Cer	862.6 $[M+H]^+$	**264.3** / 520.5	11.6	C16:0 Lactosyl-Cer	C17:0 Lactosyl-Cer
C24:1 Lactosyl-Cer	972.7 $[M+H]^+$	**264.3** / 630.7	16.6	C24:1 Lactosyl-Cer	C17:0 Lactosyl-Cer

[a] Quantifiers are given in bold

[b] Compound directly quantified *via* deuterated internal standard (one-point calibration)

Cer, ceramide; dhCer, dihydroceramide; dhSM, dihydrosphingomyelin; dhSph, dihydrosphingosine (sphinganine); ISTD, internal standard; S1P, sphingosine 1-phosphate, Sph, sphingosine; SM, sphingomyelin

Table 12: HPLC-MS/MS parameters for quantification of diacylglycerols.

Diacylglycerol	Precursor ion (*m/z*)	Product ion (*m/z*) [a]	Retention time (min)	Calibration Reference Compound	Internal Standard
d_5-C17:0 / C17:0 (ISTD)	584.6 $[M\text{-}H_2O+H]^+$	**57.2** / 253.2	18.0	-	-
C16:0 / C16:0	551.5 $[M\text{-}H_2O+H]^+$	**57.2** / 239.2	15.2	C16:0 / C16:0	d_5-C17:0 / C17:0
C18:0 / C18:0	607.6 $[M\text{-}H_2O+H]^+$	**57.2** / 267.3	21.0	C18:0 / C18:0	d_5-C17:0 / C17:0
C16:0 / C18:0	579.5 $[M\text{-}H_2O+H]^+$	**239.2** / 267.3	18.0	C16:0 / C16:0	d_5-C17:0 / C17:0
C16:0 / C18:1	612.6 $[M+NH_4]^+$	**313.3** / 339.3	16.1	C16:0 / C18:1	d_5-C17:0 / C17:0
C16:0 / C18:2	610.5 $[M+NH_4]^+$	**313.3** / 337.3	14.3	C18:0 / C20:4	d_5-C17:0 / C17:0
C18:0 / C18:1	640.6 $[M+NH_4]^+$	**341.3** / 339.3	19.0	C16:0 / C18:1	d_5-C17:0 / C17:0
C18:0 / C18:2	638.6 $[M+NH_4]^+$	**341.3** / 337.3	17.2	C18:0 / C20:4	d_5-C17:0 / C17:0
C18:0 / C20:4	662.6 $[M+NH_4]^+$	**341.3** / 361.3	17.0	C18:0 / C20:4	d_5-C17:0 / C17:0
C18:1 / C18:1	638.6 $[M+NH_4]^+$	**339.3** / 57.2	17.0	C18:0 / C20:4	d_5-C17:0 / C17:0
C18:1 / C18:2	636.6 $[M+NH_4]^+$	**339.3** / 337.3	15.2	C18:0 / C20:4	d_5-C17:0 / C17:0

[a] Quantifiers are given in bold

ISTD, internal standard

Gene expression values of pathways related to Nrf2

Table 13: Gene expression values of relevant genes collected from DeSeq2 analysis for all tested concentrations of Co and Ni and their respective description.

gene	description	Differential Expression Log2 Ratio			
		25 µM Co	150 µM Ni	25 µM Co + 150 µM Ni	12.5 µM Co + 75 µM Ni
SLC2A1	solute carrier family 2 member 1	0.562	-0.244	0.785	0.654
SLC2A3	solute carrier family 2 member 3	1.682	1.546	1.953	1.511
SLC16A3	solute carrier family 16 member 3	0.727	0.821	1.048	0.768
HK1	hexokinase 1	1.057	1.097	2.297	2.185
HK2	hexokinase 2	0.932	0.833	0.891	0.599
G6PC1	glucose-6-phosphatase catalytic subunit 1	0.345	-0.395	-1.059	-0.288
GPI	glucose-6-phosphate isomerase	0.822	0.819	1.113	0.455
FBP1	fructose-bisphosphatase 1	-0.105	0.110	-0.336	0.253
ALDOA	aldolase, fructose-bisphosphate A	1.116	1.320	1.770	1.298
ENO1	enolase 1	1.082	1.196	1.417	1.366
ENO2	enolase 2	1.091	1.086	1.893	1.646
PKM	pyruvate kinase M1/2	0.965	0.791	1.244	1.193
LDHA	lactate dehydrogenase A	0.987	0.847	1.009	0.555

PGM1	phosphoglucomutase 1	0.609	0.346	0.192	0.395
GBE1	1,4-alpha-glucan branching enzyme 1	1.608	1.347	2.075	0.700
G6PD	glucose-6-phosphate dehydrogenase	-0.417	-0.472	-0.502	-0.430
PGD	phosphogluconate dehydrogenase	0.241	0.321	0.367	0.108
TKT	transketolase	0.317	0.596	0.562	0.580
TALDO1	transaldolase 1	0.252	0.556	0.692	1.033
CS	citrate synthase	-0.068	-0.289	-0.395	-0.438
ACO1	aconitase 1	-0.071	-0.193	-0.651	-0.609
ACO2	aconitase 2	0.003	-0.109	-0.087	-0.069
IDH1	isocitrate dehydrogenase 1	-0.347	-0.683	-1.049	-1.544
IDH2	isocitrate dehydrogenase 2	0.146	0.398	-0.264	0.416
SUCLG1	succinate-CoA ligase alpha	-0.200	0.080	-0.274	1.116
SUCLG2	succinate-CoA ligase beta	-0.056	-0.138	-0.545	-0.361
SDHA	succinate dehydrogenase A	0.042	-0.033	-0.312	0.493
SDHB	succinate dehydrogenase B	-0.240	-0.429	-0.461	-0.231
SDHC	succinate dehydrogenase C	0.109	-0.307	-0.064	0.221
SDCD	succinate dehydrogenase D	-0.162	-0.498	-0.408	-1.336
FH	fumarate hydratase	-0.272	-0.281	-0.765	-0.338
PDK1	pyruvate dehydrogenase kinase 1	1.763	1.327	1.832	0.891
PDHA1	pyruvate dehydrogenase E1 subunit alpha 1	-0.176	-0.203	-0.434	0.035
PDHA2	pyruvate dehydrogenase E1 subunit alpha 2	-0.022	-0.203	-0.310	-0.862
PDHB	pyruvate dehydrogenase E1 subunit beta	-0.055	-0.074	-0.303	0.194
GLS	glutaminase	-0.271	-0.595	-0.623	-1.893
GLS2	glutaminase 2	0.154	0.018	-0.057	0.302
GLUD1	glutamate dehydrogenase 1	-0.223	-0.256	-0.774	-0.955
GLUD2	glutamate dehydrogenase 2	-0.137	-0.466	-0.951	-2.118
SQSTM1	sequestosome 1	0.351	0.706	1.901	0.899
ULK1	unc-51 like autophagy activating kinase 1	0.272	0.426	0.735	0.687
ULK2	unc-51 like autophagy activating kinase 2	0.310	1.206	1.021	1.344
ACLY	ATP citrate lyase	-0.068	-0.218	-0.554	-0.607

ACACA	acetyl-CoA carboxylase alpha	-0.272	-0.236	-0.704	-0.481
ACACB	acetyl-CoA carboxylase beta	-0.017	0.162	-0.535	-0.236
FASN	fatty acid synthase	-0.305	0.010	-0.599	0.052
HMGCS1	3-hydroxy-3-methylglutaryl-CoA synthase 1	-0.385	-0.066	-1.116	-1.068
HMGCR	3-hydroxy-3-methylglutaryl-CoA reductase	-0.299	-0.591	-1.169	-1.739
SLC7A11 (xCT)	solute carrier family 7 member 11	0.555	0.884	1.043	-0.305
GCLM	glutamate-cysteine ligase modifier subunit	0.670	0.897	1.671	0.387
GCLC	glutamate-cysteine ligase catalytic subunit	0.668	1.077	1.031	-0.330
GSS	glutathione synthetase	-0.017	0.079	-0.196	0.285
FTH1	ferritin heavy chain 1	0.383	0.782	1.443	1.458
FTL	ferritin light chain	0.095	0.840	1.100	1.113
BLVRA	biliverdin reductase A	-0.085	-0.010	-0.052	0.274
BLVRB	biliverdin reductase B	0.581	1.292	2.320	2.210
HMOX1	heme oxygenase 1	0.716	0.875	2.550	0.966
FECH	ferrochelatase	0.277	0.156	0.076	-0.409
ABCB6	ATP binding cassette subfamily B member 6	0.647	0.670	0.979	1.244

Table 14: Gene expression values of relevant genes collected from DeSeq2 analysis regarding sphingolipid metabolism for all tested concentrations of Co and Ni and their respective description.

gene	description	Differential Expression Log2 Ratio			
		25 µM Co	150 µM Ni	25 µM Co + 150 µM Ni	12.5 µM Co + 75 µM Ni
SPTLC1	serine palmitoyltransferase long chain base subunit 1	0.025	-0.419	-0.257	-0.739
SPTLC2	serine palmitoyltransferase long chain base subunit 2	-0.004	-0.071	-0.022	-0.503
SPTLC3	serine palmitoyltransferase long chain base subunit 3	-0.518	-0.883	-1.602	-1.338
KDSR	3-ketodihydrosphingosine reductase	0.076	0.139	0.328	-0.256
CERS1	ceramide synthase 1	0.503	1.380	0.868	1.589
ASAH2B	N-acylsphingosine amidohydrolase 2B	-0.231	-0.296	-0.779	-0.697
DEGS1	delta 4-desaturase, sphingolipid 1	0.006	-0.295	0.093	-1.002
DEGS2	delta 4-desaturase, sphingolipid 2	0.225	0.441	0.488	0.885
SMPD1	sphingomyelin phosphodiesterase 1	-0.007	0.297	0.367	0.828
SGMS1	sphingomyelin synthase 1	-0.322	-0.383	-0.189	-0.690
SGMS2	sphingomyelin synthase 2	0.084	-0.254	0.336	-0.762
GALC	galactosylceramidase	-0.391	-0.453	-1.153	-1.988
UGT8	UDP glycosyltransferase 8	-0.037	0.120	0.153	0.591
UGCG	UDP-glucose ceramide glucosyltransferase	-0.136	-0.213	-0.129	-0.901
GBA	glucosylceramidase beta	0.182	-0.052	0.563	0.355
GBA2	glucosylceramidase beta 2	-0.013	-0.109	-0.413	-0.167
GBA3	glucosylceramidase beta 3	0.049	-0.549	-0.199	-1.183
B4GALT6	beta-1,4-galactosyltransferase 6	-0.291	-0.422	-0.646	-1.814
CERK	ceramide kinase	0.050	-0.075	-0.220	-0.507
SGPP1	sphingosine-1-phosphate phosphatase 1	-0.336	-0.872	-0.629	-1.675
SPHK1	sphingosine kinase 1	-0.136	0.132	-0.124	0.689
SGPL1	sphingosine-1-phosphate lyase 1	-0.168	-0.276	-0.405	-0.450

Supplementary figures

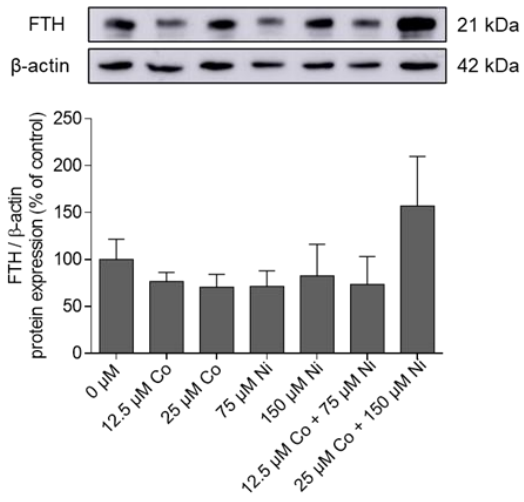

Figure 46: FTH protein levels in HepG2 cells after 24 h treatment with Co(II) and Ni(II). Protein expression was quantified via Western Blot and normalized to β-actin. Data is presented as mean + SD of n ≥ 3 independent experiments. Statistical significance was tested by an unpaired t-test.

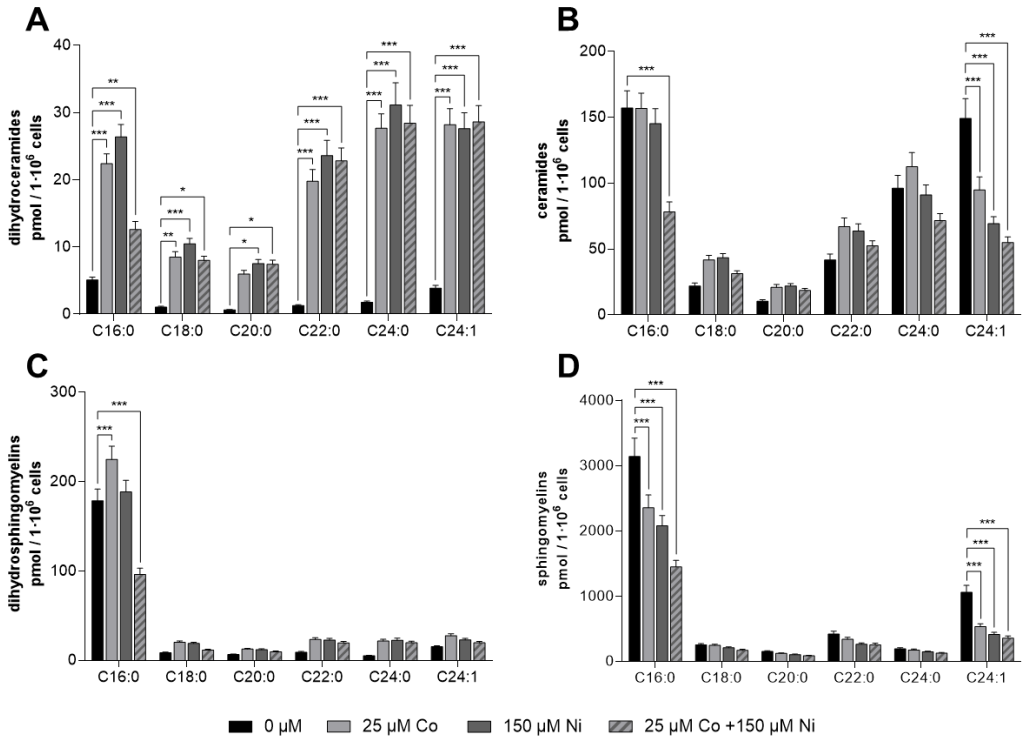

Figure 47: Quantification of dihydroceramides (A), ceramides (B), dihydrosphingomyelins (C) and sphingomyelins (D) content after individual or combined treatment with Co(II) and Ni(II) for 24 h in HepG2 cells. Sphingolipid levels were quantified using LC-MS/MS. Data is presented as mean + SD of n ≥ 3 independent experiments. Statistical significance was tested using Two-way ANOVA depicted as *p≤0.05, **p≤0.01, ***p≤0.001: compared to untreated control.

Supplementary Material for Chapter 6: Genotoxicity Assessment of Co(II) and Ni(II) in HepG2 Cells: Insights into Combined Metal Exposure

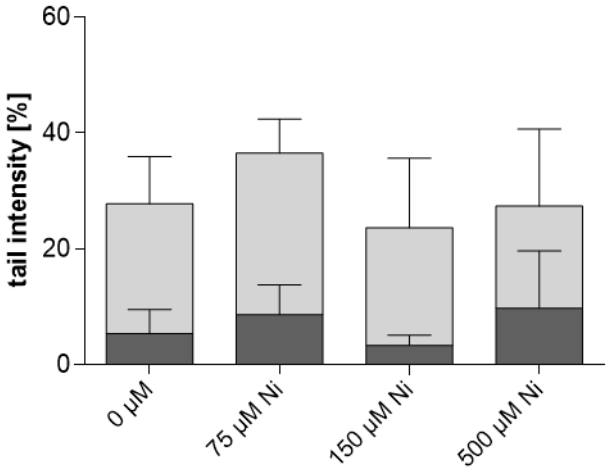

Figure 48: Genotoxic effects of Ni(II) in HepG2 cells after 24 h treatment assessed by comet assay analysis. Bottom bar: alkaline comet assay, top bar: FPG modified comet assay. Data is presented as mean + SD of n ≥ 3 independent experiments.

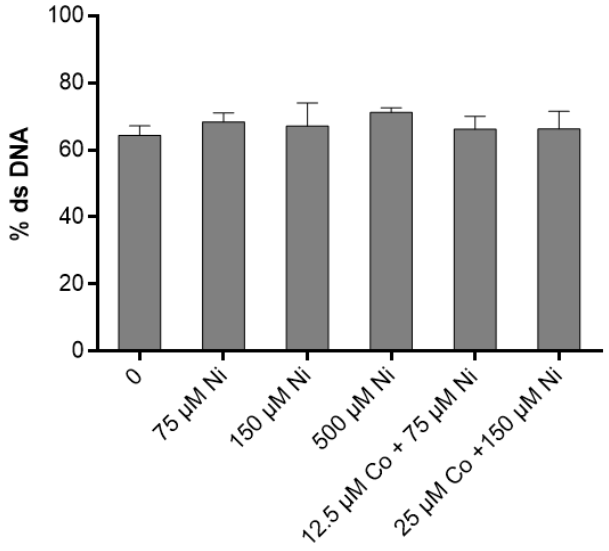

Figure 49: DNA strand breaks after 24 h of treatment with Ni(II) alone or in combination with Co(II) in HepG2 cells. A) The amount of dsDNA was determined via alkaline unwinding. Data is presented as mean + SD of n ≥ 3 independent experiments.

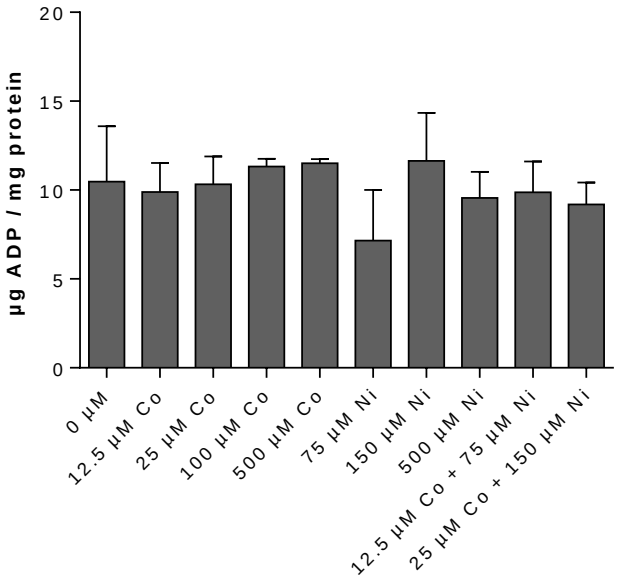

Figure 50: Energy related nucleotides after 24 h incubation of Co(II) and Ni(II) individually and combined in HepG2 cells. The amount of ADP was quantified via HPLC-DAD. Data is presented as mean + SD of n ≥ 3 independent experiments.

Supplementary Material for Chapter 7: Microbial impact to environmental toxicants Ni(II) and Co(II): Joint toxicity and cellular response in Paramecium

parameter	conditions
plasma power [W]	1500
cooling gas flow [L/min]	8.0
auxiliary gas flow [L/min]	0.2
nebulizer flow [L/min]	0.7
nebulizer	MicroMist™
torch alignment	axial
element wavelengths [nm]	Co: 238.892; Ni: 231.604; Y: 371.029
software analysis	Syngistix™

Figure 51: ICP-OES measurement parameters.

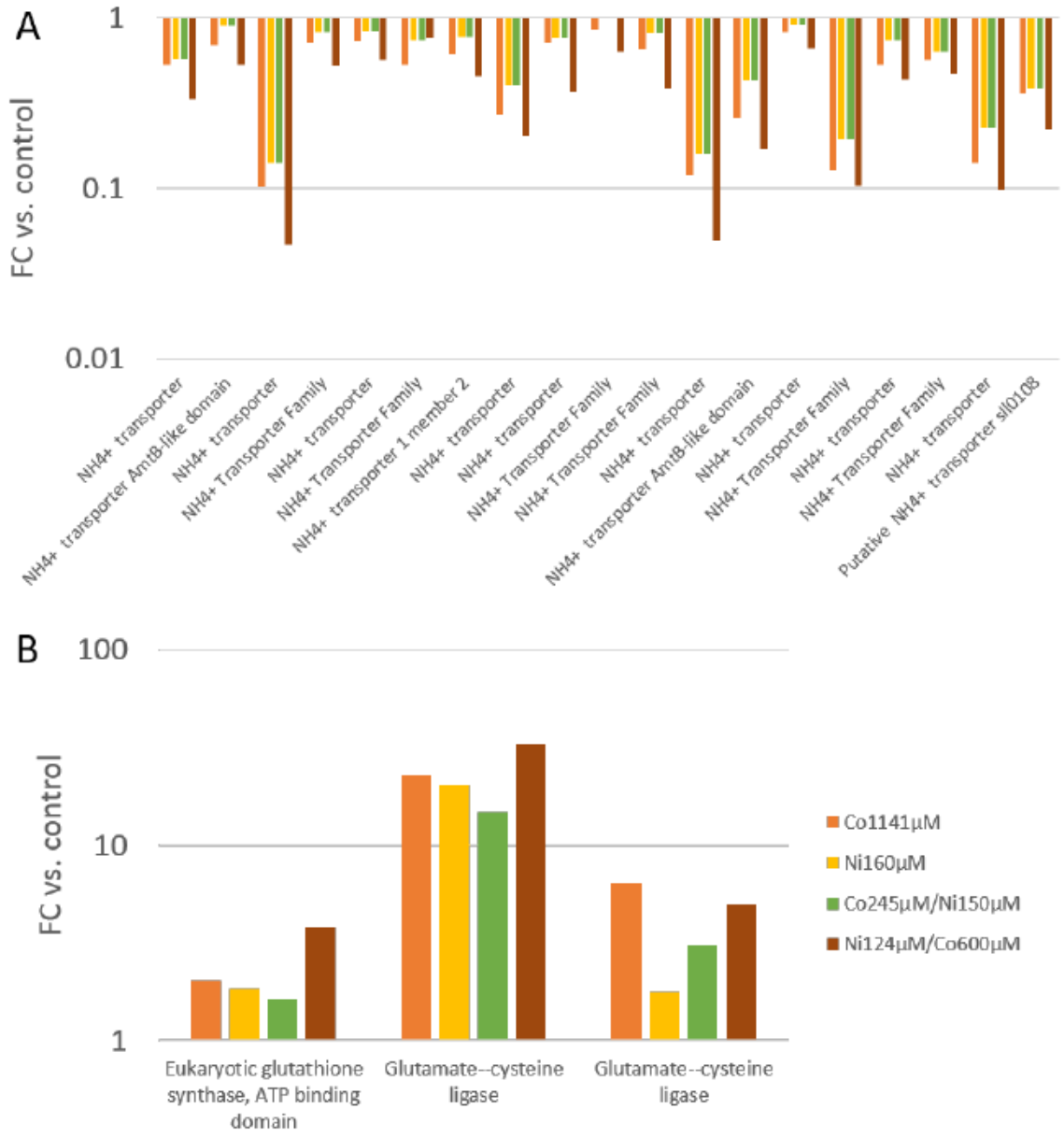

Figure 52: Deeper analysis of A. GO:0072488 Ammonium transmembrane transport with 19 genes and B. GO:0006750 Glutathione biosynthetic process with 3 genes. Both bar plots show the Fold change of mean TPM of annotated genes in relation to control treatment in logarithmic scales. A fold change of more than 1 means up-regulation, below 1 indicates down-regulation.

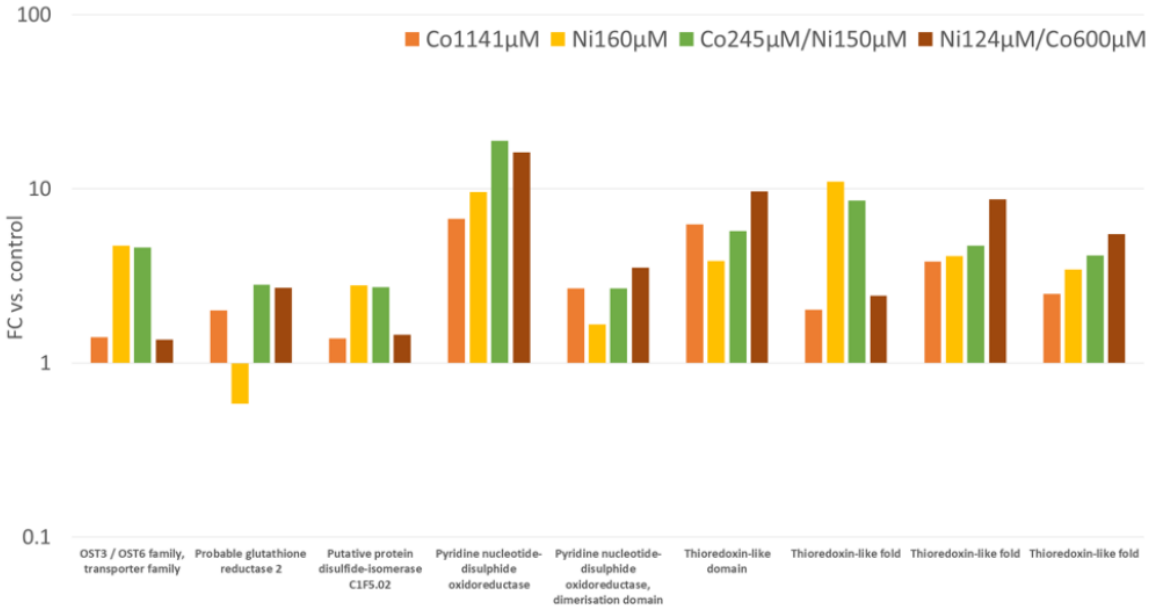

Figure 53: Deeper insight in the genes of the GO:0045454 Cell Redox Homeostasis. Bar diagram showing the fold change of the mean of TPM of individual genes of the GO term in all four treatments including the joint exposures.

References

[1] G. Genchi, A. Carocci, G. Lauria, M.S. Sinicropi, A. Catalano, Nickel: Human Health and Environmental Toxicology, Int. J. Environ. Res. Public Health 17 (2020). https://doi.org/10.3390/ijerph17030679.

[2] L. Leyssens, B. Vinck, C. van der Straeten, F. Wuyts, L. Maes, Cobalt toxicity in humans-A review of the potential sources and systemic health effects, Toxicology 387 (2017) 43–56. https://doi.org/10.1016/j.tox.2017.05.015.

[3] P. Dolara, Occurrence, exposure, effects, recommended intake and possible dietary use of selected trace compounds (aluminium, bismuth, cobalt, gold, lithium, nickel, silver), Int. J. Food Sci. Nutr. 65 (2014) 911–924. https://doi.org/10.3109/09637486.2014.937801.

[4] K. Sule, J. Umbsaar, E.J. Prenner, Mechanisms of Co, Ni, and Mn toxicity: From exposure and homeostasis to their interactions with and impact on lipids and biomembranes, Biochim. Biophys. Acta Biomembr. 1862 (2020) 183250. https://doi.org/10.1016/j.bbamem.2020.183250.

[5] B.E. Tvermoes, D.J. Paustenbach, B.D. Kerger, B.L. Finley, K.M. Unice, Review of cobalt toxicokinetics following oral dosing: Implications for health risk assessments and metal-on-metal hip implant patients, Crit. Rev. Toxicol. 45 (2015) 367–387. https://doi.org/10.3109/10408444.2014.985818.

[6] D. Schrenk, M. Bignami, L. Bodin, J.K. Chipman, J. Del Mazo, B. Grasl-Kraupp, C. Hogstrand, L.R. Hoogenboom, J.-C. Leblanc, C.S. Nebbia, E. Ntzani, A. Petersen, S. Sand, T. Schwerdtle, C. Vleminckx, H. Wallace, T. Guérin, P. Massanyi, H. van Loveren, K. Baert, P. Gergelova, E. Nielsen, Update of the risk assessment of nickel in food and drinking water, EFSA J. 18 (2020) e06268. https://doi.org/10.2903/j.efsa.2020.6268.

[7] L.O. Simonsen, H. Harbak, P. Bennekou, Cobalt metabolism and toxicology--a brief update, Sci. Total Environ. 432 (2012) 210–215. https://doi.org/10.1016/j.scitotenv.2012.06.009.

[8] D. Beyersmann, A. Hartwig, Carcinogenic metal compounds: recent insight into molecular and cellular mechanisms, Arch. Toxicol. 82 (2008) 493–512. https://doi.org/10.1007/s00204-008-0313-y.

[9] M.S. Moats, W.G. Davenport, Nickel and Cobalt Production, in: Treatise on Process Metallurgy, Elsevier, 2014, pp. 625–669.

[10] X. Sun, X. Luo, Z. Zhang, F. Meng, J. Yang, Life cycle assessment of lithium nickel cobalt manganese oxide (NCM) batteries for electric passenger vehicles, Journal of Cleaner Production 273 (2020) 123006. https://doi.org/10.1016/j.jclepro.2020.123006.

[11] S. Das, R.C. Reddy, K.S. Chadchan, A.J. Patil, M.S. Biradar, K.K. Das, Nickel and Oxidative Stress: Cell Signaling Mechanisms and Protective Role of Vitamin C, Endocr. Metab. Immune Disord. Drug Targets 20 (2020) 1024–1031. https://doi.org/10.2174/1871530319666191205122249.

[12] D.J. Paustenbach, B.E. Tvermoes, K.M. Unice, B.L. Finley, B.D. Kerger, A review of the health hazards posed by cobalt, Crit. Rev. Toxicol. 43 (2013) 316–362. https://doi.org/10.3109/10408444.2013.779633.

[13] P. Taxell, P. Huuskonen, Toxicity assessment and health hazard classification of stainless steels, Regul. Toxicol. Pharmacol. 133 (2022) 105227. https://doi.org/10.1016/j.yrtph.2022.105227.

[14] S.M. Bradberry, J.M. Wilkinson, R.E. Ferner, Systemic toxicity related to metal hip prostheses, Clin. Toxicol. (Phila) 52 (2014) 837–847. https://doi.org/10.3109/15563650.2014.944977.

[15] R.P. Brown, B.A. Fowler, S. Fustinoni, M. Costa, M. Nordberg, Toxicity of metals released from implanted medical devices, in: Handbook on the Toxicology of Metals, Elsevier, 2022, pp. 127–136.

[16] T. Hoffmeister, D. Schwenke, N. Wachsmuth, O. Krug, M. Thevis, W.C. Byrnes, W.F.J. Schmidt, Erythropoietic effects of low-dose cobalt application, Drug Test. Anal. 11 (2019) 200–207. https://doi.org/10.1002/dta.2478.

[17] M.G. Ahlström, J.P. Thyssen, M. Wennervaldt, T. Menné, J.D. Johansen, Nickel allergy and allergic contact dermatitis: A clinical review of immunology,

epidemiology, exposure, and treatment, Contact Dermatitis 81 (2019) 227–241. https://doi.org/10.1111/cod.13327©.

[18] G. Rizzo, A.S. Laganà, A.M.C. Rapisarda, G.M.G. La Ferrera, M. Buscema, P. Rossetti, A. Nigro, V. Muscia, G. Valenti, F. Sapia, G. Sarpietro, M. Zigarelli, S.G. Vitale, Vitamin B12 among Vegetarians: Status, Assessment and Supplementation, Nutrients 8 (2016). https://doi.org/10.3390/nu8120767.

[19] D. Gille, A. Schmid, Vitamin B12 in meat and dairy products, Nutr. Rev. 73 (2015) 106–115. https://doi.org/10.1093/nutrit/nuu011.

[20] D.G. Barceloux, Nickel, J. Toxicol. Clin. Toxicol. 37 (1999) 239–258. https://doi.org/10.1081/CLT-100102423.

[21] X. Wang, I. Odnevall Wallinder, Y. Hedberg, Bioaccessibility of Nickel and Cobalt Released from Occupationally Relevant Alloy and Metal Powders at Simulated Human Exposure Scenarios, Ann. Work Expo. Health 64 (2020) 659–675. https://doi.org/10.1093/annweh/wxaa042.

[22] S. Mahey, R. Kumar, R. Arora, J. Mahajan, S. Arora, R. Bhardwaj, A.K. Thukral, Effect of cobalt(II) chloride hexahydrate on some human cancer cell lines, Springerplus 5 (2016) 930. https://doi.org/10.1186/s40064-016-2405-0.

[23] G. Genchi, G. Lauria, A. Catalano, A. Carocci, M.S. Sinicropi, Prevalence of Cobalt in the Environment and Its Role in Biological Processes, Biology (Basel) 12 (2023). https://doi.org/10.3390/biology12101335.

[24] W. Bal, M. Sokołowska, E. Kurowska, P. Faller, Binding of transition metal ions to albumin: sites, affinities and rates, Biochim. Biophys. Acta 1830 (2013) 5444–5455. https://doi.org/10.1016/j.bbagen.2013.06.018.

[25] J.D. Glennon, B. Sarkar, Nickel(II) transport in human blood serum. Studies of nickel(II) binding to human albumin and to native-sequence peptide, and ternary-complex formation with L-histidine, Biochem. J. 203 (1982) 15–23. https://doi.org/10.1042/bj2030015.

[26] K. Czarnek, S. Terpiłowska, A.K. Siwicki, Selected aspects of the action of cobalt ions in the human body, Cent. Eur. J. Immunol. 40 (2015) 236–242. https://doi.org/10.5114/ceji.2015.52837.

[27] V. Battaglia, A. Compagnone, A. Bandino, M. Bragadin, C.A. Rossi, F. Zanetti, S. Colombatto, M.A. Grillo, A. Toninello, Cobalt induces oxidative stress in isolated liver mitochondria responsible for permeability transition and intrinsic apoptosis in hepatocyte primary cultures, Int. J. Biochem. Cell Biol. 41 (2009) 586–594. https://doi.org/10.1016/j.biocel.2008.07.012.

[28] D. Dudek-Adamska, T. Lech, T. Konopka, P. Kościelniak, Nickel Content in Human Internal Organs, Biol. Trace Elem. Res. 199 (2021) 2138–2144. https://doi.org/10.1007/s12011-020-02347-w.

[29] A. Muñoz, M. Costa, Elucidating the mechanisms of nickel compound uptake: a review of particulate and nano-nickel endocytosis and toxicity, Toxicol. Appl. Pharmacol. 260 (2012) 1–16. https://doi.org/10.1016/j.taap.2011.12.014.

[30] T. Davidson, H. Chen, M.D. Garrick, G. D'Angelo, M. Costa, Soluble nickel interferes with cellular iron homeostasis, Mol. Cell. Biochem. 279 (2005) 157–162. https://doi.org/10.1007/s11010-005-8288-y.

[31] V. Picard, G. Govoni, N. Jabado, P. Gros, Nramp 2 (DCT1/DMT1) expressed at the plasma membrane transports iron and other divalent cations into a calcein-accessible cytoplasmic pool, J. Biol. Chem. 275 (2000) 35738–35745. https://doi.org/10.1074/jbc.M005387200.

[32] A.C. Illing, A. Shawki, C.L. Cunningham, B. Mackenzie, Substrate profile and metal-ion selectivity of human divalent metal-ion transporter-1, J. Biol. Chem. 287 (2012) 30485–30496. https://doi.org/10.1074/jbc.M112.364208.

[33] T.A.D. Smith, Human serum transferrin cobalt complex: stability and cellular uptake of cobalt, Bioorg. Med. Chem. 13 (2005) 4576–4579. https://doi.org/10.1016/j.bmc.2005.04.052.

[34] C.D. Quarles, R.K. Marcus, J.L. Brumaghim, Competitive binding of Fe3+, Cr3+, and Ni2+ to transferrin, J. Biol. Inorg. Chem. 16 (2011) 913–921. https://doi.org/10.1007/s00775-011-0792-9.

[35] K. Bowers, S.K.S. Srai, The trafficking of metal ion transporters of the Zrt- and Irt-like protein family, Traffic 19 (2018) 813–822. https://doi.org/10.1111/tra.12602.

[36] C.-Y. Wang, S. Jenkitkasemwong, S. Duarte, B.K. Sparkman, A. Shawki, B. Mackenzie, M.D. Knutson, ZIP8 is an iron and zinc transporter whose cell-surface expression is up-regulated by cellular iron loading, J. Biol. Chem. 287 (2012) 34032–34043. https://doi.org/10.1074/jbc.M112.367284.

[37] D.W. Nebert, M. Gálvez-Peralta, E.B. Hay, H. Li, E. Johansson, C. Yin, B. Wang, L. He, M. Soleimani, ZIP14 and ZIP8 zinc/bicarbonate symporters in Xenopus oocytes: characterization of metal uptake and inhibition, Metallomics 4 (2012) 1218–1225. https://doi.org/10.1039/c2mt20177a.

[38] C. Römmelt, T. Munsch, A. Drynda, V. Lessmann, C.H. Lohmann, J. Bertrand, Periprosthetic hypoxia as consequence of TRPM7 mediated cobalt influx in osteoblasts, J. Biomed. Mater. Res. B Appl. Biomater. 107 (2019) 1806–1813. https://doi.org/10.1002/jbm.b.34273.

[39] Q. Zhu, S. Liao, X. Lu, S. Shi, D. Gong, I. Cheang, X. Zhu, H. Zhang, X. Li, Cobalt exposure in relation to cardiovascular disease in the United States general population, Environ. Sci. Pollut. Res. Int. 28 (2021) 41834–41842. https://doi.org/10.1007/s11356-021-13620-3.

[40] A.M. Preisser, L. Scheit, A. Kraft, O. Thieme, V. Harth, Long-Term Clinical and Toxicological Follow-up of Severe Cobalt and Chromium Intoxication—a Case Report, SN Compr. Clin. Med. 5 (2023). https://doi.org/10.1007/s42399-023-01393-4.

[41] S. Chamani, L. Mobasheri, Z. Rostami, I. Zare, A. Naghizadeh, E. Mostafavi, Heavy metals in contact dermatitis: A review, J. Trace Elem. Med. Biol. 79 (2023) 127240. https://doi.org/10.1016/j.jtemb.2023.127240.

[42] A. Al-Abcha, L. Wang, M.J. Reilly, K.D. Rosenman, Work-related asthma in cobalt-exposed workers, J. Asthma 58 (2021) 1032–1041. https://doi.org/10.1080/02770903.2020.1759090.

[43] M.R. Karagas, A. Wang, D.C. Dorman, A.L. Hall, J. Pi, C.M. Sergi, E. Symanski, E.M. Ward, V.H. Arrandale, K. Azuma, E. Brambila, G.M. Calaf, J.M. Fritz, S. Fukushima, J.M. Gaitens, T.K. Grimsrud, L. Guo, E. Lynge, A.P. Marinho-Reis, M.A. McDiarmid, D.R.S. Middleton, T.P. Ong, D.A. Polya, B. Quintanilla-Vega, G.K. Roberts, T. Santonen, R. Sauni, M.J. Silva, P. Wild, C.W. Zhang, Q. Zhang, Y. Grosse, L. Benbrahim-Tallaa, A. de Conti, N.L. DeBono, F. El Ghissassi, F. Madia, B. Reisfeld, L.T. Stayner, E. Suonio, S. Viegas, R. Wedekind, S. Ahmadi, H. Mattock, W.M. Gwinn, M.K. Schubauer-Berigan, Carcinogenicity of cobalt, antimony compounds, and weapons-grade tungsten alloy, Lancet Oncol. 23 (2022) 577–578. https://doi.org/10.1016/S1470-2045(22)00219-4.

[44] IARC, Cobalt, Antimony Compounds, and Weapons-Grade Tungsten Alloy, Volume firstthirty-first, IARC Monographs on the Evaluation of Carcinogenic Risks to Humans, 2023.

[45] K. Jomova, M. Makova, S.Y. Alomar, S.H. Alwasel, E. Nepovimova, K. Kuca, C.J. Rhodes, M. Valko, Essential metals in health and disease, Chem. Biol. Interact. 367 (2022) 110173. https://doi.org/10.1016/j.cbi.2022.110173.

[46] O. Karovic, I. Tonazzini, N. Rebola, E. Edström, C. Lövdahl, B.B. Fredholm, E. Daré, Toxic effects of cobalt in primary cultures of mouse astrocytes. Similarities with hypoxia and role of HIF-1alpha, Biochem. Pharmacol. 73 (2007) 694–708. https://doi.org/10.1016/j.bcp.2006.11.008.

[47] J. Muñoz-Sánchez, M.E. Chánez-Cárdenas, The use of cobalt chloride as a chemical hypoxia model, J. Appl. Toxicol. 39 (2019) 556–570. https://doi.org/10.1002/jat.3749.

[48] Q. Wu, L. You, E. Nepovimova, Z. Heger, W. Wu, K. Kuca, V. Adam, Hypoxia-inducible factors: master regulators of hypoxic tumor immune escape, J. Hematol. Oncol. 15 (2022) 77. https://doi.org/10.1186/s13045-022-01292-6.

[49] D. Lison, S. van den Brule, G. van Maele-Fabry, Cobalt and its compounds: update on genotoxic and carcinogenic activities, Crit. Rev. Toxicol. 48 (2018) 522–539. https://doi.org/10.1080/10408444.2018.1491023.

[50] S.J.L. Linde, A. Franken, J.L. Du Plessis, Skin and respiratory exposure to soluble lead, cobalt, nickel, copper, arsenic and silver at two South African precious metals refineries, Int. Arch. Occup. Environ. Health 96 (2023) 259–270. https://doi.org/10.1007/s00420-022-01921-0.

[51] IARC, Arsenic, Metals, Fibres, and Dusts, No. tenth0C, IARC Monographs on the Evaluation of Carcinogenic Risks to Humans, [Place of publication not identified], 2012.

[52] C.P. Anyachor, D.B. Dooka, C.N. Orish, C.N. Amadi, B. Bocca, F. Ruggieri, M. Senofonte, C. Frazzoli, O.E. Orisakwe, Mechanistic considerations and biomarkers level in nickel-induced neurodegenerative diseases: An updated systematic review, IBRO Neurosci. Rep. 13 (2022) 136–146. https://doi.org/10.1016/j.ibneur.2022.07.005.

[53] K.K. Lundin, Y.K. Qadeer, Z. Wang, S. Virani, R. Leischik, C.J. Lavie, M. Strauss, C. Krittanawong, Contaminant Metals and Cardiovascular Health, J. Cardiovasc. Dev. Dis. 10 (2023). https://doi.org/10.3390/jcdd10110450.

[54] H. Guo, L. Wei, Y. Wang, H. Cui, H. Deng, Y. Zhu, J. Deng, Y. Geng, P. Ouyang, W. Lai, Z. Du, X. Ni, H. Yin, J. Fang, Z. Zuo, Nickel induces hepatotoxicity by mitochondrial biogenesis, mitochondrial dynamics, and mitophagy dysfunction, Environ. Toxicol. 38 (2023) 1185–1195. https://doi.org/10.1002/tox.23758.

[55] S. Xu, M. He, M. Zhong, L. Li, Y. Lu, Y. Zhang, L. Zhang, Z. Yu, Z. Zhou, The neuroprotective effects of taurine against nickel by reducing oxidative stress and maintaining mitochondrial function in cortical neurons, Neurosci. Lett. 590 (2015) 52–57. https://doi.org/10.1016/j.neulet.2015.01.065.

[56] T.L. Davidson, H. Chen, D.M. Di Toro, G. D'Angelo, M. Costa, Soluble nickel inhibits HIF-prolyl-hydroxylases creating persistent hypoxic signaling in A549 cells, Mol. Carcinog. 45 (2006) 479–489. https://doi.org/10.1002/mc.20176.

[57] X. Song, S.S. Fiati Kenston, L. Kong, J. Zhao, Molecular mechanisms of nickel induced neurotoxicity and chemoprevention, Toxicology 392 (2017) 47–54. https://doi.org/10.1016/j.tox.2017.10.006.

[58] C.-M. Liu, G.-H. Zheng, Q.-L. Ming, C. Chao, J.-M. Sun, Sesamin protects mouse liver against nickel-induced oxidative DNA damage and apoptosis by the PI3K-Akt pathway, J. Agric. Food Chem. 61 (2013) 1146–1154. https://doi.org/10.1021/jf304562b.

[59] S. Wu, Y.N. Bai, H.Q. Pu, J. He, T.Z. Zheng, H.Y. Li, M. Dai, N. Cheng, Dynamic Changes in DNA Damage and Repair Biomarkers with Employment Length among Nickel Smelting Workers, Biomed. Environ. Sci. 28 (2015) 679–682. https://doi.org/10.3967/bes2015.095.

[60] H. Guo, H. Liu, H. Wu, H. Cui, J. Fang, Z. Zuo, J. Deng, Y. Li, X. Wang, L. Zhao, Nickel Carcinogenesis Mechanism: DNA Damage, Int. J. Mol. Sci. 20 (2019). https://doi.org/10.3390/ijms20194690.

[61] K.S. Cameron, V. Buchner, P.B. Tchounwou, Exploring the molecular mechanisms of nickel-induced genotoxicity and carcinogenicity: a literature review, Rev. Environ. Health 26 (2011) 81–92. https://doi.org/10.1515/reveh.2011.012.

[62] G.H. Kim, J.E. Kim, S.J. Rhie, S. Yoon, The Role of Oxidative Stress in Neurodegenerative Diseases, Exp. Neurobiol. 24 (2015) 325–340. https://doi.org/10.5607/en.2015.24.4.325.

[63] J. Luo, K. Mills, S. Le Cessie, R. Noordam, D. van Heemst, Ageing, age-related diseases and oxidative stress: What to do next?, Ageing Res. Rev. 57 (2020) 100982. https://doi.org/10.1016/j.arr.2019.100982.

[64] A.J.P.O. de Almeida, J.C.P.L. de Oliveira, L.V. Da Silva Pontes, J.F. de Souza Júnior, T.A.F. Gonçalves, S.H. Dantas, M.S. de Almeida Feitosa, A.O. Silva, I.A. de Medeiros, ROS: Basic Concepts, Sources, Cellular Signaling, and its Implications in Aging Pathways, Oxid. Med. Cell. Longev. 2022 (2022) 1225578. https://doi.org/10.1155/2022/1225578.

[65] K. Jomova, M. Valko, Advances in metal-induced oxidative stress and human disease, Toxicology 283 (2011) 65–87. https://doi.org/10.1016/j.tox.2011.03.001.

[66] Y.A. Hajam, R. Rani, S.Y. Ganie, T.A. Sheikh, D. Javaid, S.S. Qadri, S. Pramodh, A. Alsulimani, M.F. Alkhanani, S. Harakeh, A. Hussain, S. Haque, M.S. Reshi, Oxidative Stress in Human Pathology and Aging: Molecular Mechanisms and Perspectives, Cells 11 (2022). https://doi.org/10.3390/cells11030552.

[67] L.C. Priya Dharshini, S. Vishnupriya, K.M. Sakthivel, R.R. Rasmi, Oxidative stress responsive transcription factors in cellular signalling transduction mechanisms, Cell. Signal. 72 (2020) 109670. https://doi.org/10.1016/j.cellsig.2020.109670.

[68] C. Tonelli, I.I.C. Chio, D.A. Tuveson, Transcriptional Regulation by Nrf2, Antioxid. Redox Signal. 29 (2018) 1727–1745. https://doi.org/10.1089/ars.2017.7342.

[69] M. Yamamoto, T.W. Kensler, H. Motohashi, The KEAP1-NRF2 System: a Thiol-Based Sensor-Effector Apparatus for Maintaining Redox Homeostasis, Physiol. Rev. 98 (2018) 1169–1203. https://doi.org/10.1152/physrev.00023.2017.

[70] T.-Y. Lin, L.C. Cantley, G.M. DeNicola, NRF2 Rewires Cellular Metabolism to Support the Antioxidant Response, in: J.A. Morales-Gonzalez, A. Morales-Gonzalez, E.O. Madrigal-Santillan (Eds.), A Master Regulator of Oxidative Stress - The Transcription Factor Nrf2, InTech, 2016.

[71] K.M. Holmström, R.V. Kostov, A.T. Dinkova-Kostova, The multifaceted role of Nrf2 in mitochondrial function, Curr. Opin. Toxicol. 1 (2016) 80–91. https://doi.org/10.1016/j.cotox.2016.10.002.

[72] J.D. Hayes, A.T. Dinkova-Kostova, The Nrf2 regulatory network provides an interface between redox and intermediary metabolism, Trends Biochem. Sci. 39 (2014) 199–218. https://doi.org/10.1016/j.tibs.2014.02.002.

[73] C.H. He, P. Gong, B. Hu, D. Stewart, M.E. Choi, A.M. Choi, J. Alam, Identification of activating transcription factor 4 (ATF4) as an Nrf2-interacting protein. Implication for heme oxygenase-1 gene regulation, J. Biol. Chem. 276 (2001) 20858–20865. https://doi.org/10.1074/jbc.M101198200.

[74] R.K. Toth, N.A. Warfel, Strange Bedfellows: Nuclear Factor, Erythroid 2-Like 2 (Nrf2) and Hypoxia-Inducible Factor 1 (HIF-1) in Tumor Hypoxia, Antioxidants (Basel) 6 (2017). https://doi.org/10.3390/antiox6020027.

[75] M. Jaganjac, L. Milkovic, S.B. Sunjic, N. Zarkovic, The NRF2, Thioredoxin, and Glutathione System in Tumorigenesis and Anticancer Therapies, Antioxidants (Basel) 9 (2020). https://doi.org/10.3390/antiox9111151.

[76] F. He, L. Antonucci, M. Karin, NRF2 as a regulator of cell metabolism and inflammation in cancer, Carcinogenesis 41 (2020) 405–416. https://doi.org/10.1093/carcin/bgaa039.

[77] M. Hammad, M. Raftari, R. Cesário, R. Salma, P. Godoy, S.N. Emami, S. Haghdoost, Roles of Oxidative Stress and Nrf2 Signaling in Pathogenic and Non-Pathogenic Cells: A Possible General Mechanism of Resistance to Therapy, Antioxidants (Basel) 12 (2023). https://doi.org/10.3390/antiox12071371.

[78] M.-Y. Song, D.-Y. Lee, K.-S. Chun, E.-H. Kim, The Role of NRF2/KEAP1 Signaling Pathway in Cancer Metabolism, Int. J. Mol. Sci. 22 (2021). https://doi.org/10.3390/ijms22094376.

[79] G. Wu, Y.-Z. Fang, S. Yang, J.R. Lupton, N.D. Turner, Glutathione metabolism and its implications for health, J. Nutr. 134 (2004) 489–492. https://doi.org/10.1093/jn/134.3.489.

[80] M. Tan, Y. Yin, X. Ma, J. Zhang, W. Pan, M. Tan, Y. Zhao, T. Yang, T. Jiang, H. Li, Glutathione system enhancement for cardiac protection: pharmacological options against oxidative stress and ferroptosis, Cell Death Dis. 14 (2023) 131. https://doi.org/10.1038/s41419-023-05645-y.

[81] A. Thiel, A.-K. Weishaupt, M.M. Nicolai, K. Lossow, A.P. Kipp, T. Schwerdtle, J. Bornhorst, Simultaneous quantitation of oxidized and reduced glutathione via LC-MS/MS to study the redox state and drug-mediated modulation in cells, worms and animal tissue, Journal of Chromatography B 1225 (2023) 123742. https://doi.org/10.1016/j.jchromb.2023.123742.

[82] S.I. Dikalov, D.G. Harrison, Methods for detection of mitochondrial and cellular reactive oxygen species, Antioxid. Redox Signal. 20 (2014) 372–382. https://doi.org/10.1089/ars.2012.4886.

[83] Y. Zhang, M. Dai, Z. Yuan, Methods for the detection of reactive oxygen species, Anal. Methods 10 (2018) 4625–4638. https://doi.org/10.1039/c8ay01339j.

[84] M.P. Murphy, H. Bayir, V. Belousov, C.J. Chang, K.J.A. Davies, M.J. Davies, T.P. Dick, T. Finkel, H.J. Forman, Y. Janssen-Heininger, D. Gems, V.E. Kagan, B. Kalyanaraman, N.-G. Larsson, G.L. Milne, T. Nyström, H.E. Poulsen, R. Radi, H. van Remmen, P.T. Schumacker, P.J. Thornalley, S. Toyokuni, C.C. Winterbourn, H. Yin, B. Halliwell, Guidelines for measuring reactive oxygen species and oxidative damage in cells and in vivo, Nat. Metab. 4 (2022) 651–662. https://doi.org/10.1038/s42255-022-00591-z.

[85] D. Tsikas, Assessment of lipid peroxidation by measuring malondialdehyde (MDA) and relatives in biological samples: Analytical and biological challenges, Anal. Biochem. 524 (2017) 13–30. https://doi.org/10.1016/j.ab.2016.10.021.

[86] J. Aguilar Diaz De Leon, C.R. Borges, Evaluation of Oxidative Stress in Biological Samples Using the Thiobarbituric Acid Reactive Substances Assay, J. Vis. Exp. (2020). https://doi.org/10.3791/61122.

[87] K.A. Smith, J. Shepherd, A. Wakil, E.S. Kilpatrick, A comparison of methods for the measurement of 8-isoPGF(2α): a marker of oxidative stress, Ann. Clin. Biochem. 48 (2011) 147–154. https://doi.org/10.1258/acb.2010.010151.

[88] S. Zelzer, H. Mangge, R. Oberreither, C. Bernecker, H.-J. Gruber, F. Prüller, G. Fauler, Oxidative stress: Determination of 4-hydroxy-2-nonenal by gas chromatography/mass spectrometry in human and rat plasma, Free Radic. Res. 49 (2015) 1233–1238. https://doi.org/10.3109/10715762.2015.1059936.

[89] E. Alomari, S. Bruno, L. Ronda, G. Paredi, S. Bettati, A. Mozzarelli, Protein carbonylation detection methods: A comparison, Data Brief 19 (2018) 2215–2220. https://doi.org/10.1016/j.dib.2018.06.088.

[90] K.S. Korkmaz, B. Debelec Butuner, D. Roggenbuck, Detection of 8-OHdG as a diagnostic biomarker, J. Lab. Precis. Med 3 (2018) 95. https://doi.org/10.21037/jlpm.2018.11.01.

[91] C. Morgenstern, I. Lastres-Becker, B.C. Demirdöğen, V.M. Costa, A. Daiber, R. Foresti, R. Motterlini, S. Kalyoncu, B.I. Arioz, S. Genc, M. Jakubowska, I.P. Trougakos, A. Piechota-Polanczyk, M. Mickael, M. Santos, T.W. Kensler, A. Cuadrado, I.M. Copple, Biomarkers of NRF2 signalling: Current status and future challenges, Redox Biol. 72 (2024) 103134. https://doi.org/10.1016/j.redox.2024.103134.

[92] Y. Yagishita, T.N. Gatbonton-Schwager, M.L. McCallum, T.W. Kensler, Current Landscape of NRF2 Biomarkers in Clinical Trials, Antioxidants (Basel) 9 (2020). https://doi.org/10.3390/antiox9080716.

[93] I. Rahman, A. Kode, S.K. Biswas, Assay for quantitative determination of glutathione and glutathione disulfide levels using enzymatic recycling method, Nat. Protoc. 1 (2006) 3159–3165. https://doi.org/10.1038/nprot.2006.378.

[94] I. Marrocco, F. Altieri, I. Peluso, Measurement and Clinical Significance of Biomarkers of Oxidative Stress in Humans, Oxid. Med. Cell. Longev. 2017 (2017) 6501046. https://doi.org/10.1155/2017/6501046.

[95] Z. Haida, M. Hakiman, A comprehensive review on the determination of enzymatic assay and nonenzymatic antioxidant activities, Food Sci. Nutr. 7 (2019) 1555–1563. https://doi.org/10.1002/fsn3.1012.

[96] F. Guéraud, G. Peiro, H. Bernard, J. Alary, C. Créminon, L. Debrauwer, E. Rathahao, M.-F. Drumare, C. Canlet, J.-M. Wal, G. Bories, Enzyme immunoassay for a urinary metabolite of 4-hydroxynonenal as a marker of lipid peroxidation, Free Radic. Biol. Med. 40 (2006) 54–62. https://doi.org/10.1016/j.freeradbiomed.2005.08.011.

[97] D. Weber, M.J. Davies, T. Grune, Determination of protein carbonyls in plasma, cell extracts, tissue homogenates, isolated proteins: Focus on sample preparation and derivatization conditions, Redox Biol. 5 (2015) 367–380. https://doi.org/10.1016/j.redox.2015.06.005.

[98] A.R. Chaudhuri, E.M. de Waal, A. Pierce, H. van Remmen, W.F. Ward, A. Richardson, Detection of protein carbonyls in aging liver tissue: A fluorescence-based proteomic approach, Mech. Ageing Dev. 127 (2006) 849–861. https://doi.org/10.1016/j.mad.2006.08.006.

[99] T. Henriksen, A. Weimann, E.L. Larsen, H.E. Poulsen, Quantification of 8-oxo-7,8-dihydro-2'-deoxyguanosine and 8-oxo-7,8-dihydro-guanosine concentrations in urine and plasma for estimating 24-h urinary output, Free Radic. Biol. Med. 172 (2021) 350–357. https://doi.org/10.1016/j.freeradbiomed.2021.06.014.

[100] J. Stachniuk, P. Kubalczyk, P. Furmaniak, R. Głowacki, A versatile method for analysis of saliva, plasma and urine for total thiols using HPLC with UV detection, Talanta 155 (2016) 70–77. https://doi.org/10.1016/j.talanta.2016.04.031.

[101] M.E. McMenamin, J. Himmelfarb, T.D. Nolin, Simultaneous analysis of multiple aminothiols in human plasma by high performance liquid chromatography with fluorescence detection, J. Chromatogr. B Analyt. Technol. Biomed. Life Sci. 877 (2009) 3274–3281. https://doi.org/10.1016/j.jchromb.2009.05.046.

[102] B. Bayram, G. Rimbach, J. Frank, T. Esatbeyoglu, Rapid method for glutathione quantitation using high-performance liquid chromatography with coulometric electrochemical detection, J. Agric. Food Chem. 62 (2014) 402–408. https://doi.org/10.1021/jf403857h.

[103] World Health Organization, Chapter 4: Hazard Identifcation and Characterization: Toxicological and Human Studies. Section 4.5 Genotoxicity. Environmental Health Criteria 240: Principles and methods for

the risk assessment of chemicals in food., World Health Organization, Geneva 2020.

[104] T. Lindahl, D.E. Barnes, Repair of endogenous DNA damage, Cold Spring Harb. Symp. Quant. Biol. 65 (2000) 127–133. https://doi.org/10.1101/sqb.2000.65.127.

[105] W.K. Kaufmann, R.S. Paules, DNA damage and cell cycle checkpoints, FASEB J. 10 (1996) 238–247. https://doi.org/10.1096/fasebj.10.2.8641557.

[106] A. Carusillo, C. Mussolino, DNA Damage: From Threat to Treatment, Cells 9 (2020). https://doi.org/10.3390/cells9071665.

[107] S.P. Jackson, J. Bartek, The DNA-damage response in human biology and disease, Nature 461 (2009) 1071–1078. https://doi.org/10.1038/nature08467.

[108] C. Molinaro, A. Martoriati, K. Cailliau, Proteins from the DNA Damage Response: Regulation, Dysfunction, and Anticancer Strategies, Cancers (Basel) 13 (2021). https://doi.org/10.3390/cancers13153819.

[109] H. Wei, X. Yu, Functions of PARylation in DNA Damage Repair Pathways, Genomics Proteomics Bioinformatics 14 (2016) 131–139. https://doi.org/10.1016/j.gpb.2016.05.001.

[110]A. Ray Chaudhuri, A. Nussenzweig, The multifaceted roles of PARP1 in DNA repair and chromatin remodelling, Nat. Rev. Mol. Cell Biol. 18 (2017) 610–621. https://doi.org/10.1038/nrm.2017.53.

[111]Z. Wang, F. Wang, T. Tang, C. Guo, The role of PARP1 in the DNA damage response and its application in tumor therapy, Front. Med. 6 (2012) 156–164. https://doi.org/10.1007/s11684-012-0197-3.

[112]N. Chatterjee, G.C. Walker, Mechanisms of DNA damage, repair, and mutagenesis, Environ. Mol. Mutagen. 58 (2017) 235–263. https://doi.org/10.1002/em.22087.

[113]C. Baumstark-Khan, C.E. Hellweg, G. Reitz, Cytotoxicity and genotoxicity reporter systems based on the use of mammalian cells, Adv. Biochem. Eng. Biotechnol. 118 (2010) 113–151. https://doi.org/10.1007/10_2009_20.

[114]P.L. Olive, J.P. Banáth, The comet assay: a method to measure DNA damage in individual cells, Nat. Protoc. 1 (2006) 23–29. https://doi.org/10.1038/nprot.2006.5.

[115]P. Møller, K. Jantzen, M. Løhr, M.H. Andersen, D.M. Jensen, M. Roursgaard, P.H. Danielsen, A. Jensen, S. Loft, Searching for assay controls for the Fpg- and hOGG1-modified comet assay, Mutagenesis 33 (2018) 9–19. https://doi.org/10.1093/mutage/gex015.

[116]J. Cadet, K.J.A. Davies, M.H. Medeiros, P. Di Mascio, J.R. Wagner, Formation and repair of oxidatively generated damage in cellular DNA, Free Radic. Biol. Med. 107 (2017) 13–34. https://doi.org/10.1016/j.freeradbiomed.2016.12.049.

[117]A. Hartwig, H. Klyszcz-Nasko, R. Schlepegrell, D. Beyersmann, Cellular damage by ferric nitrilotriacetate and ferric citrate in V79 cells: interrelationship between lipid peroxidation, DNA strand breaks and sister chromatid exchanges, Carcinogenesis 14 (1993) 107–112. https://doi.org/10.1093/carcin/14.1.107.

[118]L.J. Kuo, L.-X. Yang, Gamma-H2AX - a novel biomarker for DNA double-strand breaks, In Vivo 22 (2008) 305–309.

[119]S. Sommer, I. Buraczewska, M. Kruszewski, Micronucleus Assay: The State of Art, and Future Directions, Int. J. Mol. Sci. 21 (2020). https://doi.org/10.3390/ijms21041534.

[120] C. Neumann, J. Baesler, G. Steffen, M.M. Nicolai, T. Zubel, M. Aschner, A. Bürkle, A. Mangerich, T. Schwerdtle, J. Bornhorst, The role of poly(ADP-ribose) polymerases in manganese exposed Caenorhabditis elegans, J. Trace Elem. Med. Biol. 57 (2020) 21–27. https://doi.org/10.1016/j.jtemb.2019.09.001.

[121] A.-K. Hopp, F. Teloni, L. Bisceglie, C. Gondrand, F. Raith, K. Nowak, L. Muskalla, A. Howald, P.G.A. Pedrioli, K. Johnsson, M. Altmeyer, D.M.L. Pedrioli, M.O. Hottiger, Mitochondrial NAD+ Controls Nuclear ARTD1-

Induced ADP-Ribosylation, Mol. Cell 81 (2021) 340-354.e5. https://doi.org/10.1016/j.molcel.2020.12.034.

[122] Y. Lee, Q. Wang, I. Shuryak, D.J. Brenner, H.C. Turner, Development of a high-throughput γ-H2AX assay based on imaging flow cytometry, Radiat. Oncol. 14 (2019) 150. https://doi.org/10.1186/s13014-019-1344-7.

[123] M. Nikolic, T. Sustersic, N. Filipovic, In vitro Models and On-Chip Systems: Biomaterial Interaction Studies With Tissues Generated Using Lung Epithelial and Liver Metabolic Cell Lines, Front. Bioeng. Biotechnol. 6 (2018) 120. https://doi.org/10.3389/fbioe.2018.00120.

[124] V.A. Arzumanian, O.I. Kiseleva, E.V. Poverennaya, The Curious Case of the HepG2 Cell Line: 40 Years of Expertise, Int. J. Mol. Sci. 22 (2021). https://doi.org/10.3390/ijms222313135.

[125] M.T. Donato, L. Tolosa, M.J. Gómez-Lechón, Culture and Functional Characterization of Human Hepatoma HepG2 Cells, Methods Mol. Biol. 1250 (2015) 77–93. https://doi.org/10.1007/978-1-4939-2074-7_5.

[126] L. Guo, S. Dial, L. Shi, W. Branham, J. Liu, J.-L. Fang, B. Green, H. Deng, J. Kaput, B. Ning, Similarities and differences in the expression of drug-metabolizing enzymes between human hepatic cell lines and primary human hepatocytes, Drug Metab. Dispos. 39 (2011) 528–538. https://doi.org/10.1124/dmd.110.035873.

[127] A.V. Tyakht, E.N. Ilina, D.G. Alexeev, D.S. Ischenko, A.Y. Gorbachev, T.A. Semashko, A.K. Larin, O.V. Selezneva, E.S. Kostryukova, P.A. Karalkin, I.V. Vakhrushev, L.K. Kurbatov, A.I. Archakov, V.M. Govorun, RNA-Seq gene expression profiling of HepG2 cells: the influence of experimental factors and comparison with liver tissue, BMC Genomics 15 (2014) 1108. https://doi.org/10.1186/1471-2164-15-1108.

[128] S. Catalani, M.C. Rizzetti, A. Padovani, P. Apostoli, Neurotoxicity of cobalt, Hum. Exp. Toxicol. 31 (2012) 421–437. https://doi.org/10.1177/0960327111414280.

[129] M.P. Jogalekar, L.G. Cooper, E.E. Serrano, Hydrogel Environment Supports Cell Culture Expansion of a Grade IV Astrocytoma, Neurochem. Res. 42 (2017) 2610–2624. https://doi.org/10.1007/s11064-017-2308-7.

[130] B. Li, M. Xia, R. Zorec, V. Parpura, A. Verkhratsky, Astrocytes in heavy metal neurotoxicity and neurodegeneration, Brain Res. 1752 (2021) 147234. https://doi.org/10.1016/j.brainres.2020.147234.

[131] A. Verkhratsky, C.R. Rose, Na+-dependent transporters: The backbone of astroglial homeostatic function, Cell Calcium 85 (2020) 102136. https://doi.org/10.1016/j.ceca.2019.102136.

[132] S. Pesce, J.-F. Ghiglione, E. Topp, F. Martin-Laurent, Editorial: Microbial Ecotoxicology, Front. Microbiol. 11 (2020) 1342. https://doi.org/10.3389/fmicb.2020.01342.

[133] J. Beisson, M. Bétermier, M.-H. Bré, J. Cohen, S. Duharcourt, L. Duret, C. Kung, S. Malinsky, E. Meyer, J.R. Preer, L. Sperling, Paramecium tetraurelia: the renaissance of an early unicellular model, Cold Spring Harb. Protoc. 2010 (2010) pdb.emo140. https://doi.org/10.1101/pdb.emo140.

[134] J.A. Vilas-Boas, S.J. Cardoso, M.V.X. Senra, A. Rico, R.J.P. Dias, Ciliates as model organisms for the ecotoxicological risk assessment of heavy metals: A meta-analysis, Ecotoxicol. Environ. Saf. 199 (2020) 110669. https://doi.org/10.1016/j.ecoenv.2020.110669.

[135] J.A. Vilas-Boas, M.V.X. Senra, R.J.P. Dias, 2020. Ciliates in ecotoxicological studies: A minireview. Acta Limnol. Bras. 32, e202. https://doi.org/10.1590/S2179-975X6719.

[136] Y.-F. Zhang, Y. Wang, K.-R. Zhang, H.-M. Lei, Y.-B. Tang, L. Zhu, Development and validation of a rapid, robust and sensitive UPLC-QQQ-MS/MS method for simultaneous quantification of GSH metabolism in lung cancer cells, J. Chromatogr. B Analyt. Technol. Biomed. Life Sci. 1148 (2020) 122145. https://doi.org/10.1016/j.jchromb.2020.122145.

[137] C. Perricone, C. de Carolis, R. Perricone, Glutathione: a key player in autoimmunity, Autoimmun. Rev. 8 (2009) 697–701. https://doi.org/10.1016/j.autrev.2009.02.020.

[138] A. Pastore, G. Federici, E. Bertini, F. Piemonte, Analysis of glutathione: implication in redox and detoxification, Clin. Chim. Acta 333 (2003) 19–39. https://doi.org/10.1016/S0009-8981(03)00200-6.

[139] J. Bouligand, A. Deroussent, A. Paci, J. Morizet, G. Vassal, Liquid chromatography-tandem mass spectrometry assay of reduced and oxidized glutathione and main precursors in mice liver, J. Chromatogr. B Analyt. Technol. Biomed. Life Sci. 832 (2006) 67–74. https://doi.org/10.1016/j.jchromb.2005.12.037.

[140] G. Teskey, R. Abrahem, R. Cao, K. Gyurjian, H. Islamoglu, M. Lucero, A. Martinez, E. Paredes, O. Salaiz, B. Robinson, V. Venketaraman, Glutathione as a Marker for Human Disease, Adv. Clin. Chem. 87 (2018) 141–159. https://doi.org/10.1016/bs.acc.2018.07.004.

[141] F. Tietze, Enzymic method for quantitative determination of nanogram amounts of total and oxidized glutathione: applications to mammalian blood and other tissues, Anal. Biochem. 27 (1969) 502–522. https://doi.org/10.1016/0003-2697(69)90064-5.

[142] W. Zhang, P. Li, Q. Geng, Y. Duan, M. Guo, Y. Cao, Simultaneous determination of glutathione, cysteine, homocysteine, and cysteinylglycine in biological fluids by ion-pairing high-performance liquid chromatography coupled with precolumn derivatization, J. Agric. Food Chem. 62 (2014) 5845–5852. https://doi.org/10.1021/jf5014007.

[143] A.E. Katrusiak, P.G. Paterson, H. Kamencic, A. Shoker, A.W. Lyon, Pre-column derivatization high-performance liquid chromatographic method for determination of cysteine, cysteinyl-glycine, homocysteine and glutathione in plasma and cell extracts, J. Chromatogr. B Biomed. Sci. Appl. 758 (2001) 207–212. https://doi.org/10.1016/s0378-4347(01)00182-7.

[144] R. Kand'ár, P. Záková, H. Lotková, O. Kucera, Z. Cervinková, Determination of reduced and oxidized glutathione in biological samples using liquid chromatography with fluorimetric detection, J. Pharm. Biomed. Anal. 43 (2007) 1382–1387. https://doi.org/10.1016/j.jpba.2006.11.028.

[145] M.L. Steele, L. Ooi, G. Münch, Development of a high-performance liquid chromatography method for the simultaneous quantitation of glutathione and related thiols, Anal. Biochem. 429 (2012) 45–52. https://doi.org/10.1016/j.ab.2012.06.023.

[146] I. Squellerio, D. Caruso, B. Porro, F. Veglia, E. Tremoli, V. Cavalca, Direct glutathione quantification in human blood by LC-MS/MS: comparison with HPLC with electrochemical detection, J. Pharm. Biomed. Anal. 71 (2012) 111–118. https://doi.org/10.1016/j.jpba.2012.08.013.

[147] L.-P. Yap, H. Sancheti, M.D. Ybanez, J. Garcia, E. Cadenas, D. Han, Determination of GSH, GSSG, and GSNO using HPLC with electrochemical detection, Methods Enzymol. 473 (2010) 137–147. https://doi.org/10.1016/S0076-6879(10)73006-8.

[148] M.R. Mcgill, H. Jaeschke, A direct comparison of methods used to measure oxidized glutathione in biological samples: 2-vinylpyridine and N-ethylmaleimide, Toxicol. Mech. Methods 25 (2015) 589–595. https://doi.org/10.3109/15376516.2015.1094844.

[149] D. Stempak, S. Dallas, J. Klein, R. Bendayan, G. Koren, S. Baruchel, Glutathione stability in whole blood: effects of various deproteinizing acids, Ther. Drug Monit. 23 (2001) 542–549. https://doi.org/10.1097/00007691-200110000-00008.

[150] S. Bravo-Veyrat, G. Hopfgartner, High-throughput liquid chromatography differential mobility spectrometry mass spectrometry for bioanalysis: determination of reduced and oxidized form of glutathione in human blood, Anal. Bioanal. Chem. 410 (2018) 7153–7161. https://doi.org/10.1007/s00216-018-1318-x.

[151] A.C. Enomoto, E. Schneider, T. McKinnon, H. Goldfine, M.A. Levy, Validation of a simplified procedure for convenient and rapid quantification of reduced and oxidized glutathione in human plasma by liquid chromatography tandem mass spectrometry analysis, Biomed. Chromatogr. 34 (2020) e4854. https://doi.org/10.1002/bmc.4854.

[152] K. Herzog, L. IJlst, A.G. van Cruchten, C.W.T. van Roermund, W. Kulik, R.J.A. Wanders, H.R. Waterham, An UPLC-MS/MS Assay to Measure Glutathione as Marker for Oxidative Stress in Cultured Cells, Metabolites 9 (2019). https://doi.org/10.3390/metabo9030045.

[153] D. Giustarini, F. Galvagni, A. Tesei, A. Farolfi, M. Zanoni, S. Pignatta, A. Milzani, I.M. Marone, I. Dalle-Donne, R. Nassini, R. Rossi, Glutathione, glutathione disulfide, and S-glutathionylated proteins in cell cultures, Free Radic. Biol. Med. 89 (2015) 972–981. https://doi.org/10.1016/j.freeradbiomed.2015.10.410.

[154] S.-G. Lee, J. Yim, Y. Lim, J.-H. Kim, Validation of a liquid chromatography tandem mass spectrometry method to measure oxidized and reduced forms of glutathione in whole blood and verification in a mouse model as an indicator of oxidative stress, J. Chromatogr. B Analyt. Technol. Biomed. Life Sci. 1019 (2016) 45–50. https://doi.org/10.1016/j.jchromb.2015.10.041.

[155] R. Drew, J.O. Miners, The effects of buthionine sulphoximine (BSO) on glutathione depletion and xenobiotic biotransformation, Biochem. Pharmacol. 33 (1984) 2989–2994. https://doi.org/10.1016/0006-2952(84)90598-7.

[156] H. Adnan, M. Antenos, G.M. Kirby, The effect of menadione on glutathione S-transferase A1 (GSTA1): c-Jun N-terminal kinase (JNK) complex dissociation in human colonic adenocarcinoma Caco-2 cells, Toxicol. Lett. 214 (2012) 53–62. https://doi.org/10.1016/j.toxlet.2012.08.007.

[157] J. Steinmeier, R. Dringen, Exposure of Cultured Astrocytes to Menadione Triggers Rapid Radical Formation, Glutathione Oxidation and Mrp1-Mediated

Export of Glutathione Disulfide, Neurochem. Res. 44 (2019) 1167–1181. https://doi.org/10.1007/s11064-019-02760-1.

[158] H. Finke, V.K. Wandt, F. Ebert, N. Guttenberger, R.A. Glabonjat, M. Stiboller, K.A. Francesconi, G. Raber, T. Schwerdtle, Toxicological assessment of arsenic-containing phosphatidylcholines in HepG2 cells, Metallomics 12 (2020) 1159–1170. https://doi.org/10.1039/d0mt00073f.

[159] S. Brenner, The genetics of Caenorhabditis elegans, Genetics 77 (1974) 71–94. https://doi.org/10.1093/genetics/77.1.71.

[160] H.J. Forman, H. Zhang, Targeting oxidative stress in disease: promise and limitations of antioxidant therapy, Nat. Rev. Drug Discov. 20 (2021) 689–709. https://doi.org/10.1038/s41573-021-00233-1.

[161] O.W. Griffith, Determination of glutathione and glutathione disulfide using glutathione reductase and 2-vinylpyridine, Anal. Biochem. 106 (1980) 207–212. https://doi.org/10.1016/0003-2697(80)90139-6.

[162] D. Giustarini, I. Dalle-Donne, A. Milzani, P. Fanti, R. Rossi, Analysis of GSH and GSSG after derivatization with N-ethylmaleimide, Nat. Protoc. 8 (2013) 1660–1669. https://doi.org/10.1038/nprot.2013.095.

[163] W. Chen, Y. Zhao, T. Seefeldt, X. Guan, Determination of thiols and disulfides via HPLC quantification of 5-thio-2-nitrobenzoic acid, J. Pharm. Biomed. Anal. 48 (2008) 1375–1380. https://doi.org/10.1016/j.jpba.2008.08.033.

[164] D. Carroll, D. Howard, H. Zhu, C.M. Paumi, M. Vore, S. Bondada, Y. Liang, C. Wang, D.K. St Clair, Simultaneous quantitation of oxidized and reduced glutathione via LC-MS/MS: An insight into the redox state of hematopoietic stem cells, Free Radic. Biol. Med. 97 (2016) 85–94. https://doi.org/10.1016/j.freeradbiomed.2016.05.005.

[165] T. Fahrenholz, M.M. Wolle, H.M.S. Kingston, S. Faber, J.C. Kern, M. Pamuku, L. Miller, H. Chatragadda, A. Kogelnik, Molecular speciated isotope dilution mass spectrometric methods for accurate, reproducible and direct

quantification of reduced, oxidized and total glutathione in biological samples, Anal. Chem. 87 (2015) 1232–1240. https://doi.org/10.1021/ac503933t.

[166] T. Moore, A. Le, A.-K. Niemi, T. Kwan, K. Cusmano-Ozog, G.M. Enns, T.M. Cowan, A new LC-MS/MS method for the clinical determination of reduced and oxidized glutathione from whole blood, J. Chromatogr. B Analyt. Technol. Biomed. Life Sci. 929 (2013) 51–55. https://doi.org/10.1016/j.jchromb.2013.04.004.

[167] N.L. Jenkins, S.A. James, A. Salim, F. Sumardy, T.P. Speed, M. Conrad, R. Des Richardson, A.I. Bush, G. McColl, Changes in ferrous iron and glutathione promote ferroptosis and frailty in aging Caenorhabditis elegans, Elife 9 (2020). https://doi.org/10.7554/eLife.56580.

[168] I. Gusarov, I. Shamovsky, B. Pani, L. Gautier, S. Eremina, O. Katkova-Zhukotskaya, A. Mironov, A.A. Makarov, E. Nudler, Dietary thiols accelerate aging of C. elegans, Nat. Commun. 12 (2021) 4336. https://doi.org/10.1038/s41467-021-24634-3.

[169] S.W. Caito, M. Aschner, Quantification of Glutathione in Caenorhabditis elegans, Curr. Protoc. Toxicol. 64 (2015) 6.18.1-6.18.6. https://doi.org/10.1002/0471140856.tx0618s64.

[170] J.A. Ruszkiewicz, G. Teixeira de Macedo, A. Miranda-Vizuete, A.B. Bowman, J. Bornhorst, T. Schwerdtle, F.A. Antunes Soares, M. Aschner, Sex-Specific Response of Caenorhabditis elegans to Methylmercury Toxicity, Neurotox. Res. 35 (2019) 208–216. https://doi.org/10.1007/s12640-018-9949-4.

[171] N. Urban, D. Tsitsipatis, F. Hausig, K. Kreuzer, K. Erler, V. Stein, M. Ristow, H. Steinbrenner, L.-O. Klotz, Non-linear impact of glutathione depletion on C. elegans life span and stress resistance, Redox Biol. 11 (2017) 502–515. https://doi.org/10.1016/j.redox.2016.12.003.

[172] K. Lüersen, D. Stegehake, J. Daniel, M. Drescher, I. Ajonina, C. Ajonina, P. Hertel, C. Woltersdorf, E. Liebau, The glutathione reductase GSR-1

determines stress tolerance and longevity in Caenorhabditis elegans, PLoS One 8 (2013) e60731. https://doi.org/10.1371/journal.pone.0060731.

[173] S. Ndlovu, S. Nagiah, N.S. Abdul, T. Ghazi, A.A. Chuturgoon, Deoxynivalenol downregulates NRF2-induced cytoprotective response in human hepatocellular carcinoma (HepG2) cells, Toxicon 193 (2021) 4–12. https://doi.org/10.1016/j.toxicon.2021.01.017.

[174] K. Wang, Z. Zhang, H.-I. Tsai, Y. Liu, J. Gao, M. Wang, L. Song, X. Cao, Z. Xu, H. Chen, A. Gong, D. Wang, F. Cheng, H. Zhu, Branched-chain amino acid aminotransferase 2 regulates ferroptotic cell death in cancer cells, Cell Death Differ. 28 (2021) 1222–1236. https://doi.org/10.1038/s41418-020-00644-4.

[175] J. Xu, S. Oda, T. Yokoi, Cell-based assay using glutathione-depleted HepaRG and HepG2 human liver cells for predicting drug-induced liver injury, Toxicol. In Vitro 48 (2018) 286–301. https://doi.org/10.1016/j.tiv.2018.01.019.

[176] B. Zhang, J.-L. Dong, Y.-L. Chen, Y. Liu, S.-S. Huang, X.-L. Zhong, Y.-H. Cheng, Z.-G. Wang, Nrf2 mediates the protective effects of homocysteine by increasing the levels of GSH content in HepG2 cells, Mol. Med. Rep. 16 (2017) 597–602. https://doi.org/10.3892/mmr.2017.6633.

[177] Scientific Committee on Health, Environmental and Emerging Risks, Opinion on the safety of the presence of cobalt in toys, 2023.

[178] K.K. Das, R.C. Reddy, I.B. Bagoji, S. Das, S. Bagali, L. Mullur, J.P. Khodnapur, M.S. Biradar, Primary concept of nickel toxicity - an overview, J. Basic Clin. Physiol. Pharmacol. 30 (2018) 141–152. https://doi.org/10.1515/jbcpp-2017-0171.

[179] S.-C. Xu, M.-D. He, M. Zhong, Y.-W. Zhang, Y. Wang, L. Yang, J. Yang, Z.-P. Yu, Z. Zhou, Melatonin protects against Nickel-induced neurotoxicity in vitro by reducing oxidative stress and maintaining mitochondrial function, J. Pineal Res. 49 (2010) 86–94. https://doi.org/10.1111/j.1600-079X.2010.00770.x.

[180] H.M. Meecham, P. Humphrey, Industrial exposure to cobalt causing optic atrophy and nerve deafness: a case report, J. Neurol. Neurosurg. Psychiatry 54 (1991) 374–375. https://doi.org/10.1136/jnnp.54.4.374.

[181] Y.-C. Hsu, C.-W. Chang, H.-L. Lee, C.-C. Chuang, H.-C. Chiu, W.-Y. Li, J.-T. Horng, E. Fu, Association between History of Dental Amalgam Fillings and Risk of Parkinson's Disease: A Population-Based Retrospective Cohort Study in Taiwan, PLoS One 11 (2016) e0166552. https://doi.org/10.1371/journal.pone.0166552.

[182] Agency for Toxic Substances and Disease Registry, Toxicological Profile for Cobalt (2023).

[183] K.H. Gathwan, Comparative effect of orally fed nickel intoxicants on liver of male mice and observation under scanning electron microscope (SEM) (2015).

[184] A.S. Akinrinde, O.E. Adebiyi, Neuroprotection by luteolin and gallic acid against cobalt chloride-induced behavioural, morphological and neurochemical alterations in Wistar rats, Neurotoxicology 74 (2019) 252–263. https://doi.org/10.1016/j.neuro.2019.07.005.

[185] A.S. Akinrinde, A.A. Oyagbemi, T.O. Omobowale, V.C. Nwozuzu, Cobalt Chloride-Induced Hepatic and Intestinal Damage in Rats: Protection by Ethyl Acetate and *Chloroform fractions* of Ocimum Gratissimum, ti 23 (2016) 38. https://doi.org/10.22506/ti/2016/v23/i1/146668.

[186] A.V. Skalny, I.P. Zaitseva, Y.G. Gluhcheva, A.A. Skalny, E.E. Achkasov, M.G. Skalnaya, A.A. Tinkov, Cobalt in athletes: hypoxia and doping - new crossroads, J. Appl. Biomed. 17 (2019) 28. https://doi.org/10.32725/jab.2018.003.

[187] A. Knoop, P. Planitz, B. Wüst, M. Thevis, Analysis of cobalt for human sports drug testing purposes using ICP- and LC-ICP-MS, Drug Test. Anal. 12 (2020) 1666–1672. https://doi.org/10.1002/dta.2962.

[188] Y.-F. Wang, H.-W. Shyu, Y.-C. Chang, W.-C. Tseng, Y.-L. Huang, K.-H. Lin, M.-C. Chou, H.-L. Liu, C.-Y. Chen, Nickel (II)-induced cytotoxicity and

apoptosis in human proximal tubule cells through a ROS- and mitochondria-mediated pathway, Toxicol. Appl. Pharmacol. 259 (2012) 177–186. https://doi.org/10.1016/j.taap.2011.12.022.

[189] T. Porwol, W. Ehleben, K. Zierold, J. Fandrey, H. Acker, The influence of nickel and cobalt on putative members of the oxygen-sensing pathway of erythropoietin-producing HepG2 cells, Eur. J. Biochem. 256 (1998) 16–23. https://doi.org/10.1046/j.1432-1327.1998.2560016.x.

[190] D.P. Cross, G. Ramachandran, E.V. Wattenberg, Mixtures of Nickel and Cobalt Chlorides Induce Synergistic Cytotoxic Effects: Implications for Inhalation Exposure Modeling, The Annals of Occupational Hygiene (2001). https://doi.org/10.1093/annhyg/45.5.409.

[191] E. Patel, C. Lynch, V. Ruff, M. Reynolds, Co-exposure to nickel and cobalt chloride enhances cytotoxicity and oxidative stress in human lung epithelial cells, Toxicol. Appl. Pharmacol. 258 (2012) 367–375. https://doi.org/10.1016/j.taap.2011.11.019.

[192] H. Guo, L. Chen, H. Cui, X. Peng, J. Fang, Z. Zuo, J. Deng, X. Wang, B. Wu, Research Advances on Pathways of Nickel-Induced Apoptosis, Int. J. Mol. Sci. 17 (2015). https://doi.org/10.3390/ijms17010010.

[193] S. Fernandez-Fernandez, A. Almeida, J.P. Bolaños, Antioxidant and bioenergetic coupling between neurons and astrocytes, Biochem. J. 443 (2012) 3–11. https://doi.org/10.1042/BJ20111943.

[194] M. Li, J. Lu, Cobalt in lithium-ion batteries, Science 367 (2020) 979–980. https://doi.org/10.1126/science.aba9168.

[195] J. Bornhorst, S. Meyer, T. Weber, C. Böker, T. Marschall, A. Mangerich, S. Beneke, A. Bürkle, T. Schwerdtle, Molecular mechanisms of Mn induced neurotoxicity: RONS generation, genotoxicity, and DNA-damage response, Mol. Nutr. Food Res. 57 (2013) 1255–1269. https://doi.org/10.1002/mnfr.201200758.

[196] V. Michaelis, S. Kasper, L. Naperkowski, J. Pusse, A. Thiel, F. Ebert, M. Aschner, T. Schwerdtle, H. Haase, J. Bornhorst, The Impact of Zinc on

Manganese Bioavailability and Cytotoxicity in HepG2 Cells, Mol. Nutr. Food Res. 67 (2023) e2200283. https://doi.org/10.1002/mnfr.202200283.

[197] B. Witt, M. Stiboller, S. Raschke, S. Friese, F. Ebert, T. Schwerdtle, Characterizing effects of excess copper levels in a human astrocytic cell line with focus on oxidative stress markers, J. Trace Elem. Med. Biol. 65 (2021) 126711. https://doi.org/10.1016/j.jtemb.2021.126711.

[198] J.A. Cadieux, Z. Zhang, M. Mattice, A. Brownlie-Cutts, J. Fu, L.G. Ratkay, R. Kwan, J. Thompson, J. Sanghara, J. Zhong, Y.P. Goldberg, Synthesis and biological evaluation of substituted pyrazoles as blockers of divalent metal transporter 1 (DMT1), Bioorg. Med. Chem. Lett. 22 (2012) 90–95. https://doi.org/10.1016/j.bmcl.2011.11.069.

[199] R. Teschke, Aluminum, Arsenic, Beryllium, Cadmium, Chromium, Cobalt, Copper, Iron, Lead, Mercury, Molybdenum, Nickel, Platinum, Thallium, Titanium, Vanadium, and Zinc: Molecular Aspects in Experimental Liver Injury, Int. J. Mol. Sci. 23 (2022). https://doi.org/10.3390/ijms232012213.

[200] K. Renu, R. Chakraborty, H. Myakala, R. Koti, A.C. Famurewa, H. Madhyastha, B. Vellingiri, A. George, A. Valsala Gopalakrishnan, Molecular mechanism of heavy metals (Lead, Chromium, Arsenic, Mercury, Nickel and Cadmium) - induced hepatotoxicity - A review, Chemosphere 271 (2021) 129735. https://doi.org/10.1016/j.chemosphere.2021.129735.

[201] M. Valko, H. Morris, M.T.D. Cronin, Metals, toxicity and oxidative stress, Curr. Med. Chem. 12 (2005) 1161–1208. https://doi.org/10.2174/0929867053764635.

[202] P.S. Baxter, G.E. Hardingham, Adaptive regulation of the brain's antioxidant defences by neurons and astrocytes, Free Radic. Biol. Med. 100 (2016) 147–152. https://doi.org/10.1016/j.freeradbiomed.2016.06.027.

[203] S. Gómez-Arnaiz, R.J. Tate, M.H. Grant, Cytotoxicity of cobalt chloride in brain cell lines - a comparison between astrocytoma and neuroblastoma cells, Toxicol. In Vitro 68 (2020) 104958. https://doi.org/10.1016/j.tiv.2020.104958.

[204] S.E. Green, M.W. Luczak, J.L. Morse, Z. DeLoughery, A. Zhitkovich, Uptake, p53 pathway activation, and cytotoxic responses for Co(II) and Ni(II) in human lung cells: implications for carcinogenicity, Toxicol. Sci. 136 (2013) 467–477. https://doi.org/10.1093/toxsci/kft214.

[205] A. Johansson, T. Curstedt, P. Camner, Lung lesions after combined inhalation of cobalt and nickel, Environ. Res. 54 (1991) 24–38. https://doi.org/10.1016/S0013-9351(05)80192-6.

[206] D.L. Garza Amaya, A. Thiel, M. Möller, G. Gasparoni, M. Pirritano, F. Drews, J. Bornhorst, M. Simon, Microbial impact to environmental toxicants Ni(II) and Co(II): Joint toxicity and cellular response in paramecium, Chemosphere (2023) 140434. https://doi.org/10.1016/j.chemosphere.2023.140434.

[207] N.A. Wolff, M.D. Garrick, L. Zhao, L.M. Garrick, A.J. Ghio, F. Thévenod, A role for divalent metal transporter (DMT1) in mitochondrial uptake of iron and manganese, Sci. Rep. 8 (2018) 211. https://doi.org/10.1038/s41598-017-18584-4.

[208] Z. Li, Z. Lai, K. Ya, Du Fang, Y.W. Ho, Y. Lei, Q.Z. Ming, Correlation between the expression of divalent metal transporter 1 and the content of hypoxia-inducible factor-1 in hypoxic HepG2 cells, J. Cell. Mol. Med. 12 (2008) 569–579. https://doi.org/10.1111/j.1582-4934.2007.00145.x.

[209] R. Onodera, S. Asakawa, R. Segawa, N. Mizuno, K. Ogasawara, M. Hiratsuka, N. Hirasawa, Zinc ions have a potential to attenuate both Ni ion uptake and Ni ion-induced inflammation, Sci. Rep. 8 (2018) 2911. https://doi.org/10.1038/s41598-018-21014-8.

[210] J. Tallkvist, C.L. Bowlus, B. Lönnerdal, Effect of iron treatment on nickel absorption and gene expression of the divalent metal transporter (DMT1) by human intestinal Caco-2 cells, Pharmacol. Toxicol. 92 (2003) 121–124. https://doi.org/10.1034/j.1600-0773.2003.920303.x.

[211]A. Calzolari, V. Finisguerra, I. Oliviero, S. Deaglio, G. Mariani, F. Malavasi, U. Testa, Regulation of transferrin receptor 2 in human cancer cell lines,

Blood Cells Mol. Dis. 42 (2009) 5–13. https://doi.org/10.1016/j.bcmd.2008.10.001.

[212] J.J. Pinilla-Tenas, B.K. Sparkman, A. Shawki, A.C. Illing, C.J. Mitchell, N. Zhao, J.P. Liuzzi, R.J. Cousins, M.D. Knutson, B. Mackenzie, Zip14 is a complex broad-scope metal-ion transporter whose functional properties support roles in the cellular uptake of zinc and nontransferrin-bound iron, Am. J. Physiol. Cell Physiol. 301 (2011) C862-71. https://doi.org/10.1152/ajpcell.00479.2010.

[213] N. Zhao, J. Gao, C.A. Enns, M.D. Knutson, ZRT/IRT-like protein 14 (ZIP14) promotes the cellular assimilation of iron from transferrin, J. Biol. Chem. 285 (2010) 32141–32150. https://doi.org/10.1074/jbc.M110.143248.

[214] M.K. Monteilh-Zoller, M.C. Hermosura, M.J.S. Nadler, A.M. Scharenberg, R. Penner, A. Fleig, TRPM7 provides an ion channel mechanism for cellular entry of trace metal ions, J. Gen. Physiol. 121 (2003) 49–60. https://doi.org/10.1085/jgp.20028740.

[215] J. Yang, J. Black, Competitive binding of chromium, cobalt and nickel to serum proteins, Biomaterials 15 (1994) 262–268. https://doi.org/10.1016/0142-9612(94)90049-3.

[216] V.C. Wong, J.L. Morse, A. Zhitkovich, p53 activation by Ni(II) is a HIF-1α independent response causing caspases 9/3-mediated apoptosis in human lung cells, Toxicol. Appl. Pharmacol. 269 (2013) 233–239. https://doi.org/10.1016/j.taap.2013.03.023.

[217] Y. Tong, K. Tong, Q. Zhu, Y. Wu, Y. Yang, J. Zhang, P. Hu, S. Yan, Cobalt Chloride Induced Apoptosis by Inhibiting GPC3 Expression via the HIF-1α/c-Myc Axis in HepG2 Cells, Onco. Targets. Ther. 12 (2019) 10663–10670. https://doi.org/10.2147/OTT.S227215.

[218] S. Liu, Y. Li, W. Chen, P. Zheng, T. Liu, W. He, J. Zhang, X. Zeng, Silencing glypican-3 expression induces apoptosis in human hepatocellular carcinoma cells, Biochem. Biophys. Res. Commun. 419 (2012) 656–661. https://doi.org/10.1016/j.bbrc.2012.02.069.

[219] J.N. Lee, J. Park, S.-G. Kim, M.S. Kim, J.-Y. Lim, S.-K. Choe, 3-Aminotriazole protects against cobalt (II) chloride-induced cytotoxicity by inhibiting reactive oxygen species formation and preventing mitochondrial damage in HepG2 cells, Mol. Cell. Toxicol. 13 (2017) 125–132. https://doi.org/10.1007/s13273-017-0013-x.

[220] R. Yubolphan, S. Phuagkhaopong, K. Sangpairoj, N. Sibmooh, C. Power, P. Vivithanaporn, Intracellular nickel accumulation induces apoptosis and cell cycle arrest in human astrocytic cells, Metallomics 13 (2021). https://doi.org/10.1093/mtomcs/mfaa006.

[221] Y.-J. Lee, S.-S. Lim, B.J. Baek, J.-M. An, H.-S. Nam, K.-M. Woo, M.-K. Cho, S.-H. Kim, S.-H. Lee, Nickel(II)-induced nasal epithelial toxicity and oxidative mitochondrial damage, Environ. Toxicol. Pharmacol. 42 (2016) 76–84. https://doi.org/10.1016/j.etap.2016.01.005.

[222] K. Salnikow, W. Su, M.V. Blagosklonny, M. Costa, Carcinogenic Metals Induce Hypoxia-inducible Factor-stimulated Transcription by Reactive Oxygen Species-independent Mechanism, Cancer Research 60 (2000) 3375–3378.

[223] J.B. Lewis, R.L. Messer, V.V. McCloud, P.E. Lockwood, S.D. Hsu, J.C. Wataha, Ni(II) activates the Nrf2 signaling pathway in human monocytic cells, Biomaterials 27 (2006) 5348–5356. https://doi.org/10.1016/j.biomaterials.2006.06.007.

[224] S.C. Lu, Regulation of glutathione synthesis, Mol. Aspects Med. 30 (2009) 42–59. https://doi.org/10.1016/j.mam.2008.05.005.

[225] R. Dringen, M. Brandmann, M.C. Hohnholt, E.-M. Blumrich, Glutathione-Dependent Detoxification Processes in Astrocytes, Neurochem. Res. 40 (2015) 2570–2582. https://doi.org/10.1007/s11064-014-1481-1.

[226] D. Bloch, P. Diel, B. Epe, M. Hellwig, A. Lampen, A. Mally, D. Marko, M.A. Villar Fernández, S. Guth, A. Roth, R. Marchan, A. Ghallab, C. Cadenas, P. Nell, N. Vartak, C. van Thriel, A. Luch, S. Schmeisser, M. Herzler, R. Landsiedel, M. Leist, P. Marx-Stoelting, T. Tralau, J.G. Hengstler, Basic

concepts of mixture toxicity and relevance for risk evaluation and regulation, Arch. Toxicol. 97 (2023) 3005–3017. https://doi.org/10.1007/s00204-023-03565-6.

[227] A. Thiel, V. Michaelis, M. Restle, S. Figge, M. Simon, T. Schwerdtle, J. Bornhorst, Single is not combined: The role of Co and Ni bioavailability on toxicity mechanisms in liver and brain cells, Chemosphere 357 (2024) 142091. https://doi.org/10.1016/j.chemosphere.2024.142091.

[228] M. Martin, Cutadapt removes adapter sequences from high-throughput sequencing reads, EMBnet j. 17 (2011) 10. https://doi.org/10.14806/ej.17.1.200.

[229] B. Langmead, S.L. Salzberg, Fast gapped-read alignment with Bowtie 2, Nat. Methods 9 (2012) 357–359. https://doi.org/10.1038/nmeth.1923.

[230] M.I. Love, W. Huber, S. Anders, Moderated estimation of fold change and dispersion for RNA-seq data with DESeq2, Genome Biol. 15 (2014) 550. https://doi.org/10.1186/s13059-014-0550-8.

[231] M. Ashburner, C.A. Ball, J.A. Blake, D. Botstein, H. Butler, J.M. Cherry, A.P. Davis, K. Dolinski, S.S. Dwight, J.T. Eppig, M.A. Harris, D.P. Hill, L. Issel-Tarver, A. Kasarskis, S. Lewis, J.C. Matese, J.E. Richardson, M. Ringwald, G.M. Rubin, G. Sherlock, Gene ontology: tool for the unification of biology. The Gene Ontology Consortium, Nat. Genet. 25 (2000) 25–29. https://doi.org/10.1038/75556.

[232] S.A. Aleksander, J. Balhoff, S. Carbon, J.M. Cherry, H.J. Drabkin, D. Ebert, M. Feuermann, P. Gaudet, N.L. Harris, D.P. Hill, R. Lee, H. Mi, S. Moxon, C.J. Mungall, A. Muruganugan, T. Mushayahama, P.W. Sternberg, P.D. Thomas, K. van Auken, J. Ramsey, D.A. Siegele, R.L. Chisholm, P. Fey, M.C. Aspromonte, M.V. Nugnes, F. Quaglia, S. Tosatto, M. Giglio, S. Nadendla, G. Antonazzo, H. Attrill, G. Dos Santos, S. Marygold, V. Strelets, C.J. Tabone, J. Thurmond, P. Zhou, S.H. Ahmed, P. Asanitthong, D. Luna Buitrago, M.N. Erdol, M.C. Gage, M. Ali Kadhum, K.Y.C. Li, M. Long, A. Michalak, A. Pesala, A. Pritazahra, S.C.C. Saverimuttu, R. Su, K.E. Thurlow, R.C. Lovering, C.

Logie, S. Oliferenko, J. Blake, K. Christie, L. Corbani, M.E. Dolan, L. Ni, D. Sitnikov, C. Smith, A. Cuzick, J. Seager, L. Cooper, J. Elser, P. Jaiswal, P. Gupta, S. Naithani, M. Lera-Ramirez, K. Rutherford, V. Wood, J.L. de Pons, M.R. Dwinell, G.T. Hayman, M.L. Kaldunski, A.E. Kwitek, S.J.F. Laulederkind, M.A. Tutaj, M. Vedi, S.-J. Wang, P. D'Eustachio, L. Aimo, K. Axelsen, A. Bridge, N. Hyka-Nouspikel, A. Morgat, S.R. Engel, K. Karra, S.R. Miyasato, R.S. Nash, M.S. Skrzypek, S. Weng, E.D. Wong, E. Bakker, T.Z. Berardini, L. Reiser, A. Auchincloss, G. Argoud-Puy, M.-C. Blatter, E. Boutet, L. Breuza, C. Casals-Casas, E. Coudert, A. Estreicher, M. Livia Famiglietti, A. Gos, N. Gruaz-Gumowski, C. Hulo, F. Jungo, P. Le Mercier, D. Lieberherr, P. Masson, I. Pedruzzi, L. Pourcel, S. Poux, C. Rivoire, S. Sundaram, A. Bateman, E. Bowler-Barnett, H. Bye-A-Jee, P. Denny, A. Ignatchenko, R. Ishtiaq, A. Lock, Y. Lussi, M. Magrane, M.J. Martin, S. Orchard, P. Raposo, E. Speretta, N. Tyagi, K. Warner, R. Zaru, A.D. Diehl, J. Chan, S. Diamantakis, D. Raciti, M. Zarowiecki, M. Fisher, C. James-Zorn, V. Ponferrada, A. Zorn, S. Ramachandran, L. Ruzicka, M. Westerfield, The Gene Ontology knowledgebase in 2023, Genetics 224 (2023). https://doi.org/10.1093/genetics/iyad031.

[233] P.D. Thomas, D. Ebert, A. Muruganujan, T. Mushayahama, L.-P. Albou, H. Mi, PANTHER: Making genome-scale phylogenetics accessible to all, Protein Sci. 31 (2022) 8–22. https://doi.org/10.1002/pro.4218.

[234] A. Athar, A. Füllgrabe, N. George, H. Iqbal, L. Huerta, A. Ali, C. Snow, N.A. Fonseca, R. Petryszak, I. Papatheodorou, U. Sarkans, A. Brazma, ArrayExpress update - from bulk to single-cell expression data, Nucleic Acids Res. 47 (2019) D711-D715. https://doi.org/10.1093/nar/gky964.

[235] T. Wolfram, M. Schwarz, M. Reuß, K. Lossow, M. Ost, S. Klaus, T. Schwerdtle, A.P. Kipp, N-Acetylcysteine as Modulator of the Essential Trace Elements Copper and Zinc, Antioxidants (Basel) 9 (2020). https://doi.org/10.3390/antiox9111117.

[236] V. Michaelis, L. Aengenheister, M. Tuchtenhagen, J. Rinklebe, F. Ebert, T. Schwerdtle, T. Buerki-Thurnherr, J. Bornhorst, Differences and Interactions in Placental Manganese and Iron Transfer across an In Vitro Model of Human Villous Trophoblasts, Int. J. Mol. Sci. 23 (2022). https://doi.org/10.3390/ijms23063296.

[237] B. Michalke, D. Willkommen, V. Venkataramani, Iron Redox Speciation Analysis Using Capillary Electrophoresis Coupled to Inductively Coupled Plasma Mass Spectrometry (CE-ICP-MS), Front. Chem. 7 (2019) 136. https://doi.org/10.3389/fchem.2019.00136.

[238] B. Michalke, D. Willkommen, V. Venkataramani, Setup of Capillary Electrophoresis-Inductively Coupled Plasma Mass Spectrometry (CE-ICP-MS) for Quantification of Iron Redox Species (Fe(II), Fe(III)), JoVE (2020). https://doi.org/10.3791/61055-v.

[239] X.-M. Dong, P. Wu, L.-H. Cheng, L. Shou, H. Dong, X.-Y. Chen, H.-J. Gao, J.-X. Chen, F. Xiang, Q. Zhang, D.-H. Zhang, J.-L. Zhou, T. Xie, Targeted profiling of polar metabolites in cancer metabolic reprogramming by hydrophilic interaction liquid chromatography-tandem mass spectrometry, J. Chromatogr. A 1686 (2022) 463654. https://doi.org/10.1016/j.chroma.2022.463654.

[240] S. Zeitler, F. Schumacher, J. Monti, D. Anni, D. Guhathakurta, B. Kleuser, K. Friedland, A. Fejtová, J. Kornhuber, C. Rhein, Acid Sphingomyelinase Impacts Canonical Transient Receptor Potential Channels 6 (TRPC6) Activity in Primary Neuronal Systems, Cells 9 (2020). https://doi.org/10.3390/cells9112502.

[241] E. Naser, S. Kadow, F. Schumacher, Z.H. Mohamed, C. Kappe, G. Hessler, B. Pollmeier, B. Kleuser, C. Arenz, K.A. Becker, E. Gulbins, A. Carpinteiro, Characterization of the small molecule ARC39, a direct and specific inhibitor of acid sphingomyelinase in vitro, J. Lipid Res. 61 (2020) 896–910. https://doi.org/10.1194/jlr.RA120000682.

[242] T. Bonnot, M. Gillard, D. Nagel, A Simple Protocol for Informative Visualization of Enriched Gene Ontology Terms, BIO-PROTOCOL 9 (2019). https://doi.org/10.21769/BioProtoc.3429.

[243] J. de Oliveira, M.B. Denadai, D.L. Costa, Crosstalk between Heme Oxygenase-1 and Iron Metabolism in Macrophages: Implications for the Modulation of Inflammation and Immunity, Antioxidants (Basel) 11 (2022). https://doi.org/10.3390/antiox11050861.

[244] S.J. Dixon, B.R. Stockwell, The role of iron and reactive oxygen species in cell death, Nat. Chem. Biol. 10 (2014) 9–17. https://doi.org/10.1038/nchembio.1416.

[245] F. He, X. Ru, T. Wen, NRF2, a Transcription Factor for Stress Response and Beyond, Int. J. Mol. Sci. 21 (2020). https://doi.org/10.3390/ijms21134777.

[246] S. Tan-Chen, J. Guitton, O. Bourron, H. Le Stunff, E. Hajduch, Sphingolipid Metabolism and Signaling in Skeletal Muscle: From Physiology to Physiopathology, Front. Endocrinol. (Lausanne) 11 (2020) 491. https://doi.org/10.3389/fendo.2020.00491.

[247] M. Levy, A.H. Futerman, Mammalian ceramide synthases, IUBMB Life 62 (2010) 347–356. https://doi.org/10.1002/iub.319.

[248] Z. Sun, C. Gong, J. Ren, X. Zhang, G. Wang, Y. Liu, Y. Ren, Y. Zhao, Q. Yu, Y. Wang, J. Hou, Toxicity of nickel and cobalt in Japanese flounder, Environ. Pollut. 263 (2020) 114516. https://doi.org/10.1016/j.envpol.2020.114516.

[249] L. Gölz, B.C. Buerfent, A. Hofmann, H. Rühl, N. Fricker, W. Stamminger, J. Oldenburg, J. Deschner, A. Hoerauf, M.M. Nöthen, J. Schumacher, M.P. Hübner, A. Jäger, Genome-wide transcriptome induced by nickel in human monocytes, Acta Biomater. 43 (2016) 369–382. https://doi.org/10.1016/j.actbio.2016.07.047.

[250] V. Malard, F. Berenguer, O. Prat, S. Ruat, G. Steinmetz, E. Quemeneur, Global gene expression profiling in human lung cells exposed to cobalt, BMC Genomics 8 (2007) 147. https://doi.org/10.1186/1471-2164-8-147.

[251] J. Zhao, X. Lin, Di Meng, L. Zeng, R. Zhuang, S. Huang, W. Lv, J. Hu, Nrf2 Mediates Metabolic Reprogramming in Non-Small Cell Lung Cancer, Front. Oncol. 10 (2020) 578315. https://doi.org/10.3389/fonc.2020.578315.

[252] B. Yang, H. Cheng, L. Wang, J. Fu, G. Zhang, D. Guan, R. Qi, X. Gao, R. Zhao, Protective roles of NRF2 signaling pathway in cobalt chloride-induced hypoxic cytotoxicity in human HaCaT keratinocytes, Toxicol. Appl. Pharmacol. 355 (2018) 189–197. https://doi.org/10.1016/j.taap.2018.06.030.

[253] J. Yu, H. Yang, B. Fang, Z. Zhang, Y. Wang, Y. Dai, mfat-1 transgene protects cultured adult neural stem cells against cobalt chloride-mediated hypoxic injury by activating Nrf2/ARE pathways, J. Neurosci. Res. 96 (2018) 87–102. https://doi.org/10.1002/jnr.24096.

[254] J.B. Lewis, R.L.W. Messer, L. Pitts, S.D. Hsu, J.M. Hansen, J.C. Wataha, Ni(II) ions dysregulate cytokine secretion from human monocytes, J. Biomed. Mater. Res. B Appl. Biomater. 88 (2009) 358–365. https://doi.org/10.1002/jbm.b.31063.

[255] T. Saito, Y. Ichimura, K. Taguchi, T. Suzuki, T. Mizushima, K. Takagi, Y. Hirose, M. Nagahashi, T. Iso, T. Fukutomi, M. Ohishi, K. Endo, T. Uemura, Y. Nishito, S. Okuda, M. Obata, T. Kouno, R. Imamura, Y. Tada, R. Obata, D. Yasuda, K. Takahashi, T. Fujimura, J. Pi, M.-S. Lee, T. Ueno, T. Ohe, T. Mashino, T. Wakai, H. Kojima, T. Okabe, T. Nagano, H. Motohashi, S. Waguri, T. Soga, M. Yamamoto, K. Tanaka, M. Komatsu, p62/Sqstm1 promotes malignancy of HCV-positive hepatocellular carcinoma through Nrf2-dependent metabolic reprogramming, Nat. Commun. 7 (2016) 12030. https://doi.org/10.1038/ncomms12030.

[256] H. Huang, J. Zhu, Y. Li, L. Zhang, J. Gu, Q. Xie, H. Jin, X. Che, J. Li, C. Huang, L.-C. Chen, J. Lyu, J. Gao, C. Huang, Upregulation of SQSTM1/p62 contributes to nickel-induced malignant transformation of human bronchial

epithelial cells, Autophagy 12 (2016) 1687–1703. https://doi.org/10.1080/15548627.2016.1196313.

[257] P. Maxwell, K. Salnikow, HIF-1: an oxygen and metal responsive transcription factor, Cancer Biol. Ther. 3 (2004) 29–35. https://doi.org/10.4161/cbt.3.1.547.

[258] X. Ji, H. Wang, J. Zhu, L. Zhu, H. Pan, W. Li, Y. Zhou, Z. Cong, F. Yan, S. Chen, Knockdown of Nrf2 suppresses glioblastoma angiogenesis by inhibiting hypoxia-induced activation of HIF-1α, Int. J. Cancer 135 (2014) 574–584. https://doi.org/10.1002/ijc.28699.

[259] T.-H. Kim, E. Hur, S.-J. Kang, J.-A. Kim, D. Thapa, Y.M. Lee, S.K. Ku, Y. Jung, M.-K. Kwak, NRF2 blockade suppresses colon tumor angiogenesis by inhibiting hypoxia-induced activation of HIF-1α, Cancer Research 71 (2011) 2260–2275. https://doi.org/10.1158/0008-5472.CAN-10-3007.

[260] B.-W. Huang, M. Miyazawa, Y. Tsuji, Distinct regulatory mechanisms of the human ferritin gene by hypoxia and hypoxia mimetic cobalt chloride at the transcriptional and post-transcriptional levels, Cell. Signal. 26 (2014) 2702–2709. https://doi.org/10.1016/j.cellsig.2014.08.018.

[261] E. Forti, S. Salovaara, Y. Cetin, A. Bulgheroni, R. Tessadri, P. Jennings, W. Pfaller, P. Prieto, In vitro evaluation of the toxicity induced by nickel soluble and particulate forms in human airway epithelial cells, Toxicol. In Vitro 25 (2011) 454–461. https://doi.org/10.1016/j.tiv.2010.11.013.

[262] V.I. Sayin, S.E. LeBoeuf, S.X. Singh, S.M. Davidson, D. Biancur, B.S. Guzelhan, S.W. Alvarez, W.L. Wu, T.R. Karakousi, A.M. Zavitsanou, J. Ubriaco, A. Muir, D. Karagiannis, P.J. Morris, C.J. Thomas, R. Possemato, M.G. Vander Heiden, T. Papagiannakopoulos, Activation of the NRF2 antioxidant program generates an imbalance in central carbon metabolism in cancer, Elife 6 (2017). https://doi.org/10.7554/eLife.28083.

[263] Y. Mitsuishi, K. Taguchi, Y. Kawatani, T. Shibata, T. Nukiwa, H. Aburatani, M. Yamamoto, H. Motohashi, Nrf2 redirects glucose and glutamine into

anabolic pathways in metabolic reprogramming, Cancer Cell 22 (2012) 66–79. https://doi.org/10.1016/j.ccr.2012.05.016.

[264] R. Romero, V.I. Sayin, S.M. Davidson, M.R. Bauer, S.X. Singh, S.E. LeBoeuf, T.R. Karakousi, D.C. Ellis, A. Bhutkar, F.J. Sánchez-Rivera, L. Subbaraj, B. Martinez, R.T. Bronson, J.R. Prigge, E.E. Schmidt, C.J. Thomas, C. Goparaju, A. Davies, I. Dolgalev, A. Heguy, V. Allaj, J.T. Poirier, A.L. Moreira, C.M. Rudin, H.I. Pass, M.G. Vander Heiden, T. Jacks, T. Papagiannakopoulos, Keap1 loss promotes Kras-driven lung cancer and results in dependence on glutaminolysis, Nat. Med. 23 (2017) 1362–1368. https://doi.org/10.1038/nm.4407.

[265] C.-S. Shin, P. Mishra, J.D. Watrous, V. Carelli, M. D'Aurelio, M. Jain, D.C. Chan, The glutamate/cystine xCT antiporter antagonizes glutamine metabolism and reduces nutrient flexibility, Nat. Commun. 8 (2017) 15074. https://doi.org/10.1038/ncomms15074.

[266] R.J. DeBerardinis, N.S. Chandel, We need to talk about the Warburg effect, Nat. Metab. 2 (2020) 127–129. https://doi.org/10.1038/s42255-020-0172-2.

[267] H.-S. Zhang, G.-Y. Du, Z.-G. Zhang, Z. Zhou, H.-L. Sun, X.-Y. Yu, Y.-T. Shi, D.-N. Xiong, H. Li, Y.-H. Huang, NRF2 facilitates breast cancer cell growth via HIF1α-mediated metabolic reprogramming, Int. J. Biochem. Cell Biol. 95 (2018) 85–92. https://doi.org/10.1016/j.biocel.2017.12.016.

[268] Y.A. Hannun, L.M. Obeid, Sphingolipids and their metabolism in physiology and disease, Nat. Rev. Mol. Cell Biol. 19 (2018) 175–191. https://doi.org/10.1038/nrm.2017.107.

[269] M. Bellouard, M. Gasser, S. Lenglet, F. Gilardi, N. Bararpour, M. Augsburger, A. Thomas, J.-C. Alvarez, Toxicity and Metabolomic Impact of Cobalt, Chromium, and Nickel Exposure on HepaRG Hepatocytes, Chem. Res. Toxicol. 35 (2022) 807–816. https://doi.org/10.1021/acs.chemrestox.1c00429.

[270] F. Lachkar, P. Ferré, F. Foufelle, A. Papaioannou, Dihydroceramides: their emerging physiological roles and functions in cancer and metabolic diseases,

Am. J. Physiol. Endocrinol. Metab. 320 (2021) E122-E130. https://doi.org/10.1152/ajpendo.00330.2020.

[271] M.M. Siddique, Y. Li, L. Wang, J. Ching, M. Mal, O. Ilkayeva, Y.J. Wu, B.H. Bay, S.A. Summers, Ablation of dihydroceramide desaturase 1, a therapeutic target for the treatment of metabolic diseases, simultaneously stimulates anabolic and catabolic signaling, Mol. Cell. Biol. 33 (2013) 2353–2369. https://doi.org/10.1128/MCB.00226-13.

[272] C.M. Devlin, T. Lahm, W.C. Hubbard, M. van Demark, K.C. Wang, X. Wu, A. Bielawska, L.M. Obeid, M. Ivan, I. Petrache, Dihydroceramide-based response to hypoxia, J. Biol. Chem. 286 (2011) 38069–38078. https://doi.org/10.1074/jbc.M111.297994.

[273] S. Alers, A.S. Löffler, S. Wesselborg, B. Stork, Role of AMPK-mTOR-Ulk1/2 in the regulation of autophagy: cross talk, shortcuts, and feedbacks, Mol. Cell. Biol. 32 (2012) 2–11. https://doi.org/10.1128/MCB.06159-11.

[274] S. Hernández-Tiedra, G. Fabriàs, D. Dávila, Í.J. Salanueva, J. Casas, L.R. Montes, Z. Antón, E. García-Taboada, M. Salazar-Roa, M. Lorente, J. Nylandsted, J. Armstrong, I. López-Valero, C.S. McKee, A. Serrano-Puebla, R. García-López, J. González-Martínez, J.L. Abad, K. Hanada, P. Boya, F. Goñi, M. Guzmán, P. Lovat, M. Jäättelä, A. Alonso, G. Velasco, Dihydroceramide accumulation mediates cytotoxic autophagy of cancer cells via autolysosome destabilization, Autophagy 12 (2016) 2213–2229. https://doi.org/10.1080/15548627.2016.1213927.

[275] E. Petsouki, S.N.S. Cabrera, E.H. Heiss, AMPK and NRF2: Interactive players in the same team for cellular homeostasis?, Free Radic. Biol. Med. 190 (2022) 75–93. https://doi.org/10.1016/j.freeradbiomed.2022.07.014.

[276] C.R. Vieira, J.M. Munoz-Olaya, J. Sot, S. Jiménez-Baranda, N. Izquierdo-Useros, J.L. Abad, B. Apellániz, R. Delgado, J. Martinez-Picado, A. Alonso, J. Casas, J.L. Nieva, G. Fabriás, S. Mañes, F.M. Goñi, Dihydrosphingomyelin impairs HIV-1 infection by rigidifying liquid-ordered membrane domains,

Chem. Biol. 17 (2010) 766–775. https://doi.org/10.1016/j.chembiol.2010.05.023.

[277] M. Kinoshita, T. Kyo, N. Matsumori, Assembly formation of minor dihydrosphingomyelin in sphingomyelin-rich ordered membrane domains, Sci. Rep. 10 (2020) 11794. https://doi.org/10.1038/s41598-020-68688-7.

[278] H. Tallima, H.M.E. Azzazy, R. El Ridi, Cell surface sphingomyelin: key role in cancer initiation, progression, and immune evasion, Lipids Health Dis. 20 (2021) 150. https://doi.org/10.1186/s12944-021-01581-y.

[279] K. Kolczynska, A. Loza-Valdes, I. Hawro, G. Sumara, Diacylglycerol-evoked activation of PKC and PKD isoforms in regulation of glucose and lipid metabolism: a review, Lipids Health Dis. 19 (2020) 113. https://doi.org/10.1186/s12944-020-01286-8.

[280] K. Lakatos, S. Kalomoiris, B. Merkely, J.A. Nolta, F.A. Fierro, Mesenchymal Stem Cells Respond to Hypoxia by Increasing Diacylglycerols, J. Cell. Biochem. 117 (2016) 300–307. https://doi.org/10.1002/jcb.25292.

[281] M. Matzinger, K. Fischhuber, E.H. Heiss, Activation of Nrf2 signaling by natural products-can it alleviate diabetes?, Biotechnol. Adv. 36 (2018) 1738–1767. https://doi.org/10.1016/j.biotechadv.2017.12.015.

[282] IARC, Arsenic, Metals, Fibres, and Dusts, Volume tenth0 C, IARC Monographs on the Evaluation of Carcinogenic Risks to Humans, 2012.

[283] National Toxicology Program, Report on Carcinogens Monograph on Cobalt and Cobalt Compounds That Release Cobalt Ions In Vivo: RoC Monograph 06, Research Triangle Park (NC), 2016.

[284] L.J. Smith, A.L. Holmes, S.K. Kandpal, M.D. Mason, T. Zheng, J.P. Wise, The cytotoxicity and genotoxicity of soluble and particulate cobalt in human lung fibroblast cells, Toxicol. Appl. Pharmacol. 278 (2014) 259–265. https://doi.org/10.1016/j.taap.2014.05.002.

[285] H. Xie, L.J. Smith, A.L. Holmes, T. Zheng, J. Pierce Wise, The cytotoxicity and genotoxicity of soluble and particulate cobalt in human lung epithelial

cells, Environ. Mol. Mutagen. 57 (2016) 282–287. https://doi.org/10.1002/em.22009.

[286] T. Schwerdtle, A. Hartwig, Bioavailability and genotoxicity of soluble and particulate nickel compounds in cultured human lung cells, Materialwissenschaft Werkst 37 (2006) 521–525. https://doi.org/10.1002/mawe.200600030.

[287] M.M. Nicolai, B. Witt, A. Hartwig, T. Schwerdtle, J. Bornhorst, A fast and reliable method for monitoring genomic instability in the model organism Caenorhabditis elegans, Arch. Toxicol. 95 (2021) 3417–3424. https://doi.org/10.1007/s00204-021-03144-7.

[288] Test No. 487: In Vitro Mammalian Cell Micronucleus Test, OECD, 2023.

[289] J. Bornhorst, F. Ebert, H. Lohren, H.-U. Humpf, U. Karst, T. Schwerdtle, Effects of manganese and arsenic species on the level of energy related nucleotides in human cells, Metallomics 4 (2012) 297–306. https://doi.org/10.1039/c2mt00164k.

[290] J.A. Roth, C. Horbinski, L. Feng, K.G. Dolan, D. Higgins, M.D. Garrick, Differential localization of divalent metal transporter 1 with and without iron response element in rat PC12 and sympathetic neuronal cells, J. Neurosci. 20 (2000) 7595–7601. https://doi.org/10.1523/JNEUROSCI.20-20-07595.2000.

[291] S.A.S. Langie, A. Azqueta, A.R. Collins, The comet assay: past, present, and future, Front. Genet. 6 (2015) 266. https://doi.org/10.3389/fgene.2015.00266.

[292] D. Kirkland, T. Brock, H. Haddouk, V. Hargeaves, M. Lloyd, S. Mc Garry, R. Proudlock, S. Sarlang, K. Sewald, G. Sire, A. Sokolowski, C. Ziemann, New investigations into the genotoxicity of cobalt compounds and their impact on overall assessment of genotoxic risk, Regul. Toxicol. Pharmacol. 73 (2015) 311–338. https://doi.org/10.1016/j.yrtph.2015.07.016.

[293] C. Uboldi, T. Orsière, C. Darolles, V. Aloin, V. Tassistro, I. George, V. Malard, Poorly soluble cobalt oxide particles trigger genotoxicity via multiple

pathways, Part. Fibre Toxicol. 13 (2016) 5. https://doi.org/10.1186/s12989-016-0118-8.

[294] A. Sharma, K. Singh, A. Almasan, Histone H2AX phosphorylation: a marker for DNA damage, Methods Mol. Biol. 920 (2012) 613–626. https://doi.org/10.1007/978-1-61779-998-3_40.

[295] B. Kopp, D. Zalko, M. Audebert, Genotoxicity of 11 heavy metals detected as food contaminants in two human cell lines, Environ. Mol. Mutagen. 59 (2018) 202–210. https://doi.org/10.1002/em.22157.

[296] S.E. Scanlon, C.D. Scanlon, D.C. Hegan, P.L. Sulkowski, P.M. Glazer, Nickel induces transcriptional down-regulation of DNA repair pathways in tumorigenic and non-tumorigenic lung cells, Carcinogenesis 38 (2017) 627–637. https://doi.org/10.1093/carcin/bgx038.

[297] R. Colognato, A. Bonelli, J. Ponti, M. Farina, E. Bergamaschi, E. Sabbioni, L. Migliore, Comparative genotoxicity of cobalt nanoparticles and ions on human peripheral leukocytes in vitro, Mutagenesis 23 (2008) 377–382. https://doi.org/10.1093/mutage/gen024.

[298] R.M. Speer, T. The, H. Xie, L. Liou, R.M. Adam, J.P. Wise, The Cytotoxicity and Genotoxicity of Particulate and Soluble Cobalt in Human Urothelial Cells, Biol. Trace Elem. Res. 180 (2017) 48–55. https://doi.org/10.1007/s12011-017-0989-z.

[299] S. Terpilowska, A.K. Siwicki, Interactions between chromium(III) and iron(III), molybdenum(III) or nickel(II): Cytotoxicity, genotoxicity and mutagenicity studies, Chemosphere 201 (2018) 780–789. https://doi.org/10.1016/j.chemosphere.2018.03.062.

[300] S. Di Bucchianico, A.R. Gliga, E. Åkerlund, S. Skoglund, I.O. Wallinder, B. Fadeel, H.L. Karlsson, Calcium-dependent cyto- and genotoxicity of nickel metal and nickel oxide nanoparticles in human lung cells, Part. Fibre Toxicol. 15 (2018) 32. https://doi.org/10.1186/s12989-018-0268-y.

[301] I.A. Vorobjev, S. Bekbayev, A. Temirgaliyev, M. Tlegenova, N.S. Barteneva, Imaging Flow Cytometry of Multi-Nuclearity, Methods Mol. Biol. 2635 (2023) 87–101. https://doi.org/10.1007/978-1-0716-3020-4_5.

[302] H. Guo, H. Deng, H. Liu, Z. Jian, H. Cui, J. Fang, Z. Zuo, J. Deng, Y. Li, X. Wang, L. Zhao, Nickel carcinogenesis mechanism: cell cycle dysregulation, Environ. Sci. Pollut. Res. Int. 28 (2021) 4893–4901. https://doi.org/10.1007/s11356-020-11764-2.

[303] N.K. Rana, P. Singh, B. Koch, CoCl2 simulated hypoxia induce cell proliferation and alter the expression pattern of hypoxia associated genes involved in angiogenesis and apoptosis, Biol. Res. 52 (2019) 12. https://doi.org/10.1186/s40659-019-0221-z.

[304] W. Wang, Y. Li, X. Liu, M. Jin, H. Du, Y. Liu, P. Huang, X. Zhou, L. Yuan, Z. Sun, Multinucleation and cell dysfunction induced by amorphous silica nanoparticles in an L-02 human hepatic cell line, Int. J. Nanomedicine 8 (2013) 3533–3541. https://doi.org/10.2147/IJN.S46732.

[305] A. Agarwal, R.Z. Mahfouz, R.K. Sharma, O. Sarkar, D. Mangrola, P.P. Mathur, Potential biological role of poly (ADP-ribose) polymerase (PARP) in male gametes, Reprod. Biol. Endocrinol. 7 (2009) 143. https://doi.org/10.1186/1477-7827-7-143.

[306] A. Bürkle, Physiology and pathophysiology of poly(ADP-ribosyl)ation, Bioessays 23 (2001) 795–806. https://doi.org/10.1002/bies.1115.

[307] L. Gómez-Virgilio, A. Luarte, D.P. Ponce, B.A. Bruna, M.I. Behrens, Analyzing Olfactory Neuron Precursors Non-Invasively Isolated through NADH FLIM as a Potential Tool to Study Oxidative Stress in Alzheimer's Disease, Int. J. Mol. Sci. 22 (2021). https://doi.org/10.3390/ijms22126311.

[308] K. Yan, Q. He, D. Lin, J. Liang, J. Chen, Z. Xie, Z. Chen, Promotion of NAD+ recycling by the hypoxia-induced shift in the lactate dehydrogenase isozyme profile reduces the senescence of human bone marrow-derived endothelial progenitor cells, Free Radic. Biol. Med. 208 (2023) 88–102. https://doi.org/10.1016/j.freeradbiomed.2023.07.035.

[309] G.R. Steinberg, D.G. Hardie, New insights into activation and function of the AMPK, Nat. Rev. Mol. Cell Biol. 24 (2023) 255–272. https://doi.org/10.1038/s41580-022-00547-x.

[310] S. Owada, H. Endo, Y. Shida, C. Okada, K. Ito, T. Nezu, M. Tatemichi, Autophagy-mediated adaptation of hepatocellular carcinoma cells to hypoxia-mimicking conditions constitutes an attractive therapeutic target, Oncol. Rep. 39 (2018) 1805–1812. https://doi.org/10.3892/or.2018.6279.

[311]I. Buchmann, Types of Lithium-ion, Battery University 627 (2012).

[312] A. Manthiram, An Outlook on Lithium Ion Battery Technology, ACS Cent. Sci. 3 (2017) 1063–1069. https://doi.org/10.1021/acscentsci.7b00288.

[313] R. Maurya, A.K. Pandey, Importance of protozoa Tetrahymena in toxicological studies: A review, Sci. Total Environ. 741 (2020) 140058. https://doi.org/10.1016/j.scitotenv.2020.140058.

[314] D.H. Lynn, G.L. Gilron, A brief review of approaches using ciliated protists to assess aquatic ecosystem health, J Aquat Ecosyst Stress Recov 1 (1992) 263–270. https://doi.org/10.1007/BF00044168.

[315] J.C. Gutiérrez, A. Martín-González, S. Díaz, F. Amaro, R. Ortega, A. Gallego, M.P. de Lucas, Ciliates as cellular tools to study the eukaryotic cell: Heavy metal interactions, in: Heavy Metal Pollution, 2008, pp. 1–44.

[316] M. Simon, H. Plattner, Unicellular eukaryotes as models in cell and molecular biology: critical appraisal of their past and future value, Int. Rev. Cell Mol. Biol. 309 (2014) 141–198. https://doi.org/10.1016/B978-0-12-800255-1.00003-X.

[317] F. Drews, J. Boenigk, M. Simon, Paramecium epigenetics in development and proliferation, J. Eukaryot. Microbiol. 69 (2022) e12914. https://doi.org/10.1111/jeu.12914.

[318] O. Arnaiz, E. Meyer, L. Sperling, ParameciumDB 2019: integrating genomic data across the genus for functional and evolutionary biology, Nucleic Acids Res. 48 (2020) D599-D605. https://doi.org/10.1093/nar/gkz948.

[319] N.A. Stover, R.S. Punia, M.S. Bowen, S.B. Dolins, T.G. Clark, Tetrahymena Genome Database Wiki: a community-maintained model organism database, Database (Oxford) 2012 (2012) bas007. https://doi.org/10.1093/database/bas007.

[320] D.T. Szabo, A.A. Devlin, Transcriptomic Biomarkers in Safety and Risk Assessment of Chemicals, in: Biomarkers in Toxicology, Elsevier, 2019, pp. 1125–1134.

[321] D.E. Marco, F. Abram, Editorial: Using Genomics, Metagenomics and Other "Omics" to Assess Valuable Microbial Ecosystem Services and Novel Biotechnological Applications, Front. Microbiol. 10 (2019) 151. https://doi.org/10.3389/fmicb.2019.00151.

[322] J. Beisson, M. Bétermier, M.-H. Bré, J. Cohen, S. Duharcourt, L. Duret, C. Kung, S. Malinsky, E. Meyer, J.R. Preer, L. Sperling, Mass culture of Paramecium tetraurelia, Cold Spring Harb. Protoc. 2010 (2010) pdb.prot5362. https://doi.org/10.1101/pdb.prot5362.

[323] M.C. Simon, S. Marker, H.J. Schmidt, Inefficient serotype knock down leads to stable coexistence of different surface antigens on the outer membrane in Paramecium tetraurelia, Eur. J. Protistol. 42 (2006) 49–53. https://doi.org/10.1016/j.ejop.2005.09.003.

[324] F. Drews, S. Karunanithi, U. Götz, S. Marker, R. deWijn, M. Pirritano, A.M. Rodrigues-Viana, M. Jung, G. Gasparoni, M.H. Schulz, M. Simon, Two Piwis with Ago-like functions silence somatic genes at the chromatin level, RNA Biol. 18 (2021) 757–769. https://doi.org/10.1080/15476286.2021.1991114.

[325] I. AAT Bioquest, Ld50 Calculator, 2023. https://www.aatbio.com/tools/ld50-calculator (accessed 13 September 2023).

[326] M. Cheaib, A. Dehghani Amirabad, K.J.V. Nordström, M.H. Schulz, M. Simon, Epigenetic regulation of serotype expression antagonizes transcriptome dynamics in Paramecium tetraurelia, DNA Res. 22 (2015) 293–305. https://doi.org/10.1093/dnares/dsv014.

[327] T.S. Love, T. Loveland, Exploring the Proposition of a Joint Conference Between State Science, and Technology and Engineering Education Associations, JTE 26 (2014). https://doi.org/10.21061/jte.v26i1.a.1.

[328] V. Jalili, E. Afgan, Q. Gu, D. Clements, D. Blankenberg, J. Goecks, J. Taylor, A. Nekrutenko, The Galaxy platform for accessible, reproducible and collaborative biomedical analyses: 2020 update, Nucleic Acids Res. 48 (2020) W395-W402. https://doi.org/10.1093/nar/gkaa434.

[329] M.C. Simon, J. Kusch, Communicative functions of GPI-anchored surface proteins in unicellular eukaryotes, Crit. Rev. Microbiol. 39 (2013) 70–78. https://doi.org/10.3109/1040841X.2012.691459.

[330] E. Staudt, P. Ramasamy, H. Plattner, M. Simon, Differential subcellular distribution of four phospholipase C isoforms and secretion of GPI-PLC activity, Biochim. Biophys. Acta 1858 (2016) 3157–3168. https://doi.org/10.1016/j.bbamem.2016.09.022.

[331] G. Leondaritis, D. Galanopoulou, Characterization of inositol phospholipids and identification of a mastoparan-induced polyphosphoinositide response in Tetrahymena pyriformis, Lipids 35 (2000) 525–532. https://doi.org/10.1007/s11745-000-552-8.

[332] G. Leondaritis, A. Tiedtke, D. Galanopoulou, D-3 phosphoinositides of the ciliate Tetrahymena: characterization and study of their regulatory role in lysosomal enzyme secretion, Biochim. Biophys. Acta 1745 (2005) 330–341. https://doi.org/10.1016/j.bbamcr.2005.06.011.

[333] D.A. Dickinson, H.J. Forman, Cellular glutathione and thiols metabolism, Biochem. Pharmacol. 64 (2002) 1019–1026. https://doi.org/10.1016/S0006-2952(02)01172-3.

[334] T.J. Beveridge, W.S. Fyfe, Metal fixation by bacterial cell walls, Can. J. Earth Sci. 22 (1985) 1893–1898. https://doi.org/10.1139/e85-204.

[335] K. Mathivanan, J.U. Chandirika, A. Vinothkanna, H. Yin, X. Liu, D. Meng, Bacterial adaptive strategies to cope with metal toxicity in the contaminated

environment - A review, Ecotoxicol. Environ. Saf. 226 (2021) 112863. https://doi.org/10.1016/j.ecoenv.2021.112863.

[336] F. Azam, T. Fenchel, J.G. Field, J.S. Gray, La Meyer-Reil, F. Thingstad, The Ecological Role of Water-Column Microbes in the Sea, Mar. Ecol. Prog. Ser. 10 (1983) 257–263. https://doi.org/10.3354/meps010257.

[337] T. Fenchel, The microbial loop – 25 years later, Journal of Experimental Marine Biology and Ecology 366 (2008) 99–103. https://doi.org/10.1016/j.jembe.2008.07.013.

[338] M. Bonkowski, Protozoa and plant growth: the microbial loop in soil revisited, New Phytol. 162 (2004) 617–631. https://doi.org/10.1111/j.1469-8137.2004.01066.x.

[339] R. Wichterman, The Nutritional Requirements of Paramecium: Axenic Media, in: R. Wichterman (Ed.), The Biology of Paramecium, Springer US, Boston, MA, 1986, pp. 181–196.

[340] V. Kumar, R.K. Mishra, G. Kaur, D. Dutta, Cobalt and nickel impair DNA metabolism by the oxidative stress independent pathway, Metallomics 9 (2017) 1596–1609. https://doi.org/10.1039/c7mt00231a.

[341] A.D. Gaspar, S. Cuddapah, Nickel-induced alterations to chromatin structure and function, Toxicol. Appl. Pharmacol. 457 (2022) 116317. https://doi.org/10.1016/j.taap.2022.116317.

[342] J.D. Berger, The Cell Cycle and Regulation of Cell Mass and Macronuclear DNA Content, in: H.-D. Görtz (Ed.), Paramecium, Springer Berlin Heidelberg, Berlin, Heidelberg, 1988, pp. 97–119.

[343] A. Fariq, T. Khan, A. Yasmin, Microbial synthesis of nanoparticles and their potential applications in biomedicine, J. Appl. Biomed. 15 (2017) 241–248. https://doi.org/10.1016/j.jab.2017.03.004.

[344] M. Guilger-Casagrande, R. de Lima, Synthesis of Silver Nanoparticles Mediated by Fungi: A Review, Front. Bioeng. Biotechnol. 7 (2019) 287. https://doi.org/10.3389/fbioe.2019.00287.

[345] S. Anil Kumar, M.K. Abyaneh, S.W. Gosavi, S.K. Kulkarni, R. Pasricha, A. Ahmad, M.I. Khan, Nitrate reductase-mediated synthesis of silver nanoparticles from AgNO3, Biotechnol. Lett. 29 (2007) 439–445. https://doi.org/10.1007/s10529-006-9256-7.

[346] J. Kohl, M. Schweikert, N. Klaas, M.-L. Lemloh, Intracellular bioaccumulation of the rare earth element Gadolinium in ciliate cells resulting in biogenic particle formation and excretion, Sci. Rep. 13 (2023) 5650. https://doi.org/10.1038/s41598-023-32596-3.

[347] M.S. John, J.A. Nagoth, K.P. Ramasamy, P. Ballarini, M. Mozzicafreddo, A. Mancini, A. Telatin, P. Liò, G. Giuli, A. Natalello, C. Miceli, S. Pucciarelli, Horizontal gene transfer and silver nanoparticles production in a new Marinomonas strain isolated from the Antarctic psychrophilic ciliate Euplotes focardii, Sci. Rep. 10 (2020) 10218. https://doi.org/10.1038/s41598-020-66878-x.

[348] M.S. John, J.A. Nagoth, K.P. Ramasamy, A. Mancini, G. Giuli, A. Natalello, P. Ballarini, C. Miceli, S. Pucciarelli, Synthesis of Bioactive Silver Nanoparticles by a Pseudomonas Strain Associated with the Antarctic Psychrophilic Protozoon Euplotes focardii, Mar. Drugs 18 (2020). https://doi.org/10.3390/md18010038.

[349] A. Piersanti, K. Juganson, M. Mozzicafreddo, W. Wei, J. Zhang, K. Zhao, P. Ballarini, M. Mortimer, S. Pucciarelli, W. Miao, C. Miceli, Transcriptomic responses to silver nanoparticles in the freshwater unicellular eukaryote Tetrahymena thermophila, Environ. Pollut. 269 (2021) 115965. https://doi.org/10.1016/j.envpol.2020.115965.

[350] U. Garg, Y.V. Zhang, Mass Spectrometry in Clinical Laboratory: Applications in Biomolecular Analysis, Methods Mol. Biol. 1378 (2016) 1–9. https://doi.org/10.1007/978-1-4939-3182-8_1.

[351] L. Kubens, A.-K. Weishaupt, V. Michaelis, I. Rohn, F. Mohr, J. Bornhorst, Exposure to the environmentally relevant fungicide Maneb: Studying toxicity

in the soil nematode Caenorhabditis elegans, Environ. Int. 183 (2024) 108372. https://doi.org/10.1016/j.envint.2023.108372.

[352] A. Tan, S. Hussain, A. Musuku, R. Massé, Internal standard response variations during incurred sample analysis by LC-MS/MS: Case by case trouble-shooting, J. Chromatogr. B Analyt. Technol. Biomed. Life Sci. 877 (2009) 3201–3209. https://doi.org/10.1016/j.jchromb.2009.08.019.

[353] M. Langner, D. Fröbel, J. Helm, T. Chavakis, M. Peitzsch, N. Bechmann, Accurate redox state indication by in situ derivatization with N-ethylmaleimide - Profiling of transsulfuration and glutathione pathway metabolites by UPLC-MS/MS, J. Chromatogr. B Analyt. Technol. Biomed. Life Sci. 1236 (2024) 124062. https://doi.org/10.1016/j.jchromb.2024.124062.

[354] X.-L. Qin, S.-Y. Wang, Q.-L. Li, J.-J. Wang, Z.-W. Yao, J.-H. Zhu, L.-X. Chen, J.-G. Huo, S.-L. Li, J. Zhou, H. Zhu, 2024. A robust ultra-performance liquid chromatography-tandem mass spectrometry method for simultaneous determination of 10 components in glutathione cycle. J of Separation Science 47, 2400247. https://doi.org/10.1002/jssc.202400247.

[355] K. Serafimov, Y. Aydin, M. Lämmerhofer, Quantitative analysis of the glutathione pathway cellular metabolites by targeted liquid chromatography-tandem mass spectrometry, J of Separation Science 47 (2024) e2300780. https://doi.org/10.1002/jssc.202300780.

[356] Q. Tan, X. Zhang, S. Li, W. Liu, J. Yan, S. Wang, F. Cui, D. Li, J. Li, DMT1 differentially regulates mitochondrial complex activities to reduce glutathione loss and mitigate ferroptosis, Free Radic. Biol. Med. 207 (2023) 32–44. https://doi.org/10.1016/j.freeradbiomed.2023.06.023.

[357] D.I. Bannon, R. Abounader, P.S.J. Lees, J.P. Bressler, Effect of DMT1 knockdown on iron, cadmium, and lead uptake in Caco-2 cells, Am. J. Physiol. Cell Physiol. 284 (2003) C44-50. https://doi.org/10.1152/ajpcell.00184.2002.

[358] K.M. Dean, Y. Qin, A.E. Palmer, Visualizing metal ions in cells: an overview of analytical techniques, approaches, and probes, Biochim. Biophys. Acta 1823 (2012) 1406–1415. https://doi.org/10.1016/j.bbamcr.2012.04.001.

[359] Y.-Q. Gu, W.-Y. Shen, Y. Zhou, S.-F. Chen, Y. Mi, B.-F. Long, D.J. Young, F.-L. Hu, A pyrazolopyrimidine based fluorescent probe for the detection of Cu2+ and Ni2+ and its application in living cells, Spectrochim. Acta A Mol. Biomol. Spectrosc. 209 (2019) 141–149. https://doi.org/10.1016/j.saa.2018.10.030.

[360] H.Y. Au-Yeung, E.J. New, C.J. Chang, A selective reaction-based fluorescent probe for detecting cobalt in living cells, Chem. Commun. (Camb) 48 (2012) 5268–5270. https://doi.org/10.1039/c2cc31681a.

[361] M. Blumenberg, Introductory Chapter: Transcriptome Analysis, in: M. Blumenberg (Ed.), Transcriptome Analysis, IntechOpen, 2019.

[362] T. Jiang, B. Harder, M. La Rojo de Vega, P.K. Wong, E. Chapman, D.D. Zhang, p62 links autophagy and Nrf2 signaling, Free Radic. Biol. Med. 88 (2015) 199–204. https://doi.org/10.1016/j.freeradbiomed.2015.06.014.

[363] H.R. Potteti, P.M. Noone, C.R. Tamatam, A. Ankireddy, S. Noel, H. Rabb, S.P. Reddy, Nrf2 mediates hypoxia-inducible HIF1α activation in kidney tubular epithelial cells, Am. J. Physiol. Renal Physiol. 320 (2021) F464-F474. https://doi.org/10.1152/ajprenal.00501.2020.

[364] F. Zheng, Z. Luo, C. Zheng, J. Li, J. Zeng, H. Yang, J. Chen, Y. Jin, M. Aschner, S. Wu, Q. Zhang, H. Li, Comparison of the neurotoxicity associated with cobalt nanoparticles and cobalt chloride in Wistar rats, Toxicol. Appl. Pharmacol. 369 (2019) 90–99. https://doi.org/10.1016/j.taap.2019.03.003.

[365] M.J. Kerins, A. Ooi, The Roles of NRF2 in Modulating Cellular Iron Homeostasis, Antioxid. Redox Signal. 29 (2018) 1756–1773. https://doi.org/10.1089/ars.2017.7176.

[366] C.J. Harvey, R.K. Thimmulappa, A. Singh, D.J. Blake, G. Ling, N. Wakabayashi, J. Fujii, A. Myers, S. Biswal, Nrf2-regulated glutathione recycling independent of biosynthesis is critical for cell survival during

oxidative stress, Free Radic. Biol. Med. 46 (2009) 443–453. https://doi.org/10.1016/j.freeradbiomed.2008.10.040.

[367] H.J. Forman, H. Zhang, A. Rinna, Glutathione: overview of its protective roles, measurement, and biosynthesis, Mol. Aspects Med. 30 (2009) 1–12. https://doi.org/10.1016/j.mam.2008.08.006.

[368] X.-X. Gao, C.-H. Liu, Z.-L. Hu, H.-Y. Li, X. Chang, Y.-Y. Li, Y.-Y. Zhang, Y. Zhai, C.-Q. Li, The biological effect of cobalt chloride mimetic-hypoxia on nucleus pulposus cells and the comparability with physical hypoxia in vitro, Front. Biosci. (Landmark Ed) 26 (2021) 799–812. https://doi.org/10.52586/4989].

[369] M.N. Galardo, A. Gorga, J.P. Merlo, M. Regueira, E.H. Pellizzari, S.B. Cigorraga, M.F. Riera, S.B. Meroni, Participation of HIFs in the regulation of Sertoli cell lactate production, Biochimie 132 (2017) 9–18. https://doi.org/10.1016/j.biochi.2016.10.006.

[370] M. Hayashi, M. Sakata, T. Takeda, T. Yamamoto, Y. Okamoto, K. Sawada, A. Kimura, R. Minekawa, M. Tahara, K. Tasaka, Y. Murata, Induction of glucose transporter 1 expression through hypoxia-inducible factor 1alpha under hypoxic conditions in trophoblast-derived cells, J. Endocrinol. 183 (2004) 145–154. https://doi.org/10.1677/joe.1.05599.

[371] J.D. Firth, B.L. Ebert, P.J. Ratcliffe, Hypoxic regulation of lactate dehydrogenase A. Interaction between hypoxia-inducible factor 1 and cAMP response elements, J. Biol. Chem. 270 (1995) 21021–21027. https://doi.org/10.1074/jbc.270.36.21021.

[372] K. Urbańska, A. Orzechowski, Unappreciated Role of LDHA and LDHB to Control Apoptosis and Autophagy in Tumor Cells, Int. J. Mol. Sci. 20 (2019). https://doi.org/10.3390/ijms20092085.

[373] L. Alberghina, The Warburg Effect Explained: Integration of Enhanced Glycolysis with Heterogeneous Mitochondria to Promote Cancer Cell Proliferation, Int. J. Mol. Sci. 24 (2023). https://doi.org/10.3390/ijms242115787.

[374] W. Zheng, J. Kollmeyer, H. Symolon, A. Momin, E. Munter, E. Wang, S. Kelly, J.C. Allegood, Y. Liu, Q. Peng, H. Ramaraju, M.C. Sullards, M. Cabot, A.H. Merrill, Ceramides and other bioactive sphingolipid backbones in health and disease: lipidomic analysis, metabolism and roles in membrane structure, dynamics, signaling and autophagy, Biochim. Biophys. Acta 1758 (2006) 1864–1884. https://doi.org/10.1016/j.bbamem.2006.08.009.

[375] L. Planas-Serra, N. Launay, L. Goicoechea, B. Heron, C. Jou, N. Juliá-Palacios, M. Ruiz, S. Fourcade, C. Casasnovas, C. de La Torre, A. Gelot, M. Marsal, P. Loza-Alvarez, À. García-Cazorla, A. Fatemi, I. Ferrer, M. Portero-Otin, E. Area-Gómez, A. Pujol, Sphingolipid desaturase DEGS1 is essential for mitochondria-associated membrane integrity, J. Clin. Invest. 133 (2023). https://doi.org/10.1172/JCI162957.

[376] N. Niu, Z. Li, M. Zhu, H. Sun, J. Yang, S. Xu, W. Zhao, R. Song, Effects of nuclear respiratory factor-1 on apoptosis and mitochondrial dysfunction induced by cobalt chloride in H9C2 cells, Mol. Med. Rep. 19 (2019) 2153–2163. https://doi.org/10.3892/mmr.2019.9839.

[377] S. Terpilowska, A.K. Siwicki, Cell cycle and transmembrane mitochondrial potential analysis after treatment with chromium(iii), iron(iii), molybdenum(iii) or nickel(ii) and their mixtures, Toxicol. Res. (Camb) 8 (2019) 188–195. https://doi.org/10.1039/c8tx00233a.

[378] S. Creed, M. McKenzie, Measurement of Mitochondrial Membrane Potential with the Fluorescent Dye Tetramethylrhodamine Methyl Ester (TMRM), Methods Mol. Biol. 1928 (2019) 69–76. https://doi.org/10.1007/978-1-4939-9027-6_5.

[379] C. Mas-Bargues, E. García-Domínguez, C. Borrás, Recent Approaches to Determine Static and Dynamic Redox State-Related Parameters, Antioxidants (Basel) 11 (2022). https://doi.org/10.3390/antiox11050864.

[380] R. Filograna, M. Mennuni, D. Alsina, N.-G. Larsson, Mitochondrial DNA copy number in human disease: the more the better?, FEBS Lett. 595 (2021) 976–1002. https://doi.org/10.1002/1873-3468.14021.

[381] S. Sasaki, Determination of altered mitochondria ultrastructure by electron microscopy, Methods Mol. Biol. 648 (2010) 279–290. https://doi.org/10.1007/978-1-60761-756-3_19.

[382] G. Hussain, J. Wang, A. Rasul, H. Anwar, A. Imran, M. Qasim, S. Zafar, S.K.S. Kamran, A. Razzaq, N. Aziz, W. Ahmad, A. Shabbir, J. Iqbal, S.M. Baig, T. Sun, Role of cholesterol and sphingolipids in brain development and neurological diseases, Lipids Health Dis. 18 (2019) 26. https://doi.org/10.1186/s12944-019-0965-z.

[383] J. Massart, J.R. Zierath, Role of Diacylglycerol Kinases in Glucose and Energy Homeostasis, Trends Endocrinol. Metab. 30 (2019) 603–617. https://doi.org/10.1016/j.tem.2019.06.003.

[384] E. Temes, S. Martín-Puig, J. Aragonés, D.R. Jones, G. Olmos, I. Mérida, M.O. Landázuri, Role of diacylglycerol induced by hypoxia in the regulation of HIF-1alpha activity, Biochem. Biophys. Res. Commun. 315 (2004) 44–50. https://doi.org/10.1016/j.bbrc.2004.01.015.

[385] D.J. Smart, J.K. Chipman, N.J. Hodges, Activity of OGG1 variants in the repair of pro-oxidant-induced 8-oxo-2'-deoxyguanosine, DNA Repair (Amst) 5 (2006) 1337–1345. https://doi.org/10.1016/j.dnarep.2006.06.001.

[386] S.L. Habib, A. Yadav, D. Kidane, R.H. Weiss, S. Liang, Novel protective mechanism of reducing renal cell damage in diabetes: Activation AMPK by AICAR increased NRF2/OGG1 proteins and reduced oxidative DNA damage, Cell Cycle 15 (2016) 3048–3059. https://doi.org/10.1080/15384101.2016.1231259.

[387] H.L. Kim, Y.R. Seo, Molecular and genomic approach for understanding the gene-environment interaction between Nrf2 deficiency and carcinogenic nickel-induced DNA damage, Oncol. Rep. 28 (2012) 1959–1967. https://doi.org/10.3892/or.2012.2057.

[388] K. Yoshida, S. Obata, M. Ono, M. Esaki, T. Maejima, H. Sawada, TPA-induced multinucleation of a mesenchymal stem cell-like clone is mediated primarily by karyokinesis without cytokinesis, although cell-cell fusion also

occurs, Eur. J. Cell Biol. 86 (2007) 461–471. https://doi.org/10.1016/j.ejcb.2007.04.003.

[389] Y. Kozutsumi, T. Kanazawa, Y. Sun, T. Yamaji, H. Yamamoto, H. Takematsu, Sphingolipids involved in the induction of multinuclear cell formation, Biochim. Biophys. Acta 1582 (2002) 138–143. https://doi.org/10.1016/s1388-1981(02)00148-8.

[390] C. Fernández, M.V.T. Del Lobo Md, D. Gómez-Coronado, M.A. Lasunción, Cholesterol is essential for mitosis progression and its deficiency induces polyploid cell formation, Exp. Cell Res. 300 (2004) 109–120. https://doi.org/10.1016/j.yexcr.2004.06.029.

[391] J. Menaya, M.J. Clemens, Phorbol ester-induced inhibition of proliferation of Daudi Burkitt's lymphoma cells by impairment of cytokinesis, Exp. Cell Res. 194 (1991) 260–266. https://doi.org/10.1016/0014-4827(91)90363-Y.

[392] K. Yamaguchi, K. Ogita, S. Nakamura, Y. Nishizuka, The protein kinase C isoforms leading to MAP-kinase activation in CHO cells, Biochem. Biophys. Res. Commun. 210 (1995) 639–647. https://doi.org/10.1006/bbrc.1995.1708.

[393] Y. Chen, X. Xu, Y. Wang, Y. Zhang, T. Zhou, W. Jiang, Z. Wang, J. Chang, S. Liu, R. Chen, J. Shan, J. Wang, Y. Wang, C. Li, X. Li, Hypoxia-induced SKA3 promoted cholangiocarcinoma progression and chemoresistance by enhancing fatty acid synthesis via the regulation of PAR-dependent HIF-1a deubiquitylation, J. Exp. Clin. Cancer Res. 42 (2023) 265. https://doi.org/10.1186/s13046-023-02842-7.

[394] J.M. Martí, A. Garcia-Diaz, D. Delgado-Bellido, F. O'Valle, A. González-Flores, O. Carlevaris, J.M. Rodríguez-Vargas, J.C. Amé, F. Dantzer, G.L. King, K. Dziedzic, E. Berra, E. de Álava, A.T. Amaral, E.M. Hammond, F.J. Oliver, Selective modulation by PARP-1 of HIF-1α-recruitment to chromatin during hypoxia is required for tumor adaptation to hypoxic conditions, Redox Biol. 41 (2021) 101885. https://doi.org/10.1016/j.redox.2021.101885.

[395] L.A. Pradelli, E. Villa, B. Zunino, S. Marchetti, J.-E. Ricci, Glucose metabolism is inhibited by caspases upon the induction of apoptosis, Cell Death Dis. 5 (2014) e1406. https://doi.org/10.1038/cddis.2014.371.

[396] G.V. Chaitanya, A.J. Steven, P.P. Babu, PARP-1 cleavage fragments: signatures of cell-death proteases in neurodegeneration, Cell Commun. Signal. 8 (2010) 31. https://doi.org/10.1186/1478-811X-8-31.

[397] H. Lv, C. Zhen, J. Liu, P. Yang, L. Hu, P. Shang, Unraveling the Potential Role of Glutathione in Multiple Forms of Cell Death in Cancer Therapy, Oxid. Med. Cell. Longev. 2019 (2019) 3150145. https://doi.org/10.1155/2019/3150145.

[398] P. Mirabelli, L. Coppola, M. Salvatore, Cancer Cell Lines Are Useful Model Systems for Medical Research, Cancers (Basel) 11 (2019). https://doi.org/10.3390/cancers11081098.

[399] A. Martín-González, S. Díaz, S. Borniquel, A. Gallego, J.C. Gutiérrez, Cytotoxicity and bioaccumulation of heavy metals by ciliated protozoa isolated from urban wastewater treatment plants, Res. Microbiol. 157 (2006) 108–118. https://doi.org/10.1016/j.resmic.2005.06.005.

[400] U. Kumar, M.H. Saier, Comparative genomic analysis of integral membrane transport proteins in ciliates, J. Eukaryot. Microbiol. 62 (2015) 167–187. https://doi.org/10.1111/jeu.12156.

[401] N.S. Chandel, Amino Acid Metabolism, Cold Spring Harb. Perspect. Biol. 13 (2021). https://doi.org/10.1101/cshperspect.a040584.

[402] H.K. Kim, J. Han, Tetrahydrobiopterin in energy metabolism and metabolic diseases, Pharmacol. Res. 157 (2020) 104827. https://doi.org/10.1016/j.phrs.2020.104827.

[403] K.C. Case, M. Salsaa, W. Yu, M.L. Greenberg, Regulation of Inositol Biosynthesis: Balancing Health and Pathophysiology, Handb. Exp. Pharmacol. 259 (2020) 221–260. https://doi.org/10.1007/164_2018_181.

[404] C. Xavier, X. Liu, Y. Liu, H. Wu, The Important Functions of GSH-Dependent Enzyme Glutaredoxin 2 (Grx2), in: P. Erkekoglu, B. Kocer-Gumusel (Eds.), Glutathione in Health and Disease, InTech, 2018.

Acknowledgements

Mit der Fertigstellung dieser Doktorarbeit möchte ich die Gelegenheit nutzen, den vielen Menschen zu danken, die mich auf diesem Weg begleitet und unterstützt haben. Ohne euch wären die letzten Jahre nur halb so lustig und doppelt so schwierig gewesen.

Ein riesengroßes Dankeschön geht an meine Betreuerin Julia Bornhorst. Deine unermüdliche Unterstützung, deine stets gute Laune und deine Begeisterung für jedes noch so kleine Ergebnis haben mich immer wieder aufs Neue motiviert und mir gezeigt, wie spannend Forschung sein kann. Ich bin dir sehr dankbar dafür, dass du mir das Vertrauen gegeben hast, selbstständig an diesem Projekt arbeiten zu dürfen, und ich die Möglichkeit hatte dieses auch auf internationalen Tagungen vorzustellen. Danke für die viele Zeit, die du in die Betreuung meiner Arbeit investiert hast, deine stets offene Bürotür für jede kleinste Frage, und deine konstruktiven Ratschläge.

Ganz besonders möchte ich mich bei Anni, Anna, Vivi und Lauri bedanken. Ich danke euch für eure Unterstützung und die großartige Teamarbeit, ohne die dieses Projekt nicht möglich gewesen wäre. Danke Vivi, dass du mich schon in der Masterarbeit für Zellkultur begeistert hast und wir nun insgesamt 4 Jahre das Labor zusammen schmeißen konnten. Danke für all die lustigen Cincotett-Runden mit euch, wie gemeinsame Kaffeepausen, Spieleabende, Ausflüge, Urlaube und Partys, die wir in den letzten Jahren zusammen erlebt haben!

Ich möchte mich auch bei den beiden Masterstudierenden Marco und Sabrina bedanken. Danke für eure Hilfe und dass ihr einen so großen Teil zu dieser Arbeit beigetragen habt.

Ein großer Dank geht auch an die AG Simon. Vielen lieben Dank Martin, Franzi und Marcello, für eure Hilfe und eure Erklärungen rund um die Transkriptom-Analyse und die Unterstützung beim Schreiben des Papers.

Zudem möchte ich mich bei der AG Schebb für das Mitbenutzen der Labore und Geräte bedanken. Ein großer Dank gilt allen weiteren Kooperationspartnern, insbesondere der Arbeitsgruppe Schwerdtle aus Potsdam, die zu diesem Projekt beigetragen haben.

Ich danke allen vom Doktoranden-Stammtisch für die lustigen Abende in der Kneipe, die zahlreichen kleinen und großen Schlupp-Runden, Pub-Quiz-Siege und gemeinsame Grillpartys.

Außerdem möchte ich mich bei meiner Familie und meinen Freunden außerhalb der Uni für die Unterstützung in den letzten Jahren, und auch schon während des Studiums bedanken. Danke dir, Asti, für dein Verständnis, deine Motivation und deinen Optimismus während der gesamten Zeit.

Danke!

Declaration

This semi-cumulative dissertation comprises nine distinct chapters. The papers presented in chapter 3 – 5 have been published in scientific journals and include all reviewer comments. The manuscripts in chapter 6 and 7 have been submitted and are currently undergoing the peer-reviewing process.

As the leading author of all chapters, I carried out the majority of experiments, data analysis, interpretation, and manuscript preparation myself and conceptualized the studies with my supervisor Julia Bornhorst. Contributions to all co-authors who assisted with each project are acknowledged at the end of each respective chapter.

All statements, methods, and interpretation of other research is properly cited throughout the whole dissertation.

Alicia Thiel